

Approved for public release;
distribution unlimited.

(2)

AD-A277 397



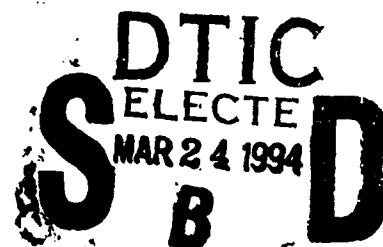
MECHANICS OF FAILURE OF HIGH TEMPERATURE METAL MATRIX COMPOSITES

FINAL REPORT FOR THE PERIOD
February 15, 1990 through September 30, 1993

Grant AFOSR-90-0235

Prepared for:

Dr. Walter Jones
AFOSR/NA Bolling Air Force Base



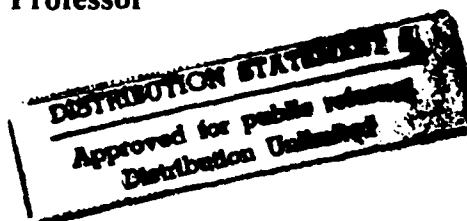
DECEMBER 1993

2480 94-09157

Demitris A. Kouris, Associate Professor



Arizona State University
Mechanical and Aerospace Engineering



DTIC QUALITY PROGRAM 1

94 3 23 010

**Best
Available
Copy**

MECHANICS OF FAILURE OF HIGH TEMPERATURE METAL MATRIX COMPOSITES

FINAL REPORT FOR THE PERIOD

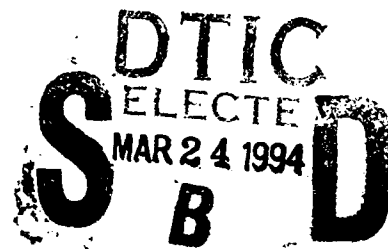
February 15, 1990 through September 30, 1993

Grant AFOSR-90-0235

Prepared for:

Dr. Walter Jones

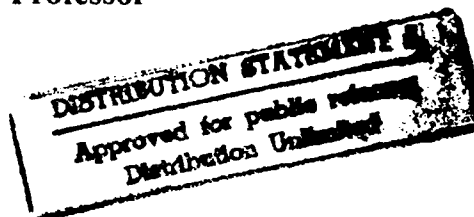
AFOSR/NA Bolling Air Force Base



DECEMBER 1993



Demitris A. Kouris, Associate Professor



Arizona State University
Mechanical and Aerospace Engineering

DTIC QUALITY INSPECTED 1

94 3 23 010

REPORT DOCUMENTATION PAGE

Public reporting burden for this collection of information is estimated to average 1 hour per response, including the time for reviewing instructions, searching existing data sources, gathering and maintaining the data needed, and completing and reviewing the collection of information. Send comments regarding this burden estimate or any other aspect of this collection of information, including suggestions for reducing this burden, to Washington Headquarters Services, Directorate for Information Operations and Reports, 1215 Jefferson Davis Highway, Suite 1204, Arlington, VA 22202-4302 and to the Office of Management and Budget, Paperwork Reduction Project (0704-0188), Washington, DC 20503.

1. AGENCY USE ONLY (Leave blank)		2. REPORT DATE 22 Dec 93		3. REPORT TYPE AND DATES COVERED 15 Feb 90 - 30 Sept 93	
4. TITLE AND SUBTITLE Failure of Metal Matrix Composites				5. FUNDING NUMBERS Grant No. AFOSR 90-0235	
6. AUTHOR(S) Dr. Demitris A. Kouris					
7. PERFORMING ORGANIZATION NAME(S) AND ADDRESS(ES) AZ Board of Regents, acting for ARIZONA STATE UNIVERSITY Department of Mechanical and Aerospace Engineering Box 876106 Tempe, AZ 85287-6106				8. PERFORMING ORGANIZATION REPORT NUMBER AFOSR-TR- 94 0072	
9. SPONSORING/MONITORING AGENCY NAME(S) AND ADDRESS(ES) Air Force Office of Scientific Research 110 Duncan Avenue, Suite B115 Bolling AFB, DC 20332-0001				10. SPONSORING/MONITORING AGENCY REPORT NUMBER	
11. SUPPLEMENTARY NOTES The view and conclusions contained in this document are those of the author and should not be interpreted as necessarily representing the official policies or endorsements, either expressed or implied, of the AFOSR or the US Government.					
12a. DISTRIBUTION/AVAILABILITY STATEMENT Approved for public release; distribution unlimited. Approved for public release; distribution unlimited.				12b. DISTRIBUTION CODE	
13. ABSTRACT (Maximum 200 words) Results of a three-year research effort aimed at developing an understanding of the factors controlling transverse strength and failure of intermetallic composites are presented. Experiments were conducted involving several aluminide matrix composites; two types of fibers were used in order to allow for large as well as small residual stresses. On the basis of the in situ observations and with the aid of high resolution strain mapping, the relevant damage mechanisms were identified. The experimental effort coupled with analytical models led to a number of conclusions that are important for the proper design of such composites. Among the important properties are the strength and sliding resistances of the interface, residual stresses, and fiber spacing. Therefore optimum strength is achieved with either strongly bonded interfaces, or interfaces that debond easily but have large resistance to circumferential sliding. The latter condition could also be compatible with the requirement of debonding and relatively easy frictional sliding for maximum benefit from fiber reinforcement in longitudinal properties. The results suggest a potential benefit from having anisotropic interfacial properties, perhaps obtained through morphology, to allow easy sliding in the axial direction and more strongly resisted sliding in the circumferential direction.					
14. SUBJECT TERMS intermetallic composites, damage, strength, mechanical properties, fracture, coatings, high temperature				15. NUMBER OF PAGES 250	
				16. PRICE CODE	
17. SECURITY CLASSIFICATION OF REPORT UNCLASSIFIED	18. SECURITY CLASSIFICATION OF THIS PAGE UNCLASSIFIED	19. SECURITY CLASSIFICATION OF ABSTRACT UNCLASSIFIED	20. LIMITATION OF ABSTRACT UL		

TABLE OF CONTENTS

		<u>Page</u>
1.0	INTRODUCTION.....	1
2.0	PUBLICATIONS, PERSONNEL and TECHNICAL PRESENTATIONS.....	3
2.1	Publications.....	3
2.2	Personnel.....	4
2.3	Technical Presentations.....	5
3.0	INTERACTION OF CLOSELY SPACED FIBERS.....	7
3.1	On the Elastic Interaction between Two Fibers in a Continuous Fiber Composite under Thermal Loading..	8
3.2	Stress Concentration due to the Interaction between Two Imperfectly Bonded Fibers in a Continuous Fiber Composite.....	9
3.3	The Elastic Field in the Vicinity of Two Elliptical Inhomogeneities.....	10
4.0	FIBERS NEAR THE SPECIMEN FREE SURFACE.....	11
4.1	An Analytical Solution for the Fiber Indentation Problem.....	12
4.2	Elastic Analysis of the Half-Plane Inhomogeneity Problem.....	13
5.0	TRANSVERSE STRENGTH AND FAILURE MECHANISMS..	14
5.1	Damage Mechanisms in Ti3Al Matrix Composites.....	15
5.2	Transverse Strengths and Failure Mechanisms in Ti3Al Matrix Composites.....	16

		<u>Page</u>
5.3	The Role of Frictional Sliding in Transverse Failure of Composites.....	17
6.0	THE ROLE OF THE INTERFACE.....	18
6.1	Experimental Measurements of Interfacial Properties in Brittle Fibrous Composites.....	19
6.2	Analysis of the Effect of Interfacial Roughness on Fiber Debonding and Sliding in Brittle Matrix Composites.....	20
6.3	The Determination of Interfacial Properties from Fiber Sliding Experiments.....	21

Accession For	
NTIS GFA&I	<input checked="" type="checkbox"/>
DTIC TAB	<input type="checkbox"/>
Unannounced	<input type="checkbox"/>
Justification	
By	
Distribution/	
Availability Codes	
Dist	Avail and/or Special
A-1	

1.0 INTRODUCTION

The overall aim of this work is to develop an understanding of the factors that control the transverse strengths of high temperature MMCs, and thereby identify the microstructural requirements to maximize this strength. Our approach is to identify the damage mechanisms that lead to transverse failure using in situ observations and high resolution strain mapping and, on the basis of these observations, develop analytical models that allow the roles of various microstructural properties to be identified. Among the important properties are the strength and sliding resistances of the interface, residual stresses, and fiber spacing. Some of the implications for optimum interfacial properties and fiber spacing run counter to "conventional wisdom."

Experimental work has involved titanium aluminide matrix composites with different fibers to vary the residual stress, and with fiber coatings to modify the interfacial properties. Different failure modes were observed in composites with large and small residual stresses.

In composites with large residual stresses several forms of damage preceded failure, but the damage that led to failure and thus limited the strength was transverse cracking. The analytical stress field solutions indicate that the stresses driving transverse cracking are greatly increased if circumferential sliding occurs, whereas this stress is *reduced* at closely spaced fibers provided circumferential sliding does not occur. Therefore optimum strength is achieved with either strongly bonded interfaces, or interfaces that debond easily but have large resistance to circumferential sliding. The latter condition could also be compatible with the requirement of debonding and relatively easy frictional sliding for maximum benefit from fiber reinforcement in longitudinal properties (i.e., increased resistance to fatigue crack growth because of crack bridging by the fibers). The results suggest a potential benefit from having anisotropic interfacial properties, perhaps obtained through morphology, to allow easy sliding in the axial direction and more strongly resisted sliding in the circumferential direction.

In composites with small residual stresses and strongly bonded interfaces, the transverse strength is limited by cracks that initiate by splitting of the fibers, or cracks that form in the matrix near the interface, where the analytical solutions indicate a large stress concentration occurs. These cracks are far more detrimental than a debonded interface which, provided the interface is sufficiently weak, becomes a hole which concentrates the applied load more weakly. Therefore the optimum transverse properties are expected for a weakly bonded interface, again compatible with the requirements for optimum longitudinal properties.

Because of the important role of interfacial sliding on transverse properties and the potential benefit from tailoring anisotropic friction, studies of the effect of interfacial roughness on sliding resistance were initiated. Previous analyses of the relation between the force and displacement during fiber sliding (pushing or pulling) were extended to include effects of interfacial roughness.

Analytical solutions were obtained for a linear roughness profile over the range of displacements that are smaller than the dominant half-wavelength of the roughness. With the equations expressed in normalized form, a convenient friction parameter, which defines the roles of the friction coefficient and the roughness angle, was defined. For certain values of the friction parameter, the effect of the roughness negates the Poisson's contraction during fiber pulling, giving solutions that are very close to the response of a system with a constant frictional stress at the interface.

Results of single fiber pulling experiments to measure frictional sliding in titanium aluminide composites that had been subjected to cyclic loading at various temperatures were interpreted in terms of these analytical solutions. The experiments involved measurement of relative sliding displacements using high resolution displacement mapping, giving sufficient resolution to distinguish various friction laws.

The results of the theoretical effort at ASU are presented in Sections 3.0 and 4.0. Section 3.0 includes the studies of fiber interaction, which was found to be essential in the analysis of the composites' transverse behavior. Section 4.0 deals with the disturbance of the local stress field in the vicinity of a free surface. A comprehensive discussion of the transverse strength and failure mechanisms of the composites under study is presented in Section 5.0 which includes the experimental observations and the relevant theoretical models. Section 6.0 presents the first stage of our study involving the effects of frictional sliding.

2.0 PUBLICATIONS, PERSONNEL and TECHNICAL PRESENTATIONS

2.1 Publications

Kouris, D. and Tsuchida, E., "On the Elastic Interaction between Two Fibers in a Continuous Fiber Composite under Thermal Loading," *Mechanics of Materials*, Vol. 12, 1991, pp. 131 - 146.

Kouris, D. and Tsuchida, E., "An Analytical Solution for the Fiber Indentation Problem," *European Journal of Mechanics / Solids*, Vol. 11(3), 1992, pp. 323 - 334.

Cox, B., and Marshall, D., "Experimental Measurements of Interfacial Properties in Brittle Fibrous Composites," *Ultramicroscopy*, Vol. 40, 1992, pp. 365 - 369.

Kouris, D. and Nuxoll, J., "Elastic Analysis of the Half-Plane Inhomogeneity Problem," *Acta Mechanica*, Vol. 97, 1993, pp. 169 - 184.

Kouris, D., "Stress Concentration due to the Interaction between Two Imperfectly Bonded Fibers in a Continuous Fiber Composite," *ASME Journal of Applied Mechanics*, Vol. 60(1), 1993, pp. 203 - 206.

Kouris, D. and Marshall, D., "Damage Mechanisms in Ti3Al Matrix Composites," *ASME Journal of Engineering Materials and Technology*, accepted for publication.

Marshall, D., Morris, W., Cox, B., Graves, J., Porter, J., Kouris, D., and Everett, R., "Transverse Strengths and Failure Mechanisms in Ti3Al Matrix Composites," *Acta Metallurgica*, submitted for publication.

Kouris, D. and Meisner, M., "The Elastic Field in the Vicinity of Two Elliptical Inhomogeneities," *Int. Journal of Solids and Structures*, to be submitted for publication.

Parthasarathy, T., Kerans, R., and Marshall, D., "Analysis of the Effect of Interfacial Roughness on Fiber Debonding and Sliding in Brittle Matrix Composites," *Journal of Mechanics and Physics of Solids*, to be submitted for publication.

Marshall, D., Morris, W., Cox, B., and Kouris, D., "The Role of Frictional Sliding in Transverse Failure of Composites," in preparation.

Marshall, D., Shaw, M., and Morris, W., "The Determination of Interfacial Properties from Fiber Sliding Experiments," in preparation.

2.2 Personnel

Professor Demitris Kouris of Arizona State University (ASU) has been responsible for the entire program. He has been in charge of the theoretical effort at ASU, which has involved a number of graduate students. The students that have been supported by the program are:

J. Nuxoll (M. S., 1991), M. Meisner (M. S., 1991; Ph. D., 1994), G. Rea (M. S., 1994).

Dr. Brian Cox of the Science Center has been responsible for Rockwell's effort (subcontract). Other principal investigators at the Science Center were David Marshall, Fred Morris, Mike James, Mahyar Dadkhah, and Cecil Rhodes.

Professor Kouris and Dr. Brian Cox have shared the responsibility for maintaining close and active collaboration between ASU and Rockwell.

2.3 Technical Presentations

ASME Winter Annual Meeting, 1990.

ASME Winter Annual Meeting, 1991.

Workshop on Solid-Solid Interfaces, Los Alamos National Laboratory, Los Alamos, NM, August 1991

International Workshop on "Composites - Materials of the Future?", Ringberg, Germany, May 1991

Titanium Matrix Composites Workshop, Orlando, FL, Nov. 1991

2nd European Conference on Advanced Materials and Processes, Keynote Speaker, Cambridge, MA, July 1991

Arizona State University Workshop on Interfaces, Wickenburg, AZ, January 4, 1991. "Experimental Measurements of Interface Properties" (invited).

Engng. Foundation Conference on Fatigue of Advanced Materials, Santa Barbara, January 16, 1991, "Fatigue and Fracture of Fibrous Composites" (invited).

ARL, Melbourne, Australia, August, 1991. "Measurements of Interfacial Properties in Brittle-Matrix Composites,"

ASTM Subcommittee D30.07, San Diego, October 17, 1991 "Engineering Aspects of Modelling Bridged Fatigue Cracks," (invited).

FAFIC '92, Cambridge, England, March 31, 1992. "Concepts for Bridged Cracks in Fracture and Fatigue," (plenary paper).

MRS Spring Meeting, San Francisco, CA, April 1992

Titanium Matrix Composites Workshop (invited), June 1993, La Jolla, CA.

ASME Winter Annual Meeting, 1993.

First Joint SES-ASME-ASCE Meeting, Symposium on Brittle Matrix Structural Composites, Charlottesville, Virginia, June, 1993. "Concepts for Bridged Cracks in Fracture and Fatigue" (invited).

U. S. National Congress of Applied Mechanics, Symposium on Inelasticity and Micromechanics of Metal Matrix Composites, Seattle, June 26 - July 1, 1994, (invited).

U. S. National Congress of Applied Mechanics, Symposium honoring J. Dundurs, Seattle, June 26 - July 1, 1994, (invited).

3.0 INTERACTION OF CLOSELY SPACED FIBERS

**3.1 On the Elastic Interaction between Two Fibers in a Continuous Fiber
Composite under Thermal Loading**

published in Mechanics of Materials

On the elastic interaction between two fibers in a continuous fiber composite under thermal loading

Demitris Kouris

Mechanical and Aerospace Engineering Department, Arizona State University, Tempe, AZ 85287-6106, U.S.A

and

Eiichiro Tsuchida

Mechanical Engineering Department, Saitama University, 255 Shimo-Okubo, Urawa 338, Japan

Received 31 October 1990; revised version received 15 April 1991

The problem of fiber interaction in unidirectional fiber composites under thermal loading is considered. A pair of fibers is modeled by two inhomogeneities that sustain an eigenstrain loading, proportional to the difference of fiber/matrix thermal expansion coefficients. Utilizing the displacement potential approach, the plane strain problem is solved analytically. The effect of incoherent interfaces is evaluated, in comparison to the case of perfect bonding.

1. Introduction

The most commonly used approach for manufacturing titanium aluminide composites is consolidation of the matrix in direct contact with the fibers. The matrix may begin as a rolled sheet or powder, or it may be applied to the fiber by plasma deposition. In both cases, the final product in all "bare-interface" Ti_3Al composites contains some degree of microcracking both of the fiber/matrix interface and the matrix between fibers (Cox, 1989).

Causes of the microcracking are, among others, the chemical reactivity of the matrix/fiber system, the brittleness of intermetallic matrices and the micromechanical damage due to the thermal loading of a material with an inherent thermal mismatch between its constituents (Cox, 1989). In intermetallic matrix composites, the local stress state is severely affected by residual thermal mismatch stresses.

The effects of the interfacial integrity¹ on the mechanical properties of thermally loaded composites are not, yet, well understood. A weak interface may enhance room temperature monotonic strength and fatigue life for loading in the fiber direction, while degrading transverse modulus, strength, and high temperature creep resistance (Cox et al., 1989). Nevertheless, the prerequisite to predicting microcracking in any material is knowledge of the local stress state.

The overall properties of composites have been the subject of a number of investigations that are primarily based on the self-consistent method (Kröner, 1958; Budiansky, 1965; Hill, 1965). An extensive list of references is included in Mura (1987).

Based on a successive iteration method introduced by Mori and Wakashima (1990), the average values of the elastic properties of a composite with randomly distributed fibers have been determined, in closed form; this approach has been extended to account for the case of sliding fibers (Shibata et al., 1990).

¹ This work has been supported by the Air Force Office of Scientific Research, through the University Research Initiative Award AFOSR 90-0235.

When the fibers are periodically distributed, the Eshelby transformation strains can be accurately estimated; consequently, the moduli of a composite can be determined, using energy considerations. An extensive treatment of the subject has been presented by Nemat-Nasser et al. (1982), Iwakuma and Nemat-Nasser (1983), and Accorsi and Nemat-Nasser (1986).

In the present study, an attempt was made to determine the local elastic field in the vicinity of two identical fibers in a continuous fiber composite under thermal loading. The plain strain analysis followed, is based upon the observation that thermal mismatch can be modelled as an appropriate eigenstrain field, sustained by the fiber cross sections.

Our primary interest is to determine how the fiber interaction relates to the local stress state of the fiber/matrix interface, as well as the surrounding matrix itself. Such an analytical investigation of the interaction is useful, since most existing closed-form solutions involve single fibers.

The geometry of the boundary value problem is shown in Fig. 1. Two circular inhomogeneities (fiber cross sections), with a central distance c , undergo an eigenstrain loading. Utilizing the displacement potentials approach, an analytical solution for the elastic field is obtained, in a series form.

2. Description of the boundary value problem

Consider two circular inhomogeneities Ω_1 and Ω_2 with centers at O_1, O_2 , respectively, embedded in an infinite elastic region. Let the centers coincide with the origins of the Cartesian coordinates (x_1, y_1) and (x_2, y_2) , and x_1, x_2 -axis be the center line (Fig. 1). If we assume that the central distance is equal to unity, then

$$x_1 = x_2 + 1, \quad y_1 = y_2. \quad (1)$$

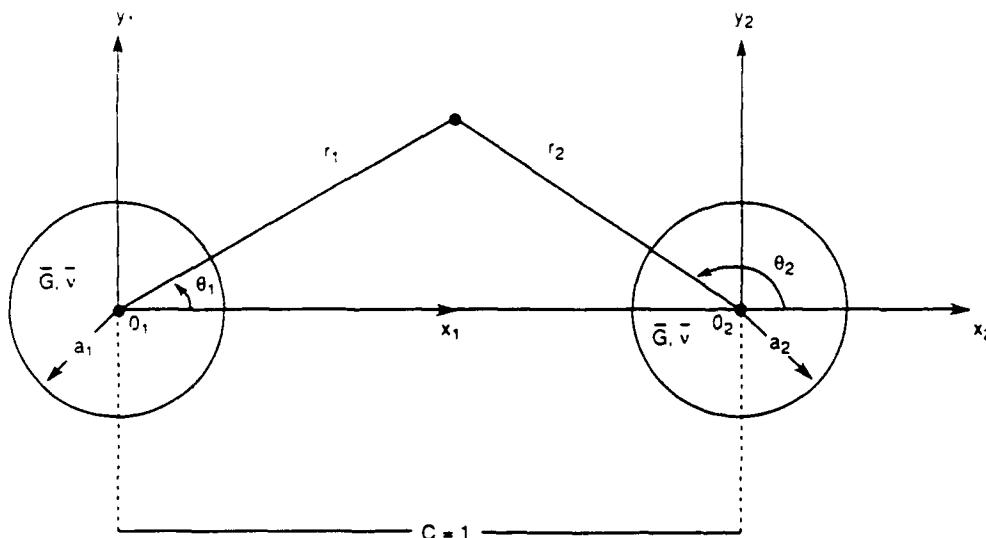


Fig. 1. Geometry of the problem.

The polar coordinates (r, θ) are defined through the transformation

$$x_i = r_i \cos \theta_i, \quad y_i = r_i \sin \theta_i \quad (i = 1, 2).$$

The displacement vector u can be expressed as the sum of the vectors corresponding to the O_1 and O_2 coordinate systems. Therefore

$$u = u_1 + u_2. \quad (2)$$

According to the Papkovitch-Neuber displacement formulation (Papkovitch, 1932; Neuber, 1934), u_1 and u_2 can be expressed as

$$2Gu_1 = \text{grad}[\phi_{01} + x_1\phi_{11} + y_1\phi_{21}] - 4(1-\nu)[\phi_{11}, \phi_{21}], \quad (3)$$

$$2Gu_2 = \text{grad}[\phi_{02} + x_2\phi_{12} + y_2\phi_{22}] - 4(1-\nu)[\phi_{12}, \phi_{22}], \quad (4)$$

where ϕ_{ij} are arbitrary harmonic functions and $[\phi_{ij}, \phi_{mn}]$ is equal to ϕ_{ij} for the x -component and ϕ_{mn} for the y -component of the displacement. G, ν denote the shear modulus and Poisson's ratio, respectively.

In order to satisfy any conditions along the boundary of the first inhomogeneity $\Omega_1 (r_1 = a_1)$, it is necessary to express (4) in terms of the (x_1, y_1) coordinate system. Such a transformation is readily available using (1) and is given by

$$2Gu_2 = \text{grad}[\phi_{02} + (x_1 - 1)\phi_{12} + y_1\phi_{22}] - 4(1-\nu)[\phi_{12}, \phi_{22}]$$

or

$$2Gu_2 = \text{grad}[(\phi_{02} - \phi_{12}) + x_1\phi_{12} + y_1\phi_{22}] - 4(1-\nu)[\phi_{12}, \phi_{22}]. \quad (5)$$

Similarly, for the second inhomogeneity $\Omega_2 (r_2 = a_2)$, we have from (1), (3)

$$2Gu_1 = \text{grad}[(\phi_{01} + \phi_{11}) + x_2\phi_{11} + y_2\phi_{21}] - 4(1-\nu)[\phi_{11}, \phi_{21}] \quad (6)$$

Due to the applied thermal loading, eigenstrains ϵ_x^* and ϵ_y^* are introduced in Ω_1 and Ω_2 . These eigenstrains are proportional to the difference of the thermal expansion coefficients between the fibers and the surrounding matrix. Consequently, the displacements corresponding to the transformation strains ϵ_x^* and ϵ_y^* are given by

$$\bar{u}_x^* = \epsilon_x^* x, \quad \bar{u}_y^* = \epsilon_y^* y,$$

or, in polar coordinates

$$\bar{u}_r^* = \frac{1}{2}r(\epsilon_x^* + \epsilon_y^*) + \frac{1}{2}r(\epsilon_x^* - \epsilon_y^*) \cos 2\theta, \quad \bar{u}_\theta^* = \frac{1}{2}(\epsilon_y^* - \epsilon_x^*)r \sin 2\theta. \quad (7)$$

If we assume that the fibers are perfectly bonded to the matrix, the boundary conditions along the circular interfaces $(r_i = a_i)$ are

$$u_r = \bar{u}_r + \bar{u}_r^*, \quad u_\theta = \bar{u}_\theta + \bar{u}_\theta^*, \quad \sigma_r = \bar{\sigma}_r, \quad \tau_{r\theta} = \bar{\tau}_{r\theta}. \quad (8)$$

In the absence of any far field mechanical loading, all the components of the stress tensor vanish as $r \rightarrow \infty$. Therefore

$$\lim_{r \rightarrow \infty} \sigma_{ij} = 0. \quad (9)$$

The unique solution of the problem can be obtained, if a set of harmonic displacement potentials is determined in such a way, that the boundary conditions (8) and (9) are satisfied.

3. Analytical solution

The displacement potentials chosen for the matrix ($r_i > a_i$) are

$$\phi_{0i} = p_0 \left(F_0' \log \rho_i + \sum_{n=1}^{\infty} A_n' \rho_i^{-n} \cos n\theta_i \right), \quad \phi_{1i} = p_0 \sum_{n=1}^{\infty} B_n' \rho_i^{-n} \cos n\theta_i, \quad \phi_{2i} \equiv 0. \quad (I)$$

and for the two inhomogeneities ($r_i < a_i$)

$$\phi_{0i} = p_0 \sum_{n=1}^{\infty} \bar{A}_n' \rho_i^n \cos n\theta_i, \quad \phi_{1i} = p_0 \sum_{n=1}^{\infty} \bar{B}_n' \rho_i^n \cos n\theta_i, \quad \phi_{2i} \equiv 0. \quad (II)$$

where $\rho_i = r_i/c$ and $p_0 = 2G\epsilon^*$.

Using the potential functions (I) and (II) we can derive stresses and displacements in the matrix and the inhomogeneities; it can be easily verified that the boundary conditions (9) at infinity are identically satisfied.

What remain to be determined are the values of the coefficients F_0' , A_n' , B_n' , \bar{A}_n' and \bar{B}_n' . This can be accomplished by enforcing the boundary conditions along the interface of the inclusions, as described by (8).

In order to proceed with the boundary of $\Omega(r_i = a_i)$ we utilize (3), (5) and the following relations between the harmonic functions:

$$\log \rho_2 = - \sum_{m=1}^{\infty} \frac{1}{m} \rho_1^m \cos m\theta_1, \quad \log \rho_1 = - \sum_{m=1}^{\infty} (-1)^m \frac{1}{m} \rho_2^m \cos m\theta_2 \quad (10)$$

and

$$\rho_2^{-n} \cos n\theta_2 = \sum_{m=0}^{\infty} (-1)^n w_m^n \rho_1^m \cos m\theta_1, \quad \rho_1^{-n} \cos n\theta_1 = \sum_{m=0}^{\infty} (-1)^m w_m^n \rho_2^m \cos m\theta_2. \quad (11)$$

where $w_m^n = (m+n-1)!/(n-1)!m!$.

Using (3), (5), $\kappa = 3 - 4\nu$, and the transformations (10) and (11), we can express the boundary conditions along the interface of $\Omega_1(r_1 = a_1)$ as follows

$$\begin{aligned} u_r &= \bar{u}_r + \bar{u}_r^* = \\ & F_0' \frac{1}{a_1} - \sum_{n=1}^{\infty} A_n' \frac{n}{a_1^{n+1}} \cos n\theta_1 - \frac{1}{2} \sum_{n=2}^{\infty} B_{n-1}' \frac{n-1+\kappa}{a_1^{n-1}} \cos n\theta_1 \\ & - \frac{1}{2} \sum_{n=0}^{\infty} B_{n+1}' \frac{n+1+\kappa}{a_1^{n+1}} \cos n\theta_1 - F_0'^2 \sum_{n=1}^{\infty} a_1^{n-1} \cos n\theta_1 \\ & + \sum_{n=0}^{\infty} \sum_{m=1}^{\infty} (-1)^m (A_m^2 - B_m^2) w_m^n n a_1^{n-1} \cos n\theta_1 \\ & + \frac{1}{2} \sum_{n=1}^{\infty} \sum_{m=1}^{\infty} (-1)^m B_m^2 w_{n-1}^m a_1^{n-1} (n-1-\kappa) \cos n\theta_1 \end{aligned}$$

$$\begin{aligned}
& + \frac{1}{2} \sum_{n=0}^{\infty} \sum_{m=1}^{\infty} (-1)^m B_m^2 w_{n+1}^m a_1^{n+1} (n+1-\kappa) \cos n\theta_1 \\
& - \frac{1}{\Gamma} \sum_{n=1}^{\infty} \bar{A}_n^1 n a_1^{n-1} \cos n\theta_1 - \frac{1}{2} \frac{1}{\Gamma} \sum_{n=2}^{\infty} \bar{B}_{n-1}^1 (n-1-\bar{\kappa}) a_1^{n-1} \cos n\theta_1 \\
& - \frac{1}{2} \frac{1}{\Gamma} \sum_{n=0}^{\infty} \bar{B}_{n+1}^1 (n+1-\bar{\kappa}) a_1^{n+1} \cos n\theta_1 \\
& = \frac{1}{2} a_1 (\epsilon_1^* + \epsilon_1^*) + \frac{1}{2} a_1 (\epsilon_1^* - \epsilon_1^*) \cos 2\theta_1.
\end{aligned} \tag{12}$$

The requirement for continuity of the tangential displacements yields

$$\begin{aligned}
u_\theta &= \bar{u}_\theta + \bar{u}_\theta^* \Rightarrow \\
& - \sum_{n=1}^{\infty} A_n^1 \frac{n}{a_1^{n-1}} \sin n\theta_1 - \frac{1}{2} \sum_{n=2}^{\infty} B_{n-1}^1 \frac{n-1-\kappa}{a_1^{n-1}} \sin n\theta_1 \\
& - \frac{1}{2} \sum_{n=1}^{\infty} B_{n+1}^1 \frac{n+1+\kappa}{a_1^{n+1}} \sin n\theta_1 + F_0^2 \sum_{n=1}^{\infty} a_1^{n-1} \sin n\theta_1 \\
& - \sum_{n=1}^{\infty} \sum_{m=1}^{\infty} (-1)^m (A_m^2 - B_m^2) w_n^m n a_1^{n-1} \sin n\theta_1 \\
& - \frac{1}{2} \sum_{n=1}^{\infty} \sum_{m=1}^{\infty} (-1)^m B_m^2 w_{n-1}^m a_1^{n-1} (n-1-\kappa) \sin n\theta_1 \\
& - \frac{1}{2} \sum_{n=1}^{\infty} \sum_{m=1}^{\infty} (-1)^m B_m^2 w_{n+1}^m a_1^{n+1} (n+1+\kappa) \sin n\theta_1 \\
& + \frac{1}{\Gamma} \sum_{n=1}^{\infty} \bar{A}_n^1 n a_1^{n-1} \sin n\theta_1 + \frac{1}{2} \frac{1}{\Gamma} \sum_{n=2}^{\infty} \bar{B}_{n-1}^1 (n-1-\bar{\kappa}) a_1^{n-1} \sin n\theta_1 \\
& + \frac{1}{2} \frac{1}{\Gamma} \sum_{n=1}^{\infty} \bar{B}_{n+1}^1 (n+1+\bar{\kappa}) a_1^{n+1} \sin n\theta_1 \\
& = \frac{1}{2} a_1 (\epsilon_y^* - \epsilon_x^*) \sin 2\theta_1.
\end{aligned} \tag{13}$$

For the normal stresses along the interface we have

$$\begin{aligned}
\sigma_r &= \bar{\sigma}_r \Rightarrow \\
& - F_0^1 \frac{1}{a_1^2} + \sum_{n=1}^{\infty} A_n^1 \frac{n(n+1)}{a_1^{n+2}} \cos n\theta_1 + \frac{1}{2} \sum_{n=2}^{\infty} B_{n-1}^1 \frac{(n-1)(n+2)}{a_1^n} \cos n\theta_1 \\
& + \frac{1}{2} \sum_{n=0}^{\infty} B_{n+1}^1 \frac{(n+1)(n+1+\kappa)}{a_1^{n+2}} \cos n\theta_1 - F_0^2 \sum_{n=1}^{\infty} (n-1) a_1^{n-2} \cos n\theta_1 \\
& + \sum_{n=0}^{\infty} \sum_{m=1}^{\infty} (-1)^m (A_m^2 - B_m^2) w_n^m n (n-1) a_1^{n-2} \cos n\theta_1 \\
& + \frac{1}{2} \sum_{n=1}^{\infty} \sum_{m=1}^{\infty} (-1)^m B_m^2 w_{n-1}^m a_1^{n-2} (n-1)(n-1-\kappa) \cos n\theta_1
\end{aligned}$$

$$\begin{aligned}
& + \frac{1}{2} \sum_{n=0}^{\infty} \sum_{m=1}^{\infty} (-1)^m B_m^2 \omega_{n+1}^m a_1^n (n+1)(n-2) \cos n\theta_1 - \sum_{n=1}^{\infty} \bar{A}_n^1 n(n-1) a_1^{n-2} \cos n\theta_1 \\
& - \frac{1}{2} \sum_{n=2}^{\infty} \bar{B}_{n-1}^1 (n-1)(n-1-\bar{\kappa}) a_1^{n-2} \cos n\theta_1 - \frac{1}{2} \sum_{n=0}^{\infty} \bar{B}_{n+1}^1 (n+1)(n-2) a_1^n \cos n\theta_1 \\
& = 0.
\end{aligned} \tag{14}$$

Finally, the shear stresses give

$$\begin{aligned}
\tau_{r\theta} = \bar{\tau}_{r\theta} = & \sum_{n=1}^{\infty} A_n^1 \frac{n(n+1)}{a_1^{n+2}} \sin n\theta_1 + \frac{1}{2} \sum_{n=2}^{\infty} B_{n-1}^1 \frac{n(n-1)}{a_1^n} \sin n\theta_1 \\
& + \frac{1}{2} \sum_{n=0}^{\infty} B_{n+1}^1 \frac{(n+1)(n+1+\kappa)}{a_1^{n+2}} \sin n\theta_1 + F_0^2 \sum_{n=1}^{\infty} (n-1) a_1^{n-2} \sin n\theta_1 \\
& - \sum_{n=0}^{\infty} \sum_{m=1}^{\infty} (-1)^m (A_m^2 - B_m^2) \omega_n^m n(n-1) a_1^{n-2} \sin n\theta_1 \\
& - \frac{1}{2} \sum_{n=1}^{\infty} \sum_{m=1}^{\infty} (-1)^m B_m^2 \omega_{n-1}^m a_1^{n-2} (n-1)(n-1-\kappa) \sin n\theta_1 \\
& - \frac{1}{2} \sum_{n=0}^{\infty} \sum_{m=1}^{\infty} (-1)^m B_m^2 \omega_{n+1}^m a_1^n n(n+1) \sin n\theta_1 \\
& + \sum_{n=1}^{\infty} \bar{A}_n^1 n(n-1) a_1^{n-2} \sin n\theta_1 + \frac{1}{2} \sum_{n=2}^{\infty} \bar{B}_{n-1}^1 (n-1)(n-1-\bar{\kappa}) a_1^{n-2} \sin n\theta_1 \\
& + \frac{1}{2} \sum_{n=0}^{\infty} \bar{B}_{n+1}^1 n(n+1) a_1^n \sin n\theta_1 \\
& = 0.
\end{aligned} \tag{15}$$

where Γ denotes the shear moduli ratio \bar{G}/G and all the overbarred letters corresponds to quantities relating to the inhomogeneities.

Using the same procedure, we can enforce the boundary conditions along the interface of the second circular inhomogeneity Ω_2 . However, since the fiber cross sections are identical and the thermal loading is symmetric, we have to satisfy the boundary conditions along the interface of Ω_1 or Ω_2 ; the other one will be satisfied automatically.

Utilizing the symmetry relations

$$\begin{aligned}
A_n^1 &= (-1)^n A_n^2 = A_n, & B_n^1 &= (-1)^{n+1} B_n^2 = B_n, \\
\bar{A}_n^1 &= (-1)^n \bar{A}_n^2 = \bar{A}_n, & \bar{B}_n^1 &= (-1)^{n+1} \bar{B}_n^2 = \bar{B}_n, \\
a_1 &= a_2 = a.
\end{aligned} \tag{16}$$

we can express the conditions (12)–(15) as follows

$$\begin{aligned}
F_0 \frac{1}{a} - A_n \frac{n}{a^{n+1}} - \frac{1}{2} B_{n-1} \frac{n-1+\kappa}{a^{n-1}} - \frac{1}{2} B_{n+1} \frac{n+1+\kappa}{a^{n+1}} - F_0 a^{n-1} (\delta_n^{(1)} - 1) \\
+ \sum_{m=1}^{\infty} (A_m + B_m) \omega_n^m n a^{n-1} (\delta_n^{(1)} - 1) - \frac{1}{2} \sum_{m=1}^{\infty} B_m \omega_{n-1}^m a^{n-1} (n-1-\kappa) (\delta_n^{(1)} - 1)
\end{aligned}$$

$$\begin{aligned}
& -\frac{1}{2} \sum_{m=1}^{\infty} B_m w_{n+1}^m a^{n+1} (n+1-\kappa) (\delta_n^{(1)} - 1) - \frac{1}{\bar{F}} \bar{A}_n n a^{n+1} \\
& - \frac{1}{2} \frac{1}{\bar{F}} \bar{B}_{n-1} (n-1-\bar{\kappa}) a^{n+1} - \frac{1}{2} \frac{1}{\bar{F}} \bar{B}_{n+1} (n+1-\bar{\kappa}) a^{n+1} \\
& = \frac{1}{2} a (\epsilon_n^* + \epsilon_n^*) \delta_n^{(0)} + \frac{1}{2} a (\epsilon_n^* - \epsilon_n^*) \delta_n^{(2)} \quad (n=0, 1, 2, \dots),
\end{aligned} \tag{17}$$

$$\begin{aligned}
& -A_n \frac{n}{a^{n+1}} - \frac{1}{2} B_{n-1} \frac{n-1-\kappa}{a^{n+1}} - \frac{1}{2} B_{n+1} \frac{n+1+\kappa}{a^{n+1}} + F_0 a^{n+1} (\delta_n^{(1)} - 1) \\
& - \sum_{m=1}^{\infty} (A_m + B_m) w_n^m n a^{n+1} (\delta_n^{(1)} - 1) + \frac{1}{2} \sum_{m=1}^{\infty} B_m w_{n-1}^m a^{n+1} (n-1-\kappa) (\delta_n^{(1)} - 1) \\
& + \frac{1}{2} \sum_{m=1}^{\infty} B_m w_{n+1}^m (n+1+\kappa) a^{n+1} + \frac{1}{\bar{F}} \bar{A}_n n a^{n+1} + \frac{1}{2} \frac{1}{\bar{F}} \bar{B}_{n-1} (n-1-\bar{\kappa}) a^{n+1} \\
& + \frac{1}{2} \frac{1}{\bar{F}} \bar{B}_{n+1} (n+1+\bar{\kappa}) a^{n+1} \\
& = \frac{1}{2} a (\epsilon_n^* - \epsilon_n^*) \delta_n^{(2)} \quad (n=1, 2, 3, \dots),
\end{aligned} \tag{18}$$

$$\begin{aligned}
& -F_0 \frac{1}{a^2} \delta_n^{(0)} + A_n \frac{n(n+1)}{a^{n+2}} + \frac{1}{2} B_{n-1} \frac{(n-1)(n+2)}{a^n} + \frac{1}{2} B_{n+1} \frac{(n+1)(n+1+\kappa)}{a^{n+2}} \\
& - F_0 (n-1) a^{n-2} + \sum_{m=1}^{\infty} (A_m + B_m) w_n^m n (n-1) a^{n-2} \\
& - \frac{1}{2} \sum_{m=1}^{\infty} B_m w_{n-1}^m (n-1)(n-1-\kappa) a^{n-2} \\
& - \frac{1}{2} \sum_{m=1}^{\infty} B_m w_{n+1}^m (n+1)(n-2) a^n - \bar{A}_n n (n-1) a^{n-2} \\
& - \frac{1}{2} \bar{B}_{n-1} (n-1)(n-1-\bar{\kappa}) a^{n-2} - \bar{B}_{n+1} (n+1)(n-2) a^n \\
& = 0 \quad (n=0, 1, 2, \dots),
\end{aligned} \tag{19}$$

and finally,

$$\begin{aligned}
& A_n \frac{n(n+1)}{a^{n+2}} + \frac{1}{2} B_{n-1} \frac{n(n-1)}{a^n} + \frac{1}{2} B_{n+1} \frac{(n+1)(n+1+\kappa)}{a^{n+2}} + F_0 (n-1) a^{n-2} \\
& - \sum_{m=1}^{\infty} (A_m + B_m) w_n^m n (n-1) a^{n-2} \\
& + \frac{1}{2} \sum_{m=1}^{\infty} B_m w_{n-1}^m (n-1)(n-1-\kappa) a^{n-2} + \frac{1}{2} \sum_{m=1}^{\infty} B_m w_{n+1}^m n (n+1) a^n \\
& + \bar{A}_n n (n-1) a^{n-2} + \frac{1}{2} \bar{B}_{n-1} (n-1)(n-1-\bar{\kappa}) a^{n-2} + \frac{1}{2} \bar{B}_{n+1} n (n+1) a^n \\
& = 0 \quad (n=1, 2, 3, \dots),
\end{aligned} \tag{20}$$

where $\delta_n^{(i)}$ denotes Kronecker's delta.

4. Incoherent interfaces

The analytical formulation followed above, is based upon the assumption that the fiber cross sections (circular inhomogeneities) are perfectly bonded to the surrounding matrix. However, the presence of thin fiber coatings or reaction zones along the fiber/matrix interface, suggest that a third *phase* may need to be considered. In order to study the effect of such a third zone, it is necessary to know in advance its thermomechanical properties; unfortunately, these in situ properties are not easily obtained.

Such difficulties can be avoided by considering a spring-type thin layer, which also accounts for the imperfect bond between the constituents of the composite. This model allows for displacement discontinuities along the fiber/matrix interface, while tractions remain continuous. Such an approach has been utilized by Lene and Leguillon (1982), Benveniste (1984, 1985) and Jasiuk et al. (1989), among others. In a comprehensive study, Hashin (1990) investigated the effect of such interfacial conditions on the thermoelastic properties of unidirectional fiber composites, using the generalized self-consistent scheme.

In the present study, as in Kouris and Mura (1989), we will assume that, along the interface, tractions and normal displacement remain continuous, while the tangential displacement discontinuity is proportional to the interfacial shear stress, i.e.

$$2G[u_\theta] = \lambda a \bar{\tau}_{r,\theta} \quad (21)$$

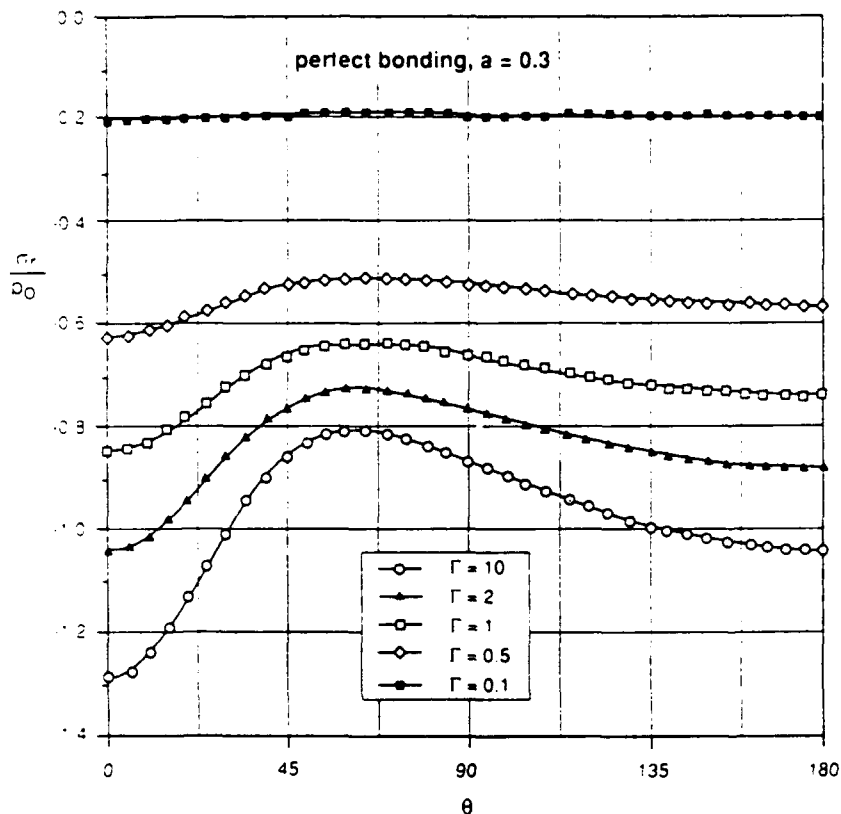


Fig. 2. Variation of the normal stress along the fiber interface, for different shear moduli ratios.

where $[u_\theta] = u_\theta - (\bar{u}_\theta + \bar{u}_\theta^*)$, G and a denote the shear moduli of the matrix and the radius of the inhomogeneity, respectively, and λ is a proportionality constant that describes the condition of the interfacial bond and corresponds to the compliance of the thin interfacial layer.

When λ is equal to zero, fibers and matrix are perfectly bonded; as λ approaches infinity, the condition of perfect sliding is obtained (no shear tractions along the interface).

In view of (21), the boundary condition (18) is transformed into

$$\begin{aligned}
 & -A_n \frac{n}{a^{n+1}} - \frac{1}{2} B_{n-1} \frac{n-1-\kappa}{a^{n-1}} - \frac{1}{2} B_{n+1} \frac{n+1+\kappa}{a^{n+1}} + F_0 a^{n-1} (\delta_n^{(1)} - 1) \\
 & - \sum_{m=1}^{\infty} (A_m + B_m) w_n^m n a^{n-1} (\delta_n^{(1)} - 1) \\
 & + \frac{1}{2} \sum_{m=1}^{\infty} B_m w_{n-1}^m a^{n-1} (n-1-\kappa) (\delta_n^{(1)} - 1) + \frac{1}{2} \sum_{m=1}^{\infty} B_m w_{n+1}^m (n+1+\kappa) a^{n+1} \\
 & + \bar{A}_n n a^{n-1} \left[\frac{1}{\bar{\Gamma}} + \lambda(n-1) \right] + \frac{1}{2} \bar{B}_{n-1} (n-1-\bar{\kappa}) a^{n-1} \left[\frac{1}{\bar{\Gamma}} + \lambda(n-1) \right] \\
 & + \frac{1}{2} \bar{B}_{n+1} a^{n+1} \left[\frac{1}{\bar{\Gamma}} (n+1+\bar{\kappa}) + \lambda n(n+1) \right] \\
 & = \frac{1}{2} a (\epsilon_r^* - \epsilon_r^*) \delta_n^{(2)} \quad (n = 1, 2, 3, \dots), \tag{22}
 \end{aligned}$$

while (17), (19) and (20) remain unchanged.

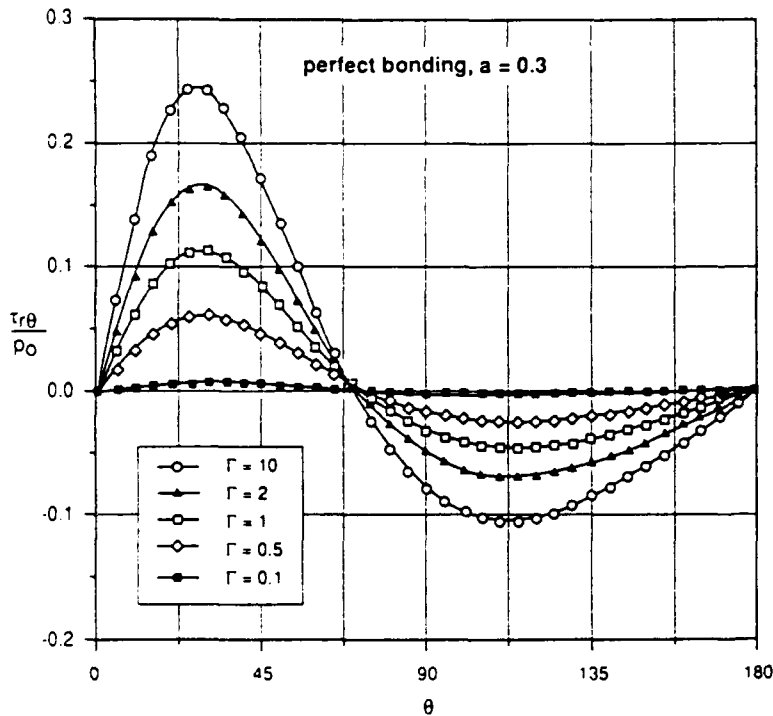


Fig. 3. Shear stress distribution along the interface for various Γ .

5. Results and discussion

The linear system (17)–(20) that was obtained by enforcing the interfacial conditions, was solved numerically. In order to ensure matching of the boundary conditions up to three significant figures, no more than 15 series terms are required. The solution yields the coefficients F_0 , A_n , B_n , \bar{A}_n , and \bar{B}_n , and its convergence is numerically evident. After evaluating the series coefficients, stresses and displacements in the matrix and the fiber cross sections can be determined, by utilizing the displacement potentials (I) and (II). It has been assumed that the thermal load $p_0 = 2G\epsilon_A^* = 2G\epsilon_f^* = 1$ and $\nu = \bar{\nu} = 0.3$.

The purpose of the parametric study that follows, is to quantify the effects of the fiber/matrix shear moduli ratio and the fiber/fiber distance, on the elastic field (stresses and displacements) in the vicinity of the fibers.

As the fiber material becomes stiffer ($\Gamma = \bar{G}/G$ increases), the absolute values of the matrix interfacial stresses increase, as shown in Fig. 2–4. The distribution of the normal stress σ_x in the matrix, along the central line, is illustrated in Fig. 5–7. When the effects of fiber interaction are negligible ($a = 0.1$), the values of σ_x along the interface are proportional to Γ , as expected from the single fiber solution. However, as the fiber radius a increases (fibers approach each other), the trend is reversed: σ_x becomes inversely proportional to Γ . In Fig. 7, the distribution of σ_x based on superposition of the single fiber solution ($\Gamma = 5^*$), a commonly used approximation, is compared with the results of the analytical solution. It can be observed that for $\Gamma = 5$, the approximation overestimates the interfacial stress by a factor of 4; in addition, the error is directly proportional to the shear moduli ratio Γ .

As the radius of the fibers increases (and for constant $\Gamma = 2$), the values of the interfacial stresses increase, as expected (Fig. 8).

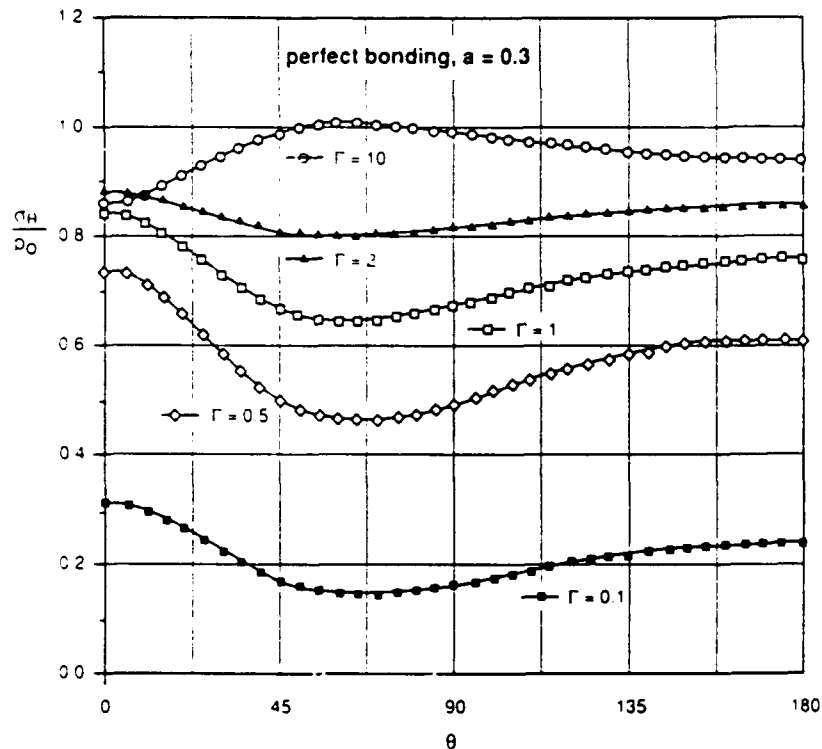


Fig. 4. Distribution of the hoop stress along the interface.

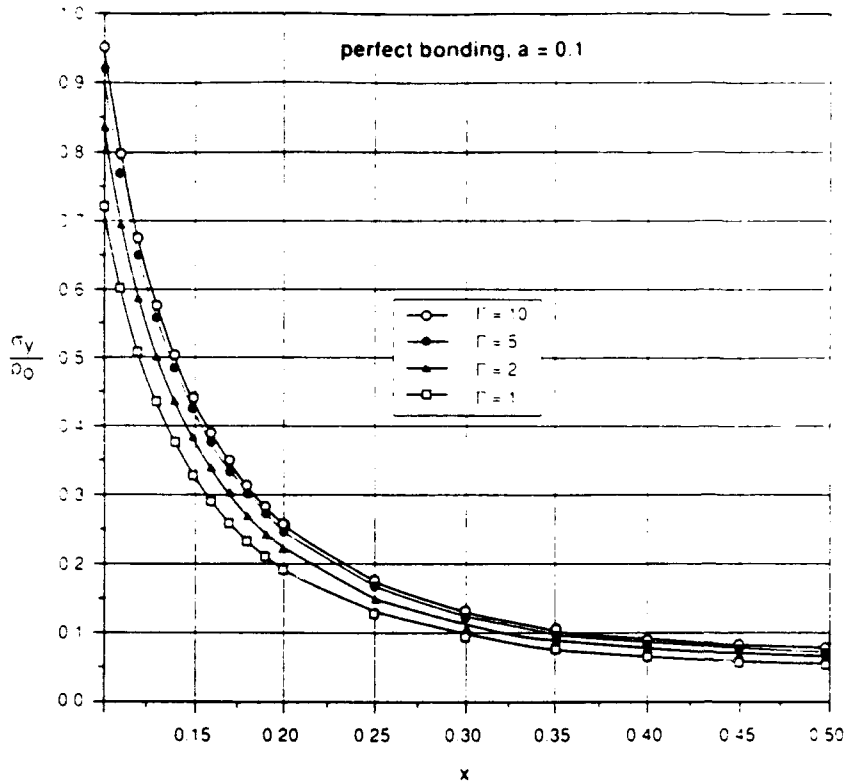


Fig. 5. Effect of Γ on the distribution of σ_y along the central axis, for $a = 0.1$.

In order to investigate the behavior of the incoherent interface defined by (21), stresses and displacements were evaluated for several values of λ between zero (perfect bonding) and infinity (sliding). The shear moduli ratio Γ and the fiber radius a were kept equal to 2 and 0.35, respectively.

It was found that as λ increases, the elastic field approaches rapidly the one corresponding to perfect sliding: for any $\lambda > 50$, stresses and displacements remain unchanged and identical to the conditions of perfect slip. As shown in Fig. 9, the shear stress along the interface tends to zero as λ increases; however, the values of the hoop stress σ_θ increase as the condition of perfect slip prevails (Fig. 10). The small tensile values observed in the case of perfect bonding ($\lambda = 0$) become significant as the degree of interfacial coherence decreases. Such high tensile values suggest the possibility of a mode I crack initiation at $\theta = 0^\circ$.

Finally, the variations of σ_y and σ_x along the x and y axes, respectively, are illustrated in Fig. 11 and 12.

6. Conclusions

An analytical solution was presented, for the problem of fiber interaction in a continuous fiber composite, under thermal loading. The fiber cross sections were modeled by two circular inhomogeneities which undergo a uniform eigenstrain loading, proportional to the mismatch of the thermal expansion coefficients.

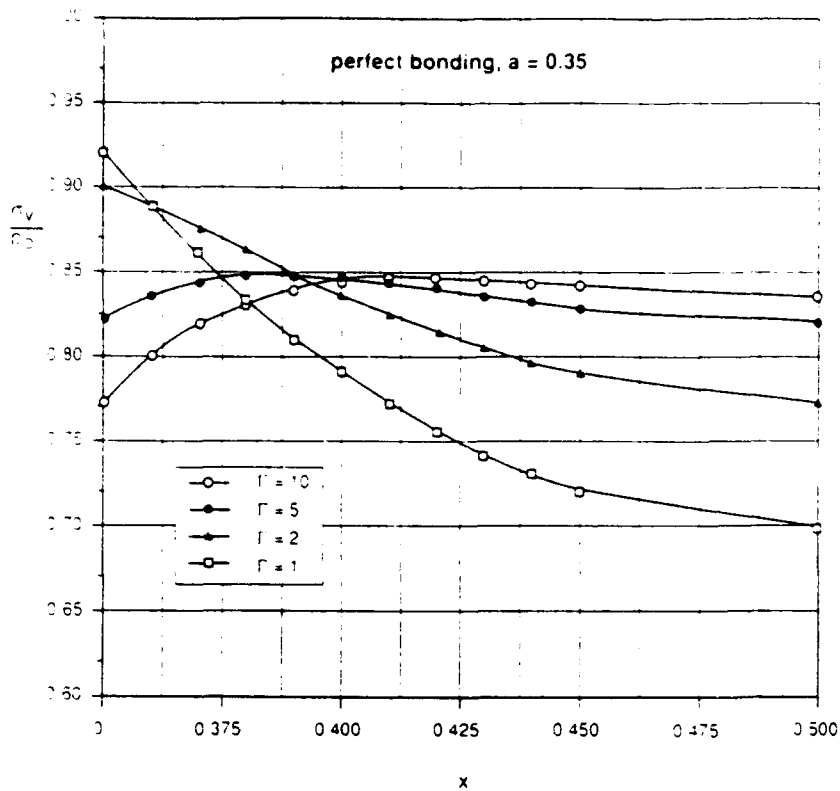
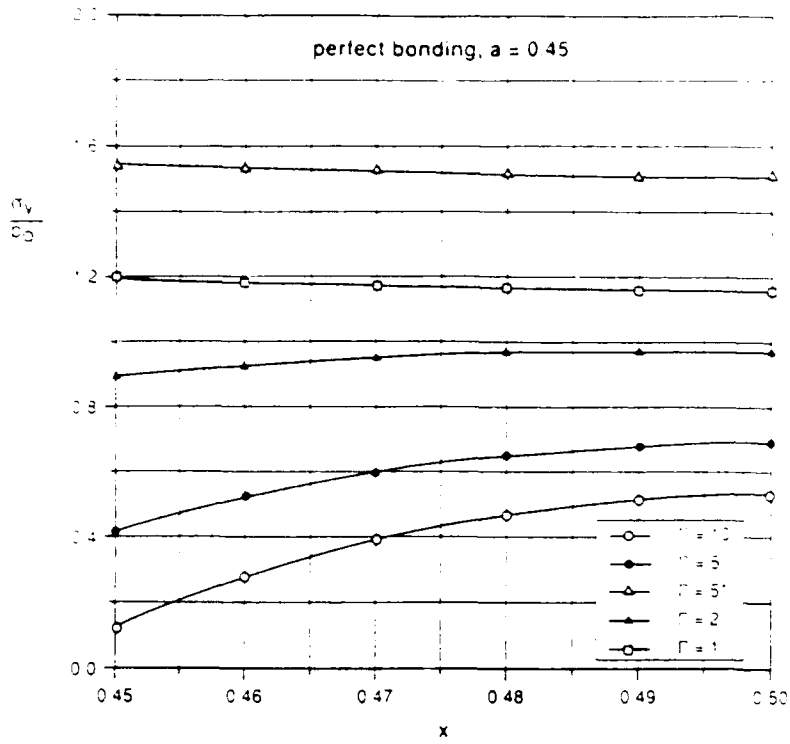
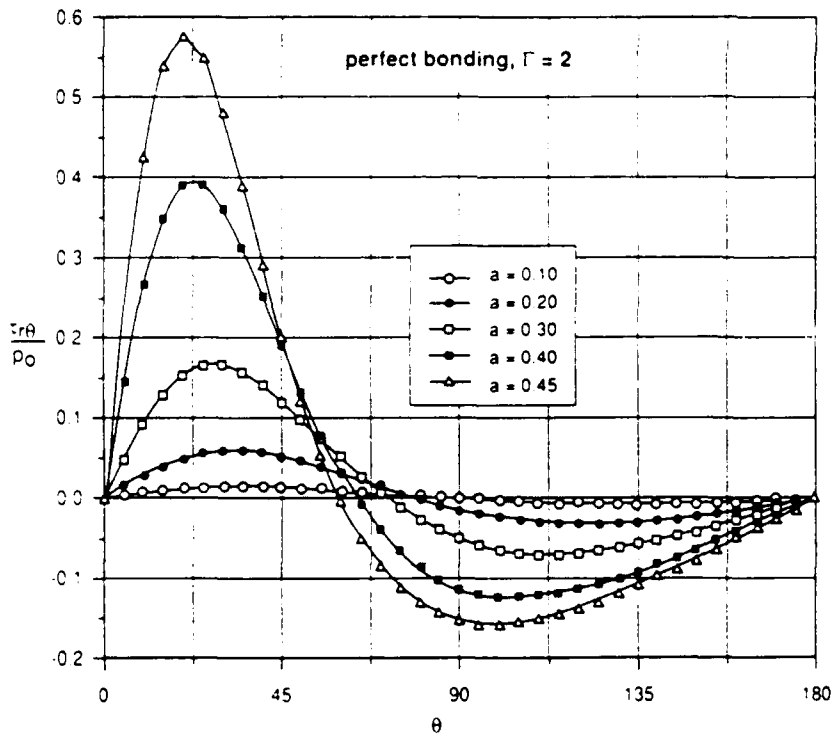


Fig. 6. Variation of σ_v along the central axis, for $a = 0.35$.

It was found that the stresses in the vicinity of the fibers, strongly depend upon the fiber matrix moduli ratio. The distance between fibers, has also a considerable effect on the elastic field: such an observation suggests that superposition of the single fiber solution, may not be a valid approximation.

Finally, a spring-type interfacial model was investigated. It was concluded that the loss of interfacial integrity, leads, very rapidly, to stress intensities that correspond to the conditions of perfect slip.

Fig. 7. Variation of σ_v along the central axis, for $a = 0.45$.Fig. 8. Shear stress along the interface for various fiber radii, a .

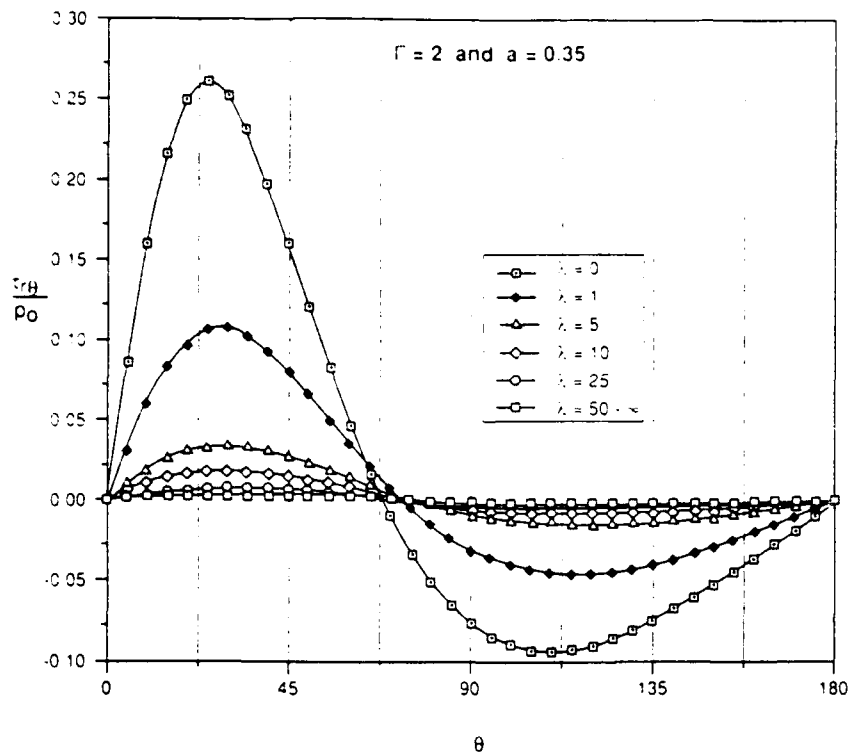


Fig. 9. Effect of the interfacial parameter λ on the shear stress distribution.

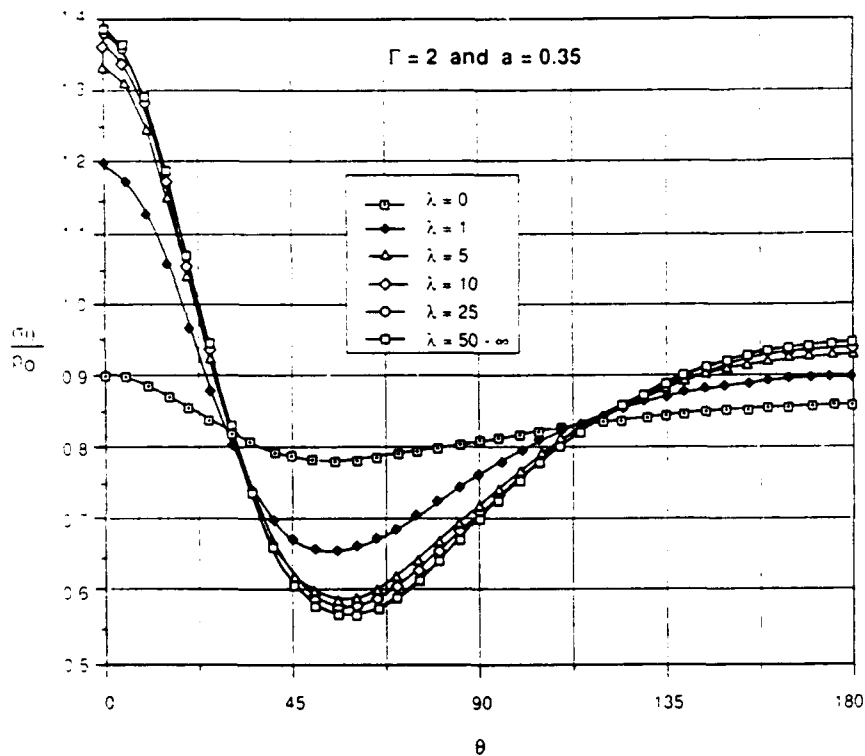
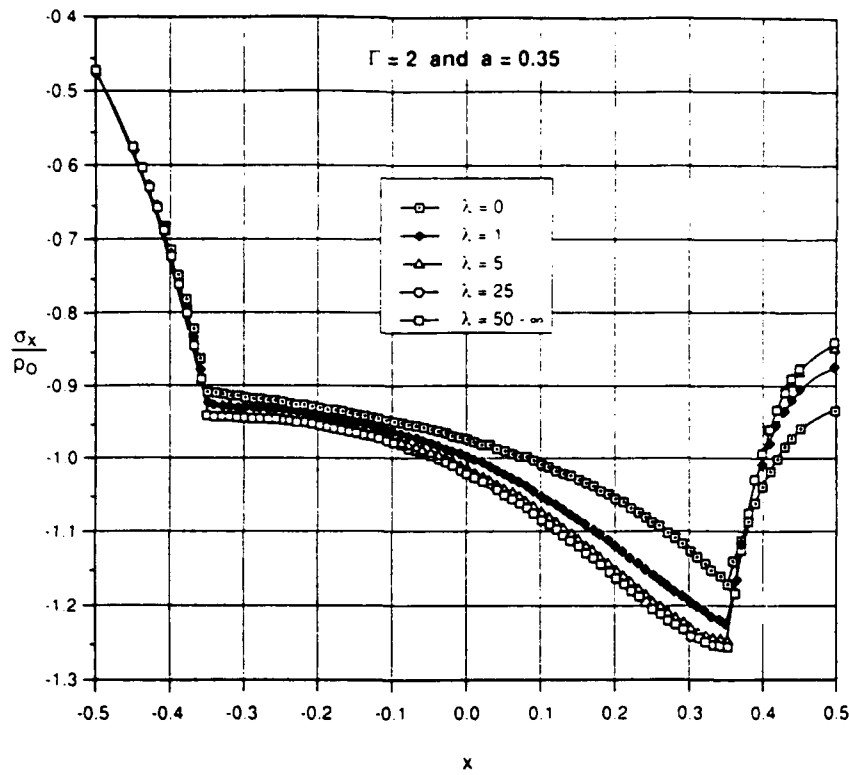
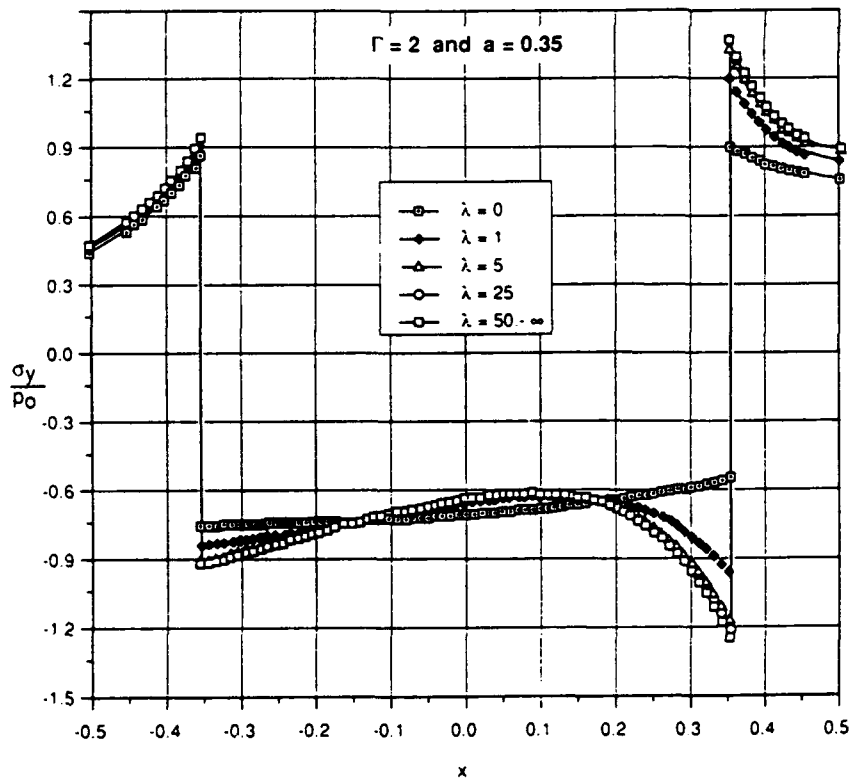


Fig. 10. Hoop stress along the interface for various values of λ .

Fig. 11. Effect of λ on σ_x along the x -axis.Fig. 12. Variation of σ_y along the x -axis for different values of λ .

Acknowledgment

The authors wish to thank Dr. Brian Cox, of the Rockwell International Science Center, for his valuable suggestions.

References

- Accorsi, M.L. and S. Nemat-Nasser (1986). Bounds on the overall elastic and instantaneous elastoplastic moduli of periodic composites. *Mech. Mater.* 5, 209.
- Benveniste, Y. (1984). On the effect of debonding on the overall behavior of composite materials. *Mech. Mater.* 3, 349.
- Benveniste, Y. (1985). The effective mechanical behavior of composite materials with imperfect contact between the constituents. *Mech. Mater.* 4, 197.
- Budiansky, B. (1965). On the elastic moduli of some heterogeneous materials. *J. Mech. Phys. Solids* 13, 223.
- Cox, B.N. (1989). Life prediction for structural materials in hypersonic engines. *Final Report to Rocketdyne*.
- Cox, B.N., M.R. James, D.B. Marshall, W.L. Morris, C.G. Rhodes and M. Shaw (1989). Mechanics of failure in titanium aluminide composites in: S. Benson, T. Cook, E. Trewin and R.M. Turner eds., *Proc. 10th International SAMPE European Chapter Conference*, Elsevier, Amsterdam, p. 313.
- Hashin, Z. (1990). Thermoelastic properties of fiber composites with imperfect interface. *Mech. Mater.* 8, 333.
- Hill, R. (1965). A self-consistent mechanics of composite materials. *J. Mech. Phys. Solids* 13, 213.
- Iwakuma, T. and S. Nemat-Nasser (1983). Composites with periodic microstructure. *Computers Struct.* 16(1-4), 13.
- Jasiuk, I., J. Chen and M.F. Thorpe (1989). The effect of interface on the elastic properties of random systems with rigid inclusions. *Proc. of the American Society for Composites*, p. 513.
- Kouris, D. and T. Mura (1989). The elastic field of a hemispherical inhomogeneity at the free surface of an elastic half space. *J. Mech. Phys. Solids* 37, 365.
- Kröner, E. (1958). Berechnung der Elastischen Konstanten des Vielkristalls aus den Konstanten des Einkristalls. *Z. Phys* 151, 504.
- Lene, F. and D. Leguillon (1982). Homogenized constitutive law for a partially cohesive composite material. *Int. J. Solids Struct.* 18, 443.
- Mori, T. and K. Wakashima (1990). Successive iteration method in the evaluation of average fields in elastically inhomogeneous materials. in: G.J. Weng, M. Taya and H. Abe, eds., *Micromechanics and Inhomogeneity, the Toshio Mura Anniversary Volume*, Springer, New York, p. 269.
- Mura, T. (1987). *Micromechanics of Defects in Solids*. 2nd ed., Martinus Nijhoff, Dordrecht.
- Nemat-Nasser, S., T. Iwakuma and M. Hejazi (1982). On composites with periodic structure. *Mech. Mater.* 1, 239.
- Neuber, H. (1934). Ein neuer Ansatz zur Lösung räumlicher Probleme der Elastizitätstheorie. *Z. Angew. Math. Mech.* 14, 203.
- Papkovich, P.F. (1932). Solution générale des équations différentielles fondamentales d'élasticité, exprimée par trois fonctions harmoniques. *C.R. Acad. Sci.* 195, 513.
- Shibata, S., I. Jasiuk, T. Mori and T. Mura (1990). Successive iteration method applied to composites containing sliding inclusions: effective modulus and anelasticity. *Mech. Mater.* 9, 229.

3.2 Stress Concentration due to the Interaction between Two Imperfectly Bonded Fibers in a Continuous Fiber Composite

published in the ASME Journal of Applied Mechanics

A Brief Note is a short paper that presents a specific solution of technical interest in mechanics but which does not necessarily contain new general methods or results. A Brief Note should not exceed 1500 words or equivalent (a typical one-column figure or table is equivalent to 250 words; a one line equation to 30 words). Brief Notes will be subject to the usual review procedures prior to publication. After approval such Notes will be published as soon as possible. The Notes should be submitted to the Technical Editor of the JOURNAL OF APPLIED MECHANICS. Discussions on the Brief Notes should be addressed to the Editorial Department, ASME, United Engineering Center, 345 East 47th Street, New York, N. Y. 10017, or to the Technical Editor of the JOURNAL OF APPLIED MECHANICS. Discussions on Brief Notes appearing in this issue will be accepted until two months after publication. Readers who need more time to prepare a Discussion should request an extension of the deadline from the Editorial Department.

Stress Concentration due to the Interaction Between Two Imperfectly Bonded Fibers in a Continuous Fiber Composite

D. Kouris¹

1 Introduction

One of the common modes of failure of intermetallic composites is attributed to the presence of interfacial cracking.

The loss of interfacial integrity is a consequence of the inherent differences between the thermoelastic properties of the matrix/fiber system as well as its chemical reactivity.

In an effort to evaluate the local stress state due to thermal residual strains, Kouris and Tsuchida (1991) obtained an analytical solution for a pair of fibers, under plane-strain conditions. The fiber cross-sections were modeled by circular inhomogeneities that sustain uniform eigenstrains, proportional to the mismatch of the coefficients of thermal expansion. It was found that the relative distance between fibers (volume fraction) has a considerable effect on the stress concentration, which cannot be accounted for by means of an "average" approach.

The problem of an infinite thin plate with two circular inclusions, perfectly bonded to the plate, has been considered by Shioya (1971). Under conditions of generalized plane stress, the solution has been obtained on the basis of Airy's stress functions by utilizing bipolar coordinates and a perturbation method.

In the present study, an analytical solution is obtained for a pair of fibers embedded in a linear elastic matrix under remote tension. The plane-strain formulation is based upon a displacement approach and the effects of the condition of the interface are examined. The results focus on the stress state of the matrix along the interface.

2 Analytical Approach

The geometry of the boundary value problem under consideration is shown in Fig. 1. The cross-sections of the two continuous fibers are modeled by two circular inhomogeneities (plane strain) and the transverse remote tension is indicated by T_x and T_y .

In the absence of the fibers, the uniform stress field is described by

$$\begin{aligned} 2Gu_r &= \frac{1}{4}(\kappa - 1)r(T_x + T_y) + \frac{1}{2}r(T_x - T_y)\cos 2\theta, \\ 2Gu_\theta &= \frac{1}{2}r(T_y - T_x)\sin 2\theta, \\ \sigma_r &= \frac{1}{2}(T_x + T_y) + \frac{1}{2}(T_x - T_y)\cos 2\theta, \\ \sigma_\theta &= \frac{1}{2}(T_x + T_y) + \frac{1}{2}(T_y - T_x)\cos 2\theta, \text{ and} \\ \tau_{r\theta} &= \frac{1}{2}(T_y - T_x)\sin 2\theta. \end{aligned} \quad (1)$$

in terms of polar coordinates, where $\kappa = 3 - 4\nu$.

The centers O_1 , O_2 of the fiber cross-sections coincide with the origins of the Cartesian coordinates (x_1, y_1) and (x_2, y_2) . If we assume that the central distance is equal to unity then

$$x_1 = x_2 + 1, y_1 = y_2 \quad (2)$$

and

$$x_i = r_i \cos \theta_i, y_i = r_i \sin \theta_i \quad (i = 1, 2).$$

The displacement vector u can be expressed as the sum of the vectors corresponding to the O_1 and O_2 coordinate systems. Therefore,

$$u = u_1 + u_2. \quad (3)$$

Due to the applied mechanical loading, the far-field boundary conditions require that the nonzero stresses σ_{xx} and σ_{yy} at infinity, are equal to the external load T_x and T_y , respectively.

In order to account for the imperfect bond between the fibers and the matrix, and spring-type thin layer along the interface is considered. Such a model allows for displacement discontinuities along the interface, while tractions remain continuous. The thin layer provides a viable alternative to the "three phase" approach and has been utilized by a number of researchers (Lene and Leguillon, 1982; Benveniste, 1984; Jasiuk et al., 1991; among others).

¹Mechanical and Aerospace Engineering Department, Arizona State University, Tempe, AZ 85287-6106. Assoc. Mem. ASME.

Manuscript received by the ASME Applied Mechanics Division, Feb. 14, 1991; final revision, Sept. 10, 1991. Associate Technical Editor: G. J. Dvorak.

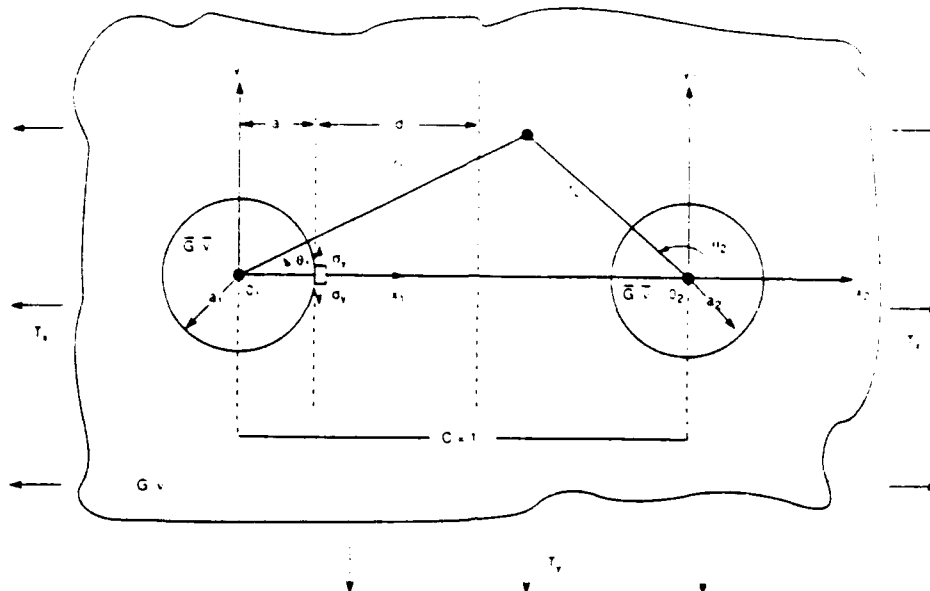


Fig. 1 Geometry of the problem

Based on the model described above, the boundary conditions along the circular interfaces ($r_i = a_i$) are

$$u_r = \bar{u}_r, [u_\theta] = \lambda \frac{a}{2G} \bar{\tau}_{\theta\theta}, \sigma_r = \bar{\sigma}_r, \text{ and } \tau_{r\theta} = \bar{\tau}_{r\theta} \quad (4)$$

where $[u_\theta] = u_\theta - \bar{u}_\theta$. Here, the quantities with a bar refer to the inhomogeneities; in addition, G and a denote the shear moduli of the matrix and the radius of the fiber cross-section, respectively. The constant of proportionality λ indicates the degree of interfacial integrity; $\lambda = 0$ corresponds to perfect bonding, while when $\lambda = \infty$, conditions of perfect slip are obtained (the interface does not sustain any shear tractions).

In order to account for the disturbance due to the presence of the inhomogeneities, we utilize the Papkovitch-Neuber displacement formulation. Consequently, the displacement fields u_i and u_2 are

$$2Gu_i = \text{grad} [\varphi_{0i} + x_i \varphi_{1i} + y_i \varphi_{2i}] - 4(1-\nu) [\varphi_{1i}, \varphi_{2i}], \quad (i = 1, 2) \quad (5)$$

where φ_{0i} , φ_{1i} , and φ_{2i} are arbitrary harmonic functions.

For the problem under consideration, the potentials chosen are: for the matrix ($r_i > a_i$)

$$\begin{cases} \varphi_{0i} = p_0 \left[F_0^i \log \rho_i + \sum_{n=1}^{\infty} A_n^i \rho_i^{-n} \cos n\theta_i \right] \\ \varphi_{1i} = p_0 \sum_{n=1}^{\infty} B_n^i \rho_i^{-n} \cos n\theta_i, \quad \varphi_{2i} = 0 \end{cases} \quad (I)$$

and for the two inhomogeneities ($r_i < a_i$)

$$\begin{cases} \varphi_{0i} = p_0 \sum_{n=1}^{\infty} \bar{A}_n^i \rho_i^n \cos n\theta_i \\ \varphi_{1i} = p_0 \sum_{n=1}^{\infty} \bar{B}_n^i \rho_i^n \cos n\theta_i, \quad \varphi_{2i} = 0 \end{cases} \quad (II)$$

where $\rho_i = r_i/c$ and $p_0 = T$. The central distance c is taken to be equal to unity and T is equal to T_x or T_y .

Using the potential functions [I] and [II], we can derive stresses and displacements in the matrix and the inhomogeneities; with the addition of the uniform field described in (1), what remain to be determined are the values of the coefficients F_0^i , A_n^i , B_n^i , \bar{A}_n^i and \bar{B}_n^i . This can be accomplished by enforcing the boundary conditions (4) along the interface of the inclusions.

Using the transformation formulas that have been given in Kouris and Tsuchida (1991), the requirement for continuity of the normal stress along the interface of the cross-section of the first fiber ($r_1 = a_1$) is expressed by:

$$\begin{aligned} \sigma_r = \bar{\sigma}_r = & -F_0^1 \frac{1}{a_1^3} + \sum_{n=1}^{\infty} A_n^1 \frac{n(n+1)}{a_1^{n+2}} \cos n\theta_1 \\ & + \frac{1}{2} \sum_{n=2}^{\infty} B_{n-1}^1 \frac{(n-1)(n+2)}{a_1^n} \cos n\theta_1 \\ & + \frac{1}{2} \sum_{n=0}^{\infty} B_{n+1}^1 \frac{n(n+1)(n+1+\kappa)}{a_1^{n+2}} \cos n\theta_1 \\ & - F_0^2 \sum_{n=1}^{\infty} (n-1) a_1^{n-2} \cos n\theta_1 \\ & + \sum_{n=0}^{\infty} \sum_{m=1}^{\infty} (-1)^m (A_m^2 - B_m^2) W_n^m n(n-1) a_1^{n-2} \cos n\theta_1 \\ & + \frac{1}{2} \sum_{n=1}^{\infty} \sum_{m=1}^{\infty} (-1)^m B_m^2 W_{n-1}^m a_1^{n-2} \\ & \quad (n-1) \times (n-1-\kappa) \cos n\theta_1 \\ & + \frac{1}{2} \sum_{n=0}^{\infty} \sum_{m=1}^{\infty} (-1)^m B_m^2 W_{n+1}^m a_1^n (n+1)(n-2) \cos n\theta_1 \\ & - \sum_{n=1}^{\infty} \bar{A}_n^1 n(n-1) a_1^{n-2} \cos n\theta_1 \\ & - \frac{1}{2} \sum_{n=2}^{\infty} \bar{B}_{n-1}^1 (n-1)(n-1-\kappa) a_1^{n-2} \cos n\theta_1 \end{aligned}$$

$$-\frac{1}{2} \sum_{n=0}^{\infty} \bar{B}_{n+1}^I (n+1)(n-2) a_1^n \cos n\theta_1$$

$$-\frac{1}{2} (1+t) - \frac{1}{2} (1-t) \cos 2\theta_1, \quad (6)$$

where $t = T_r/T_c$ ($0 < t < 1$) and $W_n^m = (m+n-1)!/(m-1)!n!$. Similar expressions are obtained for the remaining boundary conditions given in (4).

Using the same procedure, we can enforce the boundary conditions along the interface of the second circular inhomogeneity. However, since the fiber cross-sections are identical and due to the symmetry of the problem, we only have to satisfy the boundary conditions along one of the interfaces; the other will be satisfied automatically.

Utilizing the symmetry relations

$$A_n^I = (-1)^n A_n^II = A_n, \quad B_n^I = (-1)^{n+1} B_n^II = B_n, \quad (7)$$

$$\bar{A}_n^I = (-1)^n \bar{A}_n^II = \bar{A}_n, \quad \bar{B}_n^I = (-1)^{n+1} \bar{B}_n^II = \bar{B}_n, \quad a_1 = a_2 = a,$$

we can express the condition (6) as follows:

$$-F_0 \frac{1}{a_2} \delta_n^{(0)} + A_n \frac{n(n+1)}{a^{n+2}} + \frac{1}{2} B_{n-1} \frac{(n-1)(n+2)}{a^n}$$

$$+ \frac{1}{2} B_{n+1} \frac{(n+1)(n+3)}{a^{n+2}}$$

$$- F_0 (n-1) a^{n-2} + \sum_{m=1}^{\infty} (A_m + B_m) W_n^m n(n-1) a^{n-2}$$

$$- \frac{1}{2} \sum_{m=1}^{\infty} B_m W_{n-1}^m (n-1)(n-1-\kappa) a^{n-2}$$

$$- \frac{1}{2} \sum_{m=1}^{\infty} B_m W_{n+1}^m (n+1)(n-2) a^n - \bar{A}_n n(n-1) a^{n-2}$$

$$- \frac{1}{2} \bar{B}_{n-1} (n-1)(n-1-\bar{\kappa}) a^{n-2} - \bar{B}_{n+1} (n+1)(n-2) a^n$$

$$= -\frac{1}{2} (1+t) \delta_n^{(0)} - \frac{1}{2} (1-t) \delta_n^{(2)} \quad (n=0,1,2,\dots) \quad (8)$$

where $\delta_n^{(i)}$ denotes Kronecker's delta.

3 Results and Discussion

The linear system of equations consisting of (8) and the remaining boundary conditions is solved for the unknown coefficients F_0 , A_n , B_n , \bar{A}_n , and \bar{B}_n . The series solution requires no more than 15 terms to ensure matching of the boundary conditions up to the three significant figures, and its convergence is numerically evident. After evaluating the series coefficients, stresses and displacements in the matrix and the fiber cross-sections can be determined.

In order to illustrate the effects of the fiber/matrix shear moduli ratio Γ ($\Gamma = \bar{G}/G$) and the fiber/fiber distance on the stress concentration, the external load has been taken as $p_0 = T_x = T_y$ ($t = 1$).

In a number of studies that investigate effective properties of composites, the "single fiber" solution is utilized in order to obtain global properties, in an average sense. Such an approach, however, may be quite inaccurate in predicting the local stress field, which is essential from a fracture point of view. Figure 2 indicates the variation of the matrix interfacial stress σ_r/p_0 (at the central line) versus the normalized fiber distance d/a ; the shear moduli ratio is taken equal to 2, 5, and 10 and $\nu = \bar{\nu} = 0.3$.

If we denote with an asterisk (*) the values of σ_r/p_0 that are obtained from superposition of the single fiber solution, we

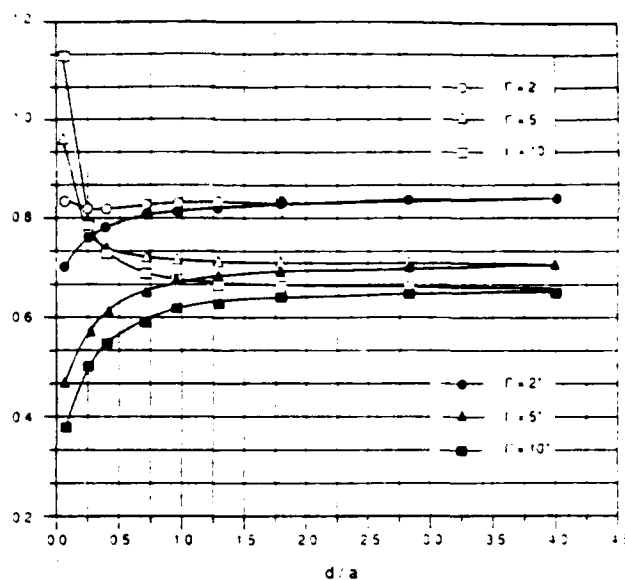


Fig. 2 Distribution of σ_r/p_0 at the interface versus the fiber distance; comparison between the exact and approximate solutions

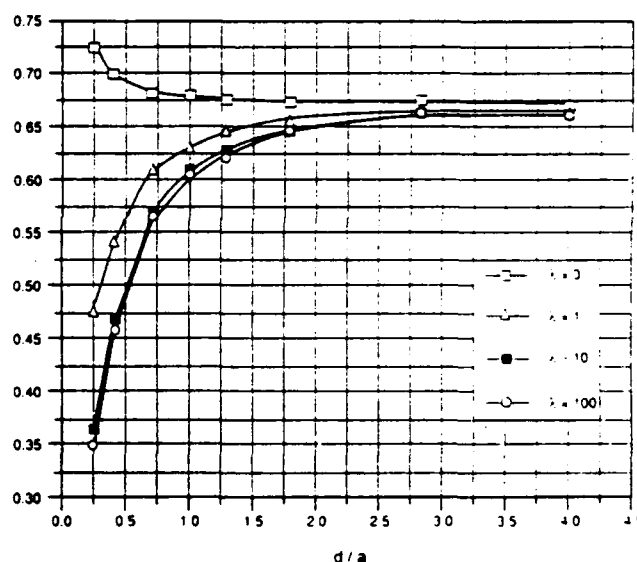


Fig. 3 Effect of the incoherent interface on the distribution of σ_r/p_0 for a $\text{Ti}_3\text{Al}/\text{SCS6}$ system

can observe that they are in error; such an error becomes significant with increasing Γ (stiffer fibers) when the fibers approach each other (high volume fraction). It is expected, however, that as the fiber distance increases, the differences between the exact and approximate solutions tend towards zero.

Another aspect of the problem relates to the effect of incoherent interfaces. As an example, we consider a $\text{Ti}_3\text{Al}/\text{SiC}$ (SCS6) composite with the following properties: (a) Ti_3Al (matrix) - $G = 30\text{GPa}$ and $\nu = 0.25$ (b) SCS6 (fibers) - $\bar{G} = 154\text{GPa}$ and $\bar{\nu} = 0.17$.

The distribution of σ_r/p_0 versus the fiber distance, is shown in Fig. 3; here $\lambda = 0$ corresponds to the condition of perfect bond, while $\lambda = 100$ indicates perfect sliding. As the fiber distance decreases, a weak interfacial bond causes a considerable relaxation of the matrix stress and, therefore, enhances the fracture toughness. However, if the fibers are far apart, the degree of the interfacial integrity has no effect on the stress concentration.

Acknowledgment

This work has been supported by the Air Force Office of Scientific Research through the University Research Initiative Award AFOSR90-0235.

References

- Benveniste, Y., 1984, "On the Effect of Debonding on the Overall Behavior of Composite Materials," *Mechanics of Materials*, Vol. 3, pp. 349-358.
- Jasiuk, I., Chen, J., and Thrope, M. F., 1989, "Elastic Moduli of Composites with Rigid Sliding Inclusions," *Journal of Mechanics and Physics of Solids*, to appear.
- Kouris, D., and Tsuchida, E., 1991, "On the Elastic Interaction between two Fibers in a Continuous Fiber Composite under Thermal Loading," *Mechanics of Materials*, Vol. 12, pp. 131-146.
- Lene, F., and Leguillon, D., 1982, "Homogenized Constitutive Law for a Partially Cohesive Composite Material," *Int. Journal of Solids and Structures*, Vol. 18, No. 5, pp. 443-458.
- Shioya, S., 1971, "On the Tension of an Infinite Thin Plate Containing a Pair of Circular Inclusions," *Bulletin of the JSME*, Vol. 14, No. 68, pp. 117-126.

A Superposition Method for One-Dimensional Axially Symmetric Elastic Waves

Zhang Xiangzhou²

Introduction

Responses of an elastic, infinite medium containing a cylindrical, circular cavity to axially symmetric dynamic loading is of fundamental interest in elastodynamics. The geometry, loading, and mathematical formulation involved in the responses are simple. Nevertheless, this problem is very difficult to solve analytically. As indicated in standard reference books, the integral in the solution of the problem is "extremely difficult" to evaluate, and there is "an essential difficulty" inherent in this kind of wave propagation (Eringen and Suhubi, 1975); the solution and its derivation are "not simple" (Miklowitz, 1978); the problem is "much more difficult to analyze" (Achenbach, 1976); and so on. Therefore, an analytic solution method, which can solve the problem effectively, still appears to be desirable.

In this Note, a superposition method, based on Lamb's formal solution, is developed to treat the problem. Numerical examples demonstrate that the method is able to solve the axially symmetric wave propagation problem accurately and neatly.

Basic Solutions for the Radial Motion Problem

A cross-section of a linearly elastic, infinite medium containing a cylindrical, circular cavity is depicted in Fig. 1. The medium is at rest initially and then undergoes a radial motion due to an axially symmetric, normal traction $g(t)$ suddenly applied on its circumferential boundary. As is well known (Achenbach, 1976), the radial displacement u and the normal stresses σ_r , σ_θ , and σ_z developed in the medium should be sought via the following basic equation and conditions:

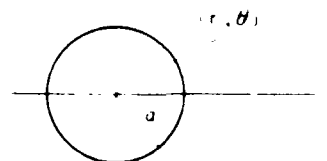


Fig. 1 Geometry of the problem

$$\frac{\partial^2 \varphi}{\partial r^2} + \frac{1}{r} \frac{\partial \varphi}{\partial r} = \frac{1}{c_1^2} \frac{\partial^2 \varphi}{\partial t^2} \quad (1)$$

$$c_1 t < a, \quad u = 0, \quad \partial u / \partial t = 0 \quad (2a, b)$$

$$c_1 t > a, \quad r = a, \quad \sigma_r = g(t) \quad (3)$$

$$r \rightarrow \infty, \quad u = 0, \quad \partial u / \partial t = 0 \quad (4a, b)$$

$$u = \frac{\partial \varphi}{\partial r}, \quad \sigma_r = \lambda \left(\frac{\partial u}{\partial r} + \frac{u}{r} \right) + 2\mu \frac{\partial u}{\partial r} \quad (5a, b)$$

$$\sigma_\theta = \lambda \left(\frac{\partial u}{\partial r} + \frac{u}{r} \right) + 2\mu \frac{u}{r}, \quad \sigma_z = \lambda \left(\frac{\partial u}{\partial r} + \frac{u}{r} \right) \quad (6a, b)$$

where λ and μ stand for Lamé constants and c_1 represents the longitudinal wave speed of the material. Equations (5b) and (6a, b) are for plane-strain state. For plane stress, λ in Eqs. (5b), (6a) should be replaced by $2\lambda\mu/(\lambda + 2\mu)$ and $\sigma_z = 0$.

Lamb provided a formal solution to Eq. (1). It reads (Eringen and Suhubi, 1975; Lamb, 1902):

$$\varphi(r, t) = \begin{cases} 0, & c_1 t < r \\ \int_0^{\cosh^{-1} c_1 t / r} f(c_1 t - r \cosh u) du, & c_1 t > r \end{cases} \quad (7a, b)$$

Subsequent to Eqs. (7a, b), the following expressions for u and $\partial u / \partial r$ can be obtained directly:

$$u(r, t) = \begin{cases} 0, & c_1 t < r \\ - \int_0^{\cosh^{-1} c_1 t / r} \cosh u f'(c_1 t - r \cosh u) du \\ - f(0) c_1 t / [r(c_1^2 t^2 - r^2)^{1/2}], & c_1 t > r \end{cases} \quad (8a, b)$$

$$\frac{\partial u}{\partial r} = \begin{cases} 0, & c_1 t < r \\ \int_0^{\cosh^{-1} c_1 t / r} \cosh^2 u f''(c_1 t - r \cosh u) du + \frac{f'(0) c_1^2 t^2}{r^2 (c_1^2 t^2 - r^2)^{3/2}} \\ + \frac{f(0) c_1 t}{(c_1^2 t^2 - r^2)^{1/2}} \left(\frac{1}{r^2} - \frac{1}{c_1^2 t^2 - r^2} \right), & c_1 t > r \end{cases} \quad (9a, b)$$

where $f'(x) = df(x)/dx$.

The displacement and stresses in the medium are developed for $t > a/c_1$. However, our main concern lies within the prime stage of the dynamic response, that is, within a certain interval of t , $[a/c_1, T]$, with T being a sufficiently large number. Within the interval, any continuous function $f(c_1 t - r)$ in Eq. (7b) can be expanded into the following form:

$$f(c_1 t - r) = a_0 + a_1(c_1 t - r) + a_2(c_1 t - r)^2 + \dots + a_n(c_1 t - r)^n + \dots \quad (10)$$

Denoting φ , u and $\partial u / \partial r$ derived from the term $a_n(c_1 t - r)^n$ in the above formula with $a_n = 1$ by σ_n , u_n and $(\partial u / \partial r)_n$.

²Department of Aircraft Engineering, Northwestern Polytechnical University, Xian, 710072, China.

Manuscript received by the ASME Applied Mechanics Division, Jan. 1, 1991; final revision, Oct. 17, 1991. Associate Technical Editor: S. K. Datta.

3.3 The Elastic Field in the Vicinity of Two Elliptical Inhomogeneities

to be submitted for publication in the Int. Journal of Solids and Structures

The Elastic Field in the Vicinity of Two Elliptical Inhomogeneities

Demitris KOURIS *

Marc MEISNER *

Key Words: Elasticity, Residual Stress, Interaction, Eigenstrain,
inhomogeneity

* Department of Mechanical and Aerospace Engineering, Arizona
State University, Tempe, Arizona 85287-6106, U.S.A.

Abstract

The paper analyzes the elastic field caused by the interaction of two elliptical inhomogeneities subjected to residual strains. The thermally induced residual field is modeled by uniform eigenstrains sustained by the inhomogeneities. The boundary value problem is formulated in terms of the Papkovitch - Neuber displacement potentials. A number of numerical examples illustrate the differences between the perfectly bonded and slipping interfaces.

1. Introduction

Prerequisite to analyzing or predicting microcracking in any material is knowledge of the local stress state. In the case of composites, whether continuous fiber or laminated, the local stress state is severely affected by residual thermal mismatch stresses. In addition, the thermo-mechanical behavior of a composite is closely related to the properties of the fiber - matrix interface. It has been shown that the tensile interfacial strength is related to the transverse and compressive strength of the composite, while the shear interfacial strength affects the transfer length and composite fracture, as well as the deformation of the matrix.

In a recent study (1), the interaction of two continuous fibers, under conditions of plane strain, has been investigated. The cross sections of the fibers were modeled by two circular inhomogeneities with elastic constants that are generally different from the ones of the surrounding matrix. The

presence of the residual field due to thermal loading was taken into account via uniform eigenstrains (2), that are sustained by the inhomogeneities. It was found that the local elastic field is severely influenced by the relative distance between fibers, the elastic properties of the constituents and the integrity of the interface.

In the present paper, the study is generalized to account for the interaction of elliptical inhomogeneities. The problem is formulated in terms of displacement potentials (Refs. 3 and 4) and solutions are obtained for perfectly bonded as well as slipping interfaces. Unlike Eshelby's result for the single inclusion (5), the stress field inside the interacting inhomogeneities is no longer uniform. The local elastic field is determined in the form of infinite series and is dependant upon the relative distance, the aspect ratio, and the elastic properties of the inhomogeneities. A number of numerical calculations are presented to illustrate the results.

2. Displacement Formulation

Consider an infinite region with two elliptic inhomogeneities, Ω_1 and Ω_2 , with centers at O_1 and O_2 , respectively. Let the centers be at the origins of the Cartesian coordinates (x_1, y_1) and (x_2, y_2) , and x_1, x_2 - axis be the center line as illustrated in Fig. 1. If the central distance $O_1O_2 = \zeta$, then

$$x_1 = x_2 + \zeta, y_1 = y_2. \quad (1)$$

The elliptic coordinates are obtained from the coordinate transformation

$$x_i = C \cosh\alpha_i \cos\beta_i, y_i = C \sinh\alpha_i \sin\beta_i \quad (2)$$

where $i = 1, 2$ and C is the eccentricity of the inclusions.

For the two inclusion problem, the displacement vector u can be represented as

$$u = u_1 + u_2 \quad (3)$$

where u_1 and u_2 are the displacement vectors corresponding to the origins, O_1 and O_2 , respectively.

A general solution of the displacement equations of equilibrium can be described according to the Papkovitch-Neuber displacement formulation. The displacement fields, u_1 and u_2 , are given by

$$2Gu_1 = \text{grad}[\phi_{01} + x_1\phi_{11} + y_1\phi_{21}] - (\kappa + 1)[\phi_{11}, \phi_{21}] \quad (4)$$

and

$$2Gu_2 = \text{grad}[\phi_{02} + x_2\phi_{12} + y_2\phi_{22}] - (\kappa + 1)[\phi_{12}, \phi_{22}] \quad (5)$$

where G is the shear modulus, $\kappa = 3 - 4\nu$ for the plane strain, ν is Poisson's ratio, ϕ_{ij} are arbitrary harmonic functions, and $[\phi_{ij}, \phi_{mn}]$ corresponds to ϕ_{ij} for the x -component and ϕ_{mn} for the y -component of the displacement field. In order to satisfy the boundary conditions along Ω_1 ($\alpha_1 = \alpha_0$), it is necessary to express (5) in terms of the O_1 coordinate system. Substitution of (1) into (5) yields,

$$2Gu_2 = \text{grad}[\phi_{02} + (x_1 - \zeta)\phi_{12} + y_1\phi_{22}] - (\kappa + 1)[\phi_{12}, \phi_{22}] \quad (6)$$

or

$$2Gu_2 = \text{grad}[\phi_{02} - \zeta\phi_{12} + x_1\phi_{12} + y_1\phi_{22}] - (\kappa + 1)[\phi_{12}, \phi_{22}]$$

According to a similar procedure for the boundary conditions along Ω_2 ($\alpha_2 = \alpha_0$), eqn (4) becomes,

$$2Gu_1 = \text{grad}[\phi_{01} + \zeta\phi_{11} + x_2\phi_{11} + y_2\phi_{21}] - (\kappa + 1)[\phi_{11}, \phi_{21}]. \quad (7)$$

The residual field due to the thermal loading is represented by a pair of uniform eigenstrains (ϵ_x^* , ϵ_y^*). These eigenstrains (Mura, 1987) are proportional to the temperature change and the mismatch of the coefficients of thermal expansion. Consequently, inelastic displacements are introduced in the inhomogeneities according to

$$\bar{u}_x^* = \epsilon_x^* x, \quad (8)$$

$$\bar{u}_y^* = \epsilon_y^* y.$$

Their corresponding components in elliptical coordinates are

$$\bar{u}_\alpha^* = \frac{C^2 h}{4} \sinh 2\alpha \left[(1 + \cos 2\beta) \epsilon_x^* + (1 - \cos 2\beta) \epsilon_y^* \right], \quad (9)$$

$$\bar{u}_\beta^* = \frac{C^2 h}{4} \sin 2\beta \left[(1 + \cosh 2\alpha) \epsilon_x^* + (1 - \cosh 2\alpha) \epsilon_y^* \right],$$

where

$$h = \frac{1}{C (\cosh^2 \alpha - \cos^2 \beta)^{1/2}}. \quad (10)$$

When the inhomogeneities are perfectly bonded along the elliptical interfaces ($\alpha_i = \alpha_0$), the boundary conditions are represented by

$$u_\alpha = \bar{u}_\alpha + \bar{u}_\alpha^*, u_\beta = \bar{u}_\beta + \bar{u}_\beta^*, \sigma_\alpha = \bar{\sigma}_\alpha, \text{ and } \tau_{\alpha\beta} = \bar{\tau}_{\alpha\beta}. \quad (11)$$

The quantities overscored are associated with the inclusions.

3. Solution of the Boundary Value Problem

If a set of harmonic displacement potentials can be determined such that the boundary conditions along the interfaces (11) as well as the requirement for vanishing tractions as $\alpha \rightarrow \infty$ are satisfied, then the unique solution can be obtained. Based on symmetry considerations, the

Papkovich-Neuber displacement potentials for the matrix ($\alpha_i > \alpha_0$) are chosen as

$$\begin{aligned}\varphi_{0i} &= p_0 \left[F_0^i \alpha_i + \sum_{n=1}^{\infty} A_n^i e^{-n\alpha_i} \cos n\beta_i \right] \\ \varphi_{1i} &= p_0 \sum_{n=1}^{\infty} B_n^i e^{-n\alpha_i} \cos n\beta_i \\ \varphi_{2i} &= 0\end{aligned}\quad (12)$$

where $p_0 = 2G\epsilon^*$ and $\epsilon_x^* = \epsilon_y^* = \epsilon^*$ (13)

Similarly, the displacement potentials for the two inhomogeneities ($\alpha_i < \alpha_0$) are chosen as

$$\begin{aligned}\bar{\varphi}_{0i} &= p_0 \sum_{n=1}^{\infty} \bar{A}_n^i \cosh n\alpha_i \cos n\beta_i \\ \bar{\varphi}_{1i} &= p_0 \sum_{n=1}^{\infty} \bar{B}_n^i \cosh n\alpha_i \cos n\beta_i \\ \bar{\varphi}_{2i} &= 0\end{aligned}\quad (14)$$

The following relations between the elliptic harmonic functions will be used to satisfy the boundary conditions at the interface of $\Omega_1(\alpha_1 = \alpha_0)$ and $\Omega_2(\alpha_2 = \alpha_0)$,

$$\begin{aligned}\alpha_1 &= \sum_{n=0}^{\infty} \omega_n \cosh n\alpha_2 \cos n\beta_2, \\ \alpha_2 &= \sum_{n=0}^{\infty} Z_n \cosh n\alpha_1 \cos n\beta_1, \\ e^{-n\alpha_1} \cos n\beta_1 &= \sum_{m=0}^{\infty} (-1)^m d_{m,n} \cosh m\alpha_2 \cos m\beta_2,\end{aligned}\quad (15)$$

$$e^{-n\alpha_2} \cos n\beta_2 = (-1)^n \sum_{n=0}^{\infty} d_{m,n} \cosh n\alpha_1 \cos n\beta_1,$$

where the coefficients ω_n , Z_n , and $d_{m,n}$ are given in Appendix A.

For the displacement potentials described above, the boundary conditions (11) lead to the evaluation of the unknown coefficients (i.e., F_0^i , A_n^i , B_n^i , \bar{A}_n^i , and \bar{B}_n^i).

Using (9), (12), (14) and (15), eight equations are obtained for the interfaces $\Omega_1(\alpha_1 = \alpha_0)$ and $\Omega_2(\alpha_2 = \alpha_0)$. However, since the inhomogeneities are identical and a symmetric load is applied, only the boundary conditions along one of the interfaces need to be considered. This can be accomplished, provided that the following symmetry relations among the coefficients are taken into account when $\alpha_1 = \alpha_2 = \alpha_0$:

$$F_0 = F_0^1 = F_0^2$$

$$A_n = A_n^1 = (-1)^n A_n^2, \bar{A}_n = \bar{A}_n^1 = (-1)^n \bar{A}_n^2 \quad (16)$$

$$B_n = B_n^1 = (-1)^{n+1} B_n^2, \bar{B}_n = \bar{B}_n^1 = (-1)^{n+1} \bar{B}_n^2.$$

Consequently, the condition $u_\alpha = \bar{u}_\alpha + \bar{u}_\alpha^*$ at $\alpha_1 = \alpha_0$ corresponds to

$$\begin{aligned} & F_0 \delta_{n,0} - \sum_{n=1}^{\infty} A_n U_{A1} - \frac{C}{4} \sum_{n=2}^{\infty} B_{n-1} U_{B1} - \frac{C}{4} \sum_{n=0}^{\infty} B_{n+1} U_{B2} \\ & + \frac{C}{4} \sum_{n=2}^{\infty} \left\{ F_0 Z_n + \sum_{m=0}^{\infty} (A_m + \zeta B_m) d_{m,n} \right\} U_{C1} - \frac{C}{4} \sum_{n=2}^{\infty} \sum_{m=0}^{\infty} B_m d_{m,n-1} U_{C2} \\ & - \frac{C}{4} \sum_{n=0}^{\infty} \sum_{m=0}^{\infty} B_m d_{m,n+1} U_{C3} - \frac{1}{\Gamma} \sum_{n=1}^{\infty} \bar{A}_n \bar{U}_{A1} - \frac{C}{4\Gamma} \sum_{n=2}^{\infty} \bar{B}_{n-1} \bar{U}_{B1} - \frac{C}{4\Gamma} \sum_{n=0}^{\infty} \bar{B}_{n+1} \bar{U}_{B2} \\ & = \frac{C^2}{2} \sinh 2\alpha_0 \{ \delta_{n,0} + \delta_{n,2} \}. \end{aligned} \quad (17)$$

where $\Gamma = \bar{G}/G$.

The condition $u_\beta = \bar{u}_\beta + \bar{u}_\beta^*$ at $\alpha_1 = \alpha_0$ gives

$$\begin{aligned} & \sum_{n=1}^{\infty} A_n V_{A1} + \frac{C}{4} \sum_{n=2}^{\infty} B_{n-1} V_{B1} + \frac{C}{4} \sum_{n=0}^{\infty} B_{n+1} V_{B2} \\ & + \sum_{n=2}^{\infty} \left\{ F_0 Z_n + \sum_{m=1}^{\infty} (A_m + \zeta B_m) d_{m,n} \right\} V_{C1} - \frac{C}{4} \sum_{n=2}^{\infty} \sum_{m=1}^{\infty} B_m d_{m,n-1} V_{C2} \\ & - \frac{C}{4} \sum_{n=0}^{\infty} \sum_{m=1}^{\infty} B_m d_{m,n+1} V_{C3} - \frac{1}{\Gamma} \sum_{n=1}^{\infty} \bar{A}_n \bar{V}_{A1} - \frac{C}{4\Gamma} \sum_{n=2}^{\infty} \bar{B}_{n-1} \bar{V}_{B1} - \frac{C}{4\Gamma} \sum_{n=0}^{\infty} \bar{B}_{n+1} \bar{V}_{B2} \\ & = \frac{C^2}{2} \delta_{n,2} \end{aligned} \quad (18)$$

The condition $\sigma_\alpha = \bar{\sigma}_\alpha$ at $\alpha_1 = \alpha_0$ yields

$$\begin{aligned} & -F_0 \frac{\sinh 2\alpha_0}{2} \delta_{n,0} - \frac{1}{4} \sum_{n=4}^{\infty} A_{n-2} S_{A1} + \frac{1}{4} \sum_{n=1}^{\infty} A_n S_{A2} - \frac{1}{4} \sum_{n=-1}^{\infty} A_{n+2} S_{A3} - \frac{C}{16} \sum_{n=4}^{\infty} B_{n-3} S_{B1} \\ & + \frac{C}{16} \sum_{n=2}^{\infty} B_{n-1} S_{B2} + \frac{C}{16} \sum_{n=0}^{\infty} B_{n+1} S_{B3} - \frac{C}{16} \sum_{n=-2}^{\infty} B_{n+3} S_{B4} \\ & - \frac{1}{4} \sum_{n=4}^{\infty} \left\{ F_0 Z_{n-2} + \sum_{m=1}^{\infty} (A_m + \zeta B_m) d_{m,n-2} \right\} S_{C1} + \frac{1}{4} \sum_{n=1}^{\infty} \left\{ F_0 Z_n + \sum_{m=1}^{\infty} (A_m + \zeta B_m) d_{m,n} \right\} S_{C2} \\ & - \frac{1}{4} \sum_{n=-1}^{\infty} \left\{ F_0 Z_{n+2} + \sum_{m=1}^{\infty} (A_m + \zeta B_m) d_{m,n+2} \right\} S_{C3} + \frac{C}{16} \sum_{n=4}^{\infty} \sum_{m=1}^{\infty} B_m d_{m,n-3} S_{C4} \\ & - \frac{C}{16} \sum_{n=2}^{\infty} \sum_{m=1}^{\infty} B_m d_{m,n-1} S_{C5} - \frac{C}{16} \sum_{n=0}^{\infty} \sum_{m=1}^{\infty} B_m d_{m,n+1} S_{C6} + \frac{C}{16} \sum_{n=-2}^{\infty} \sum_{m=1}^{\infty} B_m d_{m,n+3} S_{C7} \end{aligned}$$

$$\begin{aligned}
& + \frac{1}{4} \sum_{n=4}^{\infty} \overline{A_{n-2}} \overline{S_{A1}} - \frac{1}{4} \sum_{n=1}^{\infty} \overline{A_n} \overline{S_{A2}} + \frac{1}{4} \sum_{n=-1}^{\infty} \overline{A_{n+2}} \overline{S_{A3}} + \frac{C}{16} \sum_{n=4}^{\infty} \overline{B_{n-3}} \overline{S_{B1}} \\
& - \frac{C}{16} \sum_{n=2}^{\infty} \overline{B_{n-1}} \overline{S_{B2}} - \frac{C}{16} \sum_{n=0}^{\infty} \overline{B_{n+1}} \overline{S_{B3}} + \frac{C}{16} \sum_{n=-2}^{\infty} \overline{B_{n+3}} \overline{S_{B4}} \\
& = 0
\end{aligned} \tag{19}$$

The condition $\tau_{\alpha\beta} = \overline{\tau_{\alpha\beta}}$ at $\alpha_1 = \alpha_0$ corresponds to

$$\begin{aligned}
& - \frac{1}{2} F_0 \delta_{n,2} - \frac{1}{4} \sum_{n=4}^{\infty} A_{n-2} T_{A1} + \frac{1}{4} \sum_{n=1}^{\infty} A_n T_{A2} - \frac{1}{4} \sum_{n=-1}^{\infty} A_{n+2} T_{A3} - \frac{C}{16} \sum_{n=4}^{\infty} B_{n-3} T_{B1} \\
& + \frac{C}{16} \sum_{n=2}^{\infty} B_{n-1} T_{B2} + \frac{C}{16} \sum_{n=0}^{\infty} B_{n+1} T_{B3} - \frac{C}{16} \sum_{n=-2}^{\infty} B_{n+3} T_{B4} \\
& + \frac{1}{4} \sum_{n=4}^{\infty} \left\{ F_0 Z_{n-2} + \sum_{m=1}^{\infty} (A_m + \zeta B_m) d_{m,n-2} \right\} T_{C1} - \frac{1}{4} \sum_{n=1}^{\infty} \left\{ F_0 Z_n + \sum_{m=1}^{\infty} (A_m + \zeta B_m) d_{m,n} \right\} T_{C2} \\
& + \frac{1}{4} \sum_{n=-1}^{\infty} \left\{ F_0 Z_{n+2} + \sum_{m=1}^{\infty} (A_m + \zeta B_m) d_{m,n+2} \right\} T_{C3} - \frac{C}{16} \sum_{n=4}^{\infty} \sum_{m=1}^{\infty} B_m d_{m,n-3} T_{C4} \\
& + \frac{C}{16} \sum_{n=2}^{\infty} \sum_{m=1}^{\infty} B_m d_{m,n-1} T_{C5} - \frac{C}{16} \sum_{n=0}^{\infty} \sum_{m=1}^{\infty} B_m d_{m,n+1} T_{C6} - \frac{C}{16} \sum_{n=-2}^{\infty} \sum_{m=1}^{\infty} B_m d_{m,n+3} T_{C7} \\
& - \frac{1}{4} \sum_{n=4}^{\infty} \overline{A_{n-2}} \overline{T_{A1}} + \frac{1}{4} \sum_{n=1}^{\infty} \overline{A_n} \overline{T_{A2}} - \frac{1}{4} \sum_{n=-1}^{\infty} \overline{A_{n+2}} \overline{T_{A3}} - \frac{C}{16} \sum_{n=4}^{\infty} \overline{B_{n-3}} \overline{T_{B1}} \\
& + \frac{C}{16} \sum_{n=2}^{\infty} \overline{B_{n-1}} \overline{T_{B2}} + \frac{C}{16} \sum_{n=0}^{\infty} \overline{B_{n+1}} \overline{T_{B3}} - \frac{C}{16} \sum_{n=-2}^{\infty} \overline{B_{n+3}} \overline{T_{B4}} \\
& = 0.
\end{aligned} \tag{20}$$

where $\delta_{i,j}$ denotes the Kronecker's delta. U_{ij} , V_{ij} , S_{ij} , and T_{ij} are known functions of n , α_0 , v and \bar{v} .

After solving the system of equations (17) - (20) for the unknown coefficients F_0 , A_n , B_n , \bar{A}_n , and \bar{B}_n , stresses and displacements can be evaluated.

The analytical formulation for the problem of perfectly bonded inclusions has been demonstrated above. However, if there are no shear tractions along the interfaces, the inclusions are free to slip. The incoherent interfaces are then represented by

$$u_\alpha = \bar{u}_\alpha + \bar{u}_\alpha^*, \sigma_\alpha = \bar{\sigma}_\alpha, \tau_{\alpha\beta} = 0, \text{ and } \bar{\tau}_{\alpha\beta} = 0. \quad (21)$$

Consequently, the method of solution is similar to the perfectly bonded case.

4. Discussion

In order to illustrate the results, the linear system (17) - (20) was solved. Matching the boundary conditions up to three significant figures required no more than 15 series terms. With the values of the series coefficients known, the stresses and displacements in the matrix and inclusions can be obtained. Without loss of generality, $P_0 = 1$ and $\nu = \bar{\nu} = 0.3$ has been assumed.

Since the main focus of the present study is to investigate the mutual interaction between the inclusions, only variations in s , Γ , and λ are considered. The dimensionless parameters s and λ are defined as

$$s = \frac{a}{b}, \lambda = \frac{\zeta}{2b}. \quad (22)$$

In analyzing the normal stress along the interfaces, variations of the relative stiffness Γ (\bar{G}/G), and distance λ between the inhomogeneities are illustrated in Fig. 2 - 3. As the inclusions become stiffer relative to the matrix (Γ increases), the absolute values of the matrix interfacial stresses increase. In both cases the normal stress σ_α assumes an absolute maximum at $\beta = 0$. These values of the normal stress increase in the case of sliding.

The effect of various shear moduli ratio Γ (relative stiffness), on the hoop stress, σ_β , is more pronounced in the case of perfect bonding. Nevertheless, higher stress concentrations are again obtained at $\beta = 0$ (Fig. 4 - 5).

These results demonstrate that the interaction between the two inclusions is greatly effected by the inclusion/matrix stiffness ratio. Thus, the often used approximation that utilizes superposition of the single inclusion is not generally valid. Only for the the special case where the matrix and the inclusions have the same stiffness ($\Gamma = 1$) will the superposition method give valid results, as expected.

In order to qualify the inhomogeneity of the local stress state along the central axis, the distribution of the normal stresses σ_x and σ_y along the x - axis were studied. For the case of perfect bonding, the distribution of σ_y for various Γ is almost uniform inside the inclusions (Fig. 6(a)). However, this is not the case when sliding occurs. It is noted that the discontinuity along the interface ($x = 2$), is proportional to Γ (Fig. 6). The examination of the aspect ratio effect yields the stress distribution shown in Fig. 7. When the inhomogeneities are free to slip, the stresses are almost independent of s , except at the point of the interface ($x = 2$). As s decreases the interfacial stresses in the matrix increase considerably,

indicating the possibility of crack initiation. When the parameter $s \rightarrow 0$ (inclusions become thin inserts), the stresses in the matrix along the central line become localized around the inclusions. The results for $s = 0.99$ ($a \rightarrow b = 2$), correspond to the solution of two circular inclusions given by Kouris and Tsuchida (1991).

Finally, the effects of various shear moduli and aspect ratios on the interfacial matrix stresses is investigated. It is found that the normal matrix stress σ_x at the interface remains compressive for all values of the relative distance λ between the inclusions. This is not the case, however, for the normal stress σ_y (Fig. 8). It can be observed that the distributions of σ_y for perfect bonding and sliding are drastically different. When the effect of different aspect ratios is considered, a loss of the interfacial bonding corresponds to very high tensile values of σ_y . As the value of s decreases, the differences between perfect bonding and sliding become more pronounced.

5. Conclusions

The present study analyzes the problem of two interacting inhomogeneities subjected to a uniform eigenstrain loading. An analytical solution was obtained for a pair of elliptical inclusions with perfectly bonded or slipping interfaces.

It was concluded that the local stress field is considerably effected by the proximity of the two inserts. In addition, loss of the interfacial bond yields high stress concentrations, particularly along the interface.

The influence of the relative stiffness and the inhomogeneity aspect ratio were also investigated. It was observed that the approximation based

upon the superposition of two single inclusions leads to erroneous values of the interfacial matrix stresses.

Acknowledgements

The authors are pleased to acknowledge support from the Air Force Office of Scientific Research through Award AFOSR 90-0235.

References

- (1) Kouris, D. and Tsuchida, E., On the Elastic Interaction Between Two Fibers In a Continuous Fiber Composite Under Thermal Loading, *Mech. Mater.* Vol. 12, (1991), p. 131.
- (2) Mura, T., *Micromechanics of Defects in Solids*, Martinus Nijhoff Publishers, (1987).
- (3) Papkovitch, P. F., Solution générale des équations différentielles fondamentales d'élasticité, exprimée par trois fonctions harmoniques, *C. R. Acad. Sci.* Vol. 195, (1932), p. 513.
- (4) Neuber, H., Ein neuer Ansatz zur Lösung raumlicher Probleme der Elastizitätstheorie, *Z. Angew. Math. Mech.* Vol. 14, (1934), p. 203.
- (5) Eshelby, J. D., The Determination of the Elastic Field of an Ellipsoidal Inclusion, and Related Problems, *Proc. R. Soc. London, Ser. A*, **241**, (1957), p. 376.

Appendix A

The coefficients ω_n and Z_n can be obtained utilizing the complex-variable formulation. Let $z_j = x_j + iy_j$. The relations (1) can be written as

$$x_1 + y_1 = x_2 + iy_2 + \zeta. \quad (\text{A1})$$

Using (2) and (A1), are relations between O_1 and O_2 is given as

$$\cosh(\alpha_1 + i\beta_1) = \cosh(\alpha_2 + i\beta_2) + \frac{\zeta}{C}. \quad (\text{A2})$$

From the definitions of ω_n and Z_n , the values of ω_n and Z_n can be obtained

$$\omega_0 = Z_0 = \alpha_d + \sum_{m=1}^{\infty} \frac{(-1)^m}{m} d_{2m,0} \quad (\text{A3})$$

and

$$\left(\frac{\omega_n (-1)^n}{Z_n} \right) = -\frac{2}{n} e^{-n\alpha_d} + \sum_{m=1}^{\infty} \frac{(-1)^m}{m} d_{2m,n}$$

where $n = 1, 2, \dots$. The value of α_d is given by

$$\alpha_d = \cosh^{-1} \left(\frac{\zeta}{C} \right). \quad (\text{A4})$$

The coefficients $d_{m,n}$ can be obtained by starting with (Cooke 1956)

$$e^{-m\alpha_1} \cos m\beta_1 = m \int_0^{\infty} I_m(\lambda c) \lambda^{-1} e^{-\lambda x_1} \cos \lambda y_1 d\lambda \quad (\text{A5})$$

and

$$e^{-\lambda x_2} \cos \lambda y_2 = \sum_{n=0}^{\infty} \epsilon_n (-1)^n I_n(\lambda C) \cosh n\alpha_2 \cos n\beta_2 \quad (\text{A6})$$

where $x_2 > 0$, $m = 1, 2, \dots$, and

$$\epsilon_n = \begin{cases} 1, & n=0 \\ 2, & n=1, 2, \dots \end{cases} \quad (\text{A7})$$

From the relations (1), (A5) and (A6) can be transformed into

$$e^{-m\alpha_1} \cos m\beta_1 = m \int_0^{\infty} I_m(\lambda C) \lambda^{-1} e^{-\lambda \zeta} \sum_{n=0}^{\infty} \epsilon_n (-1)^n I_n(\lambda C) \cosh n\alpha_2 \cos n\beta_2 d\lambda \quad (\text{A8})$$

Using the definition of $d_{m,n}$, the coefficients $d_{m,n}$ are obtained by

$$d_{m,n} = \epsilon_n m \int_0^{\infty} I_m(\lambda C) I_n(\lambda C) e^{-\lambda \zeta} \lambda^{-1} d\lambda. \quad (\text{A9})$$

Appendix B

The constants U_{ij} , V_{ij} , S_{ij} , and T_{ij} are the following.

$$U_{A1} = n e^{-n\alpha_0}$$

$$U_{B1} = (n-1+\kappa) e^{-(n-2)\alpha_0} + (n-1-\kappa) e^{-n\alpha_0}$$

$$U_{B2} = (n+1+\kappa) e^{-n\alpha_0} + (n+1-\kappa) e^{-(n+2)\alpha_0}$$

$$U_{C1} = n \sinh n\alpha_0$$

$$U_{C2} = (n-1+\kappa) \sinh(n-2)\alpha_0 + (n-1-\kappa) \sinh n\alpha_0$$

$$U_{C3} = (n+1+\kappa) \sinh n\alpha_0 + (n+1-\kappa) \sinh (n+2)\alpha_0$$

$$\overline{U_{A1}} = n \sinh n\alpha_0$$

$$\overline{U_{B1}} = (n-1+\kappa) \sinh(n-2)\alpha_0 + (n-1-\kappa) \sinh n\alpha_0$$

$$\overline{U_{B2}} = (n+1+\kappa) \sinh n\alpha_0 + (n+1-\kappa) \sinh (n+2)\alpha_0$$

$$V_{A1} = n e^{-n\alpha_0}$$

$$V_{B1} = (n-1-\kappa) \{ e^{-(n-2)\alpha_0} + e^{-n\alpha_0} \}$$

$$V_{B2} = (n+1+\kappa) \{ e^{-n\alpha_0} + e^{-(n+2)\alpha_0} \}$$

$$V_{C1} = n \cosh n\alpha_0$$

$$V_{C2} = (n-1-\kappa) \{ \cosh(n-2)\alpha_0 + \cosh n\alpha_0 \}$$

$$V_{C3} = (n+1+\kappa) \{ \cosh n\alpha_0 + \cosh (n+2)\alpha_0 \}$$

$$\overline{V_{A1}} = n \cosh n\alpha_0$$

$$\overline{V_{B1}} = (n-1-\kappa) \{ \cosh (n-2)\alpha_0 + \cosh n\alpha_0 \}$$

$$\overline{V_{B2}} = (n+1+\kappa) \{ \cosh n\alpha_0 + \cosh (n+2)\alpha_0 \}$$

$$S_{A1} = (n-2)(n-3) e^{-(n-2)\alpha_0}$$

$$S_{A2} = n \{ (n+1) e^{-(n-2)\alpha_0} + (n-1) e^{-(n+2)\alpha_0} \}$$

$$S_{A3} = (n+2)(n+3) e^{-(n+2)\alpha_0}$$

$$S_{B1} = (n-3) \{ (n-2) e^{-(n-4)\alpha_0} + (n-3-\kappa) e^{-(n-2)\alpha_0} \}$$

$$S_{B2} = (n-1) \{ (n+2) e^{-(n-4)\alpha_0} - 2(\kappa-2) e^{-(n-2)\alpha_0} + 4 e^{-n\alpha_0} + (n-1-\kappa) e^{-(n+2)\alpha_0} \}$$

$$S_{B3} = (n+1) \{ (n+1+\kappa) e^{-(n-2)\alpha_0} - 4 e^{-n\alpha_0} + 2(\kappa-2) e^{-(n+2)\alpha_0} + (n-2) e^{-(n+4)\alpha_0} \}$$

$$S_{B4} = (n+3) \{ (n+3+\kappa) e^{-(n+2)\alpha_0} + (n+2) e^{-(n+4)\alpha_0} \}$$

$$S_{C1} = (n-2)(n-3) \cosh (n-2)\alpha_0$$

$$S_{C2} = n \{ (n+1) \cosh (n-2) \alpha_0 + (n-1) \cosh (n+2) \alpha_0 \}$$

$$S_{C3} = (n+2)(n+3) \cosh (n+2) \alpha_0$$

$$S_{C4} = (n-3) \{ (n-2) \cosh (n-4) \alpha_0 + (n-3-\kappa) \cosh (n-2) \alpha_0 \}$$

$$S_{C5} = (n-1) \{ (n+2) \cosh (n-4) \alpha_0 - 2(\kappa-2) \cosh (n-2) \alpha_0 \\ + 4 \cosh n\alpha_0 + (n-1-\kappa) \cosh (n+2) \alpha_0 \}$$

$$S_{C6} = (n+1) \{ (n+1+\kappa) \cosh (n-2) \alpha_0 - 4 \cosh n\alpha_0 \\ + 2(\kappa-2) \cosh (n+2)\alpha_0 + (n-2) \cosh (n+4) \alpha_0 \}$$

$$S_{C7} = (n+3) \{ (n+3+\kappa) \cosh (n+2) \alpha_0 + (n+2) \cosh (n+4) \alpha_0 \}$$

$$\overline{S_{A1}} = (n-2)(n-3) \cosh (n-2)\alpha_0$$

$$\overline{S_{A2}} = n \{ (n+1) \cosh (n-2)\alpha_0 + (n-1) \cosh (n+2)\alpha_0 \}$$

$$\overline{S_{A3}} = (n+2) (n+3) \cosh (n+2)\alpha_0$$

$$\overline{S_{B1}} = (n-3) \{ (n-2) \cosh (n-4)\alpha_0 + (n-3-\overline{\kappa}) \cosh (n-2)\alpha_0 \}$$

$$\overline{S_{B2}} = (n-1) \{ (n+2) \cosh (n-4) \alpha_0 - 2(\overline{\kappa}-2) \cosh (n-2) \alpha_0 + 4 \cosh n\alpha_0 + (n-1-\overline{\kappa}) \cosh (n+2) \alpha_0 \}$$

$$\overline{S_{B3}} = (n+1) \{ (n+1+\overline{\kappa}) \cosh (n-2)\alpha_0 - 4 \cosh n\alpha_0 - 2(\overline{\kappa}-2) \cosh (n+2)\alpha_0 + (n-2) \cosh (n+4) \alpha_0 \}$$

$$\overline{S_{B4}} = (n+3) \{ (n+3+\overline{\kappa}) \cosh (n+2)\alpha_0 + (n+2) \cosh n\alpha_0 \}$$

$$T_{A1} = (n-2)(n-3) e^{-(n-2)\alpha_0}$$

$$T_{A2} = n \{ (n+1) e^{-(n-2)\alpha_0} + (n-1) e^{-(n+2)\alpha_0} \}$$

$$T_{A3} = (n+2)(n+3) e^{-(n+2)\alpha_0}$$

$$T_{B1} = (n-3) \{ (n-4) e^{-(n-4)\alpha_0} + (n-3-\kappa) e^{-(n-2)\alpha_0} \}$$

$$T_{B2} = (n-1) \{ n e^{-(n-4)\alpha_0} - 2(\kappa-2) e^{-(n-2)\alpha_0} + (n-1-\kappa) e^{-(n+2)\alpha_0} \}$$

$$T_{B3} = (n+1) \{ (n+1+\kappa) e^{-(n-2)\alpha_0} + 2(\kappa-2) e^{-(n+2)\alpha_0} + n e^{-(n+4)\alpha_0} \}$$

$$T_{B4} = (n+3) \{ (n+3+\kappa) e^{-(n+2)\alpha_0} + (n+4) e^{-(n+4)\alpha_0} \}$$

$$T_{C1} = (n-2)(n-3) \sinh (n-2)\alpha_0$$

$$T_{C2} = n \{ (n+1) \sinh (n-2)\alpha_0 + (n-1) \sinh (n+2)\alpha_0 \}$$

$$T_{C3} = (n+2)(n+3) \sinh (n+2)\alpha_0$$

$$T_{C4} = (n-3) \{ (n-4) \sinh (n-4)\alpha_0 + (n-3-\kappa) \sinh (n-2)\alpha_0 \}$$

$$T_{C5} = (n-1) \{ n \sinh (n-4)\alpha_0 - 2(\kappa-2) \sinh (n-2)\alpha_0 + (n-1-\kappa) \sinh (n+2)\alpha_0 \}$$

$$T_{C6} = (n+1) \{ (n+1+\kappa) \sinh (n-2)\alpha_0 + 2(\kappa-2) \sinh (n+2)\alpha_0 + n \sinh (n+4)\alpha_0 \}$$

$$T_{C7} = (n+3) \{ (n+3+\kappa) \sinh (n+2)\alpha_0 + (n+4) \sinh (n+4)\alpha_0 \}$$

$$\overline{T_{A1}} = (n-2)(n-3) \sinh (n-2)\alpha_0$$

$$\overline{T_{A2}} = n \{ (n+1) \sinh (n-2)\alpha_0 + (n-1) \sinh (n+2)\alpha_0 \}$$

$$\overline{T_{A3}} = (n+2)(n+3) \sinh (n+2)\alpha_0$$

$$\overline{T_{B1}} = (n-3) \{ (n-4) \sinh (n-4)\alpha_0 + (n-3-\kappa) \sinh (n-2)\alpha_0 \}$$

$$\overline{T_{B2}} = (n-1) \{ n \sinh (n-4)\alpha_0 - 2(\kappa-2) \sinh (n-2)\alpha_0 + (n-1-\kappa) \sinh (n+2)\alpha_0 \}$$

$$\overline{T_{B3}} = (n+1) \{ (n+1+\kappa) \sinh (n-2)\alpha_0 + 2(\kappa-2) \sinh (n+2)\alpha_0 + n \sinh (n+4)\alpha_0 \}$$

$$\overline{T_{B4}} = (n+3) \{ (n+3 + \kappa) \sinh(n+2)\alpha_0 + (n+4) \sinh(n+4)\alpha_0 \}$$

Appendix C

Using the symmetry equations (20) at the interface of the inclusion Ω_1 , the corresponding equations of (17) - (19) become,

$$\begin{aligned} \sum_{n=1}^{\infty} A_n V_{A1} + \frac{1}{4} \sum_{n=2}^{\infty} B_{n-1} V_{B1} + \frac{C}{4} \sum_{n=0}^{\infty} B_{n+1} V_{B2} \\ + \sum_{n=2}^{\infty} \left\{ F_0 Z_n + \sum_{m=1}^{\infty} (A_m + \zeta B_m) d_{m,n} \right\} V_{C1} - \frac{C}{4} \sum_{n=2}^{\infty} \sum_{m=1}^{\infty} B_m d_{m,n-1} V_{C2} \end{aligned} \quad (C1)$$

$$\begin{aligned} - \frac{C}{4} \sum_{n=0}^{\infty} \sum_{m=1}^{\infty} B_m d_{m,n+1} V_{C3} - \frac{1}{\Gamma} \sum_{n=1}^{\infty} \overline{A_n} \overline{V_{A1}} - \frac{C}{4\Gamma} \sum_{n=2}^{\infty} \overline{B_{n-1}} \overline{V_{B1}} - \frac{C}{4\Gamma} \sum_{n=0}^{\infty} \overline{B_{n+1}} \overline{V_{B2}} \\ = \frac{C^2}{2} \delta_{n,2} \end{aligned}$$

$$\begin{aligned} - F_0 \frac{\sinh 2\alpha_0}{2} \delta_{n,0} - \frac{1}{4} \sum_{n=4}^{\infty} A_{n-2} S_{A1} + \frac{1}{4} \sum_{n=1}^{\infty} A_n S_{A2} - \frac{1}{4} \sum_{n=-1}^{\infty} A_{n+2} S_{A3} - \frac{C}{16} \sum_{n=4}^{\infty} B_{n-3} S_{B1} \\ + \frac{C}{16} \sum_{n=2}^{\infty} B_{n-1} S_{B2} + \frac{C}{16} \sum_{n=0}^{\infty} B_{n+1} S_{B3} - \frac{C}{16} \sum_{n=-2}^{\infty} B_{n+3} S_{B4} \\ - \frac{1}{4} \sum_{n=4}^{\infty} \left\{ F_0 Z_{n-2} + \sum_{m=1}^{\infty} (A_m + \zeta B_m) d_{m,n-2} \right\} S_{C1} + \frac{1}{4} \sum_{n=1}^{\infty} \left\{ F_0 Z_n + \sum_{m=1}^{\infty} (A_m + \zeta B_m) d_{m,n} \right\} S_{C2} \\ - \frac{1}{4} \sum_{n=-1}^{\infty} \left\{ F_0 Z_{n+2} + \sum_{m=1}^{\infty} (A_m + \zeta B_m) d_{m,n+2} \right\} S_{C3} + \frac{C}{16} \sum_{n=4}^{\infty} \sum_{m=1}^{\infty} B_m d_{m,n-3} S_{C4} \end{aligned}$$

$$\begin{aligned}
& -\frac{C}{16} \sum_{n=2}^{\infty} \sum_{m=1}^{\infty} B_m d_{m,n-1} S_{C5} - \frac{C}{16} \sum_{n=0}^{\infty} \sum_{m=1}^{\infty} B_m d_{m,n+1} S_{C6} + \frac{C}{16} \sum_{n=-2}^{\infty} \sum_{m=1}^{\infty} B_m d_{m,n+3} S_{C7} \\
& + \frac{1}{4} \sum_{n=4}^{\infty} \overline{A_{n-2}} \overline{S_{A1}} - \frac{1}{4} \sum_{n=1}^{\infty} \overline{A_n} \overline{S_{A2}} + \frac{1}{4} \sum_{n=-1}^{\infty} \overline{A_{n+2}} \overline{S_{A3}} + \frac{C}{16} \sum_{n=4}^{\infty} \overline{B_{n-3}} \overline{S_{B1}} \\
& - \frac{C}{16} \sum_{n=2}^{\infty} \overline{B_{n-1}} \overline{S_{B2}} - \frac{C}{16} \sum_{n=0}^{\infty} \overline{B_{n+1}} \overline{S_{B3}} + \frac{C}{16} \sum_{n=-2}^{\infty} \overline{B_{n+3}} \overline{S_{B4}} \\
& = 0
\end{aligned} \tag{C2}$$

$$\begin{aligned}
& -\frac{1}{2} F_0 \delta_{n,2} - \frac{1}{4} \sum_{n=4}^{\infty} A_{n-2} T_{A1} + \frac{1}{4} \sum_{n=1}^{\infty} A_n T_{A2} - \frac{1}{4} \sum_{n=-1}^{\infty} A_{n+2} T_{A3} - \frac{C}{16} \sum_{n=4}^{\infty} B_{n-3} T_{B1} \\
& + \frac{C}{16} \sum_{n=2}^{\infty} B_{n-1} T_{B2} + \frac{C}{16} \sum_{n=0}^{\infty} B_{n+1} T_{B3} - \frac{C}{16} \sum_{n=-2}^{\infty} B_{n+3} T_{B4} \\
& + \frac{1}{4} \sum_{n=4}^{\infty} \left\{ F_0 Z_{n-2} + \sum_{m=1}^{\infty} (A_m + \zeta B_m) d_{m,n-2} \right\} T_{C1} - \frac{1}{4} \sum_{n=1}^{\infty} \left\{ F_0 Z_n + \sum_{m=1}^{\infty} (A_m + \zeta B_m) d_{m,n} \right\} T_{C2} \\
& + \frac{1}{4} \sum_{n=-1}^{\infty} \left\{ F_0 Z_{n+2} + \sum_{m=1}^{\infty} (A_m + \zeta B_m) d_{m,n+2} \right\} T_{C3} - \frac{C}{16} \sum_{n=4}^{\infty} \sum_{m=1}^{\infty} B_m d_{m,n-3} T_{C4} \\
& + \frac{C}{16} \sum_{n=2}^{\infty} \sum_{m=1}^{\infty} B_m d_{m,n-1} T_{C5} - \frac{C}{16} \sum_{n=0}^{\infty} \sum_{m=1}^{\infty} B_m d_{m,n+1} T_{C6} - \frac{C}{16} \sum_{n=-2}^{\infty} \sum_{m=1}^{\infty} B_m d_{m,n+3} T_{C7} \\
& - \frac{1}{4} \sum_{n=4}^{\infty} \overline{A_{n-2}} \overline{T_{A1}} + \frac{1}{4} \sum_{n=1}^{\infty} \overline{A_n} \overline{T_{A2}} - \frac{1}{4} \sum_{n=-1}^{\infty} \overline{A_{n+2}} \overline{T_{A3}} - \frac{C}{16} \sum_{n=4}^{\infty} \overline{B_{n-3}} \overline{T_{B1}} \\
& + \frac{C}{16} \sum_{n=2}^{\infty} \overline{B_{n-1}} \overline{T_{B2}} + \frac{C}{16} \sum_{n=0}^{\infty} \overline{B_{n+1}} \overline{T_{B3}} - \frac{C}{16} \sum_{n=-2}^{\infty} \overline{B_{n+3}} \overline{T_{B4}} \\
& = 0.
\end{aligned} \tag{C3}$$

Figure Captions

Fig. 1(a) Geometry of the problem.

Fig. 1(b) Elliptical coordinate system.

Fig. 2 Normal stress along the interface for various Γ
(a) perfect bonding (b) sliding.

Fig. 3 Normal stress along the interface for various λ
(a) perfect bonding (b) sliding.

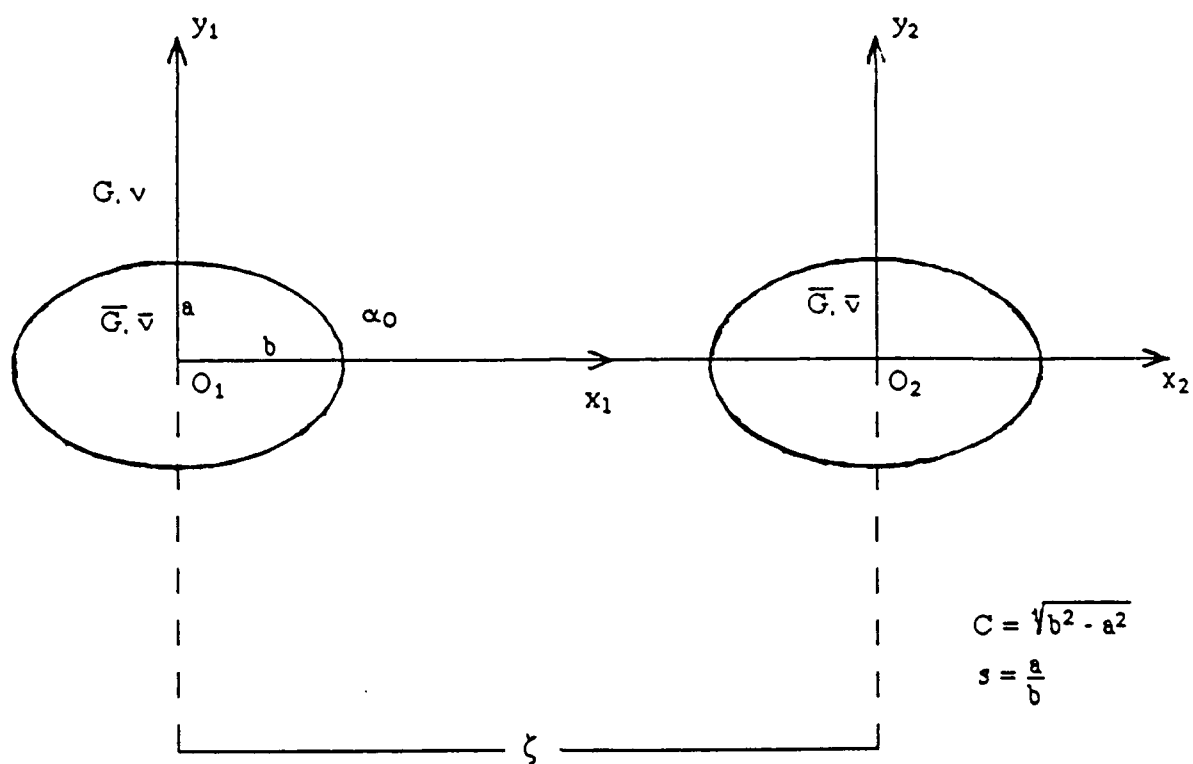
Fig. 4 Hoop stress distribution for various Γ
(a) perfect bonding (b) sliding.

Fig. 5 Variation of the interfacial hoop stress for different λ
(a) perfect bonding (b) sliding.

Fig. 6 Effect of the shear moduli ratio on σ_y
(a) perfect bonding (b) sliding.

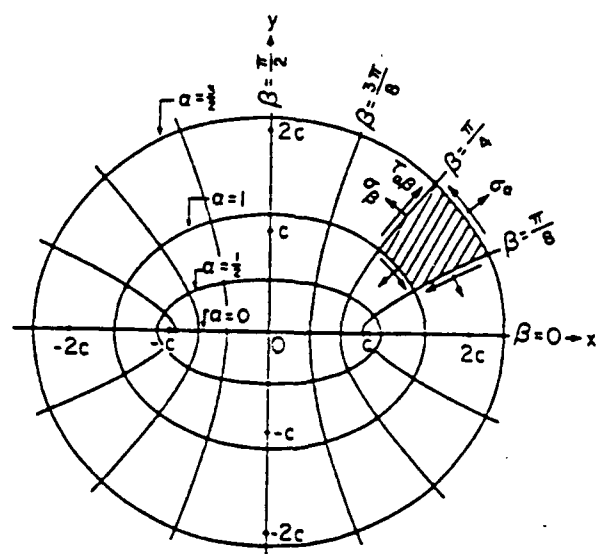
Fig. 7 Normal stress σ_y along the central axis for various s
(a) perfect bonding (b) sliding.

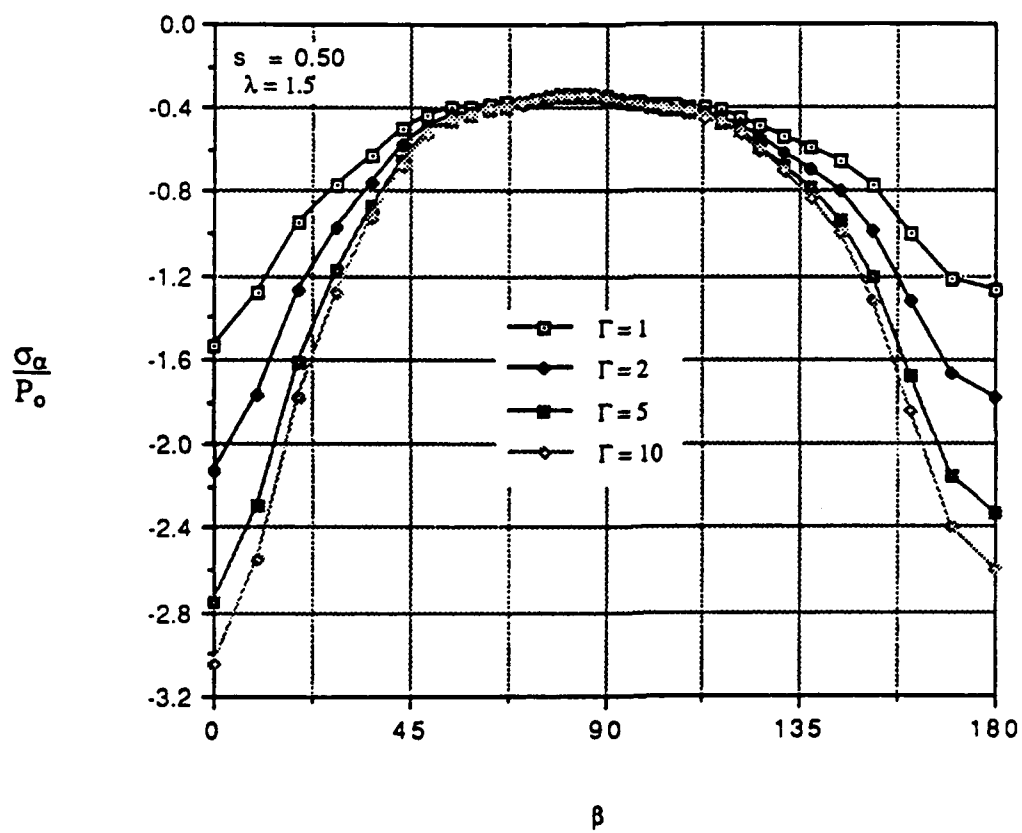
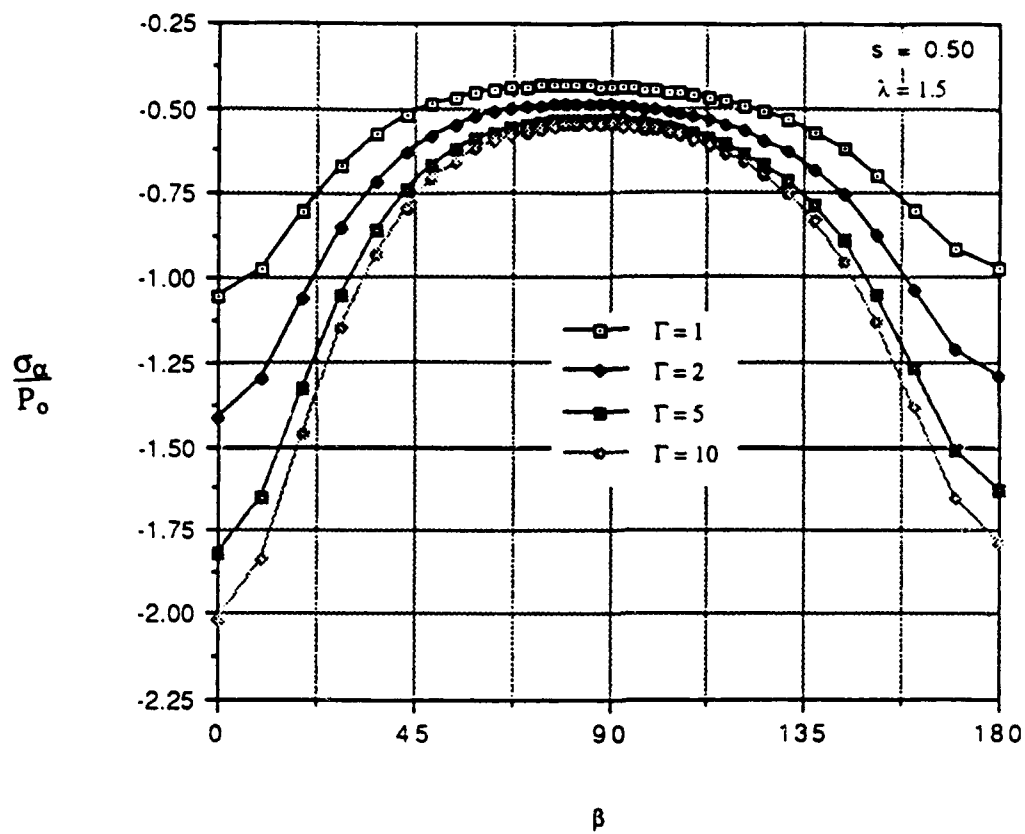
Fig. 8 Distribution of the normal stress σ_y at $x=2$
(a) perfect bonding (b) sliding.

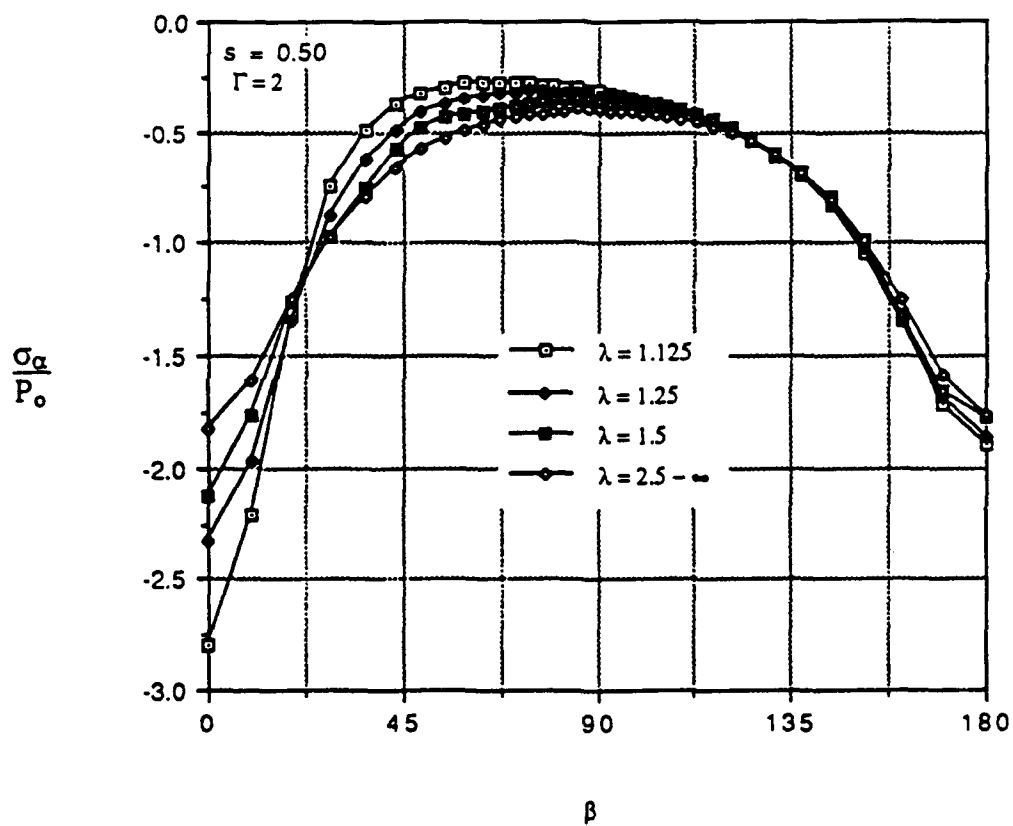
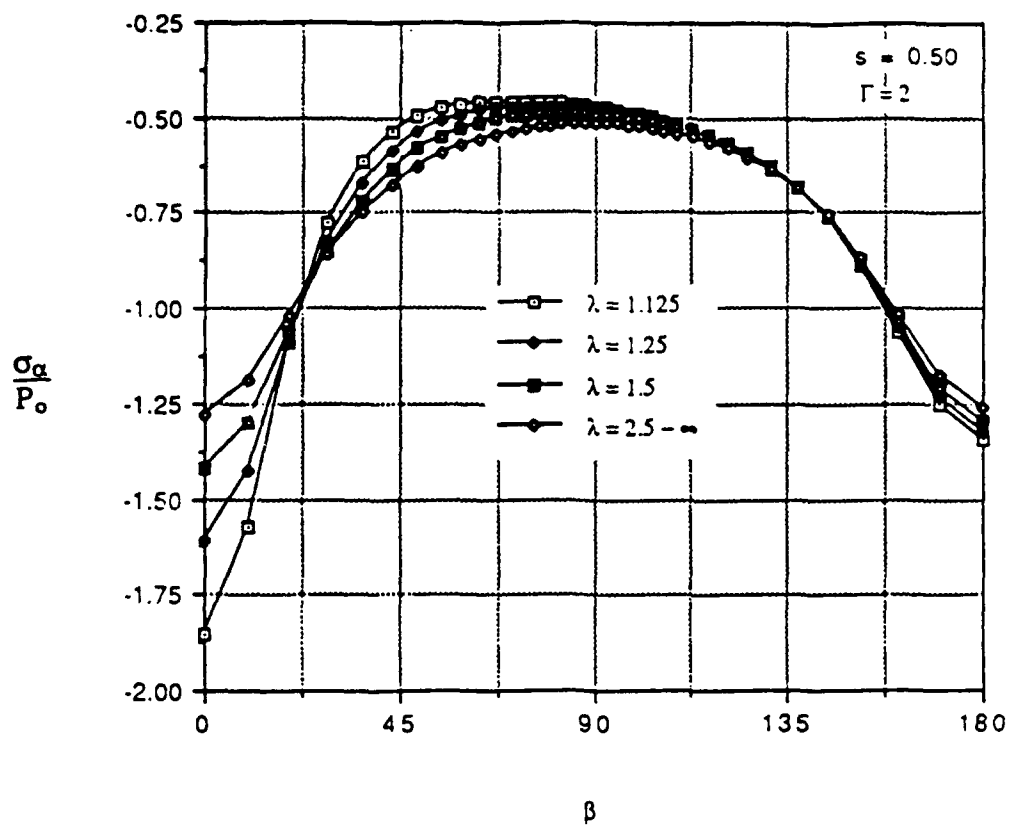


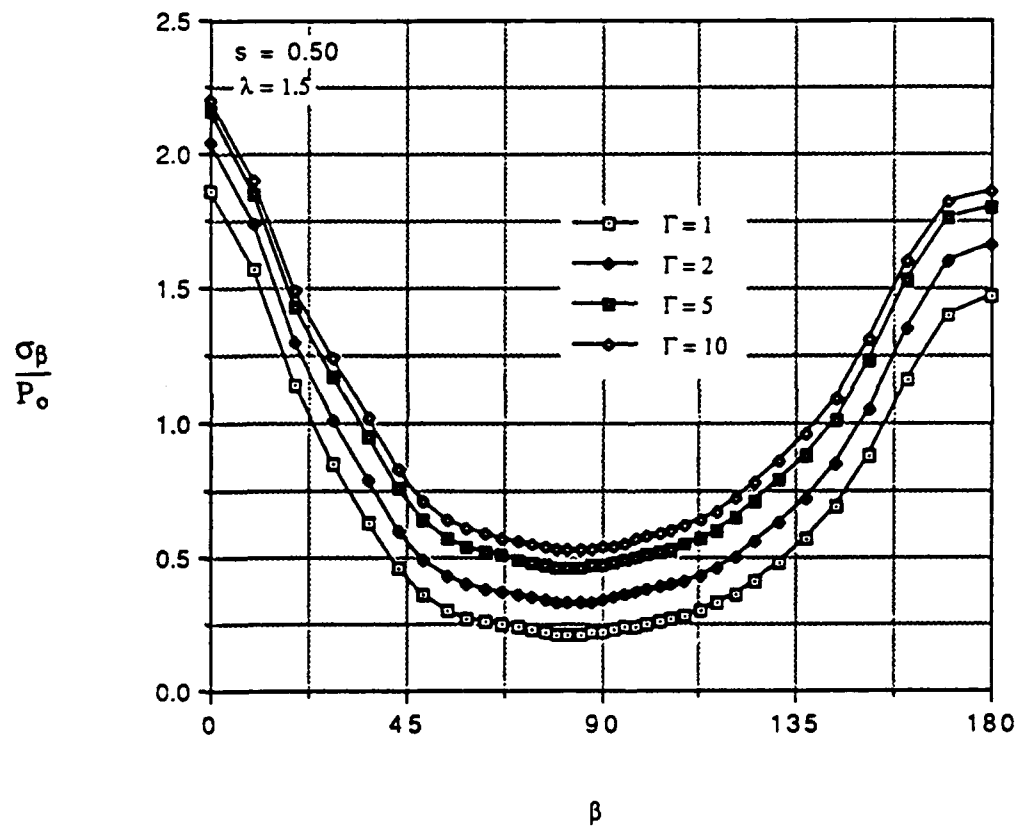
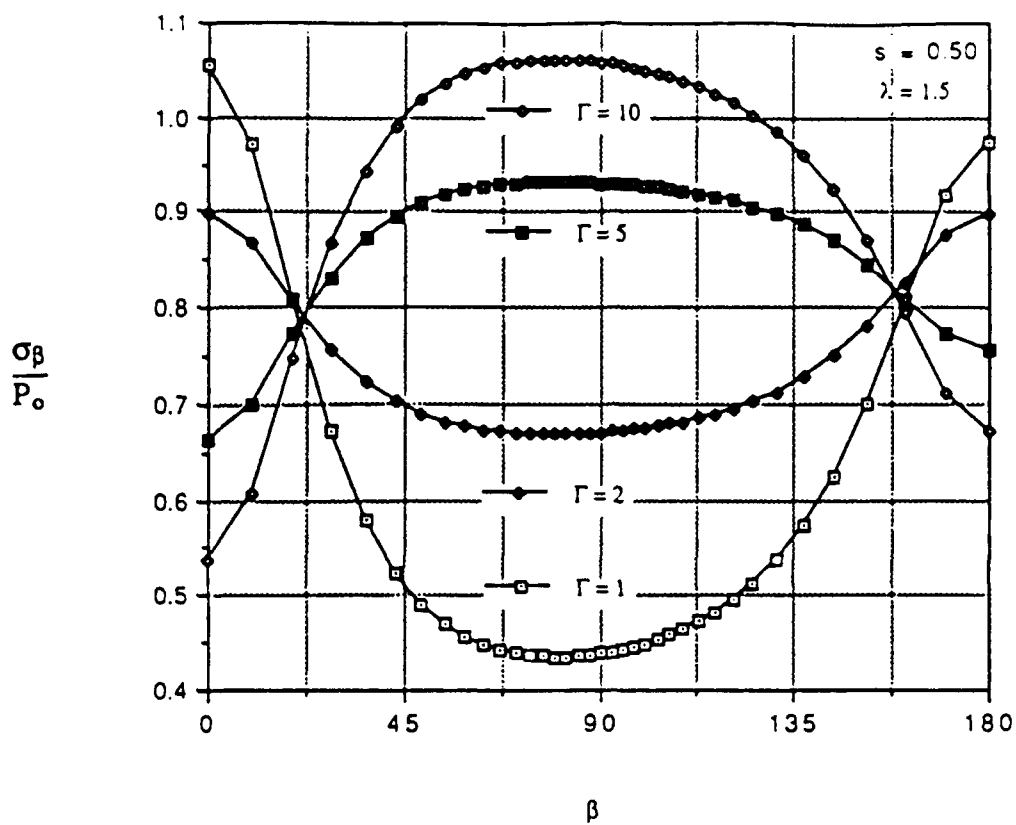
$$C = \sqrt{b^2 - a^2}$$

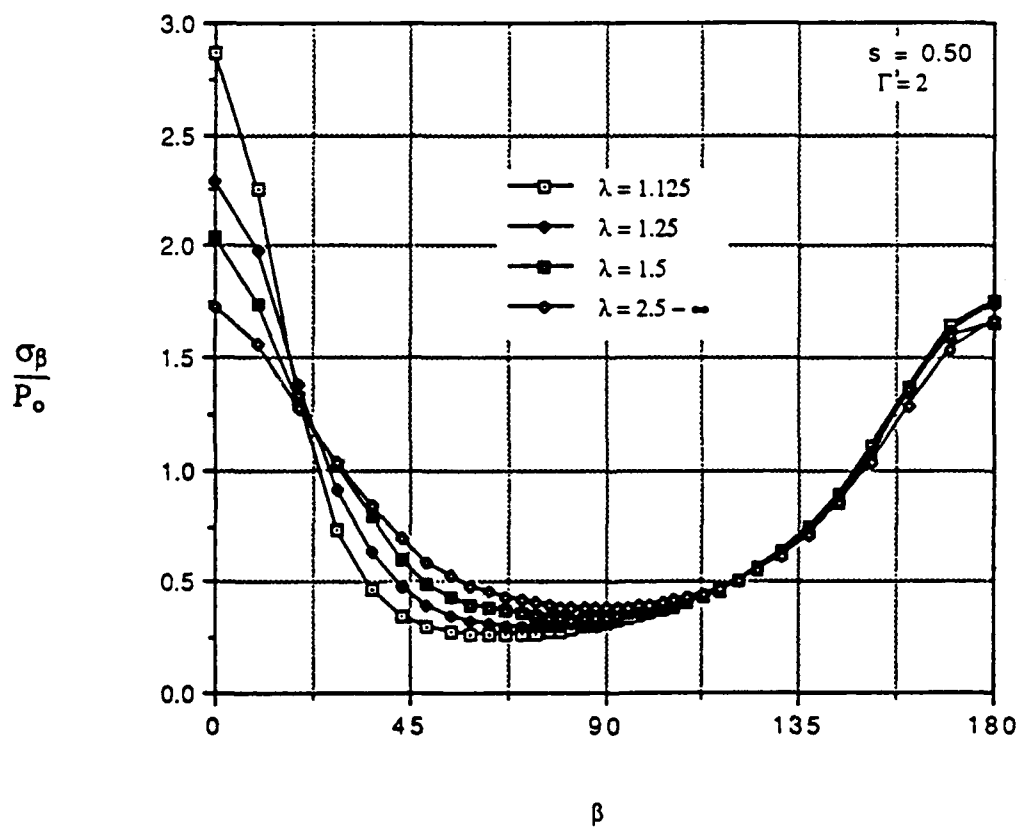
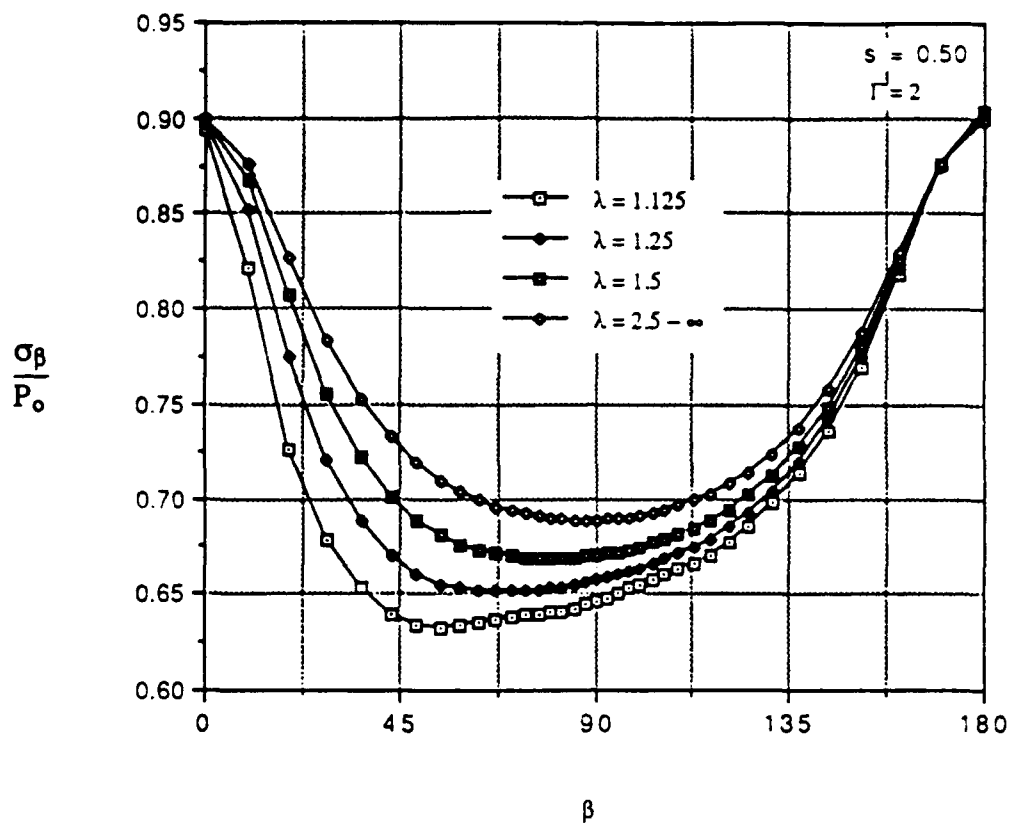
$$s = \frac{a}{b}$$

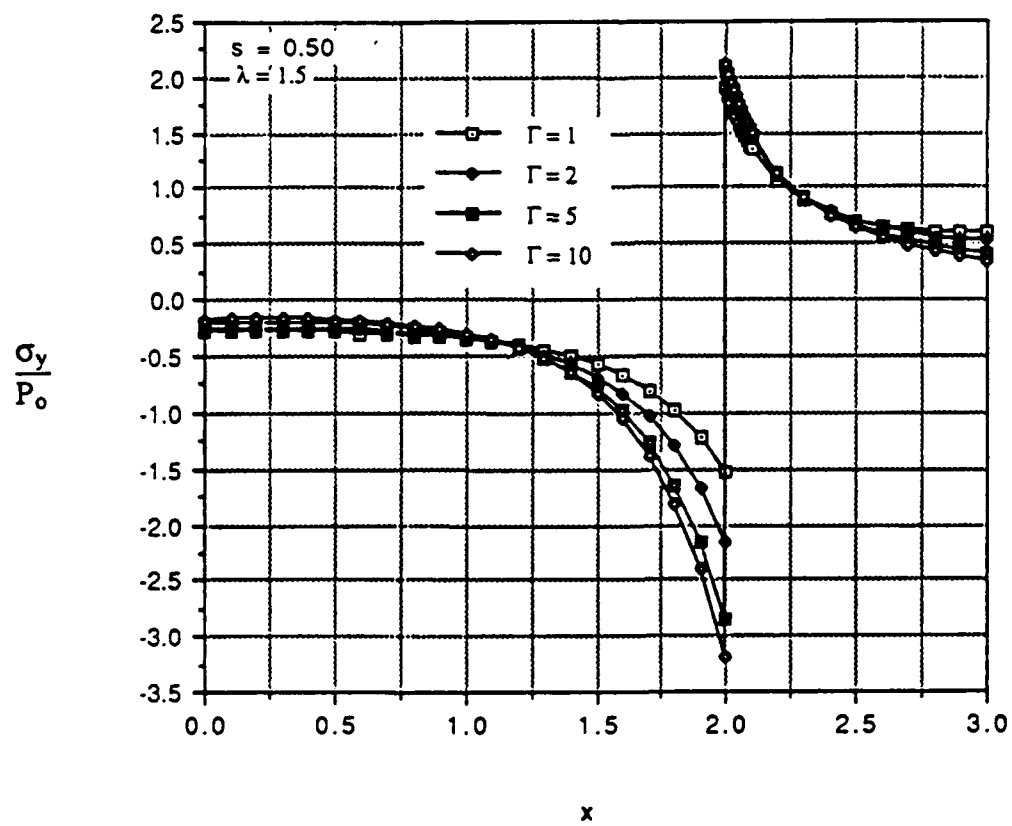
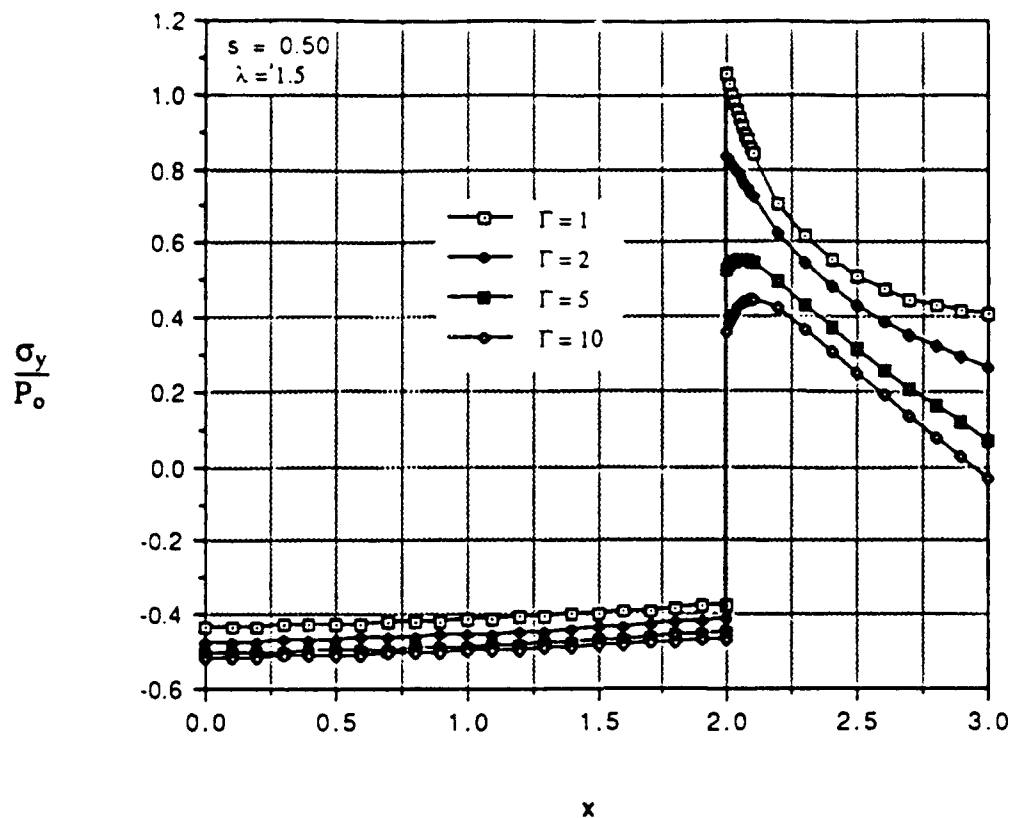


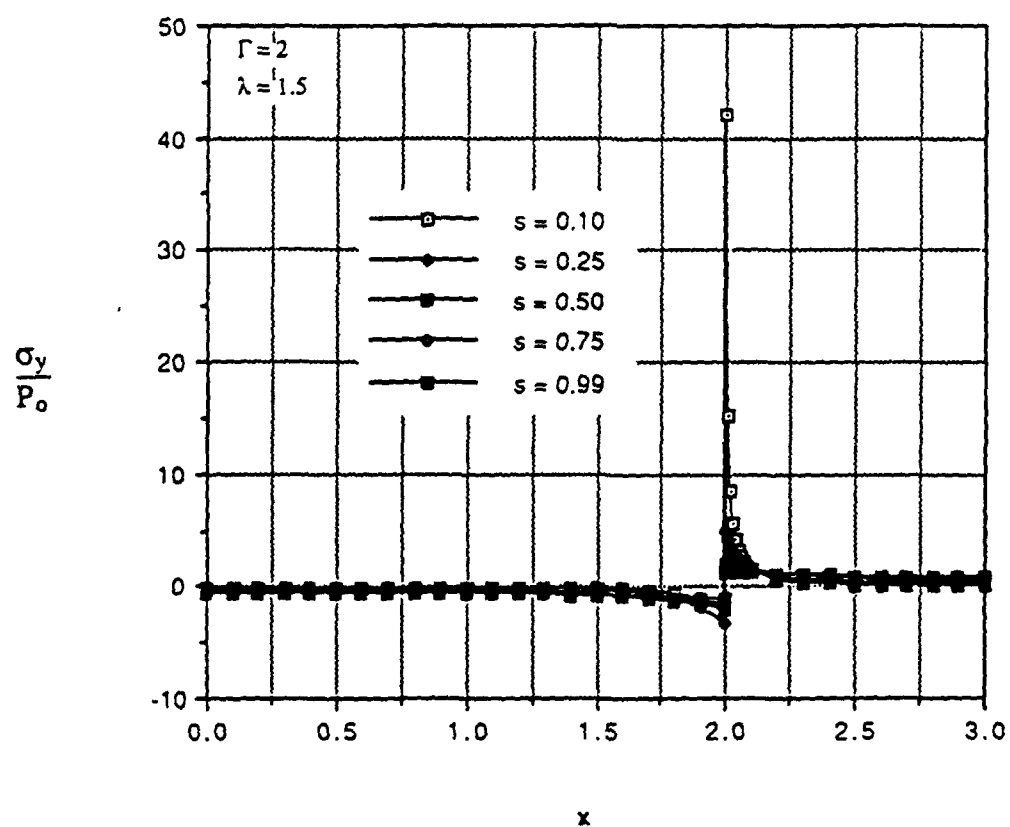
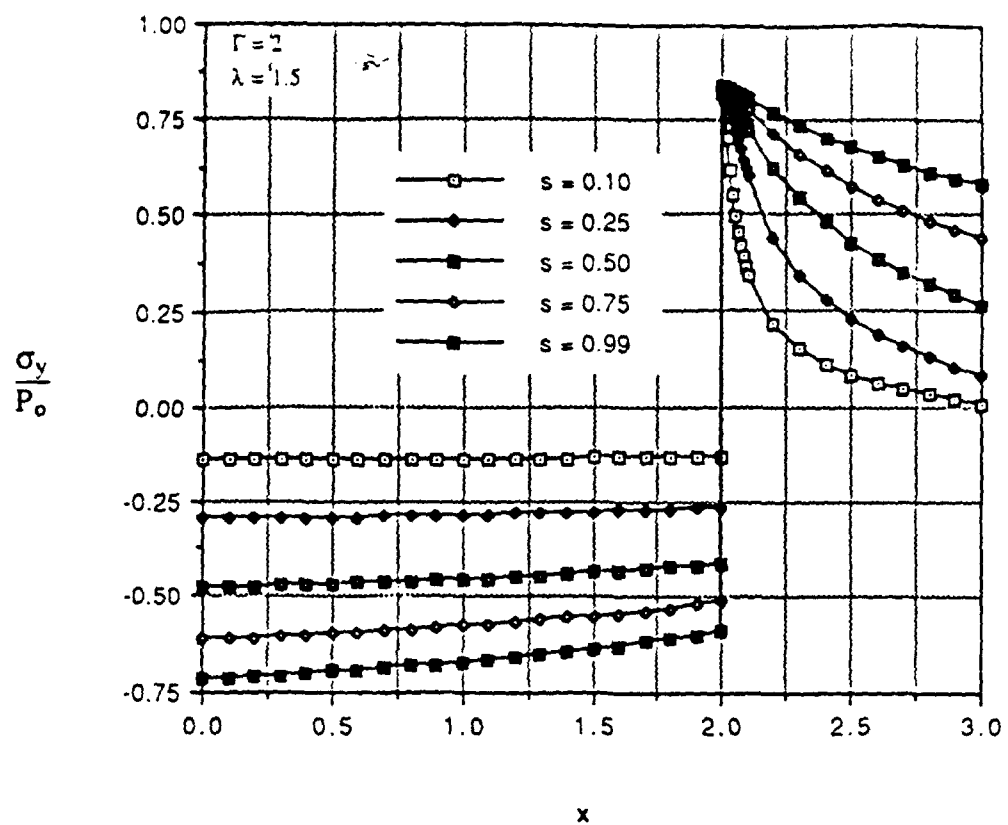


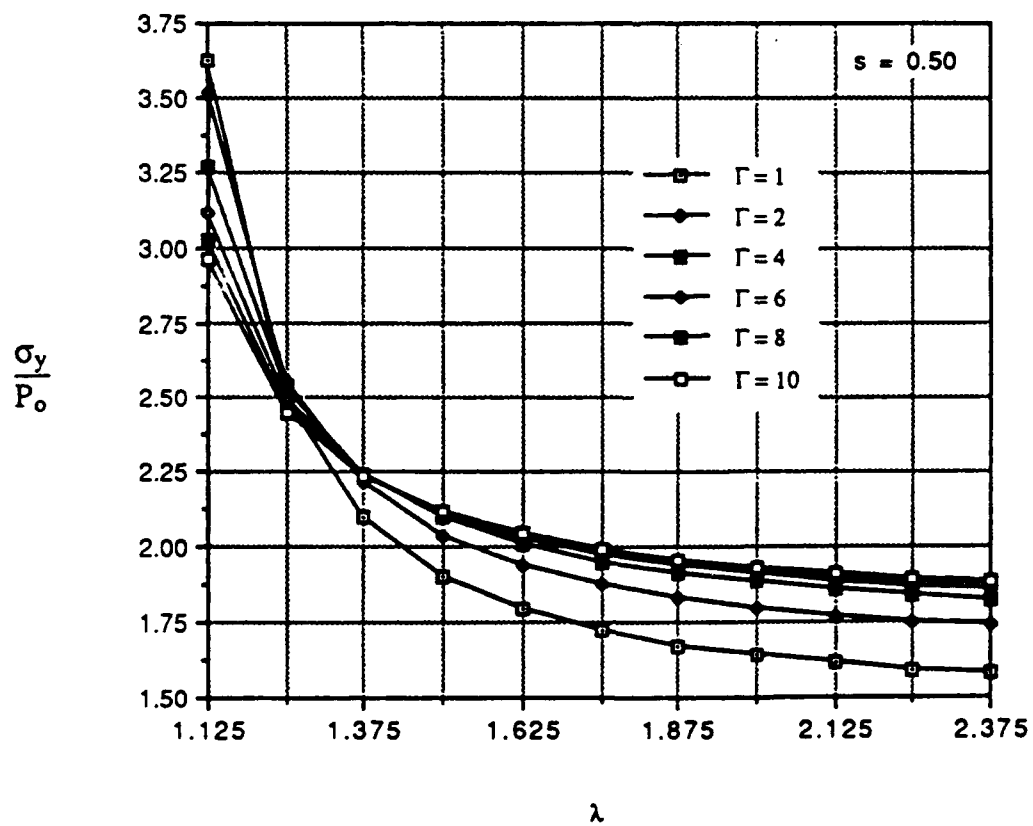
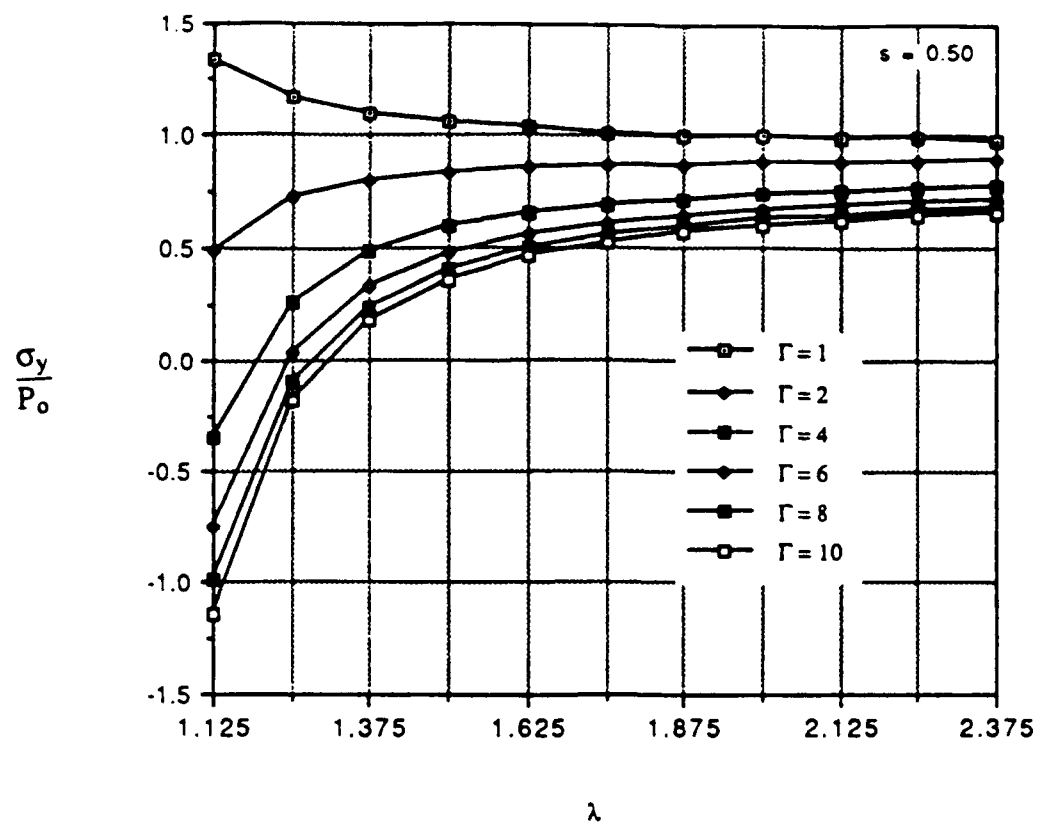












4.0 FIBERS NEAR THE SPECIMEN FREE SURFACE

4.1 An Analytical Solution for the Fiber Indentation Problem

published in the European Journal of Mechanics / Solids

An analytical solution for the fiber indentation problem

D. KOURIS * and E. TSUCHIDA **

ABSTRACT. — An analytical solution is presented for the problem of fiber indentation. The fiber is modelled by a semi-ellipsoidal inhomogeneity embedded at the free surface of an elastic half space. Using Boussinesq's displacement formulation, the local elastic field is determined for the cases of perfectly bonded and sliding interface.

1. Introduction

One of the important issues relating to the thermo-mechanical properties of composite materials is the mechanism of load transfer along the fiber/matrix interface. The inherent discontinuities of the material properties of the constituents, as well as the integrity of the interface, have a significant effect on the local stress field and consequently influence the performance of a composite.

Marshall [1984] proposed an experimental procedure for measuring the strength of the interface in ceramic composites. His approach utilizes a microindenter and approximates the interfacial stress by recording the fiber/matrix differential displacement and the applied load. The local stress field may be evaluated using shear-lag analysis [Cox, 1952].

In an exact analytical formulation, the diffusion of load from a fiber into a three-dimensional elastic medium presents significant difficulties. An approximate scheme, in terms of a Fredholm integral equation, was studied by Muki & Sternberg [1970] for the case of a finite rod, immersed in a semi-infinite solid. Other relevant studies of the fiber pull-out problem include Aveston & Kelly [1973], Phan-Thien & Goh [1981], Budiansky *et al.* [1986], Sigl & Evans [1989], and McCartney [1989].

In the present study, the fiber is modelled as an inhomogeneous semi-ellipsoidal inclusion, under the influence of a concentrated indentation force. Utilizing a three-dimensional displacement formulation, an analytical solution is obtained in a series form.

* Mechanical and Aerospace Engineering Department, Arizona State University, Tempe, AZ 85287-6106, USA.

** Mechanical Engineering Department, Saitama University, 255 Shimo-Okubo, Urawa 338, Japan.

In order to evaluate the influence of the interfacial integrity, the fiber is considered to be either perfectly bonded or free to slip along the interface. These two extreme conditions are then analyzed and compared.

2. The boundary value problem

The indented fiber is modelled as a semi-ellipsoidal inhomogeneity, loaded by a normal concentrated force. The inhomogeneity is embedded at the free surface of an elastic half space, as shown in Figure 1. Both the fiber and the surrounding matrix are considered linearly elastic and isotropic; their shear modulus and Poisson's ratio are denoted by $(\bar{G}, \bar{\nu})$ for the fiber and (G, ν) for the matrix.

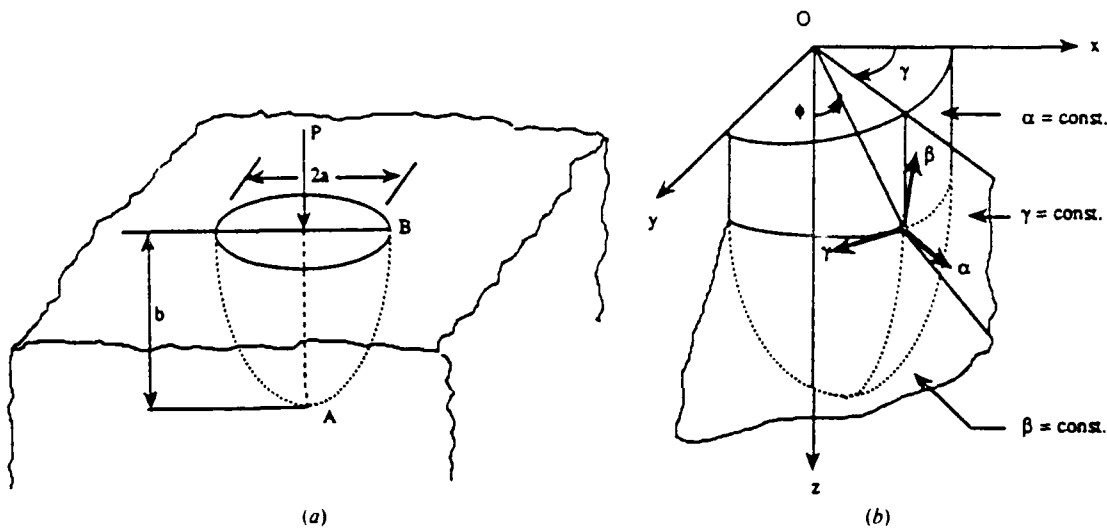


Fig. 1. - Problem geometry and coordinate system.

The purpose of the analysis is to determine the local stress and displacement fields around the fiber, under the influence of the indentation force.

Due to the geometry of the fiber, the prolate spheroidal coordinates (α, β, γ) are utilized; they are defined by the transformation:

$$(1) \quad \begin{cases} x = c \sin h \alpha \sin \beta \cos \gamma = c \bar{q} \bar{p} \cos \gamma \\ y = c \sin h \alpha \sin \beta \sin \gamma = c \bar{q} \bar{p} \sin \gamma \\ z = c \cosh \alpha \cos \beta = c q p \end{cases}$$

where $q \equiv \cosh \alpha$, $\bar{q} \equiv \sinh \alpha$, $p \equiv \cos \beta$, $\bar{p} \equiv \sin \beta$, and c indicates the half-distance between foci.

The boundary conditions at the free surface ($z=0$) require:

$$(2) \quad \begin{cases} (\sigma_{\beta})_{\beta=\pi/2} = (\tau_{\alpha\beta})_{\beta=\pi/2} = 0 \\ (\bar{\sigma}_{\beta})_{\beta=\pi/2} = (\bar{\tau}_{\alpha\beta})_{\beta=\pi/2} = 0, \end{cases}$$

where the overbar indicates quantities of the fiber.

In addition, due to the absence of a far field load, all stress components are expected to decay away from the fiber.

When the fiber/matrix system is perfectly bonded, the state of the interface ($\alpha = \alpha_0$) is characterized by continuity of tractions and displacements, *i. e.*,

$$(3) \quad \begin{cases} (u_\alpha)_{\alpha=\alpha_0} = (\bar{u}_\alpha)_{\alpha=\alpha_0}, & (u_\beta)_{\alpha=\alpha_0} = (\bar{u}_\beta)_{\alpha=\alpha_0}, \\ (\sigma_\alpha)_{\alpha=\alpha_0} = (\bar{\sigma}_\alpha)_{\alpha=\alpha_0}, & (\tau_{\alpha\beta})_{\alpha=\alpha_0} = (\bar{\tau}_{\alpha\beta})_{\alpha=\alpha_0}, \end{cases}$$

with all the other stress components being identically zero due to symmetry.

When the interface cannot sustain any shear tractions, the conditions of perfect slip require that:

$$(4) \quad \begin{cases} (u_\alpha)_{\alpha=\alpha_0} = (\bar{u}_\alpha)_{\alpha=\alpha_0}, & (\sigma_\alpha)_{\alpha=\alpha_0} = (\bar{\sigma}_\alpha)_{\alpha=\alpha_0}, \\ (\tau_{\alpha\beta})_{\alpha=\alpha_0} = 0, & \text{and} \quad (\bar{\tau}_{\alpha\beta})_{\alpha=\alpha_0} = 0. \end{cases}$$

The mathematical formulation that follows is based upon a three dimensional displacement formulation and the principal of superposition. Due to rotational symmetry the Boussinesq's [1885] displacement potentials, in prolate ellipsoidal coordinates, are given by:

$$(5) \quad \begin{cases} 2G u_\alpha = h\bar{q} \frac{\partial \Phi_0}{\partial q} + ch\bar{q}p \left\{ q \frac{\partial \Phi_3}{\partial q} - (3-4\nu) \Phi_3 \right\} \\ 2G u_\beta = -h\bar{p} \frac{\partial \Phi_0}{\partial p} - ch\bar{p}q \left\{ p \frac{\partial \Phi_3}{\partial p} - (3-4\nu) \Phi_3 \right\} \\ 2G u_\gamma = 0, \end{cases}$$

where

$$\nabla^2 = h^2 \left\{ \bar{q}^2 \frac{\partial^2}{\partial q^2} + 2\bar{q} \frac{\partial}{\partial q} + \bar{p}^2 \frac{\partial^2}{\partial p^2} - 2\bar{p} \frac{\partial}{\partial p} \right\}$$

$$c^2 h^2 = 1/(q^2 - p^2) \quad \text{and} \quad \nabla^2 \Phi_0 = \nabla^2 \Phi_3 = 0.$$

The expressions for the stresses can be deduced using Hooke's law and are given in the Appendix.

The choice of the displacement potentials Φ_0 and Φ_3 ought to be such that both the effect of the concentrated load and the disturbance due to the presence of the inhomogeneity are included in the formulation.

The elastic field due to the indentation force on the fiber can be expressed by:

$$(6) \quad \begin{cases} \Phi_0 = -(1-2\bar{\nu})/2 a^2 p_0 [Q_1(q) P_1(p) + \log \bar{q} (1+p)] \\ \Phi_3 = -(a^2/2c) p_0 Q_0(q) P_0(p) \end{cases}$$

where $P_n(p)$ and $Q_n(q)$ are Legendre functions of the first and second kind, respectively and $p_0 = P \pi a^2$. The stresses and displacements due to (6) are:

$$(7) \quad \begin{cases} 2 \bar{G} \bar{u}_x = (a^2/2) p_0 (h/\bar{q}) [(2-2\bar{\nu}) p \{ \bar{q}^2 Q_0(q) + q \} - (1-2\bar{\nu}) q] \\ 2 \bar{G} \bar{u}_\theta = -(a^2/2) p_0 h \bar{p} [(2-2\bar{\nu}) q Q_0(q) + (1-2\bar{\nu}) p/(1+p)] \\ \bar{\sigma}_x = -(a^2/2) p_0 h^2 [-(1-2\bar{\nu}) q^2/\bar{q}^2 + (2-2\bar{\nu}) p/\bar{q}^2 + p(4-2\bar{\nu}) + c^2 h^2 p^3] \\ \bar{\sigma}_\theta = -(a^2/2) p_0 h^2 p^2 [-(1-2\bar{\nu})/(1+p) - c^2 h^2 p] \\ \bar{\sigma}_r = -(a^2/2) p_0 h^2 [(1-2\bar{\nu}) q^2/\bar{q}^2 - p(1-2\bar{\nu})(2+p)/(1+p) - (2-2\bar{\nu}) p/\bar{q}^2] \\ \bar{\tau}_{\theta p} = -(a^2/2) p_0 h^2 (q/\bar{q}) p \bar{p} [-(1-2\bar{\nu})/(1+p) + c^2 h^2 p] \end{cases}$$

Due to equilibrium considerations, the matrix stresses ought to account for a force equivalent to the applied load p_0 . Therefore, a set of displacement potentials, similar to (6), is considered for the matrix region:

$$(8) \quad \begin{cases} \Phi_0 = -(1-2\nu)/2 a^2 p_0 F_0 [Q_1(q) P_1(p) + \log \bar{q} (1+p)] \\ \Phi_3 = -(a^2/2 c) p_0 F_0 Q_0(q) P_0(p) \end{cases}$$

with the unknown constant F_0 to be determined by the interfacial boundary conditions.

The presence of the inhomogeneity introduces a disturbance in the local elastic field. The choice of potential functions to represent this disturbance, is based upon the observation that the corresponding stresses must satisfy the free surface conditions and decay away from the fiber. This, together with the fact that the selected functions ought to be harmonic, lead to the choice of four potential sets.

For the matrix region ($\alpha > \alpha_0$), these potentials are:

$$(9) \quad \begin{cases} \Phi_0 = 2(1-\nu) c^2 p_0 \sum_{n=0}^{\infty} A_n \{ Q_{2n+2}(q) P_{2n+2}(p) - Q_{2n}(q) P_{2n}(p) \} \\ \Phi_3 = c p_0 \sum_{n=0}^{\infty} A_n (4n+3) Q_{2n+1}(q) P_{2n+1}(p) \end{cases}$$

and

$$(10) \quad \begin{cases} \Phi_0 = (1-2\nu) c^2 p_0 \sum_{n=0}^{\infty} B_n \{ Q_{2n+3}(q) P_{2n+3}(p) - Q_{2n+1}(q) P_{2n+1}(p) \} \\ \Phi_3 = c p_0 \sum_{n=0}^{\infty} B_n (4n+5) Q_{2n+2}(q) P_{2n+2}(p) \end{cases}$$

For the region occupied by the fiber ($\alpha < \alpha_0$), the selected potentials are:

$$(11) \quad \begin{cases} \Phi_0 = 2(1-\bar{\nu}) c^2 p_0 \sum_{n=0}^{\infty} \bar{A}_n \{ P_{2n+2}(q) P_{2n+2}(p) - P_{2n}(q) P_{2n}(p) \} \\ \Phi_3 = c p_0 \sum_{n=0}^{\infty} \bar{A}_n (4n+3) P_{2n+1}(q) P_{2n+1}(p) \end{cases}$$

and

$$(12) \quad \begin{cases} \Phi_0 = (1 - 2\bar{\nu}) c^2 p_0 \sum_{n=0}^{\infty} \bar{B}_n \{ P_{2n+1}(q) P_{2n+1}(p) - P_{2n-1}(q) P_{2n-1}(p) \} \\ \Phi_3 = c p_0 \sum_{n=0}^{\infty} \bar{B}_n (4n+1) P_{2n}(q) P_{2n}(p) \end{cases}$$

The expressions described in (7), together with the stresses and displacements that follow from (8)-(12), allow for the evaluation of the elastic field anywhere in the fiber and the matrix, in terms of the undetermined coefficients of the series. These unknowns F_0 , A_n , B_n , \bar{A}_n , and \bar{B}_n , can be determined by enforcing the boundary conditions along the fiber/matrix interface. Depending upon the interfacial requirements for perfect bonding or slip, conditions (3) or (4) are utilized.

3. Solution technique

Substituting the corresponding quantities in the conditions of perfect bond as described by (3), the continuity requirements yield a system of linear equations for the series coefficients. Specifically, the continuity of displacements yield:

$$(13) \quad [u_n/(p_0 c^2 h \bar{q})]_{\alpha=\alpha_0} = [\bar{u}_n/(p_0 c^2 h \bar{q})]_{\alpha=\alpha_0} \Rightarrow$$

$$-(a^2/2 c^2) F_0 \sum_{n=0}^1 u_n(q_0) P_n(p)$$

$$+ \sum_{n=0}^{\infty} \{ [U_{A1} A_{n-1} + U_{A2} A_n] - (1/\Gamma) [\bar{U}_{A1} \bar{A}_{n-1} + \bar{U}_{A2} \bar{A}_n] \} P_{2n}(p)$$

$$+ \sum_{n=0}^{\infty} \{ [U_{B1} B_{n-1} + U_{B2} B_n] - (1/\Gamma) [\bar{U}_{B1} \bar{B}_{n-1} + \bar{U}_{B2} \bar{B}_n] \} P_{2n+1}(p)$$

$$= -(1/\Gamma) (a^2/2 c^2) \sum_{n=0}^1 \bar{u}_n(q_0) P_n(p),$$

where $u_0(q) = (1 - 2\nu)(q_0/\bar{q}_0^2)$ and $u_1(q) = -(2 - 2\nu)[Q_0(q_0) + (q_0/\bar{q}_0^2)]$. The expressions for $\bar{u}_n(q_0)$ are obtained from $u_n(q_0)$ by replacing ν with $\bar{\nu}$. The coefficients U_{Ai} , U_{Bi} , \bar{U}_{Ai} and \bar{U}_{Bi} are known functions of n and the geometry, and can be found in Kouris *et al.* [1989].

The fiber/matrix shear moduli ratio is denoted by Γ ($\Gamma = \bar{G}/G$).

The continuity of the tangential displacement along the interface is given by:

$$\begin{aligned}
 (14) \quad [u_{\beta}/(p_0 c^2 h \bar{p})]_{\alpha=\alpha_0} &= [\bar{u}_{\beta}/(p_0 c^2 h \bar{p})]_{\alpha=\alpha_0} \Rightarrow \\
 &- (a^2/2 c^2) F_0 [(2-2\nu) q_0 Q_0(q_0) P'_1(p) + (1-2\nu) p/(1+p)] \\
 &+ \sum_{n=1}^{\infty} \{ [V_{A1} A_{n-1} + V_{A2} A_n] - (1/\Gamma) [\bar{V}_{A1} \bar{A}_{n-1} + \bar{V}_{A2} \bar{A}_n] \} P'_{2n}(p) \\
 &+ \sum_{n=0}^{\infty} \{ [V_{B1} B_{n-1} + V_{B2} B_n] - (1/\Gamma) [\bar{V}_{B1} \bar{B}_{n-1} + \bar{V}_{B2} \bar{B}_n] \} P'_{2n+1}(p) \\
 &= - (a^2/2 c^2) [(2-2\bar{\nu}) q_0 Q_0(q_0) P'_1(p) + (1-2\bar{\nu}) p/(1+p)].
 \end{aligned}$$

In addition to the displacements, tractions are continuous along the interface. These two conditions yield:

$$\begin{aligned}
 (15) \quad [\sigma_z/(p_0 c^4 h^4)]_{\alpha=\alpha_0} &= [\bar{\sigma}_z/(p_0 c^4 h^4)]_{\alpha=\alpha_0} \Rightarrow \\
 &- (a^2/2 c^2) F_0 \sum_{n=0}^3 s_n(q_0) P_n(p) \\
 &+ \sum_{n=0}^{\infty} \{ [S_{A1} A_{n-2} + S_{A2} A_{n-1} + S_{A3} A_n + S_{A4} A_{n+1}] \\
 &- [S_{A1} \bar{A}_{n-2} + S_{A2} \bar{A}_{n-1} + S_{A3} \bar{A}_n + S_{A4} \bar{A}_{n+1}] \} P_{2n}(p) \\
 &+ \sum_{n=0}^{\infty} \{ [S_{B1} B_{n-2} + S_{B2} B_{n-1} + S_{B3} B_n + S_{B4} B_{n+1}] \\
 &- [S_{B1} \bar{B}_{n-2} + S_{B2} \bar{B}_{n-1} + S_{B3} \bar{B}_n + S_{B4} \bar{B}_{n+1}] \} P_{2n+1}(p) \\
 &= - (a^2/2 c^2) \sum_{n=0}^3 \bar{s}_n(q_0) P_n(p),
 \end{aligned}$$

where

$$s_0 = (1-2\nu) q^2 (1-3q^2)/(3\bar{q}^2).$$

$$s_1 = 1/(5\bar{q}^2) [(5q^2-1)(4q^2-3) - 2\nu q^2(5q^2-3)],$$

$$s_3 = (1-2\nu) 2q^2/(3\bar{q}^2) \quad \text{and}$$

$$s_4 = -2/(5\bar{q}^2) [\bar{q}^2 + (2-2\nu) q^2],$$

for the normal stress, and:

$$\begin{aligned}
 (16) \quad [\tau_{\alpha\beta}/(\rho_0 c^4 h^4 \bar{q}p)]_{\alpha=\alpha_0} &= [\bar{\tau}_{\alpha\beta}/(\rho_0 c^4 h^4 \bar{q}p)]_{\alpha=\alpha_0} \Rightarrow \\
 &-(a^2/2c^2) F_0 \left[\sum_{n=1}^3 t_n(q_0) P'_n(p) + (1-2\nu) q/(1+p) \right] \\
 &+ \sum_{n=1}^{\infty} \{ [T_{A1} A_{n-2} + T_{A2} A_{n-1} + T_{A3} A_n + T_{A4} A_{n+1}] \\
 &- [T_{A1} \bar{A}_{n-2} + T_{A2} \bar{A}_{n-1} + T_{A3} \bar{A}_n + T_{A4} \bar{A}_{n+1}] \} P'_{2n}(p) \\
 &+ \sum_{n=0}^{\infty} \{ [T_{B1} B_{n-2} + T_{B2} B_{n-1} + T_{B3} B_n + T_{B4} B_{n+1}] \\
 &- [T_{B1} \bar{B}_{n-2} + T_{B2} \bar{B}_{n-1} + T_{B3} \bar{B}_n + T_{B4} \bar{B}_{n+1}] \} P'_{2n+1}(p) \\
 &= -(a^2/2c^2) \left[\sum_{n=1}^3 \bar{t}_n(q_0) P'_n(p) + (1-2\bar{\nu}) q/(1+p) \right],
 \end{aligned}$$

for the shear stress, where

$$\begin{aligned}
 t_1 &= [(2-2\nu)/(5\bar{q}^2) - (1-2\nu)] q, \\
 t_2 &= -(1-2\nu) q^2/(3\bar{q}^2), \\
 t_3 &= (2-2\nu) 2q/(15\bar{q}^2) \quad \text{and} \quad P'_n(p) = \frac{\partial P_n(p)}{\partial p}.
 \end{aligned}$$

In order to obtain a linear system of equations for the series coefficients, Legendre functions of odd order that appear in (13)-(16) are expressed in terms of Legendre functions of even order. Such a transformation is possible for $0 < p < 1$, and is given by:

$$(17) \quad P_{2k+1}(p) = \sum_{n=0}^{\infty} w_k^{(n)} P_{2n}(p), \quad P'_{2k+1}(p) = \sum_{n=1}^{\infty} w_k^{(n)} P'_{2n}(p)$$

where

$$w_k^{(n)} = (4n+1)(2k+1)/(2k+1-2n)/(2k+2+2n) P_{2n}(0) P_{2k}(0).$$

By employing this complete expansion and equating the coefficients of $P_{2n}(p)$ and $P'_{2n}(p)$, equations (13)-(16) yield the following system of linear equations:

$$\begin{aligned}
 (18) \quad &-(a^2/2c^2) F_0 [u_0(q_0) \delta_0^{(n)} + u_1(q_0) w_0^{(n)}] \\
 &+ [U_{A1} A_{n-1} + U_{A2} A_n] - (1/\Gamma) [\bar{U}_{A1} \bar{A}_{n-1} + \bar{U}_{A2} \bar{A}_n] \\
 &+ \sum_{k=0}^{\infty} \{ [U_{B1} B_{k-1} + U_{B2} B_k] - (1/\Gamma) [\bar{U}_{B1} \bar{B}_{k-1} + \bar{U}_{B2} \bar{B}_k] \} w_k^{(n)} \\
 &= -(1/\Gamma) (a^2/2c^2) [\bar{u}_0(q_0) \delta_0^{(n)} + \bar{u}_1(q_0) w_0^{(n)}], \quad (n=0, 1, 2, \dots),
 \end{aligned}$$

$$\begin{aligned}
(19) \quad & -(a^2/2c^2)F_0 \left[\{ (2-2\nu)q_0Q_0(q_0) + (1-2\nu) \} w_0^{(n)} \right. \\
& + (1-2\nu) \{ (4n+1)/(2n)/(2n+1) \} - \sum_{k=0}^{\infty} (4k+3)/(2k+1)/(2k+2) w_k^{(n)} \Big] \\
& + [V_{A1}A_{n-1} + V_{A2}A_n] - (1/\Gamma)[\bar{V}_{A1}\bar{A}_{n-1} + \bar{V}_{A2}\bar{A}_n] \\
& + \sum_{k=0}^{\infty} \{ [V_{B1}B_{k-1} + V_{B2}B_k] - (1/\Gamma)[\bar{V}_{B1}\bar{B}_{k-1} + \bar{V}_{B2}\bar{B}_k] \} w_k^{(n)} \\
& = -(a^2/2c^2)(1/\Gamma) \left[\{ (2-2\bar{\nu})q_0Q_0(q_0) + (1-2\bar{\nu}) \} w_0^{(n)} \right. \\
& + (1-2\bar{\nu}) \{ (4n+1)/(2n)/(2n+1) \} - \sum_{k=0}^{\infty} (4k+3)/(2k+1)/(2k+2) w_k^{(n)} \Big] \\
& \quad (n=1, 2, 3, \dots),
\end{aligned}$$

$$\begin{aligned}
(20) \quad & -(a^2/2c^2)F_0 [s_0(q_0)\delta_0^{(n)} + s_1(q_0)w_0^{(n)} + s_2(q_0)\delta_1^{(n)} + s_3(q_0)w_1^{(n)} \\
& + [S_{A1}A_{n-2} + S_{A2}A_{n-1} + S_{A3}A_n + S_{A4}A_{n+1}] \\
& - [S_{A1}\bar{A}_{n-2} + S_{A2}\bar{A}_{n-1} + S_{A3}\bar{A}_n + S_{A4}\bar{A}_{n+1}] \\
& + \sum_{k=0}^{\infty} \{ [S_{B1}B_{k-2} + S_{B2}B_{k-1} + S_{B3}B_k + S_{B4}B_{k+1}] \\
& - [S_{B1}\bar{B}_{k-2} + S_{B2}\bar{B}_{k-1} + S_{B3}\bar{B}_k + S_{B4}\bar{B}_{k+1}] \} w_k^{(n)} \\
& = -(a^2/2c^2) [\bar{s}_0(q_0)\delta_0^{(n)} + \bar{s}_1(q_0)w_0^{(n)} + \bar{s}_2(q_0)\delta_1^{(n)} + \bar{s}_3(q_0)w_1^{(n)}] \\
& \quad (n=0, 1, 2, \dots),
\end{aligned}$$

and

$$\begin{aligned}
(21) \quad & -(a^2/2c^2)F_0 \left[t_1(q_0)w_0^{(n)} + t_2(q_0)\delta_1^{(n)} + t_3(q_0)w_1^{(n)} \right. \\
& + (1-2\nu)q_0 \{ (4n+1)/(2n)/(2n+1) \} - \sum_{k=0}^{\infty} (4k+3)/(2k+1)/(2k+2) w_k^{(n)} \Big] \\
& + [T_{A1}A_{n-2} + T_{A2}A_{n-1} + T_{A3}A_n + T_{A4}A_{n+1}] \\
& - [T_{A1}\bar{A}_{n-2} + T_{A2}\bar{A}_{n-1} + T_{A3}\bar{A}_n + T_{A4}\bar{A}_{n+1}] \\
& + \sum_{k=0}^{\infty} \{ [T_{B1}B_{k-2} + T_{B2}B_{k-1} + T_{B3}B_k + T_{B4}B_{k+1}] \\
& - [T_{B1}\bar{B}_{k-2} + T_{B2}\bar{B}_{k-1} + T_{B3}\bar{B}_k + T_{B4}\bar{B}_{k+1}] \} w_k^{(n)} \\
& = -(a^2/2c^2) \left[\bar{t}_1(q_0)w_0^{(n)} + \bar{t}_2(q_0)\delta_1^{(n)} + \bar{t}_3(q_0)w_1^{(n)} \right. \\
& + (1-2\bar{\nu})q_0 \{ (4n+1)/(2n)/(2n+1) \} - \sum_{k=0}^{\infty} (4k+3)/(2k+1)/(2k+2) w_k^{(n)} \Big] \\
& \quad (n=1, 2, 3, \dots).
\end{aligned}$$

After determining the coefficients F_0 , A_n , B_n , \bar{A}_n and \bar{B}_n from the system (18)-(21), the elastic field can be evaluated at any point in the matrix or the fiber.

In the case of a sliding fiber, the problem is formulated similarly based on the boundary conditions (4).

4. Results and discussion

According to the approach that was described in the preceding sections, the unknown coefficients of the displacement potentials can be obtained by solving the linear system of equations (18)-(21). In order to ensure that the interfacial boundary conditions match up to three significant figures, no more than twenty series terms are required. Such a truncation is justified due to the evident numerical convergence of the solution.

The purpose of the parametric study performed, was to identify the influence of two basic parameters on the elastic field; namely the shear moduli ratio Γ ($\Gamma = \bar{G}/G$) and the inhomogeneity aspect ratio S ($S = a/b$). In order to determine the effects of the interfacial bond, the fiber was initially assumed to be perfectly bonded to the matrix; consequently, by relaxing the interfacial shear stress, the case of perfect sliding was considered, and the results were compared. The comparison was focused on the interfacial stresses and the distribution of the displacements along the free surface.

The distribution of the normal stress σ_n along the interface, for a fixed shear moduli ratio ($\Gamma = 5$), is illustrated in Figure 2. The stress concentration at point A increases for the case of sliding and is inversely proportional to the inhomogeneity aspect ratio. The variation of the material properties has a significant effect on σ_n , when the inhomogeneity is perfectly bonded to the matrix (Fig. 3). This is not the case, however, when sliding occurs.

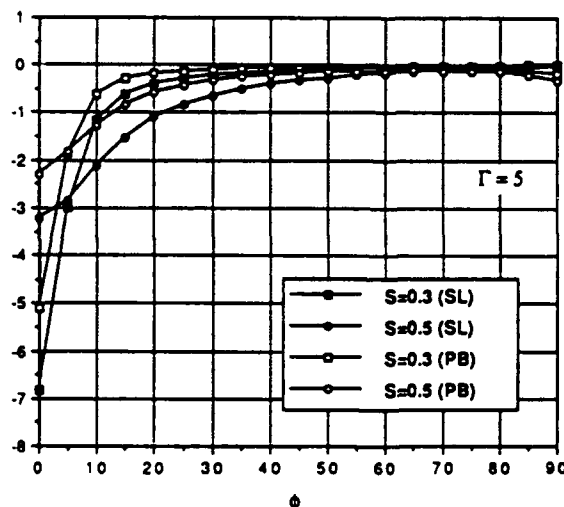


Fig. 2. — Normal stress along the interface as a function of S (PB and SL).

The fiber hoop stress σ_γ along the interface is illustrated in Figure 4. Here, the geometry of the insert appears to affect the stress concentration much more than the condition of the interface. The significant tensile values of σ_γ suggest the possibility of crack initiation in the vicinity of point A.

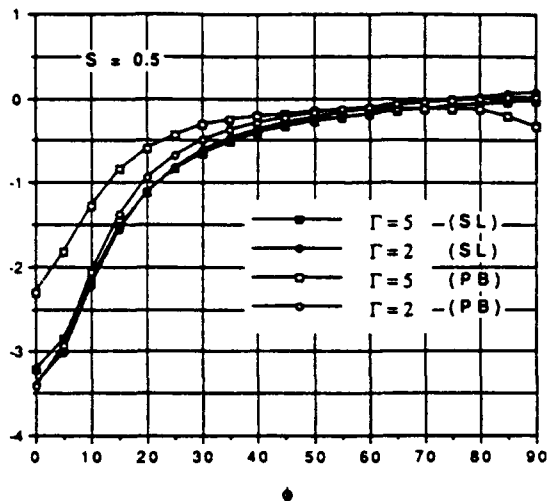


Fig. 3. — Normal stress along the interface as a function of Γ (PB and SL).

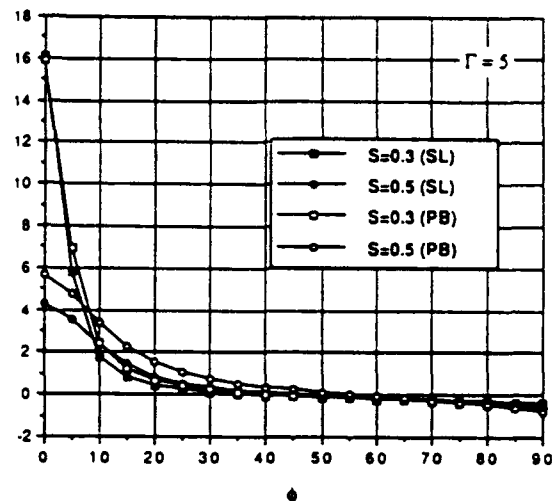


Fig. 4. — Fiber hoop stress along the interface as a function of S .

Another important aspect of the problem involves the distribution of displacements along the free surface of the composite. If we denote by R the normalized distance from

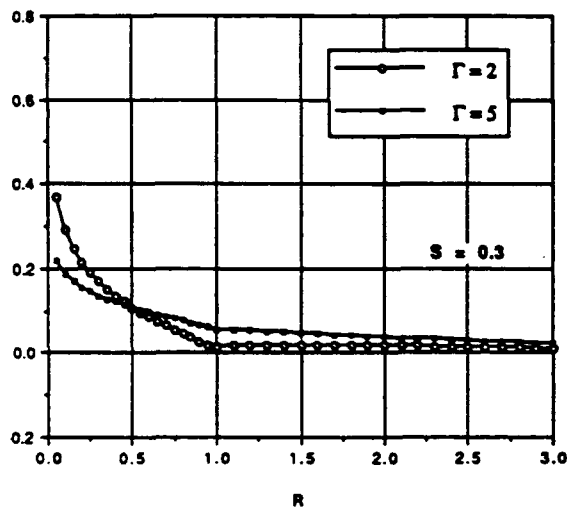


Fig. 5. — Normal displacement along the free surface for $\Gamma = 2, 5$ (PB).

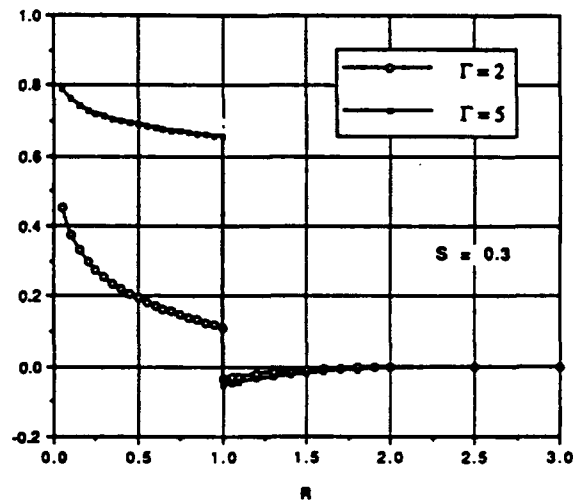


Fig. 6. — Normal displacement along the free surface for $\Gamma = 2, 5$ (SL).

the point of application of the load ($R = r/a$), the regions $0 < R < 1$ and $R > 1$ correspond to the free surface of the fiber and the matrix, respectively.

The condition of the interface has a significant effect on the normal displacement u_z , as shown in Figures 5-6. When the inhomogeneity is relatively "soft" ($\Gamma = 2$), the normal displacement of the fiber does not exhibit significant differences between perfect bonding (PB) and sliding (SL). This is not true, however, for a "stiffer" fiber ($\Gamma = 5$). In the case of SL, u_z in the matrix decays rapidly and is almost independent of Γ .

For a given material combination, the dependence of u_z on the geometry of the inhomogeneity is illustrated in Figure 7.

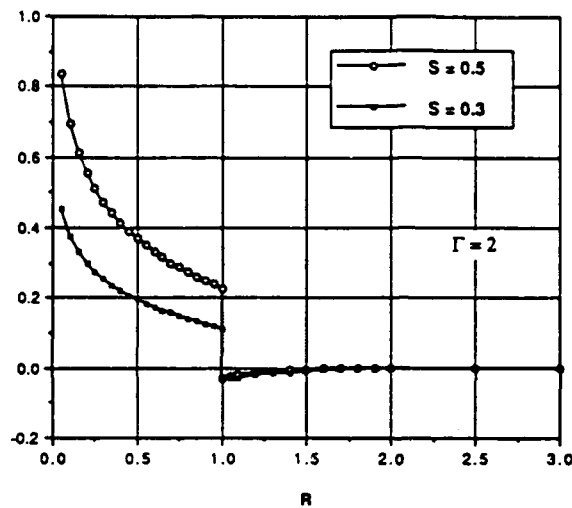


Fig. 7. — Normal displacement along the free surface for $S = 0.3, 0.5$ (SL).

Finally, it should be noted that the normal displacement along the free surface of the fiber, does not appear to be uniform; such a simplifying assumption that sometimes has been made in the literature, may be misleading.

5. Conclusions

In an effort to evaluate the local elastic field in the vicinity of an indented fiber, an analytical solution was presented based upon the three-dimensional displacement formulation. The results suggest that the stress concentration along the interface depends on the fiber aspect ratio and the given material combination. The influence of the interfacial integrity was studied by considering the extreme conditions of perfect bonding and sliding. It was found that the loss of bonding introduces high displacement discontinuities along the interface. In addition, the distribution of the normal displacement along the free surface of the fiber is not uniform.

APPENDIX

The non-zero stress components that correspond to the displacement field describing by (5) are:

$$(A1) \quad \sigma_x = h^2 \left\{ \bar{q}^2 \frac{\partial^2 \Phi_0}{\partial q^2} + c^2 h^2 \bar{p}^2 \left(q \frac{\partial \Phi_0}{\partial q} - p \frac{\partial \Phi_0}{\partial p} \right) \right\} \\ + ch^2 \left[q \bar{q}^2 p \frac{\partial^2 \Phi_3}{\partial q^2} + \{ c^2 h^2 q^2 \bar{p}^2 - 2(1-\nu) \bar{q}^2 \} p \frac{\partial \Phi_3}{\partial q} - (c^2 h^2 p^2 + 2\nu) q \bar{p}^2 \frac{\partial \Phi_3}{\partial p} \right].$$

$$(A2) \quad \sigma_p = h^2 \left\{ \bar{p}^2 \frac{\partial^2 \Phi_0}{\partial p^2} + c^2 h^2 \bar{q}^2 \left(q \frac{\partial \Phi_0}{\partial q} - p \frac{\partial \Phi_0}{\partial p} \right) \right\} \\ + ch^2 \left[q \bar{p}^2 p \frac{\partial^2 \Phi_3}{\partial p^2} - \{ c^2 h^2 p^2 \bar{q} + 2(1-\nu) \bar{p}^2 \} q \frac{\partial \Phi_3}{\partial q} + (c^2 h^2 p^2 - 2\nu) p \bar{q}^2 \frac{\partial \Phi_3}{\partial p} \right].$$

$$(A3) \quad \sigma_y = h^2 \left(q \frac{\partial \Phi_0}{\partial q} - p \frac{\partial \Phi_0}{\partial p} \right) + ch^2 \{ (q^2 - 2\nu \bar{q}^2) \} p \frac{\partial \Phi_3}{\partial p} - (p^2 + 2\nu \bar{p}^2) q \frac{\partial \Phi_3}{\partial q}.$$

$$(A4) \quad \tau_{xp} = h^2 \bar{q} \bar{p} \left\{ - \frac{\partial^2 \Phi_0}{\partial q \partial p} + c^2 h^2 \left(q \frac{\partial \Phi_0}{\partial p} - p \frac{\partial \Phi_0}{\partial q} \right) \right\} \\ - ch^2 \bar{q} \bar{p} \left[qp \frac{\partial^2 \Phi_3}{\partial q \partial p} + \{ c^2 h^2 p^2 - (1-2\nu) \} q \frac{\partial \Phi_3}{\partial q} - \{ c^2 h^2 q^2 + (1-2\nu) \} p \frac{\partial \Phi_3}{\partial p} \right].$$

Acknowledgment

This work has been supported by the Air Force Office of Scientific Research, through the University Research Initiative Award 90-0235.

REFERENCES

- AVESTON J., COOPER G. A., KELLY A., 1971, Single and multiple fracture, *The Properties of Fibre Composites*, Conference Proceedings, National Physical Laboratory, Guildford, U.K., IPC Science and Technology Press Ltd, 15-26.
- BOUSSINESQ J., 1985, Application des potentiels, Gauthier-Villars, Paris.
- BUDIANSKY B., HUTCHINSON J. W., EVANS A. G., 1989, Matrix fracture in fiber-reinforced ceramics, *J. Mech. Phys. Solids*, 34, 167-189.
- COX H. L., 1952, The elasticity and strength of paper and other fibrous materials, *British J. Appl. Phys.*, 3, 72-79.
- KOURIS D., TSUCHIDA E., MURA T., 1989, Hemispheroidal inhomogeneity at the free surface of an elastic half space, *J. Appl. Mech.*, 56, 70-76.
- MARSHALL D. B., 1984, An indentation method for measuring matrix-fiber frictional stresses in ceramic composites, *J. Am. Cer. Soc.*, 67, [12], C-259-260.
- MCCARTNEY L. N., 1989, New theoretical model of stress transfer between fibre and matrix in a uniaxially fibre-reinforced composite, *Proc. R. Soc. London*, A 425, 215-244.
- MUKI R., STERNBERG E., 1970, Elastostatic load-transfer to a half-space from a partially embedded axially loaded rod, *Int. J. Solids Struct.*, 6, 69-90.
- SIGL L. S., EVANS A. G., 1989, Effects of residual stress and frictional sliding on cracking and pull-out in brittle matrix composites, *Mech. Mat.*, 8, [1], 1-12.

(Manuscript received June 7, 1991;
accepted July 11, 1991.)

4.2 Elastic Analysis of the Half-Plane Inhomogeneity Problem

published in Acta Mechanica

Elastic analysis of the half plane inhomogeneity problem

D. A. Kouris and J. P. Nuxoll, Tempe, Arizona

(Received September 23, 1991; revised January 14, 1992)

Summary. The paper presents an analytical solution for the elastic field in the vicinity of a semi-circular inhomogeneity, embedded at the free surface of an elastic half-plane. This bi-material system is loaded by uniform remote tension or a constant eigenstrain sustained by the inhomogeneity.

1 Introduction

The thermomechanical response of multi-phase materials has been the subject of considerable interest due to their importance in structural applications. Issues relating to the local elastic fields and the integrity of the interfaces between the constituents are essential in determining the overall properties as well as the fracture behavior of composites.

In order to optimize the design of such complicated materials, one needs to understand the mechanics of the microstructure. Such knowledge can be utilized in an effort to qualify possible modes of failure. In addition, the micromechanical analysis of the matrix/inhomogeneity system may serve as the basis for estimating the bulk properties.

The focus of the present study is the elastic behavior of a plane bi-material system which consists of a semi-circular inhomogeneity, located at the free surface of an elastic half-plane (Fig. 1). The analysis was motivated by experiments involving continuous fiber composites (Kouris [1]). In this context, Kouris and Tsuchida [2] investigated the local interaction between fibers, under thermal loading. In addition, a similar analysis was presented by Kouris [3] for the case of mechanical loading and imperfectly bonded fibers.

However, some of the specimens tested in transverse tension contained fibers that were located near or at the free surface. These fibers can be modeled by semi-circular inhomogeneities, under conditions of plane strain. A related elasticity problem which involved the stress distribution in a notched plate under tension was solved by Maunsell [4]. This solution was generalized by Atsumi [5] for the case of a plate containing an infinite row of semi-circular notches, under similar loading conditions.

The inhomogeneity problem is formulated in terms of displacement potentials. The loading consists of uniaxial remote tension or a uniform eigenstrain sustained by the inhomogeneity. Solutions are obtained for a perfectly bonded as well as a sliding interface and the results are compared.

2 Displacement formulation

A semi-circular inhomogeneity of radius a is embedded at the free surface of a semi-infinite plane, as shown in Fig. 1. The surrounding matrix as well as the inhomogeneity are assumed to be linearly elastic and isotropic.

In the absence of body forces, the equilibrium equations in terms of displacements are

$$u_{i,jj} + \frac{2}{\kappa - 1} u_{j,ji} = 0 \quad (i, j = x, y) \quad (1)$$

where $\kappa = 3 - 4\nu$ for plane strain and $\kappa = (3 - \nu)/(1 + \nu)$ for plane stress.

According to Boussinesq [6] and for rotational symmetry, Eqs. (1) are satisfied identically by

$$2Gu_x = \frac{\partial \Phi_0}{\partial x} + y \frac{\partial \Phi_2}{\partial x} \quad (2)$$

$$2Gu_y = \frac{\partial \Phi_0}{\partial y} + y \frac{\partial \Phi_2}{\partial y} - \kappa \phi_2$$

Φ_0 and Φ_2 are arbitrary harmonic functions. For a particular problem, these functions are selected based on the geometry, the applied load and the appropriate boundary conditions.

In the present investigation, two types of loading have been considered. At first, a solution is sought for the case of mechanical loading, represented by remote uniform tension p_0 along the y -axis. Consequently, the specified tractions at infinity yield

$$(\sigma_y)_{r \rightarrow \infty} = p_0 \quad \text{and} \quad (\sigma_x)_{r \rightarrow \infty} = (\tau_{xy})_{r \rightarrow \infty} = 0. \quad (3)$$

The displacement potentials that correspond to the load p_0 are given by

$$\Phi_0 = -\frac{1}{8} p_0 (3 - \kappa) (x^2 - y^2) \quad \text{and} \quad \Phi_2 = -\frac{1}{2} y,$$

which, in polar coordinates, yield

$$\Phi_0 = -\frac{1}{8} p_0 (3 - \kappa) r^2 \cos 2\theta \quad (4)$$

$$\Phi_2 = -\frac{1}{2} r \sin 2\theta.$$

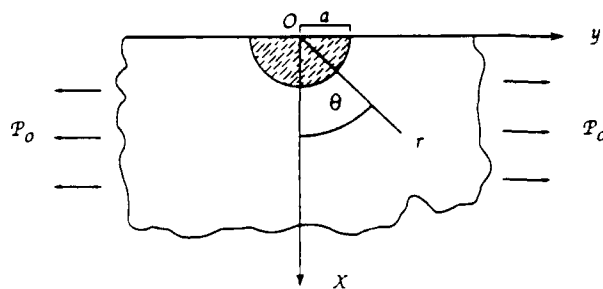


Fig. 1. Geometry of the problem

In addition, a non-elastic displacement is being introduced in the form of a uniform eigenstrain ε_y^* , sustained by the inclusion, i.e.

$$\bar{u}_y^* = \varepsilon_y^* y$$

which leads to

$$2G\bar{u}_r^* = \frac{1}{2} (2G\varepsilon_y^*) r(1 - \cos 2\theta) \quad (5)$$

$$2G\bar{u}_\theta^* = \frac{1}{2} (2G\varepsilon_y^*) r \sin 2\theta,$$

where G is the shear modulus of the matrix and the overbar is used to denote quantities that correspond to the inhomogeneity.

Consequently, the boundary conditions at infinity in the case of the eigenstrain loading are

$$(\sigma_x)_{r \rightarrow \infty} = (\sigma_y)_{r \rightarrow \infty} = (\tau_{xy})_{r \rightarrow \infty} = 0. \quad (6)$$

The requirement for zero tractions along the free surface yields

$$\begin{aligned} (\sigma_x)_{x=0} &= (\tau_{xy})_{x=0} = 0 \\ (\bar{\sigma}_x)_{x=0} &= (\bar{\tau}_{xy})_{x=0} = 0. \end{aligned} \quad (7)$$

In order to complete the formulation of the boundary value problem, one needs to account for the disturbance due to the presence of the inhomogeneity. This disturbance is represented by four sets of displacement potentials, given by

$$\Phi_0 = -p_0 \sum_{n=0}^{\infty} A_n \frac{4n+1+\kappa}{4n} r^{-2n} \cos 2n\theta \quad (8)$$

$$\Phi_2 = p_0 \sum_{n=0}^{\infty} A_n r^{-(2n+1)} \sin (2n+1)\theta,$$

$$\Phi_0 = -p_0 \sum_{n=0}^{\infty} B_n \frac{4n+5+\kappa}{2(2n+1)} r^{-(2n+1)} \cos (2n+1)\theta \quad (9)$$

$$\Phi_2 = p_0 \sum_{n=0}^{\infty} B_n r^{-(2n+2)} \sin (2n+2)\theta$$

for the matrix ($r > x$), and

$$\Phi_0 = p_0 \sum_{n=0}^{\infty} \bar{A}_n \frac{4n+3-\bar{\kappa}}{2(2n+2)} r^{2n+1} \cos (2n+2)\theta \quad (10)$$

$$\Phi_2 = p_0 \sum_{n=0}^{\infty} \bar{A}_n r^{2n+1} \sin (2n+1)\theta,$$

$$\Phi_0 = p_0 \sum_{n=0}^{\infty} \bar{B}_n \frac{4n-1-\bar{\kappa}}{2(2n+1)} r^{2n+1} \cos (2n+1)\theta \quad (11)$$

$$\Phi_2 = p_0 \sum_{n=0}^{\infty} \bar{B}_n r^{2n} \sin 2n\theta$$

for the inhomogeneity ($r < x$). The variable p_0 represents the remote tension or the quantity $2G\epsilon_0^*$ (eigenstrain case).

The elastic solution anywhere in the matrix or the inhomogeneity can be obtained by superimposing the displacement potentials given by Eqs. (4), (8), (9), (10) and (11). What remain to be found are the values of the unknown coefficients A_n , B_n , \bar{A}_n and \bar{B}_n . This can be accomplished by utilizing the boundary conditions along the matrix inhomogeneity interface.

3 Interface boundary conditions

When the semi-circular inhomogeneity is perfectly bonded to the surrounding matrix, the boundary conditions require continuity of tractions and displacements, i.e.

$$(\sigma_r)_{r=x} = (\bar{\sigma}_r)_{r=x}, \quad (\tau_{r\theta})_{r=x} = (\bar{\tau}_{r\theta})_{r=x} \quad (12)$$

and

$$(u_r)_{r=x} = (\bar{u}_r)_{r=x}, \quad (u_\theta)_{r=x} = (\bar{u}_\theta)_{r=x}. \quad (13)$$

In the case of the eigenstrain loading, Eqs. (13) have to be modified in order to account for the inelastic displacement. Consequently, Eqs. (13) become

$$\begin{aligned} (u_r)_{r=x} &= (\bar{u}_r)_{r=x} + (\bar{u}_r^*)_{r=x}, \\ (u_\theta)_{r=x} &= (\bar{u}_\theta)_{r=x} + (\bar{u}_\theta^*)_{r=x}. \end{aligned} \quad (14)$$

Based on the stresses and displacements that are derived from the chosen displacement potentials, Eqs. (12) yield

$$\begin{aligned} & \sum_{n=0}^{\infty} A_n \frac{2n+1}{x^{2n+2}} \{n \cos 2n\theta + (n+2) \cos (2n+2)\theta\} \\ & + \sum_{n=0}^{\infty} B_n \frac{n+1}{x^{2n+3}} \{(2n+3) \cos (2n+1)\theta + (2n+5) \cos (2n+3)\theta\} \\ & + \sum_{n=0}^{\infty} \bar{A}_n (2n+1) x^{2n} \{(n-1) \cos 2n\theta + (n+1) \cos (2n+2)\theta\} \\ & + \sum_{n=0}^{\infty} \bar{B}_n n x^{2n-1} \{(2n-1) \cos (2n+1)\theta + (2n-3) \cos (2n-1)\theta\} \\ & = \frac{1}{2} (1 - \cos 2\theta) \end{aligned} \quad (15)$$

and

$$\begin{aligned}
 & \sum_{n=0}^{\infty} A_n \frac{2n+1}{x^{2n+2}} \{n \sin 2n\theta + (n+1) \sin (2n+2)\theta\} \\
 & + \sum_{n=0}^{\infty} B_n \frac{n+1}{x^{2n+3}} (2n+3) \{\sin (2n+1)\theta + \sin (2n+3)\theta\} \\
 & + \sum_{n=0}^{\infty} \bar{A}_n (2n+1) x^{2n} \{n \sin 2n\theta + (n+1) \sin (2n+2)\theta\} \\
 & - \sum_{n=0}^{\infty} \bar{B}_n n (2n-1) x^{2n-1} \{\sin (2n+1)\theta + \sin (2n-1)\theta\} \\
 & = \frac{1}{2} \sin 2\theta.
 \end{aligned} \tag{16}$$

The conditions of continuity of the displacements along the interface expressed by Eqs. (13) or (14) become

$$\begin{aligned}
 & - \sum_{n=0}^{\infty} A_n \frac{1}{2x^{2n+1}} \{2n \cos 2n\theta + (2n+1+\kappa) \cos (2n+2)\theta\} \\
 & - \sum_{n=0}^{\infty} B_n \frac{1}{2x^{2n+2}} \{(2n+3) \cos (2n+1)\theta + (2n+2+\kappa) \cos (2n+3)\theta\} \\
 & + \frac{1}{2\Gamma} \sum_{n=0}^{\infty} \bar{A}_n x^{2n+1} \{(2n+1-\bar{\kappa}) \cos 2n\theta + (2n+2) \cos (2n+2)\theta\} \\
 & + \frac{1}{2\Gamma} \sum_{n=0}^{\infty} \bar{B}_n x^{2n} \{(2n-1) \cos (2n+1)\theta + (2n-\bar{\kappa}) \cos (2n-1)\theta\} \\
 & = \frac{1}{4} (\kappa-1) x - \frac{1}{2} x \cos 2\theta + \left\langle -\frac{1}{2} \varepsilon_y^* x (1 - \cos 2\theta) \right\rangle
 \end{aligned} \tag{17}$$

and

$$\begin{aligned}
 & - \sum_{n=0}^{\infty} A_n \frac{1}{2x^{2n+1}} \{2n \sin 2n\theta + (2n+1-\kappa) \sin (2n+2)\theta\} \\
 & - \sum_{n=0}^{\infty} B_n \frac{1}{2x^{2n+2}} \{(2n+3) \sin (2n+1)\theta + (2n+2-\kappa) \sin (2n+3)\theta\} \\
 & - \frac{1}{2\Gamma} \sum_{n=0}^{\infty} \bar{A}_n x^{2n+1} \{(2n+1+\bar{\kappa}) \sin 2n\theta + (2n+2) \sin (2n+2)\theta\} \\
 & - \frac{1}{2\Gamma} \sum_{n=0}^{\infty} \bar{B}_n x^{2n} \{(2n-1) \sin (2n+1)\theta + (2n+\bar{\kappa}) \sin (2n-1)\theta\} \\
 & = \frac{1}{2} x \sin 2\theta + \left\langle -\frac{1}{2} x \varepsilon_y^* \sin 2\theta \right\rangle.
 \end{aligned} \tag{18}$$

Here Γ denotes the inhomogeneity/matrix shear moduli ratio ($\Gamma = \bar{G}/G$) and the quantities included in the brackets $\langle \rangle$ correspond to the eigenstrain loading.

The boundary conditions (15)–(18) form a system of equations for the unknown coefficients of the series. In order to proceed with the solution, it is necessary to eliminate the dependence on θ . This can be accomplished if the odd arguments of the trigonometric functions are expressed in terms of even, using the "half-range" expansion

$$\begin{aligned}\cos(2k+1)\theta &= \frac{4}{\pi} \sum_{n=0}^{\infty} W_k^{(n)} \cos 2n\theta, \\ \sin(2k+1)\theta &= \frac{4}{\pi} \sum_{n=1}^{\infty} t_k^{(n)} \sin 2n\theta.\end{aligned}\quad (19)$$

The coefficients of this complete expansion are given by

$$W_k^{(0)} = \frac{(-1)^k}{2(2k+1)}, \quad W_k^{(n)} = \frac{(-1)^{k+n}(2k+1)}{(2k+1)^2 - 4n^2} \quad \text{and} \quad t_k^{(n)} = \frac{(-1)^{k+n}2n}{(2k+1)^2 - 4n^2}.$$

Utilizing the expansions (19) and equating the coefficients of $\cos 2n\theta$ and $\sin 2n\theta$ in Eqs. (15)–(18), one can deduce a linear system of equations for the coefficients A_n , B_n , \bar{A}_n and \bar{B}_n .

Therefore, Eq. (15) yields

$$\begin{aligned}& A_n \frac{n(2n+1)}{x^{2n+2}} + A_{n-1} \frac{(n+1)(2n-1)}{x^{2n}} \\& + \sum_{k=0}^{\infty} B_k \frac{2}{\pi} \frac{2k+2}{x^{2k+3}} \{(2k+3)W_k^{(n)} + (2k+5)W_{k+1}^{(n)}\} \\& + \bar{A}_n(2n+1)(n-1)x^{2n} + \bar{A}_{n-1}n(2n-1)x^{2n-2} \\& + \sum_{k=1}^{\infty} \bar{B}_k \frac{4}{\pi} kx^{2k-1} \{(2k-1)W_k^{(n)} + (2k-3)W_{k-1}^{(n)}\} \\& = \frac{1}{2} \{\delta_0^{(n)} - \delta_1^{(n)}\}, \quad (n = 0, 1, 2, \dots).\end{aligned}\quad (20)$$

Similarly, Eq. (16) becomes

$$\begin{aligned}& A_n \frac{n(2n+1)}{x^{2n+2}} + A_{n-1} \frac{n(2n-1)}{x^{2n}} \\& + \sum_{k=0}^{\infty} B_k \frac{2}{\pi} \frac{(2k+2)(2k+3)}{x^{2k+3}} \{t_k^{(n)} + t_{k+1}^{(n)}\} \\& - \bar{A}_n(2n+1)nx^{2n} - \bar{A}_{n-1}n(2n-1)x^{2n-2} \\& - \sum_{k=1}^{\infty} \bar{B}_k \frac{4}{\pi} k(2k-1)x^{2k-1} \{t_k^{(n)} + t_{k-1}^{(n)}\} \\& = \frac{1}{2} \delta_1^{(n)}, \quad (n = 1, 2, 3, \dots).\end{aligned}\quad (21)$$

The continuity of the normal and tangential displacements given by Eqs. (17)–(18) are transformed into

$$\begin{aligned}
 & -A_n \frac{n}{x^{2n+1}} - A_{n-1} \frac{(2n-1+x)}{2x^{2n-1}} \\
 & - \sum_{k=0}^{\infty} B_k \frac{2}{\pi} \frac{1}{x^{2k+2}} \{(2k+3) W_k^{(n)} + (2k+2+x) W_{k+1}^{(n)}\} \\
 & + \frac{1}{2f} \{\bar{A}_n(2n+1-x) x^{2n+1} + \bar{A}_{n-1} 2n x^{2n-1}\} \\
 & + \frac{1}{2f} \left\{ \sum_{k=0}^{\infty} \bar{B}_k \frac{4}{\pi} x^{2k} [(2k-1) W_k^{(n)} + 2(2k-x) W_{k-1}^{(n)}] \right\} \\
 & = \frac{1}{4} (x-1) x \delta_0^{(n)} - \frac{1}{2} x \delta_1^{(n)} + \left\langle -\frac{1}{2} x \varepsilon_y^* (\delta_0^{(n)} - \delta_1^{(n)}) \right\rangle, \quad (n=0, 1, 2, \dots), \quad (22)
 \end{aligned}$$

and

$$\begin{aligned}
 & -A_n \frac{n}{x^{2n+1}} - A_{n-1} \frac{(2n-1-x)}{2x^{2n-1}} \\
 & - \sum_{k=0}^{\infty} B_k \frac{2}{\pi} \frac{1}{x^{2k+2}} \{(2k+3) t_k^{(n)} + (2k+2-x) t_{k+1}^{(n)}\} \\
 & - \frac{1}{2f} \{\bar{A}_n(2n+1+x) x^{2n+1} + \bar{A}_{n-1} 2n x^{2n-1}\} \\
 & - \frac{1}{2f} \left\{ \sum_{k=0}^{\infty} \bar{B}_k \frac{4}{\pi} x^{2k} [(2k-1) t_k^{(n)} + 2(2k+x) t_{k-1}^{(n)}] \right\} \\
 & = \frac{1}{2} x \delta_1^{(n)} + \left\langle -\frac{1}{2} x \varepsilon_y^* \delta_1^{(n)} \right\rangle, \quad (n=1, 2, 3, \dots). \quad (23)
 \end{aligned}$$

For a sliding interface, the boundary conditions become

$$\begin{aligned}
 & (\sigma_r)_{r=z} = (\bar{\sigma}_r)_{r=z}, \quad (\tau_{r\theta})_{r=z} = 0 \\
 & \text{and} \\
 & (u_r)_{r=z} = (\bar{u}_r)_{r=z} + (\bar{u}_r^*)_{r=z}, \quad (\bar{\tau}_{r\theta})_{r=z} = 0.
 \end{aligned} \quad (24)$$

As in the case of perfect bonding, Eqs. (24) yield a linear system of equations for the expansion coefficients.

4 Results and discussion

The solution of the linear system of Eqs. (20)–(23) yields the coefficients A_n , B_n , \bar{A}_n and \bar{B}_n . Consequently, stresses and displacements at any point of the matrix or the inhomogeneity can be evaluated. The necessary series truncation requires no more than 15 terms so that the interfacial

boundaries are met with an accuracy of three significant figures. No proof of absolute convergence is offered since the numerical convergence of the stresses and displacements is evident.

Separate calculations are performed for the tensile and the eigenstrain loads. All the resulting quantities are evaluated per unit load and the inhomogeneity radius is taken equal to unity. The examples that follow illustrate the effects of the shear moduli ratio Γ and the integrity of the interface (perfect bond versus perfect slip).

In the case of remote tension, stresses and displacements were calculated for various values of Γ between $\Gamma = 10$ ("hard" inhomogeneity) and $\Gamma = 0.1$ ("soft" inhomogeneity). The eigenstrain case is treated like an inclusion problem ($\Gamma = 1$). Both Poisson's ratios for the inhomogeneity and the matrix were taken equal to 0.3.

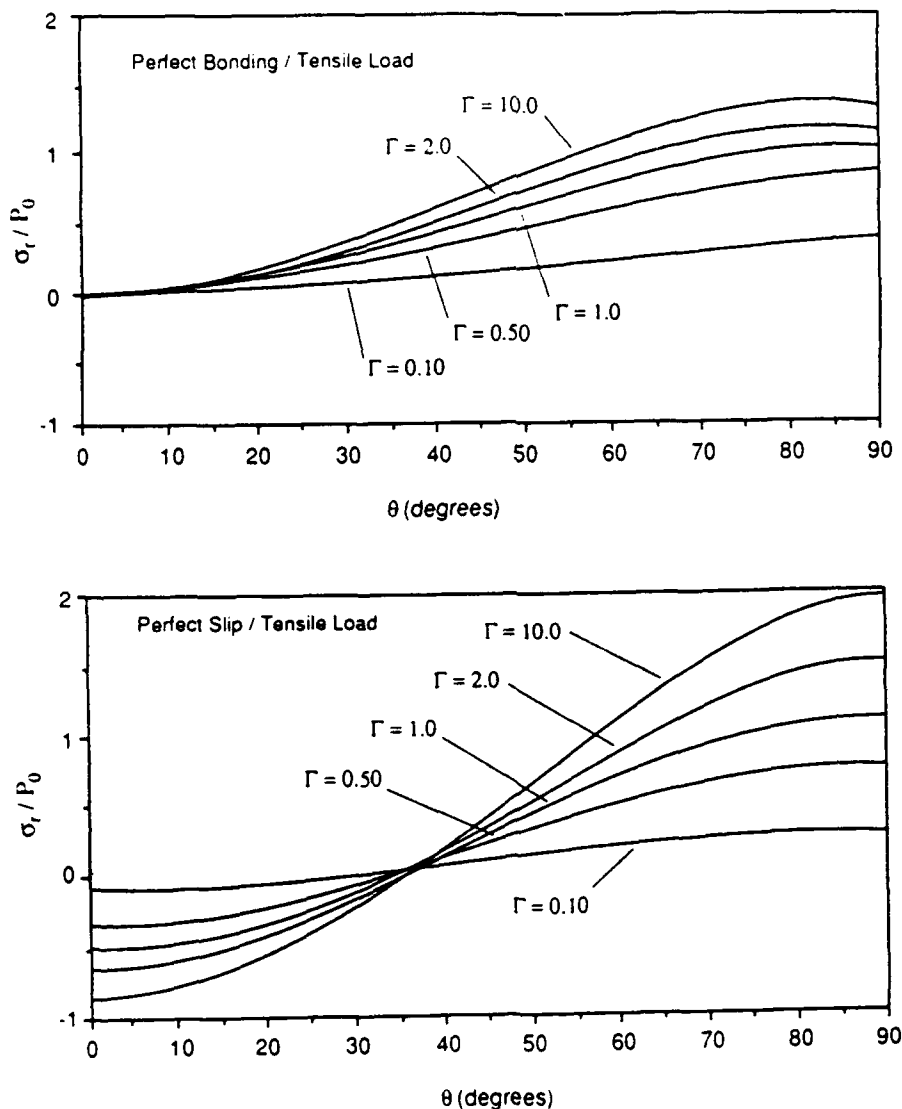


Fig. 2. Effect of the shear moduli ratio Γ on the normal stress along the interface for perfect bonding and sliding

4.1 Uniaxial tension

In the case of uniform tension at infinity, we have studied the effects of the shear moduli ratio on the elastic field along the interface, as well as along the free surface.

Figure 2 illustrates the variation of the normal stress σ_r along the interface. In both the cases of perfect bonding (PB) and sliding (SL), the magnitude of σ_r is proportional to Γ . However, the stress concentration is higher in the case of SL, particularly at the free surface ($\theta = 90^\circ$).

The matrix hoop stress σ_θ exhibits high tensile values at the bottom of the inhomogeneity (Fig. 3). These values of σ_θ are inversely proportional to Γ ; as $\Gamma \rightarrow 0$, σ_θ approaches the value $\sigma_\theta/p_0 = 3$, as predicted in the paper by Maunsell [4]. Nevertheless, there are no significant differences between PB and SL.

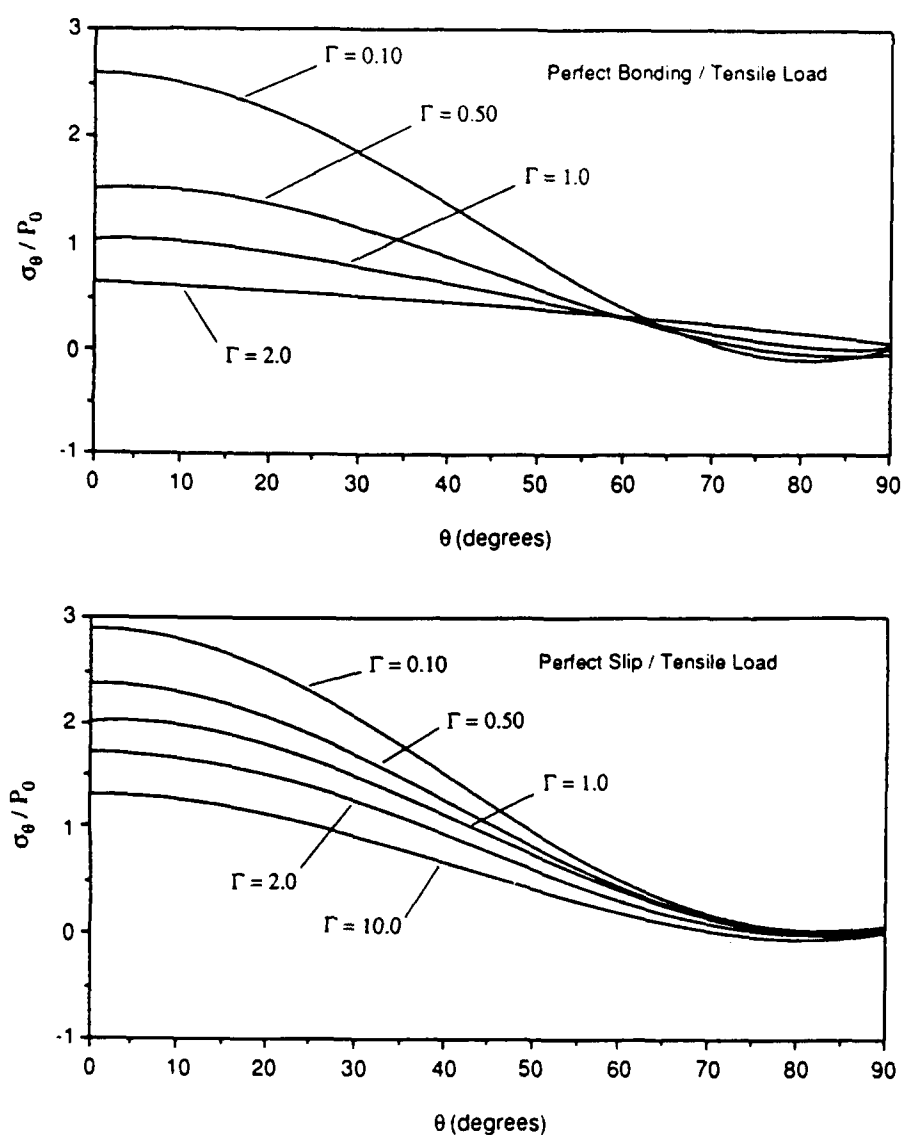


Fig. 3. Effect of the shear moduli ratio Γ on the matrix hoop stress along the interface for perfect bonding and sliding

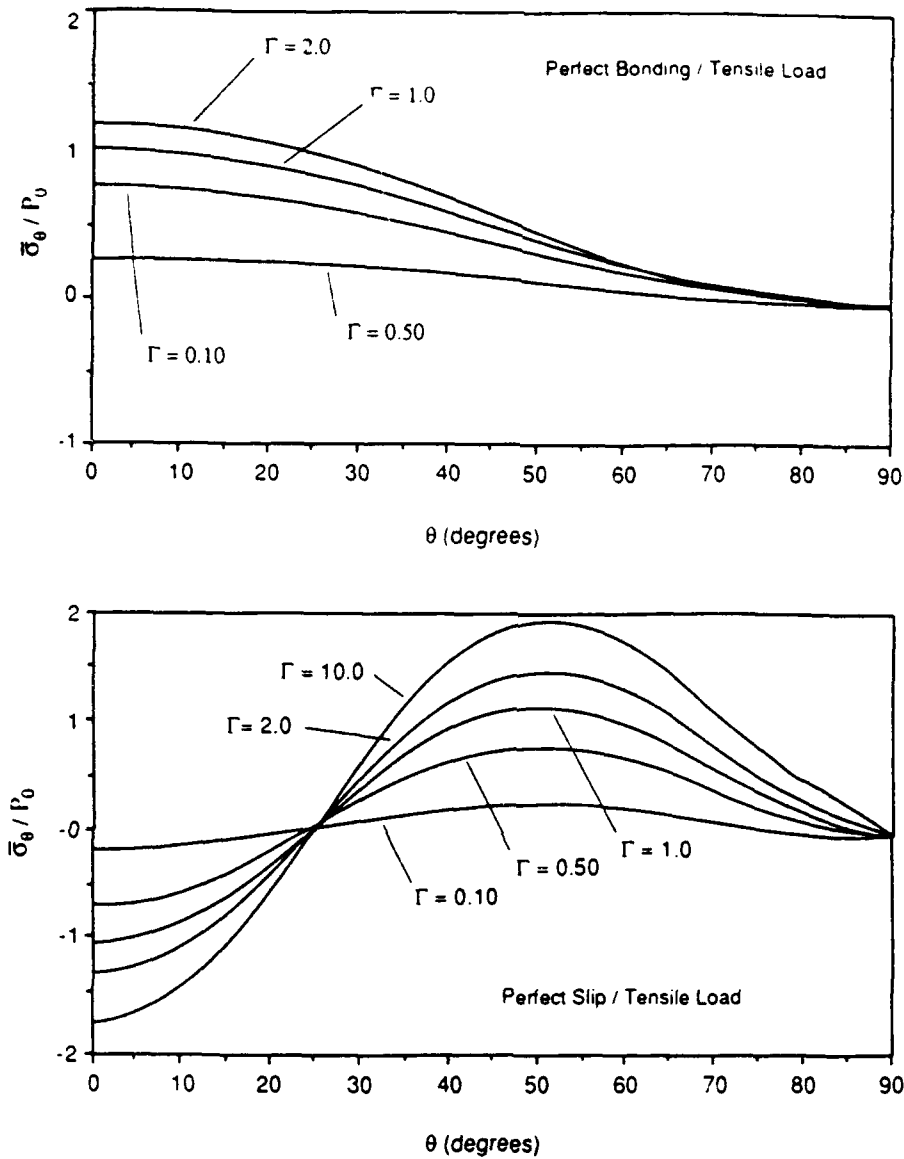


Fig. 4. Hoop stress along the interface of the inhomogeneity versus Γ , for PB and SL

This is not the case, however, for the inhomogeneity hoop stress $\bar{\sigma}_\theta$ (Fig. 4). Even though stress concentrations remain modest, the sliding case involves tension and compression along parts of the interface.

Figure 5 illustrates the distribution of the matrix normal stress σ_r (equivalent to σ_x) along the free surface, versus the relative distance R ($R \approx r/x$) from the center of the inhomogeneity. In the case of a perfectly bonded inhomogeneity with $\Gamma > 1$ (stiffer than the matrix), σ_r exhibits a maximum not at the interface, but at a distance $r \approx 1.3x$ from the center of the inhomogeneity. Therefore, crack initiation is more likely to occur at that point, instead of the interface. However, this is not the case if perfect slip prevails, where for $\Gamma > 1$, σ_r has a maximum value at the interface ($R = 1$). It is interesting that for a softer inhomogeneity ($\Gamma < 1$), the same point $r \approx 1.3x$ corresponds to a local minimum for both PB and SL.

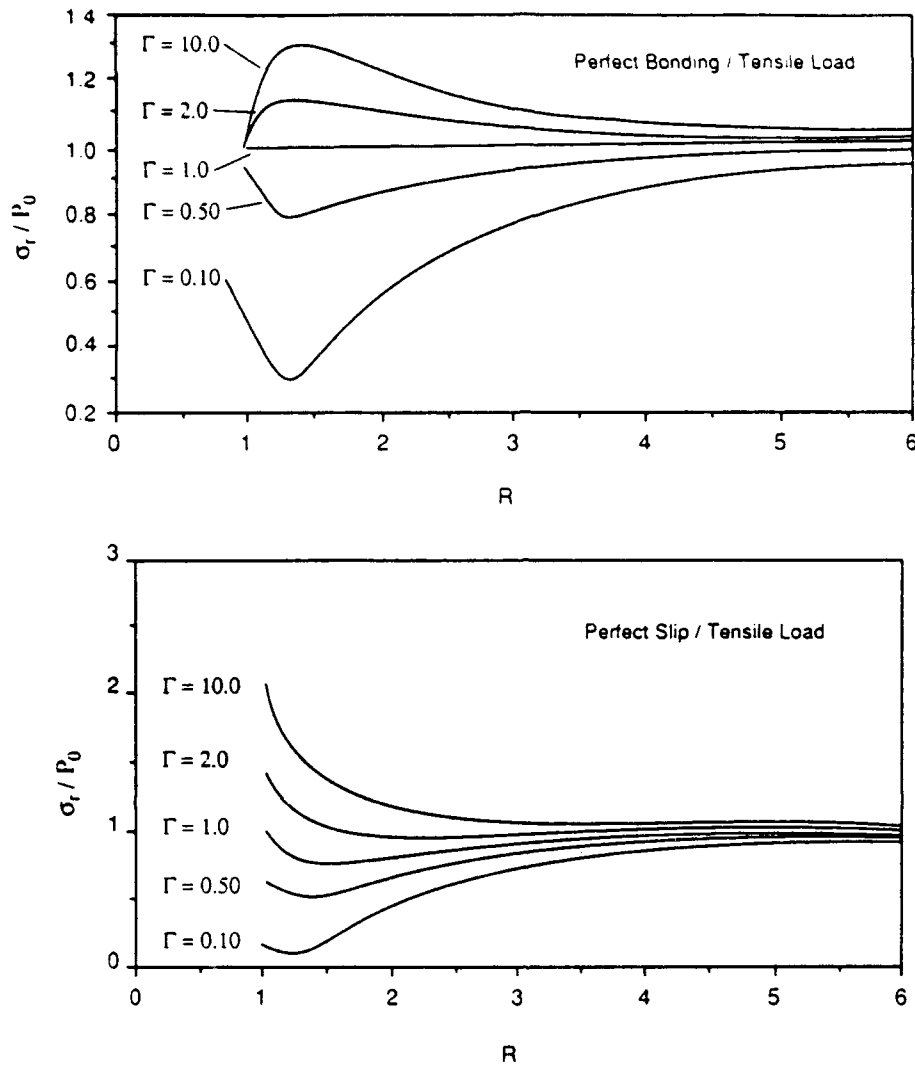


Fig. 5. Effect of Γ on the distribution of the axial stress along the free surface of the matrix, for PB and SL

Figures 6 and 7 represent the variation of the normal displacement u_θ along the free surface of the inhomogeneity and the matrix. In the case of the inhomogeneity (Fig. 6), \bar{u}_θ remains almost constant for PB and $\Gamma > 1$. When sliding occurs, \bar{u}_θ decays as R approaches unity (interface). The values of u_θ along the free surface of the matrix (Fig. 7) tend towards zero as the distance from the inhomogeneity increases.

4.2 Eigenstrain

This non-elastic, uniform load is represented by $2G\epsilon_y^* = 1$. The semi-circular insert is assumed to be of the same material as the one of the matrix ($\Gamma = 1$). Our interest here is focused on the effects of the interfacial integrity.

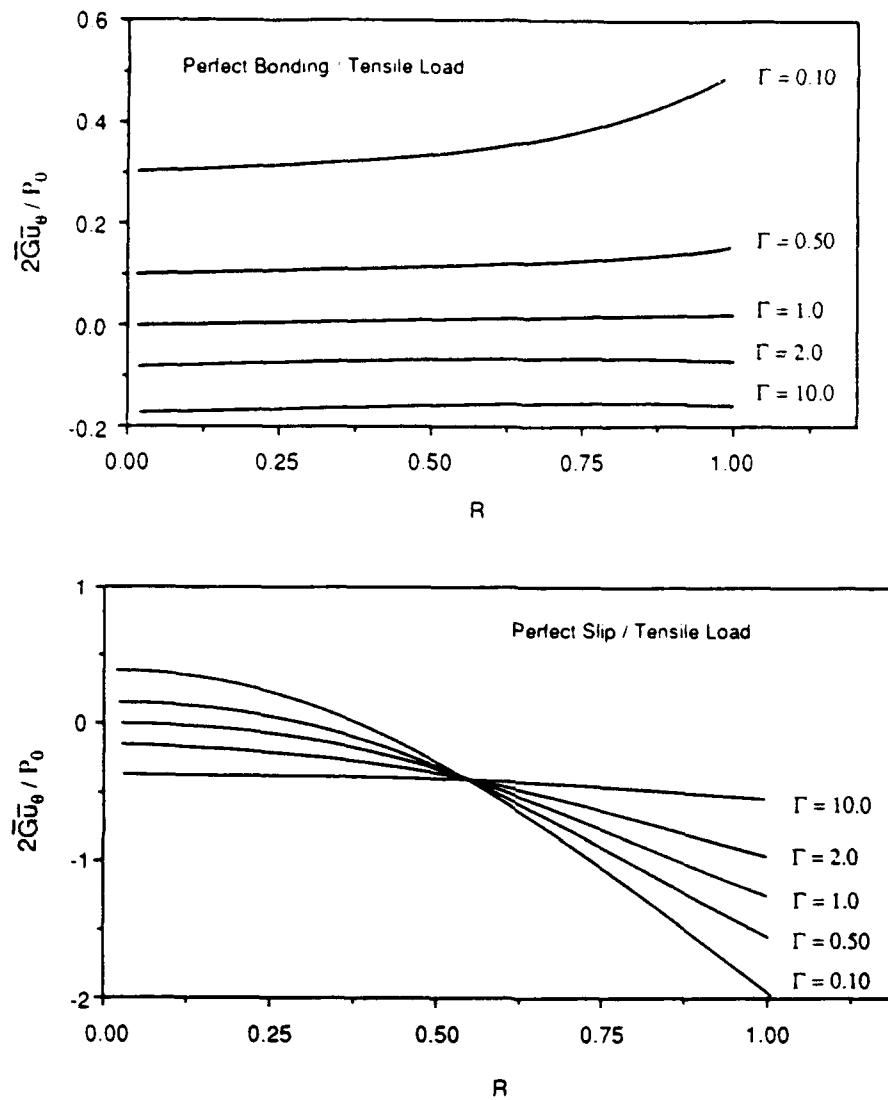


Fig. 6. Normal displacement along the free surface of the inhomogeneity

As shown in Fig. 8, conditions of perfect slip correspond to higher values of the normal stress σ_r .

The two components of the displacement vector, along the free surface of the matrix and the inclusion, are given in Figs. 9–10. These distributions indicate that when the inclusion is free to slip, it tends to force itself "up" and "out" of the pit. On the other hand, conditions of perfect slip appear to decrease the values of u_r and u_θ along the free surface of the matrix.

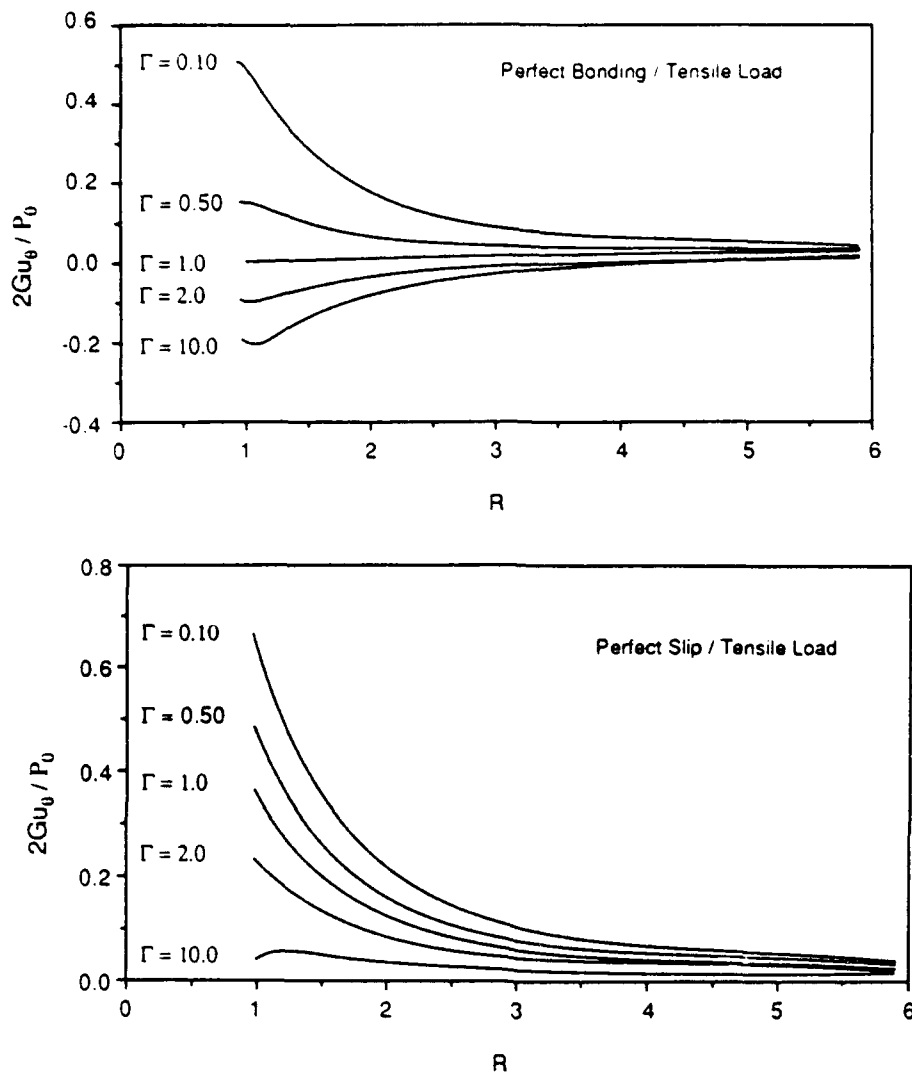


Fig. 7. Normal displacement along the free surface of the matrix

5 Conclusions

An elastic analysis was presented for the problem of a semi-circular inhomogeneity embedded at the free surface of a half-plane.

It was found that under the influence of uniaxial tension, local stresses and displacements are strongly dependent upon the inhomogeneity/matrix stiffness ratio. Comparisons were made between perfectly bonded and slipping interfaces which indicate that, in general, loss of the interfacial bond corresponds to higher stress concentrations.

Similar comparisons were considered in the case of an inclusion under the influence of eigenstrain loading.

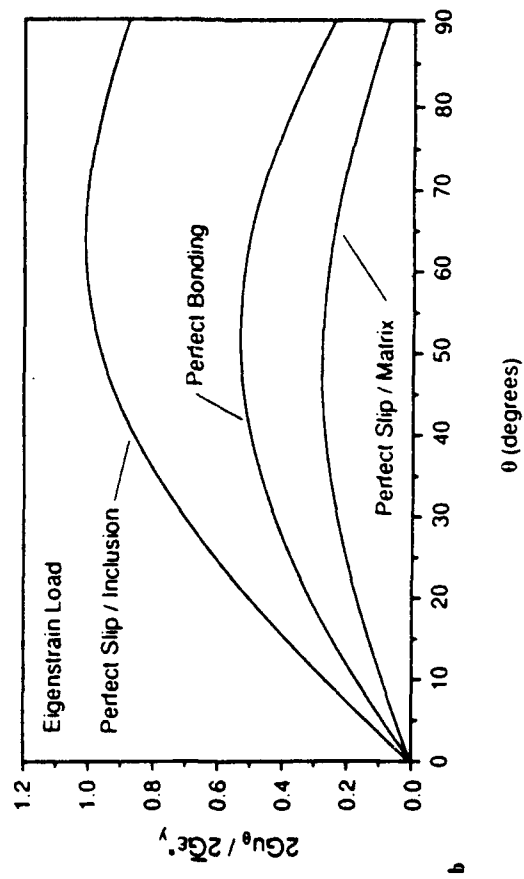
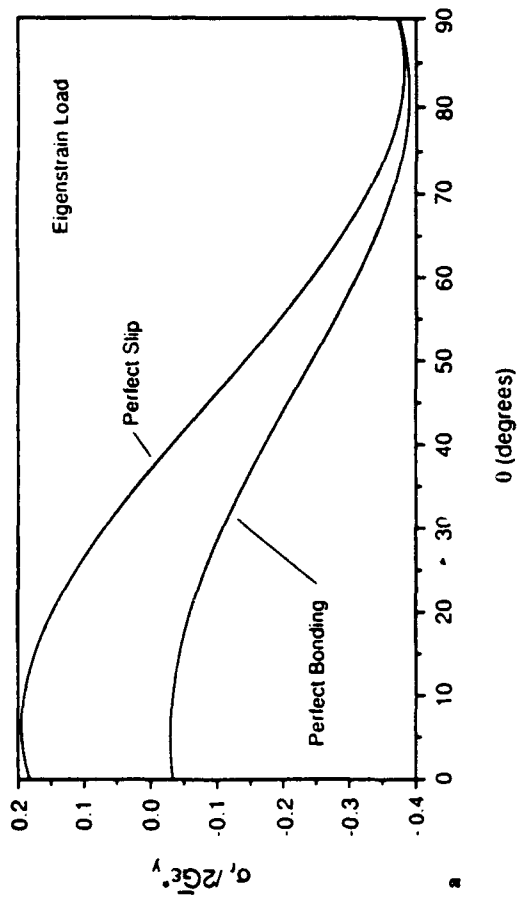


Fig. 8. Effect of PB and SL on the variation of **a** the radial stress and **b** the tangential displacement, along the interface

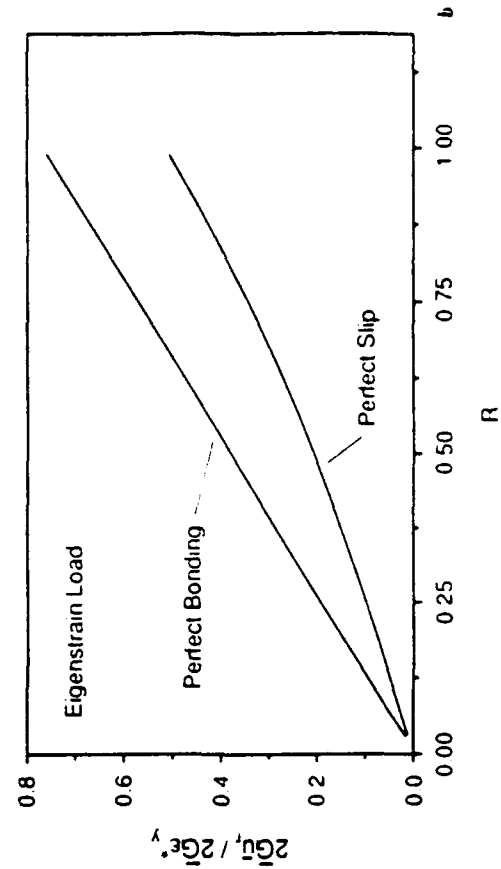
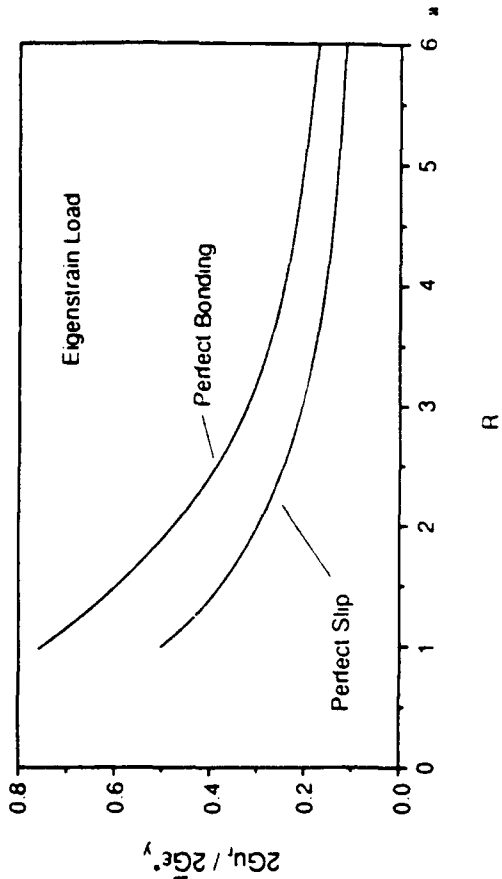


Fig. 9. Radial displacement along the free surface of **a** the matrix and **b** the inclusion, for PB and SL.

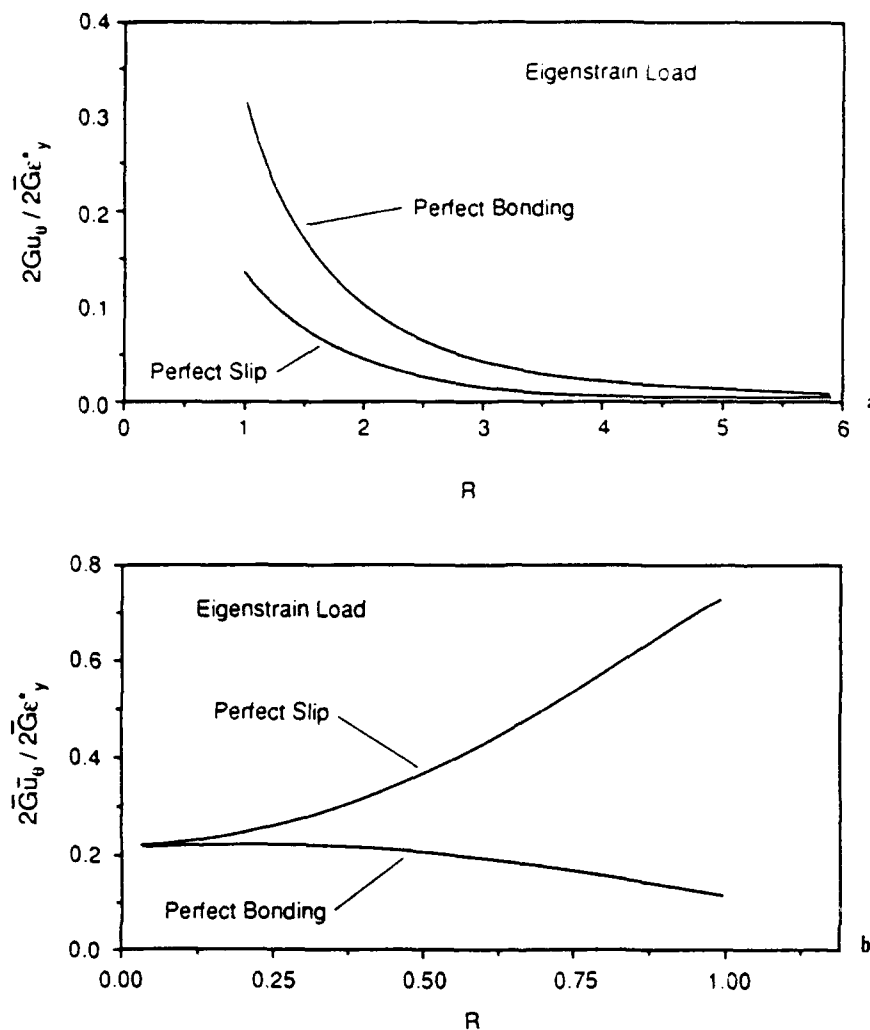


Fig. 10. Normal displacement along the free surface of **a** the matrix and **b** the inclusion, for PB and SL

Acknowledgement

This study has been supported by the Air Force Office of Scientific Research, through the University Research Initiative Award AFOSR 90-0235.

References

- [1] Kouris, D. A.: First-year report. AFOSR-90-0235 (1991).
- [2] Kouris, D. A., Tsuchida, E.: On the elastic interaction between two fibers in a continuous fiber composite under thermal loading. *Mech. Mat.* **12**, 131–146 (1991).
- [3] Kouris, D. A.: Stress concentration due to the interaction between two imperfectly bonded fibers in a continuous fiber composite. *J. Appl. Mech.* (in press).

- [4] Maunsell, F. G.: Stresses in a notched plate under tension. *Phil. Mag.* **21**, 765–773 (1936).
- [5] Atsumi, A.: Stresses in a plate under tension and containing an infinite row of semi-circular notches. *ZAMP* **8**, 466–477 (1957).
- [6] Boussinesq, J.: *Applications des potentiels*. Paris: Gauthier-Villars 1885.

Authors' address: D. A. Kouris and J. P. Nuxoll, Department of Mechanical and Aerospace Engineering, Arizona State University, Tempe, AZ 85287-6106, U.S.A.

5.0 TRANSVERSE STRENGTH AND FAILURE MECHANISMS

5.1 Damage Mechanisms in Ti3Al Matrix Composites

accepted for publication in the ASME Journal of Engineering Materials and Technology

DAMAGE MECHANISMS IN Ti_3Al MATRIX COMPOSITES

Demitris Kouris

Department of Mechanical and Aerospace Engineering

Arizona State University

Tempe, AZ 85287-6106

David Marshall

Rockwell International Science Center

1049 Camino Dos Rios

Thousand Oaks, CA 91360

ABSTRACT

The paper discusses experimental observations and some related theoretical results associated with the mechanical response of two Ti_3Al matrix composites, subjected to transverse loading. Both composites contain continuous unidirectional fibers; however, there are considerable differences in the composition of the two interfaces. The $Ti_3Al/SCS-6$ system contains brittle reaction products around the fibers that degrade the strength of the composite. The second composite consists of a Ti_3Al matrix reinforced by sapphire fibers that are strongly bonded to the matrix. Experimental observations indicate that the damage mechanisms in the two composites are substantially different. Utilizing elastic analyses of the local stress field, an attempt was made to explain the dependence of the observed damage mechanisms on the residual field and the properties of the interface.

1 Introduction

The next generation of advanced turbine engines requires high temperature intermetallic and ceramic matrix composites. Because of their low density and high strength at elevated temperatures, titanium aluminide alloys are the most likely materials to advance the high temperature performance of aerospace structures. For highly stressed components such as compressor disks in advanced gas turbine engines, reinforcement of these alloys with high strength continuous fibers is necessary. The most suitable material appears to be SiC, although fiber coatings are necessary in order to obtain optimum interfacial properties and to control interfacial reactions under severe service and fabrication conditions.

Most previous studies of titanium aluminide composites have involved either β -stabilized titanium alloy matrices or matrices based on the α_2 Ti₃Al phase. High stiffness, strength and fatigue resistance have been achieved in both systems (Johnson et al., 1990; Revelos and Smith, 1992). However, they are both limited in application; the β -stabilized matrices by high temperature stability and the α_2 -based matrices by severe degradation during thermal fatigue in air (Revelos and Smith, 1992).

The interfaces between the fibers and matrix in these composites play the dominant role in determining the mechanical properties of the composite. Until now the design and fabrication of the interface has been largely empirical, with the choice of constituents being dictated by compatibility considerations and very little guidance being available for the optimum choice of interfacial properties. Indeed, the composites that have shown the most promising properties have all possessed serendipitous layers of carbon at the interface, either formed by reaction with the matrix or deposited as a protective coating on the fiber. The carbon layer provides a weak interface, which is necessary to allow debonding and toughening by fiber bridging. The properties of the interface between the fibers and matrix dictate the overall properties of ceramic and intermetallic matrix composites (Marshall et al., 1991; Evans and Marshall, 1989).

Generally, weak interfaces that allow debonding are required in order to achieve optimum longitudinal properties in unidirectionally reinforced composites. In brittle matrix composites, matrix cracking is the first damage to develop. If the fiber/matrix interface is sufficiently weak to deflect an incident crack into the interface rather than allow it to penetrate the fibers, and if the fibers are sufficiently strong relative to the sliding resistance of the interface, then the strength of the composite is dictated by the fiber strength and is insensitive to damage and notches. Moreover, the stress strain curve is usually nonlinear prior to the peak stress, and noncatastrophic beyond the peak. On the other hand, if the interface is strong enough for the first matrix crack to penetrate the fiber, the composite behaves as a monolithic brittle material with linear stress strain curve to failure, and with strength that is sensitive to pre-existing damage and notches.

Design and reliability analysis of intermetallic composites must be mechanism based. This involves development of micromechanical models that relate damage to mechanical properties of the individual constituents and their interfaces, and use of direct in situ measurements of these properties in combination with the models to provide the input to design codes. Therefore, the material properties needed to characterize these composites differ from the properties, such as strength and toughness, used to characterize monolithic structural materials: direct information about the mechanical properties of the interface is essential. Moreover this information is needed over the full range of service temperatures and environments. Substantial advances have been made in developing techniques for obtaining these measurements coupled with parallel advances in micromechanical modeling.

In unidirectionally reinforced intermetallic matrix composites, in which the matrix exhibits limited ductility, fiber fracture can occur before failure of the matrix under monotonic loading. Interfacial debonding then leads to improved strength by allowing the damage in the matrix to be spread out rather than being concentrated near the fiber cracks, thus delaying rupture (Marshall et al., 1991). However the largest potential

benefit from reinforcement of intermetallic matrix composites is in the improved resistance to fatigue cracking. Under cyclic loading, fatigue cracks initiate in the matrix. If interfacial debonding occurs, the reinforcing fibers remain intact, spanning the crack faces and restricting the range of displacements that are transmitted to the crack tip, thereby reducing the crack growth rate. With optimum interfacial properties this reduction in growth rate due to crack bridging can be dramatic, either arresting a crack that would otherwise accelerate indefinitely, or reducing its growth rate to a low constant velocity.

The need to produce weak interfaces for optimum longitudinal properties conflicts with the requirements for high transverse strength, where strong interfaces are beneficial. Therefore a compromise is needed, either in the interface properties or in the design requirements. This topic has received very little attention. For instance, very little is known of the effect of interfacial friction on transverse strength.

The present study involves two composites with Ti_3Al matrices, subjected to transverse tensile loading. The first matrix is reinforced by "bare" SiC fibers (SCS-6) and the second by sapphire fibers coated with a thin ($\sim 1\mu\text{m}$) Ta layer. The experimental observations are coupled with analytical solutions of the local stress field, in an effort to provide a better understanding of the relevant damage mechanisms.

2 Experiments

Transverse loading experiments were conducted at Rockwell (Marshall et al., 1993) involving two Ti₃Al based composites (Table 1).

Table 1

	Matrix	Fibers	Coating	V _f
Composite (a)	super α_2^1	SiC (SCS-6, Textron)	None	37%
Composite (b)	super α_2	sapphire (Saphikon)	Ta (PVD at NRL)	20%

The specimens (~ 50 x 2 x 1 mm) were polished on the sides containing the fiber ends and were loaded in tension, with the largest dimension perpendicular to the fibers. The in situ optical micrographs were analyzed by utilizing a high resolution strain mapping facility (James et al., 1990). Micrographs from the two composites are shown in Figs. 1 and 2. Composite (a) contained a thin reaction layer (~ 1 μ m thickness) around the fibers, consisting of carbides and silicides. No such reaction products were found in composite (b). However, there was a β depleted matrix layer around each fiber, with a thickness of ~ 5 μ m.

As expected, the failure stress and strain in transverse loading are considerably lower when compared to the ones corresponding to longitudinal loading. Young's modulus in the transverse direction was 150 MPa for composite (a) and 141 MPa for composite (b). The initially linear stress-strain curves (Fig. 3) became nonlinear at applied stresses above 150 MPa and 270 MPa for composites (a) and (b), respectively.

¹ Two phase (α_2 - β) Ti-25Al-10Nb-3V-1Mo alloy.

2.1 Evolution of Damage

2.1.1 SCS-6 Composite. The first observed damage was sliding of the fibers relative to the matrix, in the direction perpendicular to the surface of the specimen. This is caused by the difference in the axial residual stresses between the fibers and the matrix. Sliding initiated at applied stresses of ~ 40 MPa and the corresponding displacement increased with increasing applied loads. After unloading, the fibers remained protruding from the surface of the specimen.

At higher loads (120 - 150 MPa), separation of the fiber/matrix interface was observed. Most fibers ($\sim 70\%$) separated between the reaction matrix layer and the outer layer of the fibers. The remaining fibers were also debonded along the carbon layer between the outer layers of the fibers.

As the loading increased (150 MPa), cracks were formed between closely spaced fibers, on planes parallel to the direction of the applied load. These parallel cracks initiated next to the fibers and grew in a stable manner (Fig. 4).

At load levels above 160 MPa, transverse cracks initiated in the reaction layers along the interface and grew stably with increasing load, across the regions between pairs of fibers. Failure was caused by the linking of debonded interfaces with transverse cracks, across the specimen.

2.1.2 Sapphire Composite. In this composite, the mechanisms of damage due to transverse loading are quite different from the ones observed in the case of the SiC composite. Here the interface strength is high (higher than that of the matrix). Interfacial debonding and plasticity were not a factor in the failure process.

At a loading level consistent with the onset of nonlinearity of the stress-strain curve, cracks were formed in the fibers. These cracks were oriented along planes perpendicular to the direction of the applied load. With increasing load, cracks appeared

in many fibers and grew into the surrounding matrix. In addition, matrix cracks formed along the boundaries of the β - depleted zones around the fibers. Linkage of the cracks in and near adjacent fibers led to composite failure.

The high strength of the interfacial bond in the sapphire composite is demonstrated by the two following observations. The matrix cracks formed at $\sim 10 \mu\text{m}$ away from the interface, even though the maximum tensile stress did not occur there (the tensile stress is maximum at the interface). In addition, no interfacial debonding was observed. The second observation is that the fiber cracks grew into the matrix without being deflected or offset by the interface.

3 Theoretical Modeling

An attempt was made to model the observed damage by utilizing some relatively simple analytical solutions for the local elastic stress fields. The use of elastic solutions is justified by the fact that the stress-strain curves for both composites are linear up to the initiation of the damage being considered.

When the composite is loaded by a uniform remote stress, the elastic field consists of the applied load, the disturbance due to the presence of the fibers (inhomogeneities), and the residual field. The residual stresses are due to the misfit strains (eigenstrains) caused by the different thermal expansion coefficients of the fibers and the matrix.

3.1 Residual Field. The presence of a residual stress field is dependent upon the difference in thermal expansion coefficients (CTE's) between the fibers and the surrounding matrix. Consequently, the residual stresses in the sapphire fiber composite were neglected, since the CTE's of Al_2O_3 and super α_2 are similar (Table 2).

Table 2

	Young's Modulus (GPa)	Poisson's Ratio	Coefficient of Thermal Expansion ($\times 10^{-6} / ^\circ\text{C}$)
super α_2 matrix	80	0.3	9.25
SCS-6 fiber	414	0.3	4.86
sapphire fiber	400	0.3	8.5

Based on measurements of the fiber relaxation after removing the matrix by etching (Marshall et al., 1992a and 1992b), the misfit strain ϵ^* in the SiC composite was found ($\epsilon^* = 0.0061$). Assuming a uniform ϵ^* , the residual stresses were calculated utilizing the concentric cylinder model. It was found that the normal and hoop stresses along the interface were equal to -260 MPa and 565 MPa, respectively. A finite element solution for a square array of fibers yielded very similar results (Fig. 5). Given the isotropy of the eigenstrain ϵ^* , the concentric cylinder model provides an adequate approximation of the local field. More elaborate models (Kouris and Tsuchida, 1991) could be useful in cases of extreme inhomogeneity of the fiber distribution (closely spaced fibers).

3.2 Remote Transverse Load. As a first approximation, the local stress field due to remote tension can be determined by considering an isolated fiber that is perfectly bonded to the matrix material. However, this approach leads to erroneous results in the case of closely spaced fibers. Therefore, the interaction effects of neighboring fibers as well as interfacial debonding and sliding require a more elaborate model. In this context, an attempt was made to analytically determine the stress field in the vicinity of a pair of fibers (Fig. 6), under plane conditions. The fiber cross sections were modeled by circular inhomogeneities, surrounded by an infinitely extended matrix.

It seems reasonable to assume that the stresses along the central line of two closely spaced fibers are well approximated by considering a single pair of inhomogeneities.

The displacements u_1 and u_2 corresponding to the coordinate systems (x_1, y_1) and (x_2, y_2) , can be represented by:

$$2\mu u_i = \text{grad}(\Phi_{0i} + x_i \Phi_{1i} + y_i \Phi_{2i}) - 4(1-\nu)[\Phi_{1i}, \Phi_{2i}], \quad (i=1,2) \quad (1)$$

where Φ 's denote arbitrary harmonic functions. The disturbance due to the presence of the fibers is expressed by:

$$\begin{aligned} \Phi_{0i} / p_0 &= F_0^i \log \rho_i + \sum_{n=1}^{\infty} A_n^i \rho_i^{-n} \cos n\theta_i \\ \Phi_{1i} / p_0 &= \sum_{n=1}^{\infty} B_n^i \rho_i^{-n} \cos n\theta_i \\ \Phi_{2i} &= 0 \end{aligned} \quad (2)$$

for the matrix region and:

$$\begin{aligned} \Phi_{0i} / p_0 &= \sum_{n=1}^{\infty} \bar{A}_n^i \rho_i^n \cos n\theta_i \\ \Phi_{1i} / p_0 &= \sum_{n=1}^{\infty} \bar{B}_n^i \rho_i^n \cos n\theta_i \\ \Phi_{2i} &= 0 \end{aligned} \quad (3)$$

for the fibers, where c is the central distance, $\rho_i = r_i / c$, and $p_0 = T_x$.

The boundary conditions along the fiber/matrix interface can be expressed by:

$$\sigma_r = \bar{\sigma}_r, \quad \tau_{r\theta} = \bar{\tau}_{r\theta}, \quad 2\mu[u_r] = \beta a \bar{\sigma}_r, \quad \text{and} \quad 2\mu[u_\theta] = \lambda a \bar{\tau}_{r\theta} \quad (4)$$

where β and λ are proportionality constants, μ is the shear modulus of the matrix, a is the radius of the fibers, and $[u] = u - \bar{u}$. According to (4), $\beta, \lambda \rightarrow 0$ corresponds to perfect bonding, while $\beta, \lambda \rightarrow \infty$ corresponds to maximum debonding and perfect slip. These constants may represent a compliance measure associated with spring-type interfacial layers of infinitesimal thickness (Lene and Leguillon, 1982).

By including the influence of the remote transverse load, the boundary value problem as described by (2), (3), (4) can be solved analytically.

4 Analysis of Damage

The preceding analysis was utilized in an effort to provide some understanding of the mechanisms of damage associated with the two composites under consideration.

4.1 Sapphire Composite. In the absence of a residual field, the maximum tensile stress is the radial stress at $\theta = 0$. Its distribution inside the fibers is almost uniform while a local maximum occurs in the matrix. This is consistent with the experimental observations in the strongly bonded sapphire-fiber composite. However, matrix cracking is probably affected by the presence of the β - depleted layer. The interfacial stresses normalized by the applied tension are shown in Fig. 7. For a perfectly bonded interface, the radial stress as a function of fiber spacing varies between $1.7 T_X$ and $2.6 T_X$. Since crack initiation was observed at $T_X \sim 280$ MPa, the local radial stress was estimated between 480 and 730 MPa.

Fiber splitting and matrix cracking occurred at similar stress levels; however, these stress values are substantially lower when compared to the strength of the fibers. This observation suggests that specimen preparation (cutting and polishing) was responsible for the considerable degradation of the fiber strength. Such a conclusion is supported by other experimental evidence (Marshall et al., 1993) and implies that fiber splitting may not occur in composites with unsectioned fibers.

4.2 SiC Composite. Application of remote transverse tension generates tensile stresses along most of the interface. These stresses tend to relax the pre-existing residual field. As a consequence, sliding of the fibers relative to the matrix occurs, in a direction normal to the surface of the specimen. A shear-lag analysis incorporating Coulomb friction can provide an estimate of the sliding displacement (Marshall et al., 1993). Due to Poisson's effect, the in-plane stresses are altered with the occurrence of axial fiber

sliding. These changes can be taken into account via an adjustment of the eigenstrain (misfit strain) that is responsible for the residual field. The relaxation of residual compression in the fiber leads to an increase in the effective mismatch strain. Following the analysis of Hutchinson and Jensen (1990), this increase is approximated to a level of $0.1 \epsilon^*$.

At stress levels corresponding to the onset of nonlinearity in the stress-strain curve, interfaces began to separate. Upon unloading and subsequent reloading, the curve was linear over the same stress range and retained the same slope as the initial loading curve. Since the stresses required to initiate interfacial separation during the first and second loading were almost identical, it can be concluded that the tensile strength of the interface is negligible. In addition, it seems that initial departure from linearity is due to interfacial separation; this conclusion is consistent with observations related to other metal-matrix composites (Johnson et al., 1990; Nimmer et al., 1991). Given the negligible strength of the interface, separation is expected to occur when the tensile stresses due to the remote load approach the values of the compressive residual stresses. For the given fiber volume fraction (37%) of the SiC composite, the stresses due to the applied tension range between $1.7 T_X$ (perfect bonding) and $2.0 T_X$ (perfect slip). Therefore, the bounds of the applied stress required to initiate separation are estimated by:

$$1.7 T_X = 260 \text{ MPa} \quad \text{and} \quad 2.0 T_X = 260 \text{ MPa} \quad (5)$$

which yield:

$$153 \text{ MPa} \geq T_X \geq 130 \text{ MPa} \quad (6)$$

These estimates are consistent with the experimental observations (Section 2.1.1).

Parallel cracking in the matrix between fibers occurred when the fiber spacing was less than a ($d / a \leq 1$). According to Fig. 7, the corresponding local stress varies between $0.6 T_X$ and $1.1 T_X$. Based on the measured applied load required for cracking ($\sim 150 \text{ MPa}$) and the residual hoop stress (565 MPa), the local stresses are bounded

between 655 and 730 MPa. The elastic solution due to the transverse load indicates that the interfacial hoop stress in the matrix is higher at the position of longitudinal cracking ($\theta = 0$) than at the site of the transverse cracking (Fig. 8). Thus, it is not surprising that parallel cracking preceded the formation of transverse cracks. For stress concentrations due to the transverse load T_x ranging between -0.08 and 0.15 (Fig. 9), the local stresses are estimated between 552 and 589 MPa. These values are considerably lower than the ones corresponding to parallel cracking, thus suggesting that circumferential sliding occurred. The hoop stresses in the case of a freely slipping interface would be ~760 to 895 MPa. The question is whether sliding along the interface is possible. At the applied stress of 160 MPa (when transverse cracking takes place), interfacial shear stresses exceed the sliding resistance τ_0 over a substantial part of the interface. The value of τ_0 , measured by fiber pulling experiments, was ~70 MPa. Therefore, at least some sliding ought to be expected at the stress levels required for transverse cracking.

5 Discussion

The experimental observations coupled with the analytical results presented above provide some insight into the optimum composite properties and design. The two composite systems examined are very useful in this regard, since they enable the parallel examination of two different interfaces (weak for the SiC - super α_2 and strong for the sapphire - super α_2 composites). The question of what constitutes an optimal interfacial strength is probably the most important; at the same time it is probably the least understood aspect of design involving composites with intermetallic matrices.

In the case of unidirectional composites under longitudinal fatigue loading, it has been well established that interfacial debonding is desirable; it maximizes the benefits of fiber reinforcement since it increases the resistance to fatigue crack growth due to crack bridging. However, when similar composites are loaded in the transverse direction, intuition suggests that perfectly bonded interfaces ought to increase transverse strength.

Nevertheless, the composites of this study do not confirm such an expectation². The transverse strength of the sapphire/Ta/super α_2 composite was higher than that of the SCS-6/super α_2 composite (300 versus 200 MPa). However, studies (Marshall et al., 1993) involving SCS-6/Ag-Ta/super α_2 yield a transverse strength of 400 MPa for this composite that includes a Ag-Ta coating around the carbon fibers. It seems, therefore, that a strong interface does not necessarily yield higher values of the transverse strength compared to a weak interface. In any case it should be possible to improve the measured properties of the sapphire composite by avoiding the fiber damage which is probably present due to the preparation of the transverse cross section. In addition, improvements could be made in controlling oxygen diffusion and thus eliminating the relatively brittle, β - depleted matrix layer around the fibers.

The failure mechanisms in the two composites studied are illustrated in Fig. 10. In the case of the SCS-6 system, debonding of the interface relieves the radial stresses. In addition, the residual field yields compressive radial stresses and tensile hoop stresses at $\theta = 0$. As a result, circumferential matrix cracking is suppressed, while the higher hoop stresses cause radial cracking. Before the onset of debonding, the hoop stress σ_θ is higher at $\theta = 0$ than at $\theta = \pi / 2$. This explains why parallel cracks are formed first. Debonding results in an increase of $\sigma_\theta(\pi / 2)$ and a decrease of $\sigma_\theta(0)$. Consequently, transverse cracks appear, leading to the composite failure.

6 Conclusions

The behavior of two intermetallic composites (SCS-6/super α_2 and sapphire/Ta/super α_2) under transverse tension was examined. The experimental observations were coupled with analytical solutions that provided a qualitative understanding of the failure mechanisms.

² The issue is more complicated than implied here since microstructural variations also affect relative strength.

Damage in the sapphire composite consisted of fiber cracking as well as circumferential matrix cracking prior to failure. In the case of the SCS-6 fiber composite, failure occurred after (a) fiber/matrix sliding in the axial direction, (b) matrix cracking in the direction parallel to the applied tension, (c) debonding along the interface, and (d) transverse matrix cracking. The differences in the behavior of the two material systems were attributed to the condition of the interfaces and the residual field.

Improvement of the transverse strength in composites with perfectly bonded interfaces may be accomplished by allowing for an intermediate mismatch in the thermal expansion coefficients of the two constituents. The subsequent residual field would decrease the radial stresses and increase the hoop stresses (in comparison with the case of negligible residual stresses). Assuming that the transverse cracks responsible for the composite failure initiate at the location of the maximum tensile stress, an optimum residual field would correspond to equal radial (at $\theta = 0$) and hoop stress ($\theta = \pi/2$), at the point of failure.

In composites with weak interfaces, the radial tensile stress at $\theta = 0$ is relaxed upon debonding. If interfacial sliding accompanies debonding, the hoop stress at $\theta = \pi/2$ increases. This stress is responsible for the transverse cracks leading to failure. It seems reasonable to assume that the overall transverse strength could be improved by allowing debonding and, at the same time preventing sliding along the interface. Then, the hoop stress at $\theta = \pi/2$ would be lower. Consequently, an optimal interface ought to not only debond easily, but also resist circumferential sliding (large frictional resistance). This would be compatible with the requirements for improved longitudinal properties.

Acknowledgments

Funding for this work was provided by the U. S. Air Force Office of Scientific Research (AFOSR 90-0235) and by Wright Patterson Air Force Base (F33615-90-C-5928).

References

Evans, A. G., and Marshall, D. B., "The Mechanical Behavior of Ceramic Matrix Composites," *Acta Metall.*, Vol. 37(10), 1989, pp. 2567-2583.

Hutchinson, J. W., and Jensen, H. M., "Models of Fiber Debonding and Pullout in Brittle Composites with Friction," *Mech. Mater.*, Vol. 9, 1990, pp. 139-163.

James, M. R., Morris, W. L., and Cox, B. N., "A High Accuracy Automated Strain Field Mapper," *Exp. Mech.*, Vol. 30, 1990, pp. 60-68.

Johnson, S. W., Lubowinski, S. J., and Highsmith, A. L., "Mechanical Characterization of SCS-6/Ti-15-3 Metal Matrix Composites at Room Temperature," in *Thermal and Mechanical Behavior of Metal Matrix and Ceramic Matrix Composites*, ASTM STP1080, J. M. Kennedy, H. M. Moeller, and W. S. Johnson, eds., 1990, pp. 193-218.

Kouris, D., and Tsuchida, E., "On the Elastic Interaction between two Fibers in a Continuous Fiber Composite under Thermal Loading," *Mech. Mat.*, Vol. 12, 1991, pp. 131-146.

Lene, F., and Leguillon, D., "Homogenized Constitutive Law for a Partially Cohesive Composite Material," *Int. J. Solids Struct.*, Vol. 18, 1982, pp. 443-458.

Marshall, D. B., Shaw, M. C., Morris, W. L., and Graves, J., "Interfacial Properties and Residual Stresses in Titanium and Titanium Aluminide Matrix Composites," in *Titanium Matrix Composites*, W. Revelos and P. R. Smith eds., WL-TR-92-4035, 1992a, pp. 329-347.

Marshall, D. B., Shaw, M. C., Morris, W. L., "Measurement of Debonding and Sliding Resistance in Fiber Reinforced Intermetallics," *Acta Metall.*, Vol. 40(3), 1992b, pp. 443-454.

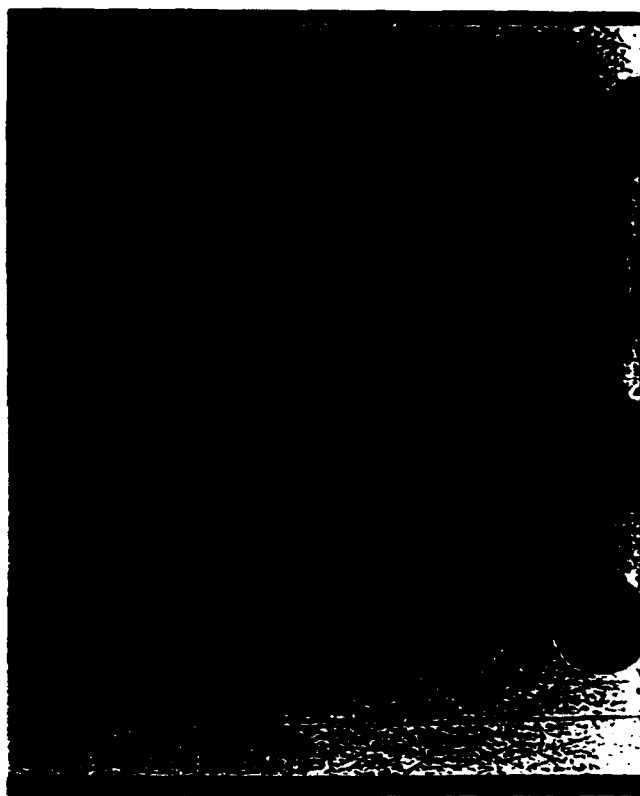
Marshall, D. B., Morris, W. L., Cox, B. N., Graves, J., Porter, J. R., Kouris, D., and Everett, R., "Transverse Strengths and Failure Mechanisms in Ti₃Al Matrix Composites," 1993, to be submitted for publication.

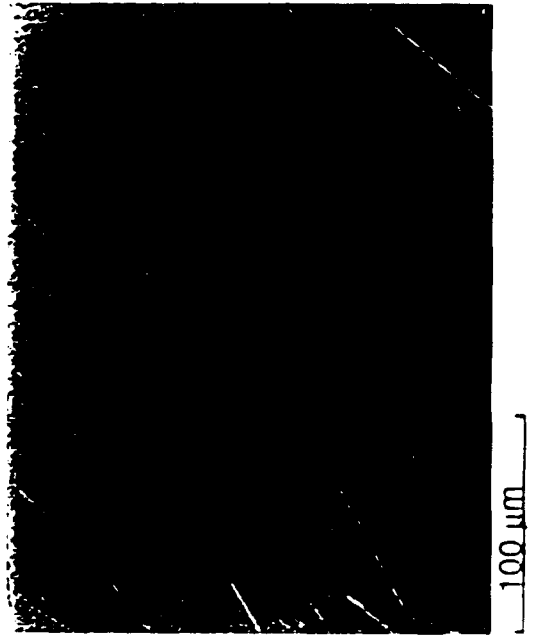
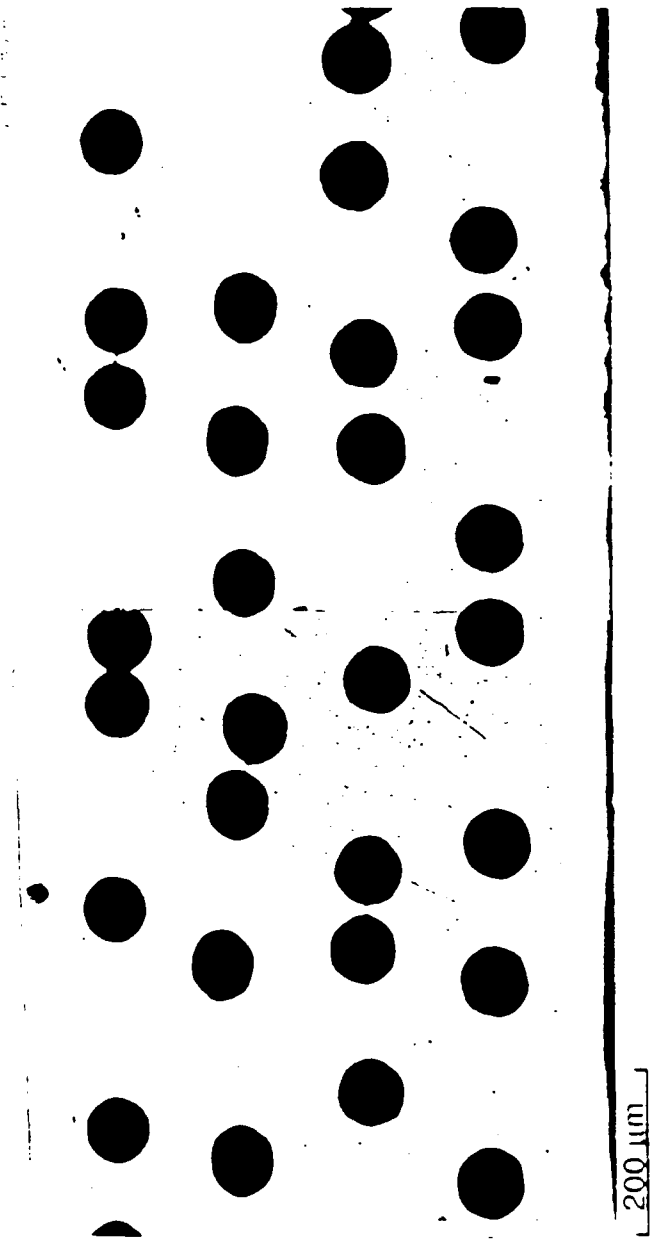
Nimmer, R. P., Baukert, R. J., Russell, E. S., Smith, G. A., and Wright, P. K.,
"Micromechanical Modeling of Fiber-Matrix Interface Effects in Transversely Loaded
SiC/Ti-6-4 Metal Matrix Composites," *ASTM J. Composites Technology and Research*,
Vol. 13(1), 1991, pp. 3-13.

Revelos, W. C., and Smith, P. R., "Effect of Environment on the Thermal Fatigue
Response of a SCS-6/Ti-24Al-11Nb Composite," *Met. Trans. A* , Vol. 23A, 1992, pp.
587-595.

Figure Captions

1. Sections of the SCS-6/super α_2 composite used in the study.
2. Sapphire/super α_2 composite with Ta coating.
3. Stress-strain curves of : (a) SCS-6 fiber composite, (b) sapphire fiber composite.
4. Illustration of the damage mechanisms in the SiC-fiber composite.
5. Calculations involving the residual field along the interface.
6. Geometry of the model used to determine fiber interaction of closely spaced fibers.
7. Matrix stresses at the interface as a function of fiber spacing.
8. Comparison of the hoop stress at the locations of parallel and transverse cracks.
9. Matrix stresses at the interface as a function of fiber spacing for perfect bonding and sliding.
10. Schematic diagram illustrating the damage mechanisms observed during transverse loading.





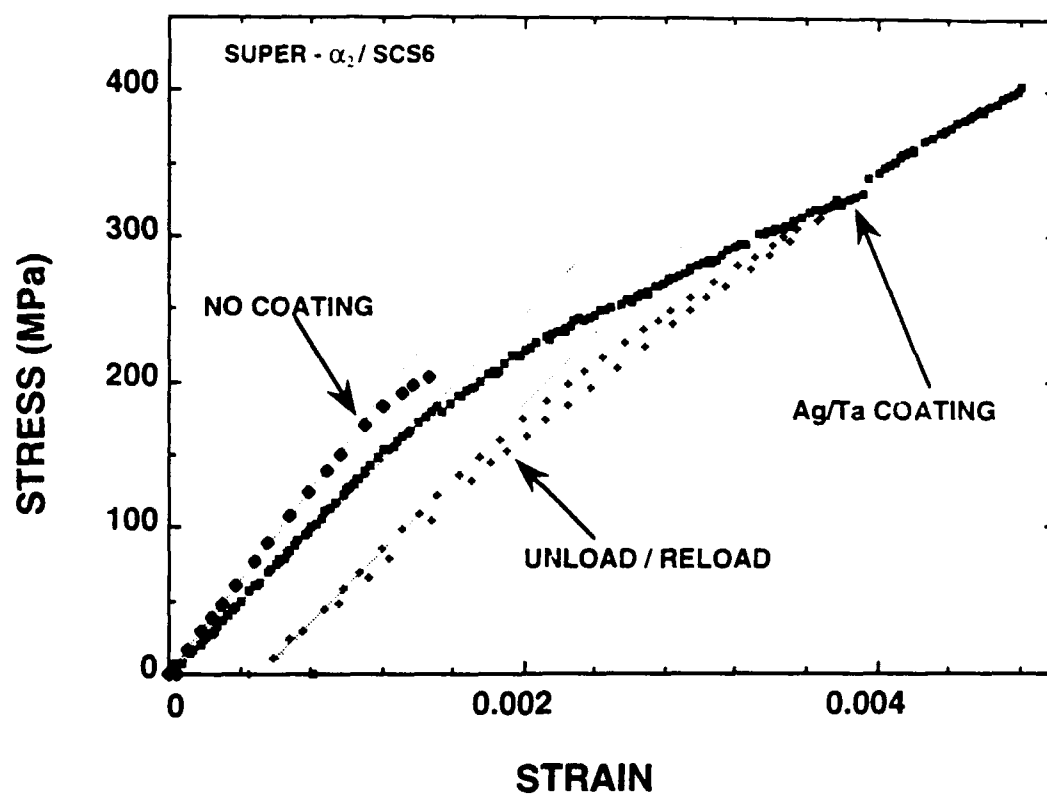


Fig. 311

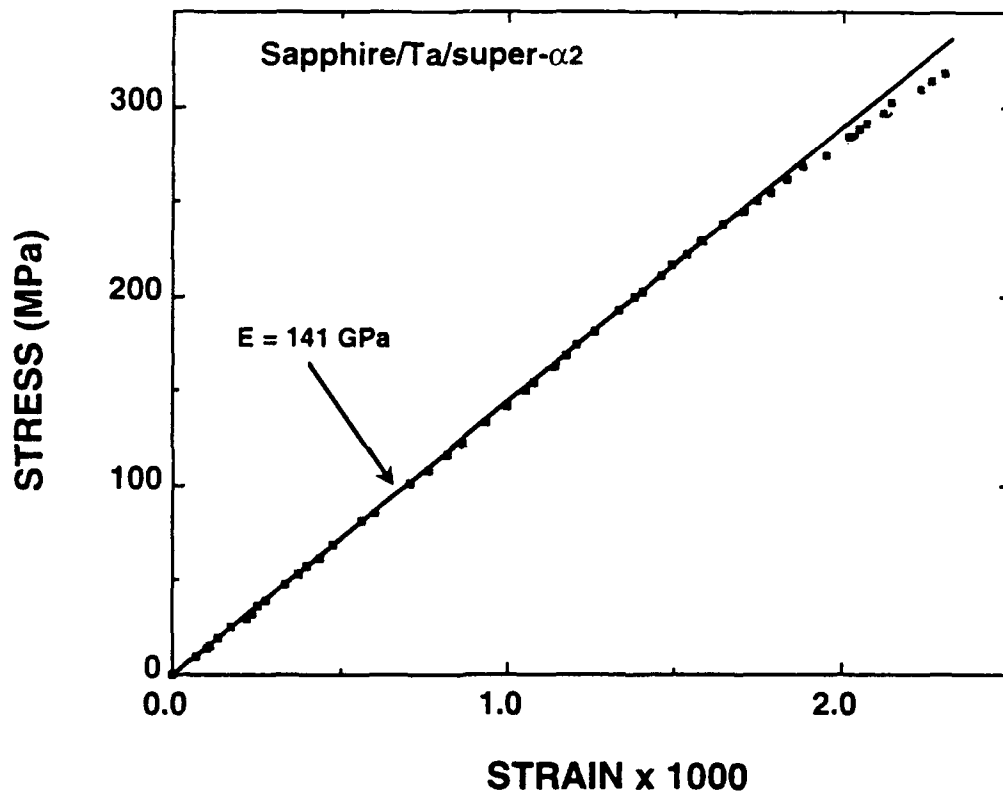
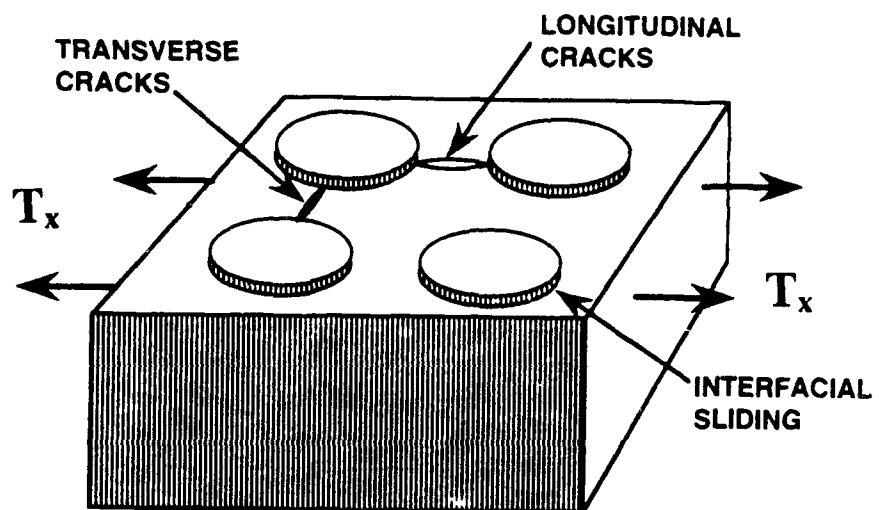
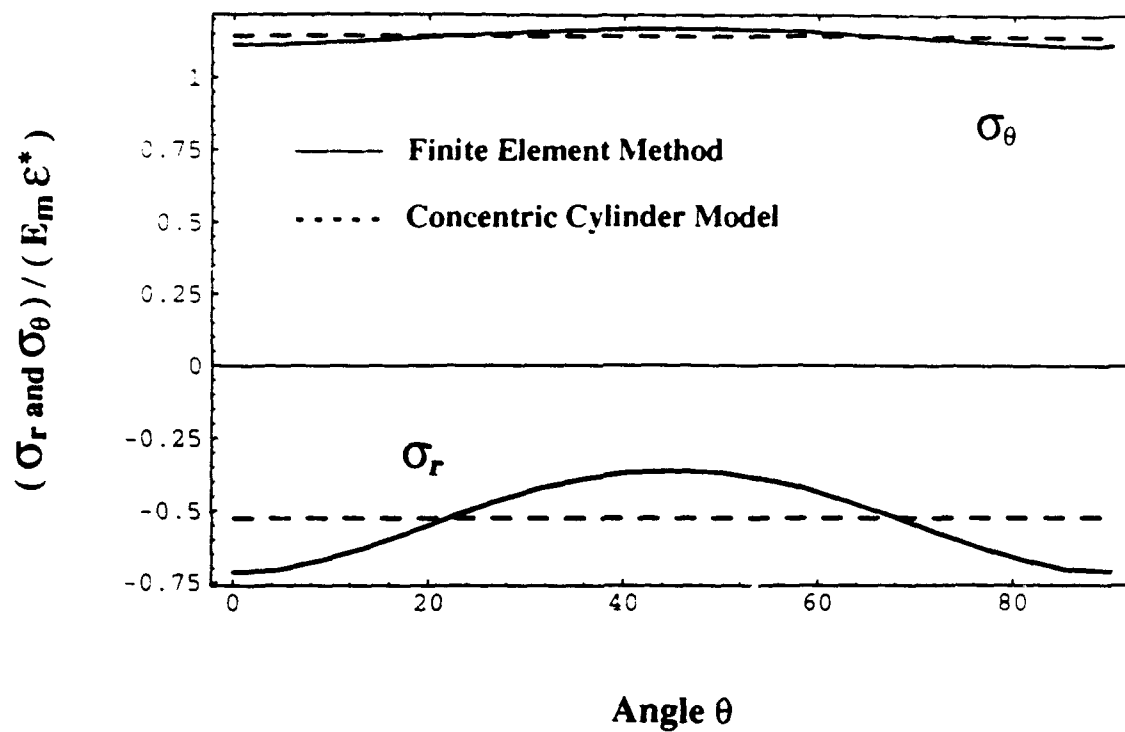


Fig. 5.20





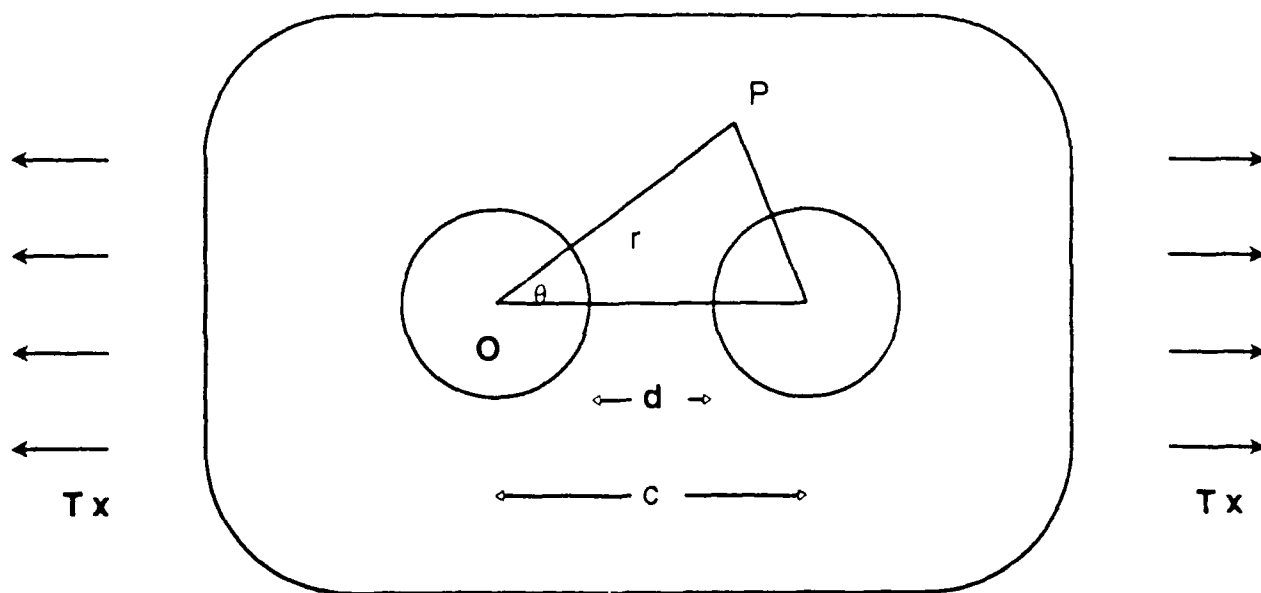
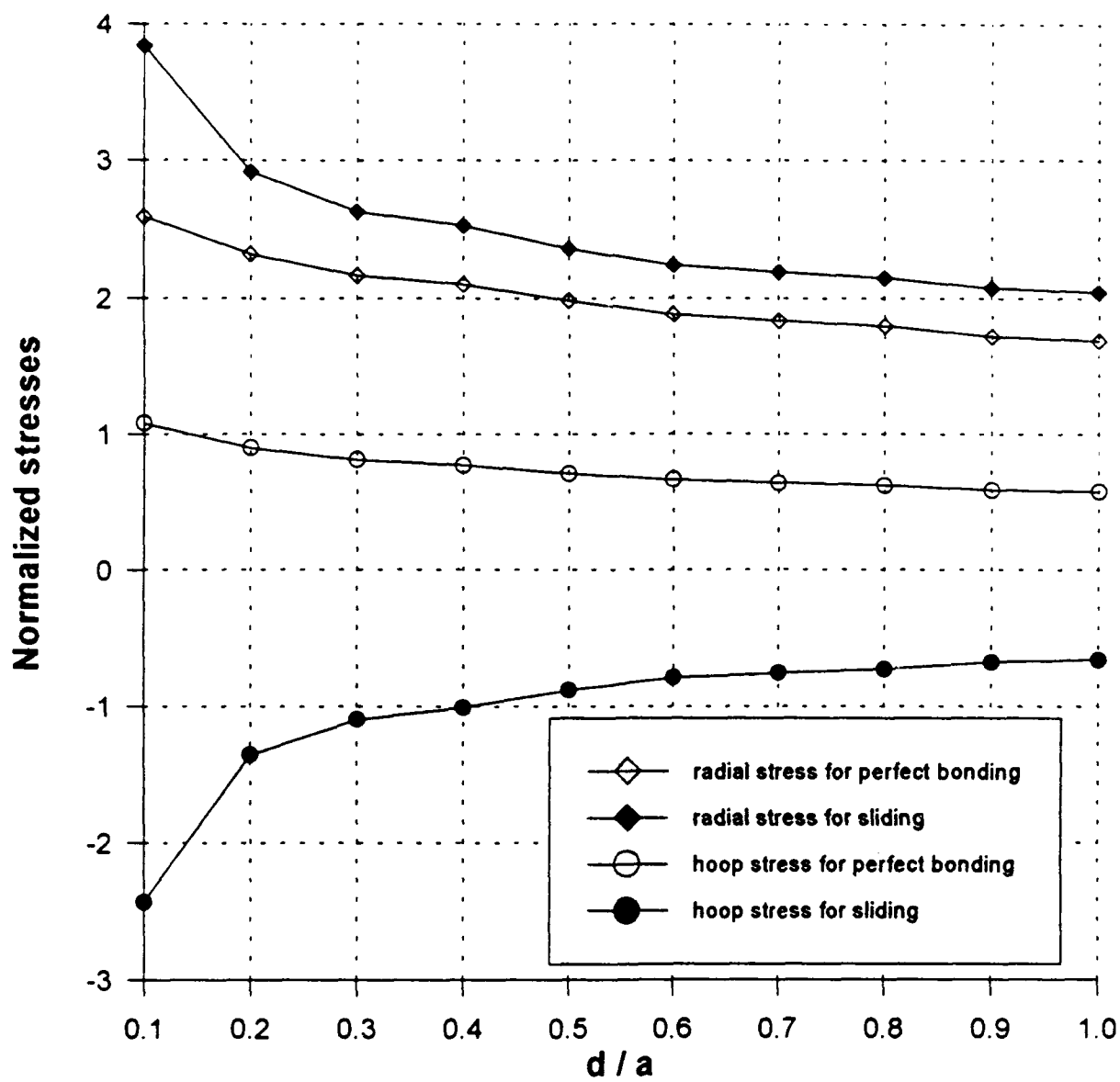
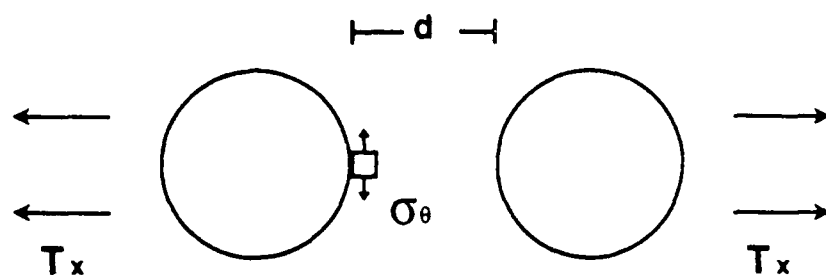
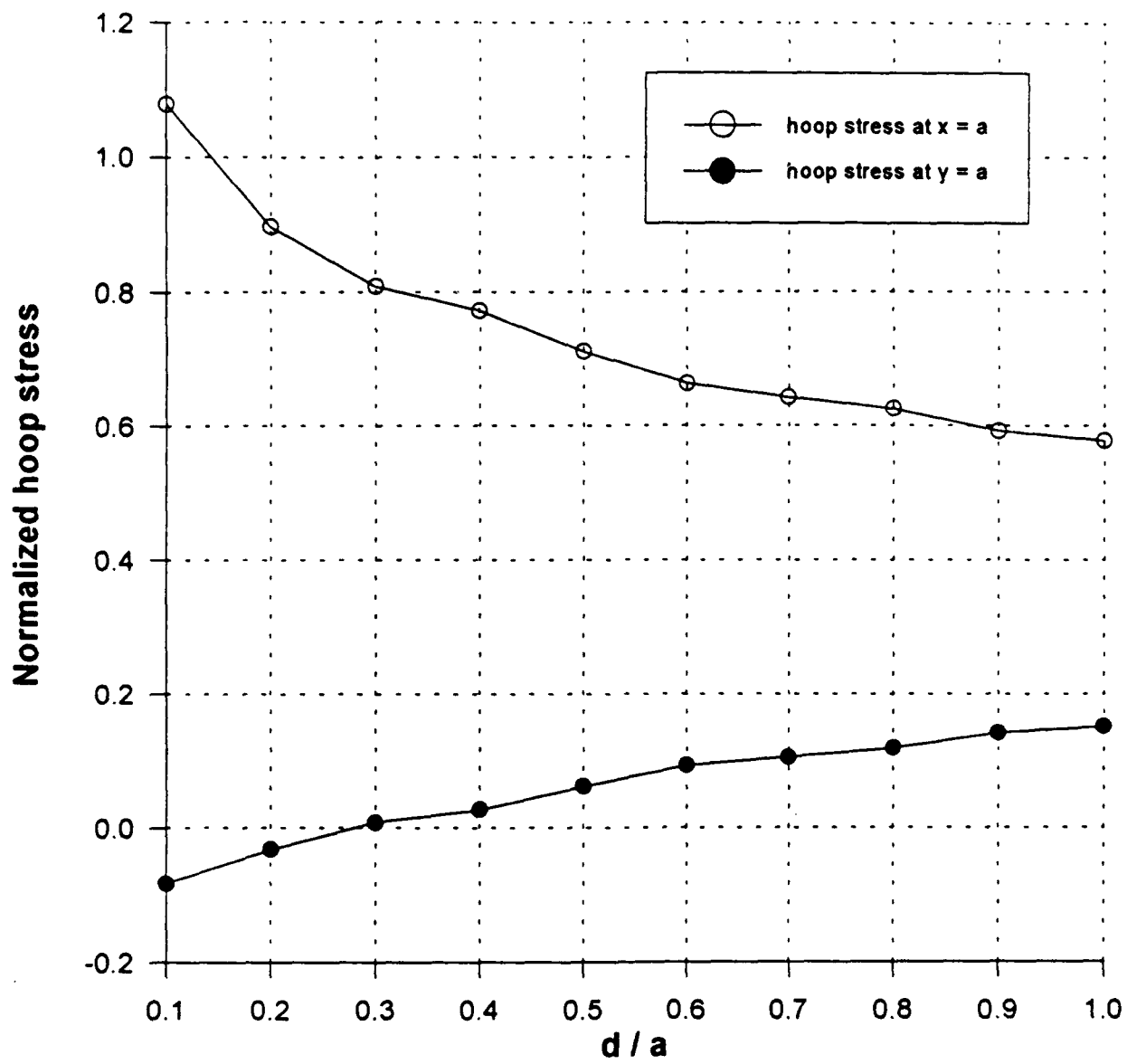
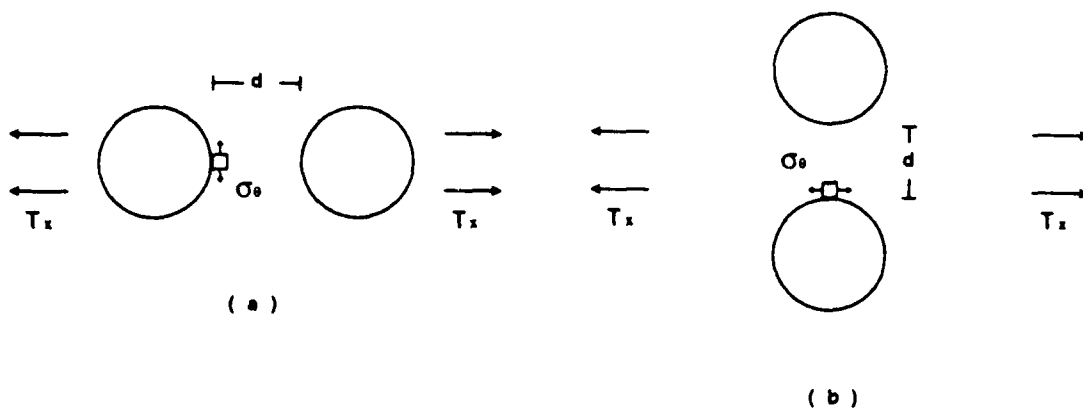
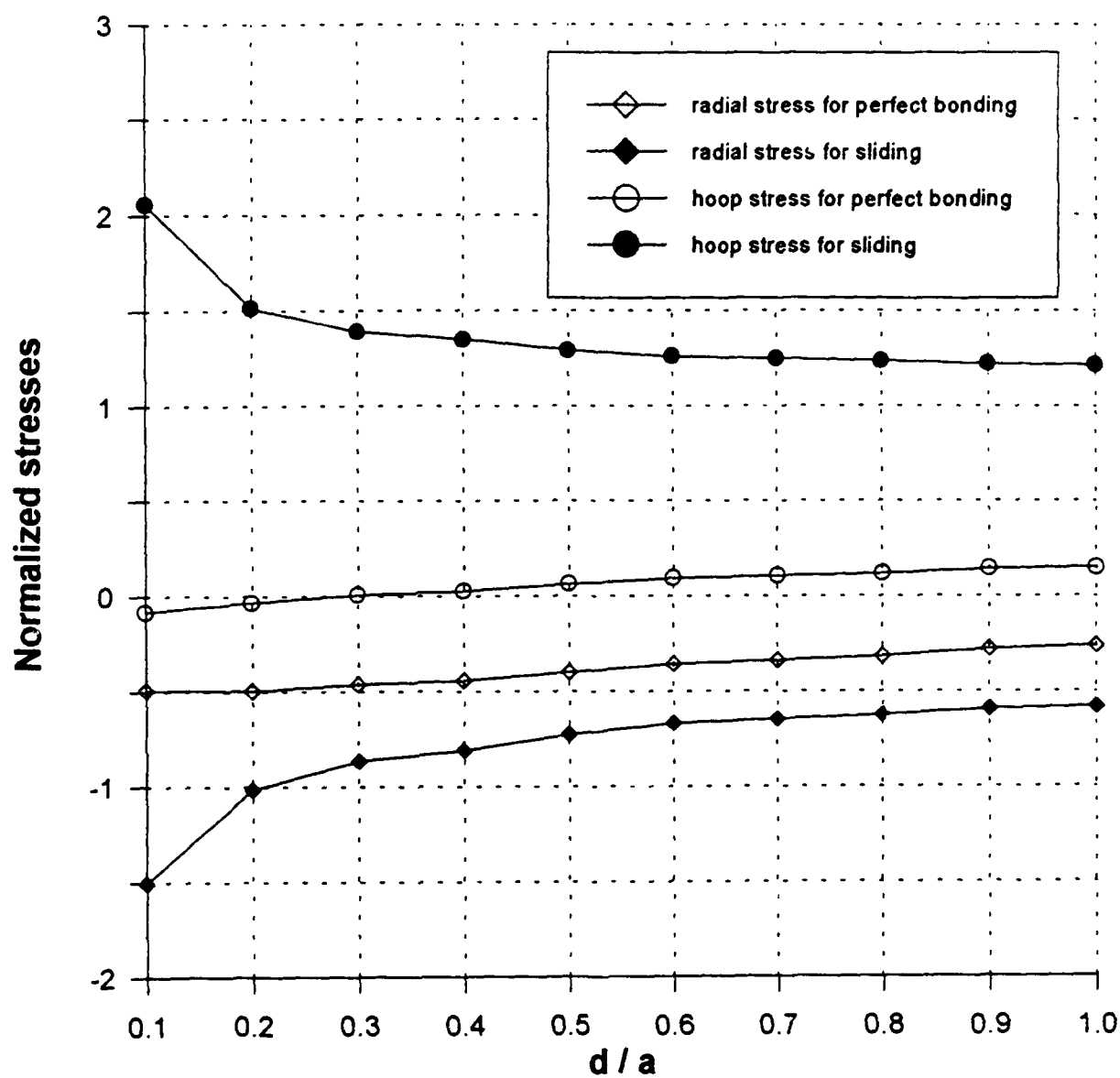
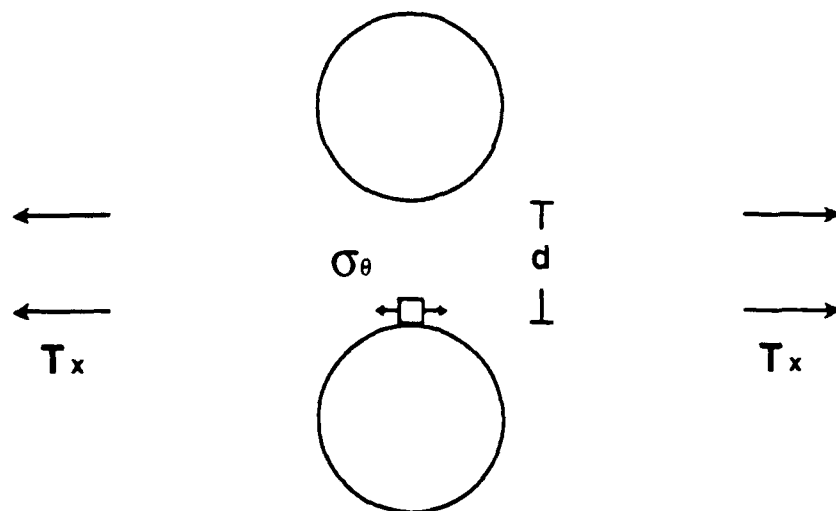
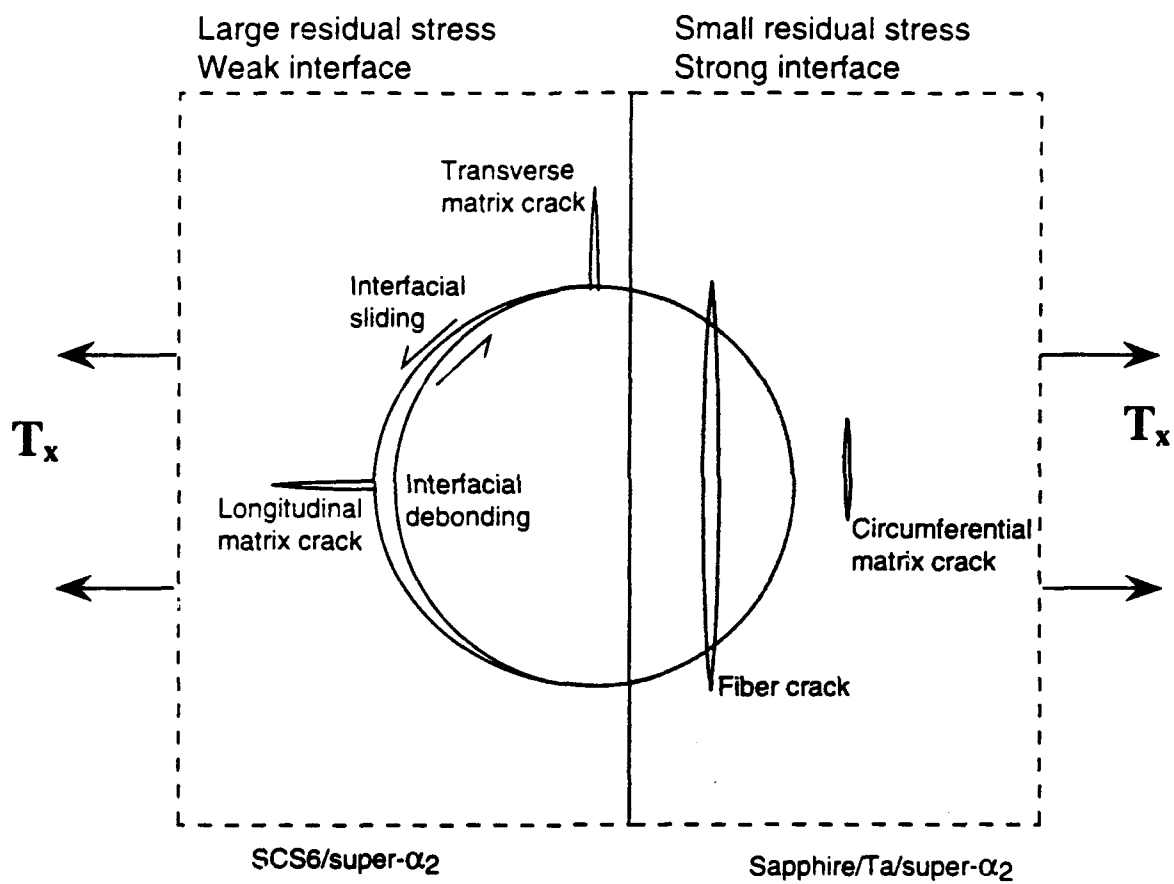


Fig. 2









5.2 Transverse Strengths and Failure Mechanisms in Ti3Al Matrix Composites

submitted for publication in Acta Metallurgica

TRANSVERSE STRENGTHS AND FAILURE MECHANISMS IN Ti_3Al MATRIX COMPOSITES

D.B. Marshall, W.L. Morris, B.N. Cox, J. Graves and J.R. Porter
Rockwell International Science Center
1049 Camino Dos Rios
Thousand Oaks, CA 91360

D. Kouris
Department of Mechanical and Aerospace Engineering
Arizona State University
Tempe, AZ 85287-6106

R.K. Everett
Naval Research Laboratory
Washington, DC 20375-5343

ABSTRACT

Transverse mechanical properties have been measured, and damage mechanisms identified, in three Ti_3Al matrix composites with different interface compositions and residual stress states. Two of the composites contained SiC fibers with weak interfaces. Large improvements in transverse strength and rupture strain were found in one of these composites, in which brittle reaction products in the matrix around the fibers had been avoided by coating the fibers with Ag and Ta before consolidation. The third composite contained sapphire fibers that were strongly bonded to the matrix. Different damage mechanisms were observed in the strongly and weakly bonded composites. Insight into the damage mechanisms and their dependence on residual stress fields and interface properties is gained from comparison of the observations with analytical solutions of elastic stresses. The conditions for optimum transverse properties are discussed; the results indicate that strong interfacial bonding does not necessarily lead to optimum transverse strength of the composite.

1. INTRODUCTION

The reinforcement of titanium aluminides by unidirectionally aligned high strength SiC fibers leads to improved mechanical properties under loading parallel to the fibers. However, this gain is at the expense of properties in the transverse direction: the strength and strain to failure, as well as resistance to fatigue crack growth, are generally much lower under loading normal to the fibers than under loading parallel to them.¹⁻⁵ Although certain components can be designed with the fibers parallel to the maximum tension, complete avoidance of transverse loads is usually not possible. Therefore an understanding of factors controlling transverse properties is needed.

This study identifies some of the factors that control transverse strength and rupture strain under monotonic loading. In situ observations are used to reveal mechanisms of damage that precede and lead to failure of several composites with various interfacial compositions and with fibers of different thermal expansion properties. By relating the observed damage mechanisms to relatively simple analytical stress fields, progress is made in understanding the influence of interfacial strength and residual stresses on transverse properties.

2. EXPERIMENTS

Failure mechanisms under transverse loading were investigated in three composites with nominally identical matrices, but different fibers and interfacial compositions. The matrix material was a two-phase (α_2 - β) Ti-25Al-10Nb-3V-1Mo alloy (super α_2). Two of the composites contained CVD SiC fibers (SCS-6, Textron Specialty Materials) with several carbon-rich outer layers. Both were consolidated by Textron using a foil/fiber/foil method, one containing three rows of fibers without any additional fiber coatings and the other containing four rows of fibers that had been coated with Ag and Ta (several microns thickness) by a PVD method before consolidation. The final volume fractions of fibers were 0.37 and 0.30, respectively.

To allow investigation of interfacial bond strengths that are higher than those limited by the weak carbon layers in the SCS-6 SiC fibers, a third composite containing sapphire fibers was fabricated. A layer of tantalum was introduced at the interface to prevent reaction between the fibers and matrix. The Ta coating was applied to the fibers[†] by PVD (at NRL) and the composite was consolidated (at Rockwell) using the foil/fiber/foil method, with four layers of fibers giving a volume fraction of 20%. Cross-weave material was not used during fabrication. Since the thermal expansion coefficients of Al₂O₃ and super- α_2 are similar ($\sim 8 \times 10^{-6} \text{ }^\circ\text{C}^{-1}$), residual stresses in this composite are expected to be much smaller than in the SiC fiber composites, in which the fibers have a lower thermal expansion coefficient (4.5×10^{-6}) than the matrix.⁶

Beams with dimensions $\sim 50 \times 2 \times 1$ mm were cut from the composite sheets with the longest dimension normal to the fibers. The beams were polished on the sides containing the fiber ends and loaded in tension using a fixture attached to the stage of an optical microscope. High magnification micrographs were obtained from the polished sides of the beams during loading. The applied loads were measured with a load cell and the corresponding strains were measured using strain gages attached to the sides of the specimens (in most cases, two strain gages on opposite sides of the specimen).

Some of the in situ optical micrographs were analyzed using a high resolution strain mapping technique.^{7,8} This involved comparing images taken before and during loading and measuring relative displacements of corresponding image features. Measurements were obtained either stereoscopically or using a computerized image analysis system (HASMAP - High Accuracy Strain Mapping), both of which provide sensitivity of ~ 10 nm in differential displacement measurements from optical micrographs. The image analysis was improved in some cases by depositing MgO crystals on the surface of the specimen to provide additional sharp image detail.

[†] Manufactured by Saphikon.

3. RESULTS

3.1 Composite Microstructures

Micrographs of the cross sections from the two SiC fiber composites are shown in Figs. 1(a) and (b). The composite with uncoated fibers contained a thin reaction layer ($\sim 1 \mu\text{m}$ thickness) of carbides and silicides surrounding the fibers.⁹ This reaction layer was not present in the composite containing fibers that had been coated with Ag and Ta. However, the matrix in the composite with Ag-Ta layers was enriched in the β -phase within a distance of $\sim 10 \mu\text{m}$ from each fiber.

An optical micrograph of a cross section of the sapphire fiber composite is shown in Fig. 1(c). Movement of the fibers occurred during consolidation, although most fibers remained well spaced. Most fibers have a rounded hexagonal cross section. Observation of longitudinal sections indicated that most fibers were broken during consolidation into two or three pieces within the 50 mm lengths of composite. These breaks did not affect the transverse loading experiments described below. The typical transverse test specimen of $\sim 2 \text{ mm}$ thickness contained ~ 10 broken fibers, which could be readily identified; and failure was never observed to initiate from the fiber breaks. The broken fibers were identified by viewing the surface in reflected polarized light with an analyzing polarizer set at 90° . Fibers that were intact through the entire section appeared black, whereas fibers that contained fractures appeared bright because of internal reflections which changed polarization and allowed light to pass through the analyzer.

In the sapphire fiber composite, the Ta coatings on most fibers were continuous with uniform thicknesses of $\sim 1 \mu\text{m}$ (Fig. 2). Surrounding each fiber was a layer of matrix of $\sim 5 \mu\text{m}$ thickness in which the β phase was depleted. Otherwise, there was no evidence of reaction among the matrix, coating, or fiber. However, there were occasional small regions where the coating was missing (Fig. 3), typically on several fibers within a cross section containing approximately 400 fibers. These bare patches may have been caused by spalling due to residual stress or fiber

handling. In these regions, dissolution of the fiber into the matrix had begun during consolidation. This observation demonstrates the importance of the Ta coatings in protecting the fibers. However, the small regions of missing coating did not appear to act as initiation sites for damage in the transverse tension experiments described below.

The uniformity of the β -depleted zone around each fiber suggests that the β -depletion is associated with the fully coated fiber rather than being due to the occasional small region in which the coating was missing. This is puzzling since any diffusion of Ta from the coating into the matrix would lead to stabilization of the β phase. The only apparent source of β depletion is oxygen, either from the Ta coating or from the Al_2O_3 fiber via diffusion through the Ta coating. The Ta coating was deposited in a high-purity argon atmosphere (5×10^{-3} torr) that was introduced into the deposition chamber after evacuating it to $\sim 10^{-7}$ torr. Therefore, a large amount of oxygen would not be expected in the coating. However, there is insufficient information about the amount of oxygen needed to stabilize the α_2 phase in this region to distinguish these two possibilities.

3.2 Stress-Strain Response

The transverse stress-strain curves for the SiC fiber composites (obtained from strain gage data and measured loads) are compared with the longitudinal stress-strain curve of the composite with uncoated fibers (from Ref. 5) in Fig. 4(a). The stresses and strains at failure are much smaller in transverse loading than in longitudinal loading. The SiC fiber composite that contained Ag-Ta fiber coatings exhibited the better transverse properties, with failure stress and strain larger by factors of 2 and 3, respectively, than for the composite containing uncoated SiC fibers (Fig. 4(b)). The transverse failure stress and strain of the sapphire-fiber composite fell between those of the two SiC fiber composites (Fig. 4(c)).

All of the stress-strain curves are linear at low loads but nonlinear at high loads. The low load regions are elastic, as confirmed by unload-reload cycles. Young's modulus for the SiC

composite under longitudinal loading (from the low-load region) is 200 ± 10 GPa. This value, with the rule-of-mixtures expression

$$E = f E_f + (1 - f) E_m \quad (1)$$

where f is the volume fraction of fibers, E , E_m and E_f are the Young's moduli for the composite, matrix and fibers, has been used to evaluate E_m ; with independently measured values $E_f = 414$ GPa and $f = 0.37$, the result $E_m = 80 \pm 7$ GPa was obtained.⁶ There is, however, some uncertainty in the Young's modulus of the matrix, for large variations (up to 30%) with textural anisotropy have been observed.⁶ Reported measurements in monolithic alloy fall in the range 90-120 GPa.^{10,11} The measured transverse Young's moduli for all of the composites are compared with the predicted upper and lower bounds of Hashin¹² in Fig. 4(d) with various assumed values of E_m (calculations for isotropic matrix and fibers). For both of the SiC fiber composites, the results are consistent with $E_m \approx 90$ GPa, whereas the result for the sapphire fiber composite suggests a higher value ($E_m = 110$ GPa). This difference could be related to differences in texture in the matrices, since the matrix foils originated from different lots of material.

The stress-strain curves became nonlinear at applied stresses above 180 MPa for both of the SiC fiber composites and 270 MPa for the sapphire fiber composite. The extent of nonlinear strain before failure was substantially larger in the composite containing Ag-Ta-coated SiC fibers than in the other two composites. The response of this composite during an unload-reload cycle that began from the nonlinear region is shown in Fig. 4(b)). The initial slope of the unloading curve is lower (100 GPa) than that of the initial loading curve. However, the reloading curve is approximately bi-linear with slope at stresses below ~ 180 MPa equal to the slope of the initial loading curve. This response is similar to that reported by Johnson et al³ and Nimmer et al¹³ for several other titanium-aluminide/SCS-6 composites, and is consistent with their interpretation of the change in slope at stress of 180 MPa during reloading being due to separation of the fiber-matrix interface. Direct evidence supporting this hypothesis is presented below.

3.3 In Situ Observations of Damage During Transverse Loading

SiC Fiber Composites

The types of damage observed prior to failure of the SiC-fiber composites during in situ experiments are illustrated schematically in Fig. 5. The first damage to occur was sliding of the fibers relative to the matrix in a direction normal to the specimen surface, driven by the residual axial stresses in the fibers and matrix (compressive in the fibers, tensile in the matrix). Sliding was first evident in conventional optical observations as phase contrast due to the height difference of the fiber surface and the surrounding matrix, which gives rise to a dark fringe at the interface. The sliding displacement increased with increasing applied stress, and at high stresses was detectable from the difference in focus positions of the fiber and matrix. The occurrence of sliding was also confirmed by optical interference microscopy and scanning electron microscopy. Sliding began at applied stresses of 40 MPa in the composite with uncoated fibers and 60 MPa in the composite with coated fibers. After unloading the composites, the fibers remained protruding from the surface. Scanning electron micrographs of fibers in fractured test pieces are shown in Fig. 6: the residual displacement is larger in the composite containing Ag-Ta coated fibers ($\sim 2 \mu\text{m}$) than in the composite containing uncoated fibers ($0.5 \mu\text{m}$) because of the higher failure stress of the former (Fig. 2).

A map of in-plane surface distortions at an applied load of 160 MPa in the composite with uncoated fibers is shown in Fig. 7. The arrows superimposed on the optical image are relative displacement vectors for corresponding image features located at the beginnings of the arrows within a reference micrograph at zero load and a second micrograph of the same area with the load applied. (The magnitudes of the displacement vectors are magnified by a factor of 40 compared with the dimensions on the micrograph.) The following deformations are evident: tensile strains parallel to the applied load; Poisson's contraction from top to bottom of the micrograph; debonding

and rotation of the right-hand fiber; and tensile strains in the matrix between the fibers in the direction normal to the applied stress.

Tensile separation of the fiber-matrix interfaces was observed in the stress ranges of 120-170 MPa in the composite with uncoated fibers and 150-180 MPa in the composite with Ag-Ta coated fibers. The locations of interfacial separation differed in the two composites: in the composite containing uncoated fibers, most fibers (~ 70%) separated between the outer C/SiC coating of the fiber and the reaction layer in the matrix; whereas in the composite with Ag-Ta-coated fibers, most (~ 85%) separation took place at the carbon layer between the outer C/SiC coatings of the fiber. The remaining fibers in both composites were debonded at both of these locations. The stress at which separation occurred was determined more accurately than could be done from single micrographs by making use of the differential strain mapping technique described in Section 2. This was done by measuring the changes in separation of two image features on either side of the interface in a series of micrographs obtained at increasing load. A plot of the relative displacements as a function of applied load then revealed the separation stress by extrapolation to zero displacement. The separation loads determined in this manner varied from fiber to fiber over the ranges indicated above; a correlation between separation load and the proximity of neighboring fibers was not found.

The first observable damage in the matrix was highly localized deformation in the regions between closely spaced fibers within the same row (i.e., located along a line parallel to the applied stress and normal to the tensile strains observed in Fig. 7). This deformation was first observed at an applied stress of 100 MPa in the composite with uncoated fibers and 128 MPa in the composite with Ag-Ta-coated fibers. At higher loads (150 MPa and 180 MPa) cracks formed in some of these regions on planes parallel to the applied load. These cracks, hereafter referred to as "load-axis cracks," initiated adjacent to the fibers and grew stably between the fibers with increasing load (Figs. 8(a)-(d). At closely spaced fibers (separation $\leq 20 \mu\text{m}$) a pair of load-axis cracks usually formed (Fig. 8(d)), symmetrically displaced from the center line between the two fibers by about

10° (relative to the centers of the fibers). By the time failure occurred, load-axis cracks had formed at about 30% of the fibers in both composites, mostly at fibers that were relatively closely spaced ($\leq 70 \mu\text{m}$).

In the composite containing uncoated fibers, transverse cracks (on radial planes normal to the applied stress) formed at stresses above $\sim 160 \text{ MPa}$. These cracks initiated in the reaction layers adjacent to the fibers (Fig. 9) and grew stably with increasing load across the regions between pairs of fibers. Such cracks eventually formed at approximately 20% of the fibers. Failure of the composite occurred by the linking of transverse cracks and previously debonded interfaces across the specimen; a sequence of in situ micrographs showing development of these cracks leading to failure is shown in Fig. 10.

Stable transverse cracks were not observed prior to failure in the composite containing fibers coated with Ag-Ta, even though the applied stress at failure was more than double that of the composite with uncoated fibers. Instead, failure occurred suddenly, leaving a fracture surface that linked a series of debonded fibers across the specimen.

Sapphire Fiber Composite

In situ observations revealed the sequence of damage prior to failure as shown in Fig. 11, in which the micrographs (a), (b) and (c) were taken at the loads indicated in Fig. 4(c). The first damage, which coincided approximately with the onset of nonlinearity of the stress-strain curve, was in the form of cracks in the fibers, oriented normal to the applied load. With continued loading, similar cracks formed in larger numbers of fibers and extended into the matrix. Cracks also formed within the matrix near the edges of the β -depleted zones surrounding the fibers (Fig. 11(b)). Failure resulted from linkage of cracks in and near adjacent fibers, as shown in Fig. 11(c). At the failure point, approximately 20% of the fibers within the test section contained cracks, and another 20% had cracks in the adjacent regions of matrix.

Several observations indicate that the strength of the fiber/matrix interface is high in this composite and that interfacial debonding or plasticity was not a factor in the failure process under tensile transverse loading. The first observation is that the cracks in the fibers penetrated into the matrix without any sign of deflection or offset at the interface, even when the cracks were inclined to the interface (Fig. 12). The absence of interaction between the crack and the interface is seen also on the fracture surface (Fig. 13). The second observation is that circumferential matrix cracks formed in the matrix parallel to, and about 10 μm from, the interfacial regions that were subject to the maximum tensile stress; while no debonding was observed at the interface.

4. DISCUSSION

The damage mechanisms that preceded failure in the three composites are summarized schematically in Fig. 14. In the sapphire-fiber composite, in which residual stresses were small and the fiber-matrix interfaces were strongly bonded, cracking of the fibers and circumferential matrix cracking (both normal to the applied stress) occurred prior to failure. In the SiC-fiber composites, which had large residual stresses and weakly bonded fiber-matrix interfaces, a different sequence of damage development was observed: (1) sliding of the matrix and fibers normal to the specimen surface that contained the exposed fiber ends (driven by the residual stresses); (2) formation of radial cracks in the matrix parallel to the applied load ("load-axis cracks"); (3) separation of the fiber-matrix interface; and (4) in the composite without Ag-Ta fiber coatings, formation of transverse radial cracks in the matrix. Failure occurred by linking of transverse radial cracks and debonded interfaces of adjacent fibers.

4.1 Stresses

Some qualitative and semi-quantitative insight into these damage mechanisms can be gained from relatively simple analytical solutions for elastic stress fields. The elastic stress field within a composite loaded transversely by uniform remote stress is given by the sum of the applied stress, a

perturbation on the applied field due to the "elastic inhomogeneity" of the fibers and the residual field due to the misfit strain, e^T , between the fibers and matrix (difference in thermal contraction of fibers and matrix). The use of elastic solutions is justified by the observed linearity of the stress-strain curves, at least up to the initiation of the damage being considered. A significant amount of nonlinearity was evident only in the composite containing Ag-Ta-coated SiC fibers, and this occurred after the initiation of the load-axis cracks.

4.1.1 Residual Stresses

The residual hoop stresses near the fiber-matrix interface, where damage initiated in the SiC fiber composites, are closely approximated by the concentric cylinder solution. Typical errors involved in this solution are less than $\sim 3\%$ for a regular array of fibers, as exemplified by the comparison in Fig. 15 of the concentric cylinder solution with a finite element solution for a square array of fibers (corresponding to the SiC-fiber composite without Ag-Ta coatings, with volume fraction of fibers $= f = 0.37$, $E_f/E_m = 5$, $\nu_f = \nu_m = 0.3$, and isotropic misfit strain, e^T). The errors in the normal interfacial stresses are larger, although the average value from the finite element analysis is within $\sim 0.5\%$ of the concentric cylinder solution.

The magnitudes of the residual stresses in both of the SiC-fiber composites have been deduced previously from measurements of the relaxation of the fibers following removal of the matrix by etching.^{14,15} The residual stresses thus calculated using the concentric cylinder analysis and assuming an isotropic misfit strain, e^T , are listed in Table 1. The presence of Ag-Ta layers did not alter the residual stresses, as shown by the misfit strains being equal in the two composites: the differences in residual stresses in Table 1 arise solely from the different volume fractions of fibers in the two composites. The frictional stresses that resist interfacial sliding are also listed in Table 1. These were evaluated from measured forces and displacements during single fiber pulling experiments.^{14,15}

Table 1
Residual Stresses and Frictional Sliding Resistance (from refs. 14, 15)

Composite	Measured Relaxation ϵ_f	Misfit Strain ϵ^T	Normal Interface Stress σ_r^R (MPa)	Tangential Interface Stress σ_t^R (MPa)	Axial Fiber Stress σ_f^R (MPa)	Interface Sliding Resistance τ_o (MPa)
Super- α_2 /SCS6	0.00156	0.00610	-260	565	-800	70
Super- α_2 /Ag-Ta/SCS6	0.00203	0.00611	-300	557	-1020	100

4.1.2 Applied Stresses

Stresses in the vicinity of an isolated, strongly bonded fiber, due to a remotely applied uniform stress, σ_a , are shown in Fig. 16. The local perturbation of the applied stress due to the fiber is dependent on the ratio of the elastic moduli of the fibers and matrix:¹⁶ the results in Fig. 16 correspond to $E_f/E_m = 5$ and $\nu_f = \nu_m = 0.3$. The sign of the perturbation field for this combination of properties (fiber stiffer than matrix) is opposite to that for a hole (or more generally, a fiber with lower stiffness than the matrix); the tangential perturbation stress is tensile at $\theta = 0$ and compressive at $\theta = 90^\circ$. The strains associated with this tensile transverse stress at $\theta = 0$ are evident in the measured displacement map of Fig. 7. The perturbation field is concentrated mainly within an area about one fiber radius from the edge of the fiber. Therefore, the single fiber solution would be expected to be a reasonable representation of the stress fields in a composite with fibers spaced by more than double this value. For a square array of fibers, this corresponds to $f = 0.2$.

Several features of the superimposed residual and applied fields for the isolated fiber may be correlated in a preliminary way with the observed damage. In a composite with small residual stresses and strongly bonded interfaces, the largest tensile stress is the radial component at $\theta = 0$ (i.e., $\sigma_r(0)$ in Fig. 16(b)), consistent with the observed circumferential matrix cracking in the sapphire fiber composite. It is noteworthy, but perhaps coincidental, that $\sigma_r(0)$ is maximum at a

position $\sim 0.2R$ (R = fiber radius) away from the interface, where the matrix cracking occurred. In composites with residual stresses due to thermal misfit strains, compressive radial and tensile hoop stresses are superimposed onto the stresses of Fig. 16, thus favoring a change in damage mechanism from circumferential to radial cracking, as observed in the SiC fiber composites. In this case, the tangential stress is larger at $\theta = 0$ than at $\theta = \pi/2$ (Fig. 17(b)) consistent with the observation of load-axis cracking before transverse cracking in these composites. However, the difference in stresses at these two locations is not large for the isolated fiber.

A more detailed correlation with experimental observations requires account to be taken of interfacial debonding and sliding as well as the interaction effects of near-neighbor fibers that are closer together than average. When the separation of a pair of fibers is smaller than $\sim R$, the elastic inhomogeneity fields overlap. In this case, the resultant field is not a linear superposition of the two fields for isolated fibers. Analytical solutions to this problem for pairs of fibers with the lines joining their centers aligned parallel and normal to the applied stress have been obtained recently by Kouris.¹⁷ These solutions include various interfacial bond conditions, ranging from fully bonded interfaces to interfaces that can slide without restriction. This was achieved by allowing discontinuities in shear displacements but not in normal displacements at the interface, with the shear displacement discontinuity being restricted by springs of various stiffnesses. The stresses relevant to the observed damage, with either of the two limiting cases of completely bonded or freely sliding interfaces, are compared with single fiber solutions in Appendix A. The results indicate that, for fibers separated by $0.85 R$ (corresponding to $f = 0.39$ for a square array), the additional perturbation on the interfacial stresses due to the second fiber is maximum along the line joining the pair of fibers as expected, but that it becomes small at angles larger than $\sim 45^\circ$ from this line. Therefore, the solutions for pairs of fibers provide reasonable approximations for the interfacial stresses around a fiber surrounded by four others in a square array.

The effect of varying the separations of the pertinent pairs of fibers is shown in Fig. 17. As the pairs of fully bonded fibers move closer together, the stress $\sigma_r(0)$ that causes interfacial

separation and circumferential matrix cracking at $\theta = 0$ increases (Fig. 17(a)), the stress σ_θ that causes load-axis radial cracks at $\theta = 0$ increases (Fig. 17(a)), and the stress σ_θ that causes transverse radial cracks at $\theta = \pi/2$ decreases (Fig. 17(b)). Therefore, the propensity for load-axis radial cracks in preference to transverse radial cracks increases as the fiber spacings decrease. In fact, for $d/R \leq 0.3$, the stress driving transverse cracking becomes negative, suggesting that transverse cracking would never occur between such closely spaced fibers during loading if the interfaces were to remain fully bonded. However, large changes occur in all of these stresses if circumferential sliding occurs. The stress driving load-axis radial cracks decreases and becomes compressive for a freely sliding interface, whereas the stress driving transverse radial cracks increases. Therefore, the preference for load-axis cracks over transverse cracks reverses.

4.2 Damage in SiC-Fiber Composites

4.2.1 Axial Fiber Sliding

The observed sliding of fibers relative to the matrix in the direction normal to the specimen surface is driven by the residual axial stresses in the fibers and matrix and is restrained by friction. The frictional stresses are dependent upon the normal stress at the fiber-matrix interface. The applied transverse load generates tensile stress over most of the interface, with only a small region of compression near $\theta = \pi/2$ (Fig. 16(b)). Since the average normal stress is tensile, the resistance to frictional sliding is reduced, thus allowing the residual axial stresses to relax by sliding.

An estimate of the degree of sliding can be obtained by assuming that the sliding resistance, as given by the Coulomb friction law, is proportional to the normal interfacial stress. An approximate shear-lag analysis of fiber sliding (Appendix B) gives an upper bound for the sliding displacement

$$u = \sigma_f^2 \left(\frac{R(1-f)E_m}{4\tau_0 E_f E} \right) \left[\frac{\langle \sigma \rangle / \sigma_R}{1 - \langle \sigma \rangle / \sigma_R} \right] \quad (2)$$

where R is the fiber radius, τ_0 is the frictional stress at the interface in the absence of applied transverse stresses, σ_f is the axial residual stress in the fiber, σ_R is the residual stress normal to the interface, and $\langle \sigma \rangle$ is the average normal tensile stress component at the interface due to the applied load. For isolated fibers in these composites, $\langle \sigma \rangle = 0.65 \sigma_a$ (Appendix 1). With the parameters given in Table 1, the elastic properties given in Section 3, and $R = 70 \mu\text{m}$, the sliding displacements at failure given by Eq. (2) are $0.1 \mu\text{m}$ for the composite containing uncoated fibers and $0.8 \mu\text{m}$ for the composite containing fibers coated with Ag-Ta. These values are reasonably close to the observed values (0.2 and $2 \mu\text{m}$), given that the analysis used to calculate $\langle \sigma \rangle$ holds for an isolated fiber with a bonded interface (see Appendix B). Fiber interaction effects (especially with fibers preferentially aligned in rows parallel to the applied stress) and circumferential sliding would both increase $\langle \sigma \rangle$ and thus increase the sliding displacements.

4.2.2 Interfacial Separation

Interfacial separation began at the same stage during loading as the initial departure from linearity of the stress strain curves (cf. Table 2 and Fig. 4), a correlation that has also been observed in other titanium matrix composites.^{3,13} Moreover, the reloading portion of an unload/reload cycle for the composite with Ag-Ta layers (Fig. 4(b)) is linear over the same stress range and with the same slope as the initial loading curve. This suggests that the tensile strength of the interface is negligibly small (since the stresses for interface separation during the first and subsequent loadings were approximately the same).

A small or zero tensile strength is also inferred from comparison of the loads required for interfacial separation and the residual compressive stresses normal to the interface (Table 2). The residual radial stresses in Table 2 are given as ranges of values that approximately account for fiber interactions: residual radial stresses are more sensitive than the tangential stresses to the proximity

of near-neighbor fibers (Fig. 15). Although the average radial stress is very close to the value calculated from the concentric cylinder model (listed in Table 1), the local stress deviates by up to $\pm 30\%$ from the average value. At the location of interest ($\theta = 0$ in Fig. 15) for the SiC fiber composites (in which the fibers are aligned in rows) the compressive interfacial stress is $\sim 30\%$ larger than the average value. For different fiber arrangements, such as those obtained by distorting the square array used for the FEM calculation of Fig. 15 to parallelograms (which might more accurately describe the distributions in Fig. 1) this difference would be expected to be smaller. On the other hand, for fibers that are closer together than average it would be larger. Therefore a reasonable estimate for the range of residual stresses that must be overcome to allow interfacial separation would be from the concentric cylinder values given in Table 1 to values $\sim 30\%$ larger. The applied load contributes interfacial stresses that are approximately double the applied stress (Fig. 17). At the observed separation loads from Section 3.3, these values are close in magnitude to the estimated residual stresses (Table 2), thus implying negligible tensile strengths of the interfaces.

Separation of the interfaces under transverse loading occurred at different locations in the two composites: between the outer layer of the fiber and the reaction products in the matrix of the composite containing uncoated fibers, and within the carbon layer beneath the outermost SCS-6 layers of the fibers in the composite containing Ag-Ta coated fibers. The same failure locations were observed previously for single fiber pullout experiments,¹⁴ which involve Mode II loading rather than tension. These results indicate that the Ag-Ta layers adhere to the outer surface of the fibers more strongly than do the reaction products in the composite without Ag-Ta coatings. However, the overall response of the interfacial region to shear or tensile loading is not greatly affected by the Ag-Ta layers because of the availability of alternative weak interfaces within the SCS-6 layers of the fibers.

4.2.3 Radial Cracking

The local stresses at which load-axis radial cracking initiated can be estimated from the results in Figs. 16 and 17. For fibers with bonded interfaces and spacings smaller than $\sim R$ (corresponding to the range of spacings for which such cracking was observed), the pertinent local stress due to the applied load lies between about $0.6 \sigma_a$ and $1.1 \sigma_a$ (Fig. 17(a)). With the measured applied loads for cracking and the residual stresses σ_0^R from Table 1, the following local initiation stresses are calculated: 655-730 MPa for the composite without fiber coating and 670-750 MPa for the composite with Ag-Ta fiber coatings (Table 2).

A similar estimate for the local stress responsible for transverse radial cracking in the composite containing bare fibers (recall that transverse cracking was not observed before failure in the other composite) gives values in the range 550 to 600 MPa for a bonded interface (stresses due to applied load range from $0.1 \sigma_a$ to $0.2 \sigma_a$ from Fig. 17(b)). Thus, even though transverse cracking initiated at a higher applied load than did load-axis cracking, the calculated local stress, assuming a bonded interface, was smaller for the transverse cracks. Since both types of radial cracks would be expected to initiate at the same value of local stress, these calculations suggest that circumferential sliding may have occurred after the onset of load-axis cracking, thereby increasing the local stress that causes transverse cracking. For a freely sliding interface this stress would be ~ 750 to 880 MPa (Table 2).

The mechanics of circumferential sliding is complex because of the variation in interfacial shear stress around the interface (see Fig. A1(c)). Nevertheless, the following crude estimate confirms that some sliding would be expected at the applied load that caused transverse cracking. In the bare-fiber composite, the interfacial sliding resistance measured by fiber pulling experiments is $\tau_0 \approx 70$ MPa (Table 1). At the applied stress of 160 MPa, where transverse cracking initiated, the interfacial shear stress exceeds τ_0 over a substantial fraction of the interface: between the angles of 20° and 70° (Fig. A3). In the composite with Ag-Ta fiber coatings, τ_0 is larger (~ 100 MPa)

implying that the applied stress required for the interfacial shear stress to exceed τ_0 over the same angular range and thus cause equivalent sliding is correspondingly larger (240 MPa).

4.2.4 The Role of the Ag-Ta Fiber Coating

The presence of Ag-Ta coatings on the fibers had a large effect on the transverse properties of the composite: the failure stress was increased by a factor of 2 (from 200 to 400 MPa) and the failure strain was increased by a factor of 3.7 (from 0.0013 to 0.0048). In the composite without Ag-Ta layers, failure was caused by growth of transverse cracks, which initiated within the reaction layers adjacent to the fiber-matrix interface at stresses below the failure stress. In the composite with Ag-Ta coatings, the reaction products were eliminated and transverse cracks were not observed prior to failure, even though the applied loads were much higher.

Several factors may have contributed to these differences. One is that the layers of brittle reaction products degraded the strength of the composite without Ag-Ta coatings by providing initiation sites for transverse cracks, whereas the Ag-Ta coatings eliminated this source of degradation. Crack initiation would also be suppressed both by the zone around the Ag-Ta-coated fibers that was found to be enriched in the more ductile β phase and by the higher frictional sliding resistance (Table 1) in the composite with Ag-Ta layers, which would delay the onset of circumferential sliding and thus maintain lower tensile stresses at the location of transverse cracking.

The role of brittle reaction layers in degrading transverse properties is further illustrated in Fig. 18. This shows a composite with a different Ti_3Al based matrix (Ti-24Al-11Nb) that was also fabricated with Ag-Ta layers on the fibers, but with foils that were contaminated on their surfaces, leading to formation of large zones containing carbides (dark rings) surrounding the fibers. Extensive transverse cracking, as shown in Fig. 18, initiated at very low loads and caused low transverse strength.

4.3 Damage in Sapphire-Fiber Composites

In composites with small or zero residual stresses, the largest tensile stress under transverse loading is the radial stress at $\theta = 0$, which tends to cause splitting of the fibers, debonding of the interface, and circumferential matrix cracking (Figs. 16 and 17). This is consistent with the damage mechanisms observed in the strongly bonded sapphire-fiber composite in which fiber splitting and circumferential matrix cracking occurred. Indeed, a weak maximum in this stress component occurs at a distance $\sim R/10$ away from the interface in the matrix, coinciding with the observed position of crack initiation. However, the location of this matrix cracking is more likely to be dictated by the variation of microstructural properties near the fibers: the region of matrix around the fiber that is depleted in β phase would be expected to be more brittle than the matrix elsewhere.

The local stress for initiation of circumferential cracking can be estimated from Fig. 17(a) (assuming that residual stresses in this composite are negligibly small). For a fully bonded interface, the radial stress at the interface for fiber spacing between $0.1R$ and R is between about $2 \sigma_a$ and $2.8 \sigma_a$. Crack initiation was observed at $\sigma_a \sim 280$ MPa, implying a local stress of 600 to 800 MPa. The variation of the radial stress within the fiber and in the nearby matrix is small, so this stress range applies to both the splitting of the fibers and the circumferential matrix cracking.

The stress at which fiber splitting occurred is substantially lower (by a factor of 4 to 5) than the longitudinal strength of the fibers. Although the transverse strengths of the fibers has not been measured, it would be expected to be similar to the longitudinal strength. These results suggest that the fiber strength was degraded by cutting and polishing during specimen preparation. The measured strength is indeed typical of the strength of polished bulk sapphire. Moreover, failure origins at the polished ends of some fibers could be identified on the separated fracture surfaces (Fig. 13(a)). Therefore, the fiber splitting observed in these experiments may not be representative of the behavior of composites without sectioned fibers. On the other hand, since circumferential

matrix cracking occurs at a similar stress level, the presence of fiber splitting may not have greatly affected the strength of the composite.

5. IMPLICATIONS FOR MATERIAL DESIGN

The different damage mechanisms observed in the composites of this study, combined with a qualitative correlation with the analytically calculated elastic stress fields, provide some insight into the material properties required for optimum transverse properties of the composite. The results suggest that the transverse strength is strongly affected by residual stresses and the ductility of the matrix in the critical regions immediately adjacent to the fibers, while strong interfacial bonding does not always lead to optimum transverse strength.

In composites with small residual stresses and strongly bonded interfaces (the sapphire/Ta/super- α_2 composite of the present study), the transverse strength is limited by cracks that initiate by splitting of the fibers, or by cracks that form in the matrix near the interface, where analytical solutions indicate a large stress concentration ($\sigma_r(0)$ in Fig. 17(a)). If, in a weakly bonded composite, the interface were to debond completely before the formation of these cracks, the stress $\sigma_r(0)$ would be relieved and the cracks would not form with further load increase. The resultant hole would lead instead to transverse radial cracking driven by the stress $\sigma_\theta(\pi/2)$ in Fig. 17(b), as observed in the SiC-fiber composites. For a freely sliding interface, this stress is similar in magnitude to the stress $\sigma_r(0)$ that is responsible for the cracking observed in the strongly bonded composite, implying that the strengths of strongly and weakly bonded composites in this case would be similar. However, if the debonded interface was restricted from sliding circumferentially (e.g., by friction), the stress $\sigma_\theta(\pi/2)$ would decrease substantially and the strength of the weakly bonded composite would be higher than that of the composite with strong interfaces.

In composites with large residual stresses (fibers in compression, as in the SiC fiber composites of this study), the residual hoop stress promotes radial cracking, whereas the radial compression inhibits the type of cracking observed in the stress-free sapphire fiber composite. Although radial cracks first form parallel to the load axis, transverse radial cracks eventually cause failure and limit the strength. The analytical stress solutions indicate that the stress driving transverse cracking is greatly increased if circumferential sliding occurs, whereas this stress is reduced next to closely spaced fibers if sliding does not occur. Therefore, the optimum strength would be expected with either strongly bonded interfaces or interfaces that debond easily but experience large resistance to circumferential sliding.

The optimum transverse strength in composites with strongly bonded interfaces may be achieved with an intermediate mismatch in thermal expansion coefficients of the fibers and matrix. In the absence of residual strains, the maximum tensile stress during transverse loading is the radial stress that causes circumferential cracking of the interface or nearby matrix. The presence of residual thermal strains (fibers of lower thermal expansion coefficient than that of the matrix) causes the radial stress to decrease and the hoop stresses to increase. Therefore, if transverse failure is dictated by crack initiation at the site of the largest tensile stress, then the optimum residual strain would be that for which the radial stress at $\theta = 0$ and the hoop stress at $\theta = \pi/2$ are equal at the point of failure. More rigorous analysis of this problem, including the effects of plasticity,¹³ partial interfacial debonding and sliding, multiple fiber interactions,^{17,20,21} and modeling of crack initiation would seem to be a fruitful avenue for further defining optimum composite properties.

The longitudinal properties of intermetallic matrix composites benefit from fiber reinforcement because of crack bridging effects, which lead to increased resistance to fatigue crack growth. This requires a weakly bonded interface and relatively easy frictional sliding. Therefore, the requirements for optimizing both the transverse and the longitudinal properties (regardless of residual stresses) might be satisfied by weakly bonded interfaces with anisotropic frictional

properties (perhaps achieved through control of the surface morphology of the fibers) to allow easy sliding in the axial direction and more strongly resisted sliding in the circumferential direction.

6. SUMMARY AND CONCLUSIONS

In situ observations during transverse loading of several Ti_3Al matrix (super- α_2) composites revealed the damage mechanisms, depending on residual stress states and interfacial bond strength, summarized in Fig. 14. The various forms of cracking coincided with locations of maximum tensile stress predicted from analytical solutions for elastic stress fields (which included effects of fiber-pair interactions and interfacial sliding). The results indicate that the transverse strengths of such composites are strongly influenced by residual thermal strains and matrix ductility in the critical regions near the fiber-matrix interfaces. They also suggest that, contrary to common perception, a strongly bonded interface between the fiber and matrix does not always lead to optimum transverse properties: the optimum interface appears to be one that allows tensile debonding (which relieves a stress concentration due to elastic mismatch), but restricts circumferential sliding (and thereby minimizes the stresses that drive transverse radial cracking).

ACKNOWLEDGMENTS

Funding for this work was supplied by the U.S. Air Force Office of Scientific Research under contract No. AFOSR 90-0235, by Wright Patterson Air Force Base under Contract No. F33615-90-C-5928, and by the Office of Naval Research as part of the Naval Research Laboratory's Basic Research Program. The SiC fiber containing composites were supplied by Rockwell's Rocketdyne and NAA divisions.

APPENDIX A: ELASTIC STRESSES IN TRANSVERSELY LOADED COMPOSITES

Isolated Fiber

The elastic stress field around an isolated strongly bonded fiber is given by¹⁶

$$\frac{\sigma_r}{\sigma_a} = 1/2 \{ [1 - \gamma/r^2 + [1 - 4\delta/r^2 - 3\delta/r^4] \cos 2\theta] \} \quad (A1)$$

$$\frac{\sigma_\theta}{\sigma_a} = 1/2 \{ 1 + \gamma/r^2 - [1 - 3\delta/r^4] \cos 2\theta \} \quad (A2)$$

where r is the radial distance normalized by the fiber radius and γ and δ are functions of the elastic mismatch

$$\gamma = \frac{(\kappa_f - 1) - (\kappa_m - 1)\Gamma}{2\Gamma + (\kappa_f - 1)} \quad (A3)$$

$$\delta = (\Gamma - 1)/(1 + \kappa_m \Gamma) \quad (A4)$$

where $\kappa = 3 - 4\nu$ (for plane strain), $\Gamma = \mu_f/\mu_m$, μ is the shear modulus, and ν is Poisson's ratio. In the composites of interest here, the Poisson's ratios of the fibers and matrix are approximately equal ($\nu = 0.3$), so that $\Gamma = E_f/E_m = 5$. The stresses from Eqs. (A1) and (A2) are plotted in Fig. 16. The average normal interfacial stress is (from Eq. A1):

$$\frac{\langle \sigma_r \rangle}{\sigma_a} = 1 - \gamma/2 = 0.65 \quad (A5)$$

Pairs of Fibers

Two-fiber solutions¹⁷ for the interfacial stresses due to a remotely applied field are compared with the single-fiber solution in Fig. A1. The fiber spacing in this case is $d/R = 0.85$, corresponding to $f = 0.37$ for a square array of fibers. The elastic properties are the same as for

Figs. 14-17. Results are shown for two orientations of the pair of fibers (parallel and normal to the applied stress) and for fully bonded and freely sliding interfaces for each orientation. For fully bonded interfaces, the additional perturbation due to the second fiber is maximum along the line joining the fiber centers and becomes small at angles larger than $\sim 45^\circ$ from this line. Therefore, a simple combination of these results would provide a close approximation for the interfacial stresses at a fiber surrounded by four other fibers in these orientations. The ratio of the tangential stress at $\theta = 0$ to that at $\theta = \pi/2$ is larger for both fiber-pair orientations with strongly bonded interfaces than for the single fiber solution. Therefore, the preference for parallel cracking rather than tangential cracking is made stronger by the fiber interaction effects. For fibers in a square array, the ratio of these stresses would be $\sigma_\theta(0)/\sigma_\theta(\pi/2) \approx 5$. However, if circumferential sliding occurs, these stresses change dramatically: the stress at $\theta = 0$ becomes compressive and the tensile stress at $\theta = \pi/2$ increases by a factor of 5 to 10. Therefore, the onset of sliding prevents parallel cracking and promotes transverse cracking.

The radial tension at $\theta = 0$, which is responsible for interfacial debonding and circumferential matrix cracking, is increased by the interaction effect of a fiber in the parallel orientation. This stress enhancement is further increased if circumferential sliding occurs.

APPENDIX B: FIBER SLIDING NORMAL TO FREE SURFACE

The preparation of a cross section of a composite that contains residual stresses due to mismatch of fiber and matrix can cause spontaneous debonding and sliding of the fiber relative to the matrix if the interfacial debond energy is smaller than a critical value.¹⁵ Since the degree of sliding is dependent upon the interfacial frictional forces that resist sliding, any subsequent change in these frictional forces (due for example to transverse loading) causes further sliding. Detailed analysis of the closely related phenomenon of sliding during thermal cycling is given in Ref. (22).

Fiber pulling experiments with the SiC fiber composites of this study indicate that spontaneous debonding occurs and that frictional forces are approximately uniform along the debonded section of interface.* In this case, a shear lag analysis indicates that the displacement is equivalent to that produced by pulling on the fibers in a stress-free composite with a stress equal to the residual axial stress, σ_f , in the fibers. This displacement is given by²³

$$u_o = \frac{\sigma_f^2 R(1-f) E_m}{4\tau_o E_f E} \quad (B1)$$

where τ_o is the frictional stress at the interface. If the frictional stress is proportional to the normal interfacial stress, then transverse loading, which decreases the average normal stress by $\langle\sigma\rangle$ (Eq. (A5)), causes the frictional stress to change to

$$\tau = \tau_o (1 - \langle\sigma\rangle/\sigma_R) , \quad (B2)$$

where σ_R is the residual stress normal to the interface. The corresponding change in displacement is

$$u = u_o \left(\frac{\tau_o}{\tau} - 1 \right) = \frac{\sigma_f^2 R(1-f) E_m}{4\tau_o E_f E} \left[\frac{\langle\sigma\rangle/\sigma_R}{1 - \langle\sigma\rangle/\sigma_R} \right] \quad (B3)$$

* Detailed analysis of fiber pullout experiments¹⁵ has indicated that surface morphology plays an important role in the constrained sliding of fibers: the surface roughness of the fibers causes an increase in the normal interfacial stress when the fibers slide, and this increase cancels the effect of Poisson's contraction of the fiber to give an approximately uniform normal stress (and thus friction) along the section of fiber that undergoes sliding.

With the onset of fiber sliding normal to the specimen surfaces, changes occur in the in-plane stresses because of Poisson's effects. These changes can be accounted for (within the concentric cylinder solutions) by a change in the effective radial mismatch strain that is responsible for residual stresses. With the elastic constants given in Section 3.2, the relaxation of residual axial compression in the fiber leads to an increase in the effective mismatch strain. The magnitude of this increase is calculated to be approximately 10%, a result that can be obtained straightforwardly from the analyses in Hutchinson and Jensen.¹⁸

REFERENCES

1. J.M. Larsen, W.C. Revelos and M.L. Gambone, "An Overview of Potential Titanium Aluminide Composites in Aerospace Applications," in *Intermetallic Matrix Composites II*, Ed. D.B. Miracle, D.L. Anton and J.A. Graves. M.R.S. Symposium Proceedings V273, 113-16 (1992).
2. J.M. Larsen, K.A. William, S.J. Balsone and M.A. Stuke, "Titanium Aluminides for Aerospace Applications," p. 363, *Proc. Titanium Aluminide Composites Workshop*, Orlando, FL, 1990, Eds. P.R. Smith, S.J. Balsone and T. Nicholas, U.S. Air Force publication WL-TR-91-4020.
3. S.W. Johnson, S.J. Lubowinski and A.L. Highsmith, "Mechanical Characterization of SCS-6/Ti-15-3 Metal Matrix Composites at Room Temperature," in *Thermal and Mechanical Behavior of Metal Matrix and Ceramic Matrix Composites*, ASTM STP1080, Eds. J.M. Kennedy, H.M. Moeller and W.S. Johnson, American Society for Testing and Materials, Philadelphia, 1990, pp. 193-218.
4. R.A. Naik and W.S. Johnson, "Observations of Fatigue Crack Initiation and Damage Growth in Notched Titanium Matrix Composites," NASA Technical Memorandum 101688, Dec. 1989.
5. D.B. Marshall, B.N. Cox, W.L. Morris and M.C. Shaw, *Mechanical Properties of Ceramic and Intermetallic Matrix Composites* in Advanced Composite Materials, pp. 503-512, Ed. M. Sacks, The American Ceramic Society, 1991.
6. B.N. Cox, M.R. James, D.B. Marshall and R.C. Addison, Jr., "Determination of Residual Stresses in Thin Sheet Titanium Aluminide Composites," *Met. Trans.* 21A, 2701-07 (1990).

7. D.R. Williams, D.L. Davidson and J. Lankford, *Expt. Mech.* 20, 134-149 (1980).
8. M.R. James, W.L. Morris and B.N. Cox, "A High Accuracy Automated Strain Field Mapper," *Exp. Mech.* 30, 60-68 (1990).
9. C. Rhodes, "Characterization of Fiber/Matrix Interfaces by Transmission Electron Microscopy in Titanium Aluminide/SiC Composites," in *Intermetallic Composites II*, Ed. D.B. Miracle, D.L. Anton and J.A. Graves, MRS Symposium Proceedings, V273, 17-24 (1992).
10. Titanium Aluminide Composites, Contract No. F33657-86-C-2136 with USAF, Interim Report No. 2, G.E. Aircraft Engines, Cincinnati, OH, Sept. 1987.
11. P. Bania, Timet Corporation, Henderson, NV, private communication (1989).
12. Z. Hashin, "Analysis of Properties of Fiber Composites with Anisotropic Constituents," *J. Appl. Mech.* 46, 543-550 (1979).
13. R.P. Nimmer, R.J. Baukert, E.S. Russell, G.A. Smith, and P.K. Wright, "Micromechanical Modeling of Fiber-Matrix Interface Effects in Transversely Loaded SiC/Ti-6-4 Metal Matrix Composites," *ASTM J. Composites Technology and Research*, 13[1], 3-13 (1991).
14. D.B. Marshall, M.C. Shaw, W.L. Morris and J. Graves "Interfacial Properties and Residual Stresses in Titanium and Titanium Aluminide Matrix Composites," pp. 329-347 in *Titanium Matrix Composites*, Ed. W. Revelos and P.R. Smith, Wright Patterson Air Force Base, WL-TR-92-4035, 1992.
15. D.B. Marshall, M.C. Shaw and W.L. Morris, "Measurement of Debonding and Sliding Resistance in Fiber Reinforced Intermetallics," *Acta Metall.*, 40 [3] 443-454 (1992).

16. N.I. Muskhelishvili, "Some Basic Problems of the Mathematical Theory of Elasticity," P. Noordhoff Ltd, The Netherlands, 1963.
17. D. Kouris, "Stress Concentration Due to the Interaction Between Two Imperfectly Bonded Fibers in a Continuous Fiber Composite," J. Appl. Mech., 60[1] 203-206 (1993).
18. J.W. Hutchinson and H.M. Jensen, Mech. Mater. 2, 139 (1990).
19. J.R. Porter, "Reinforcements for Ceramic-Matrix Composites for Elevated Temperature Applications," Mat. Sci. Eng. A166, 179-184 (1993).
20. D. Kouris and E. Tsuchida, "On the Elastic Interaction Between Two Fibers in a Continuous Fiber Composite under Thermal Loading," Mechanics of Materials 12, 131-146 (1991).
21. R.P. Nimmer, "Fiber-Matrix Interface Effects in the Presence of Thermally Induced Residual Stresses," ASTM J. Composite Technology and Research 12[2], 65-75 (1990).
22. B.N. Cox, Acta. Metall. Mater. 38, 2411 (1990).
23. D.B. Marshall, B.N. Cox and A.G. Evans, "The Mechanics of Matrix Cracking in Brittle-Matrix Fiber Composites," Acta. Metall. 33[11], 2013-21 (1985).

FIGURE CAPTIONS

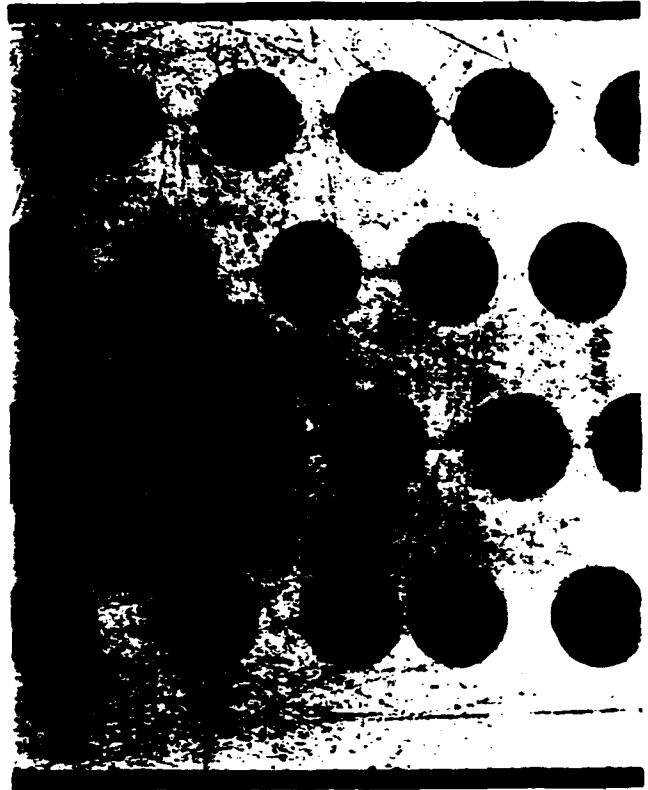
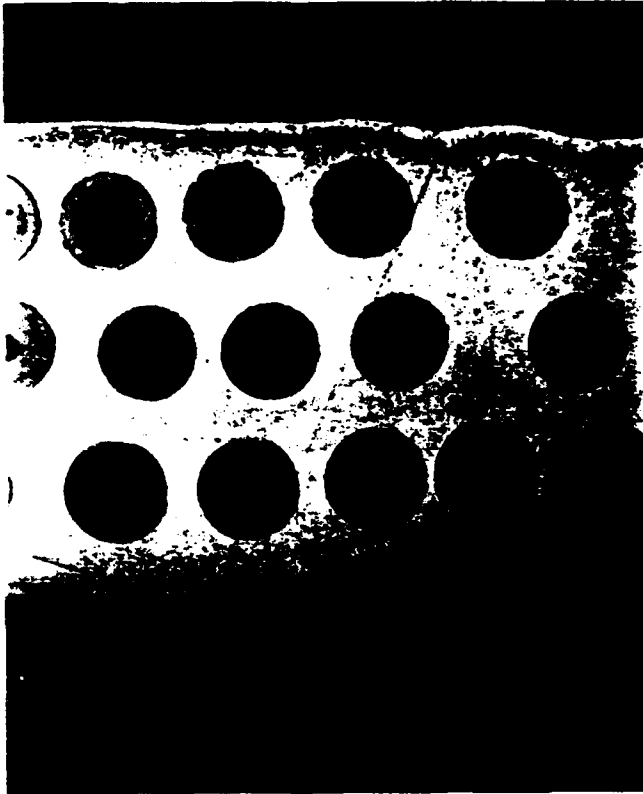
1. Composites used for transverse property evaluation (super- α_2 titanium aluminide matrix).
(a) SCS-6 SiC fibers without additional coatings, (b) SCS-6 SiC fibers with Ag-Ta coating,
(c) Sapphire fibers with Ta coating.
2. Scanning electron micrographs showing sapphire fiber in super- α_2 matrix. Bright line surrounding fiber is Ta coating. Bright regions of matrix are β phase; dark regions are α_2 phase.
3. Scanning electron micrograph from sapphire fiber composite showing region of fiber-matrix interface in which Ta layer was missing.
4. Stress-strain curves: (a) SiC fiber composites, comparison of responses under transverse and longitudinal loading, (b) SiC-fiber composites, transverse loading. (c) Sapphire fiber composite, transverse loading (labels a, b and c indicate loads at which in situ micrographs of Fig. 11 were obtained). (d) Comparison of measured transverse Young's moduli with predicted bounds from Hashin¹² for several assumed values of E_m . Full curves lower bounds from Hashin; broken curves upper bounds.
5. Schematic diagram illustrating observed damage mechanisms in SiC-fiber composites.
6. Scanning electron micrographs of (a) SiC-fiber composite with Ag-Ta coated fibers, and (b) composite with uncoated fibers, after loading to failure in transverse tension.
7. HASMAP analysis showing in-plane surface displacements caused by applied transverse load, $\sigma_a = 160$ MPa, in composite containing uncoated SiC fibers. Reference arrow at bottom left represents displacement of $0.23 \mu\text{m}$.

8. Parallel cracks in transversely loaded SiC-fiber composites (scanning electron micrographs): (a) (c) (d) composite containing uncoated fibers, (b) composite containing fibers coated with Ag-Ta. Loading direction is horizontal.
9. Transverse cracks in SiC-fiber composite containing uncoated fibers (scanning electron micrographs).
10. Series of in situ optical micrographs showing development of transverse cracks leading to failure in SiC-fiber composite containing uncoated fibers. Loading direction is vertical. Applied stresses: (a) 160 MPa; (b) 190 MPa; (c) 198 MPa.
11. Sequence of in situ optical micrographs taken from one area of sapphire fiber composite at loads of (a) 0.9, (b) 0.95, (c) 0.99 of the failure load, corresponding to the positions labeled (a), (b) and (c) in Fig. 15. Failure occurred by linking of the cracks in (c). Applied load horizontal.
12. Scanning electron micrographs showing crack path across the fiber-matrix interfacial region of sapphire-fiber composite.
13. Scanning electron micrograph showing fracture surface resulting from transverse tensile loading of sapphire-Ta/super- α_2 composite. Smooth region is axial split within the sapphire fiber; rough region is the super- α_2 matrix.
14. Schematic diagram summarizing damage mechanisms observed in transverse loading.
15. Comparison of elastic residual stresses in matrix at interface, calculated using concentric cylinder model (broken lines) and finite element analysis of square fiber array (solid curves).

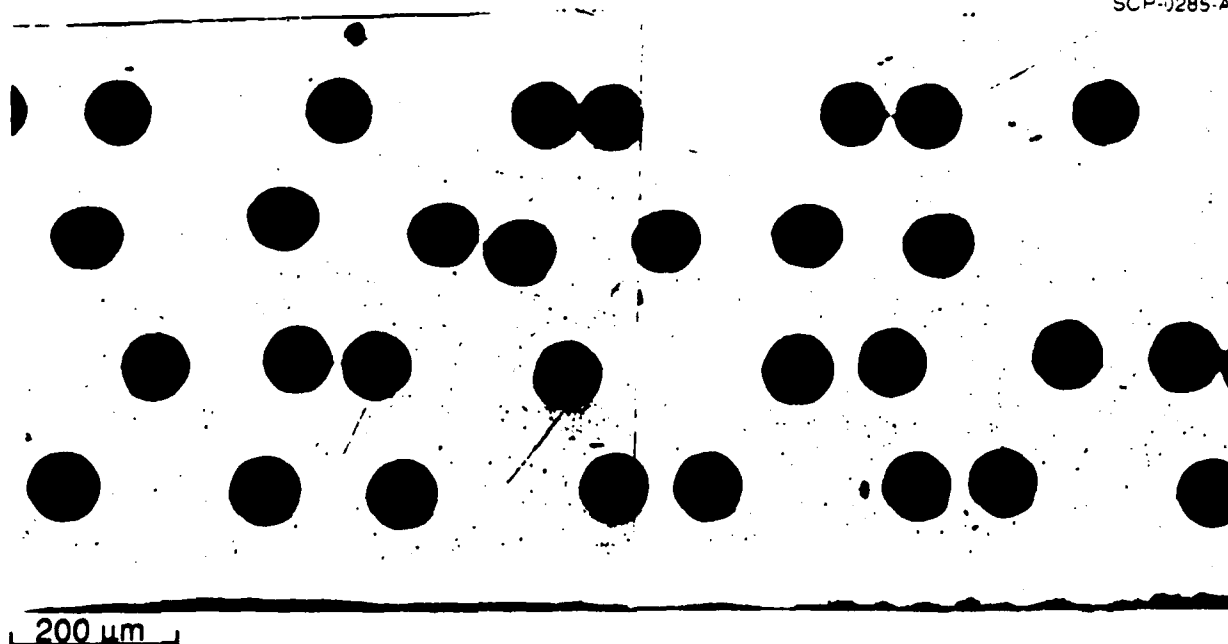
16. (a) Elastic stresses in matrix around isolated fiber ($E_f/E_m = 5$, $\nu = 0.3$). Uniform remote stress.
(b) Interface stresses from (a).
(c) Radial and tangential stresses in matrix corresponding to (a).
17. (a) and (b) Interfacial stresses (elastic) for pairs of fibers.
18. Transverse cracks in composite containing large layer of carbides (dark region) surrounding fibers.
- A1. Comparison of interfacial stresses for an isolated fiber and pairs of fibers under uniform remotely applied stress ($E_f/E_m = 5$, $\nu = 0.3$). Fiber separation is $d/R = 0.85$ corresponding to $f = 0.35$ in a square fiber array. (a) tangential stress, (b) radial stress, and (c) shear stress.

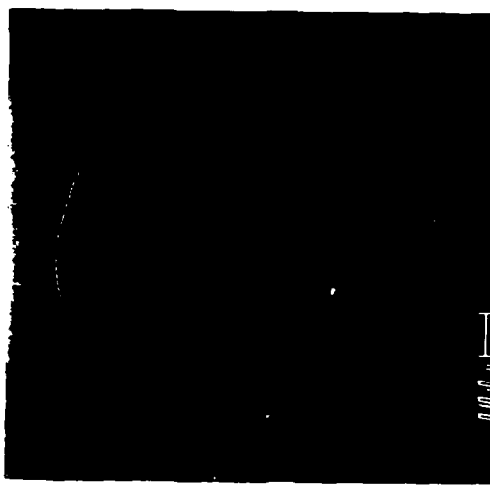
Table 2
Estimated Stresses for Damage Initiation

	Residual Stress from Table 1 (MPa)	Applied Stress for Damage Initiation (MPa)	Local Stress Due to Applied Load (Fig. 17) (MPa)	Resultant Local Stress (MPa)
SIC-FIBER COMPOSITES Interfacial Separation uncoated fibers Ag-Ta coated fibers	- $\sigma_r^R = 260-350$ - $\sigma_r^R = 300-400$ (1.0 to 1.3 x concentric cylinder soln.)	120-170 150-180	240-340 300-360 ($\sigma_r^A \approx 2 \sigma_a$)	0 0
Load-axis radial cracks uncoated fibers Ag-Ta coated fibers	$\sigma_\theta^R = 565$ $\sigma_\theta^R = 557$	150 180	90-165 108-200 ($\sigma_\theta^A \approx 0.6 \sigma_a$ to $1.1 \sigma_a$)	655-730 670-750
Transverse radial cracks uncoated fibers	$\sigma_\theta^R = 565$	160	-18 to 36 (bonded) ($\sigma_\theta^A \approx -0.1 \sigma_a$ to $0.2 \sigma_a$) 185 to 320 (sliding) ($\sigma_\theta^A \approx 1.15 \sigma_a$ to $2 \sigma_a$)	550-600 (bonded) 750-880 (sliding)
SAPPHIRE FIBER COMPOSITES circumferential matrix cracks/fiber splitting	zero	280	600 to 800 ($\sigma_\theta^A(0) \approx 2 \sigma_a$ to $2.8 \sigma_a$)	600-800



SCP-0285-A







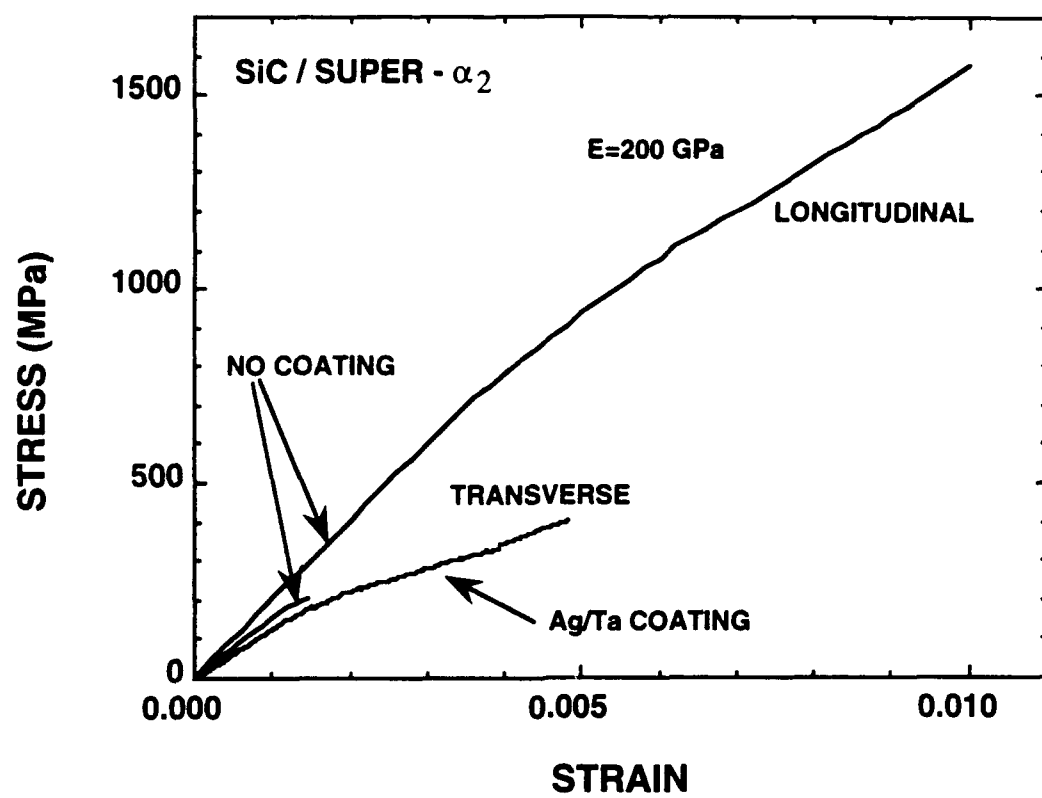


Fig 4a

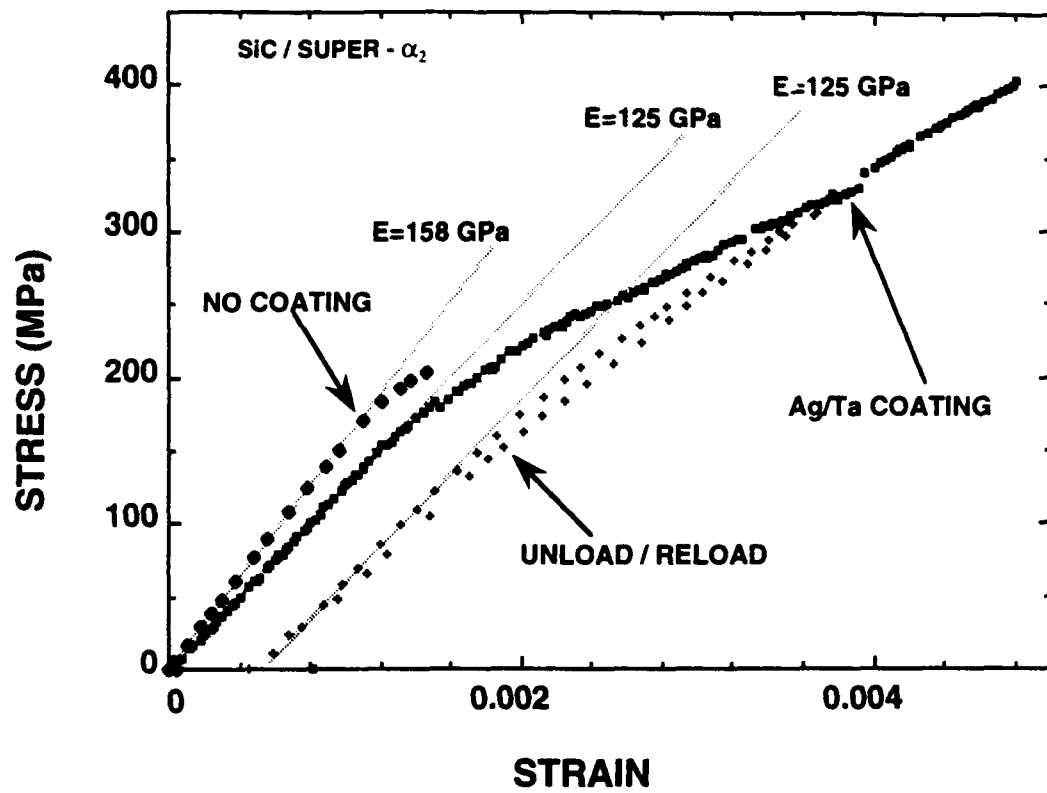


Fig. 4 b

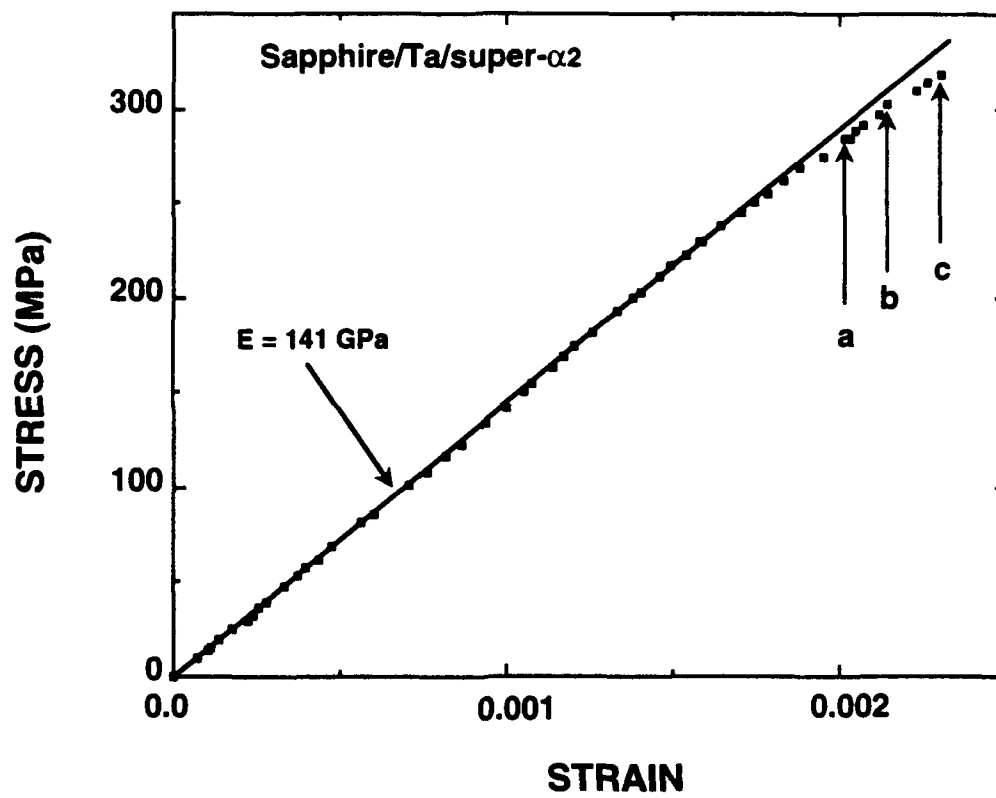


Fig. 4c

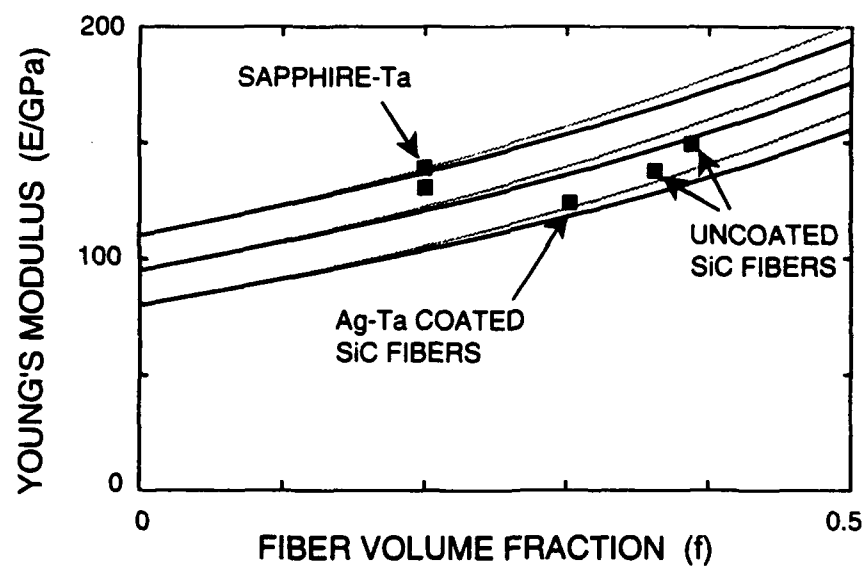


Fig. 4(d)

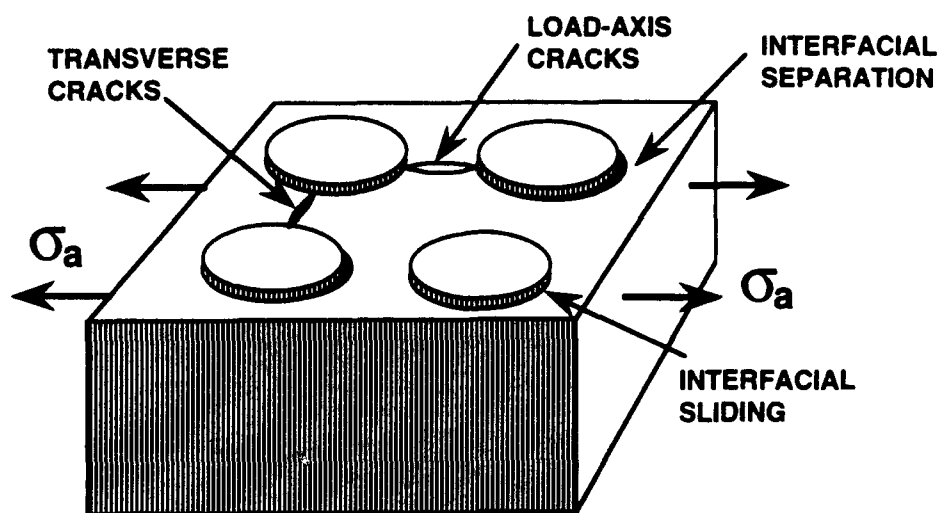
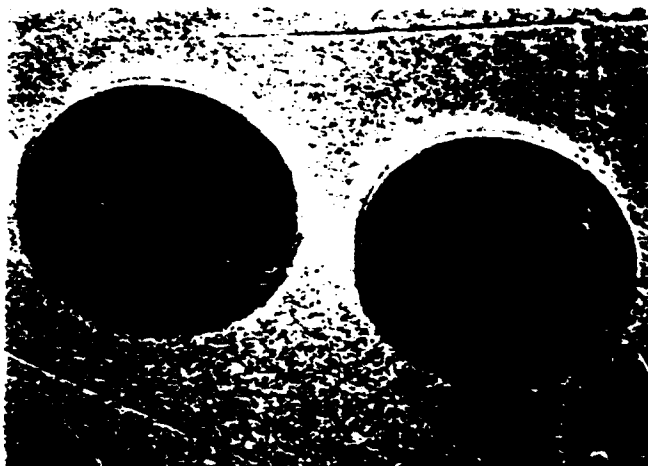
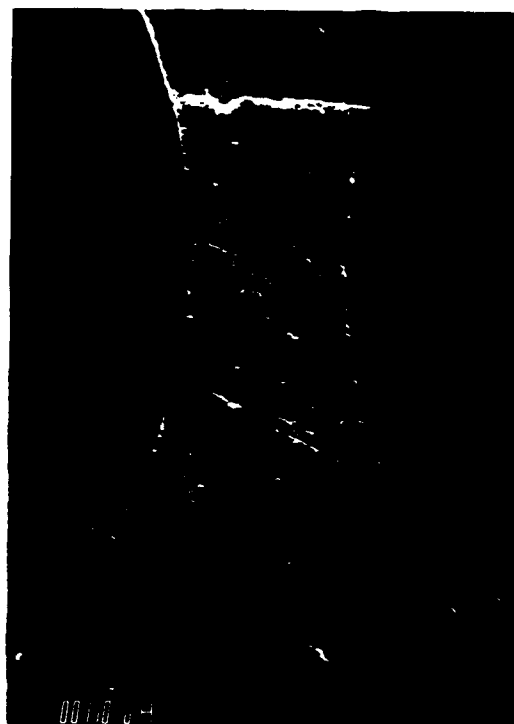
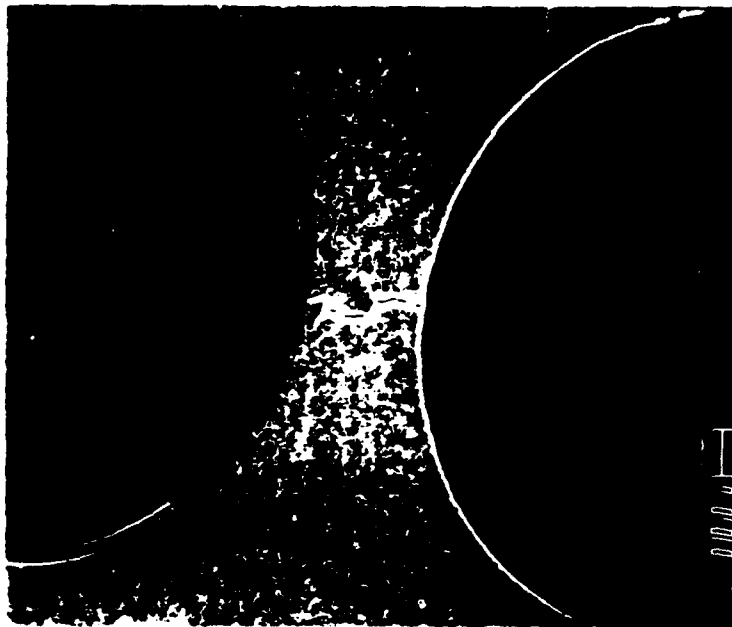


Fig. 5

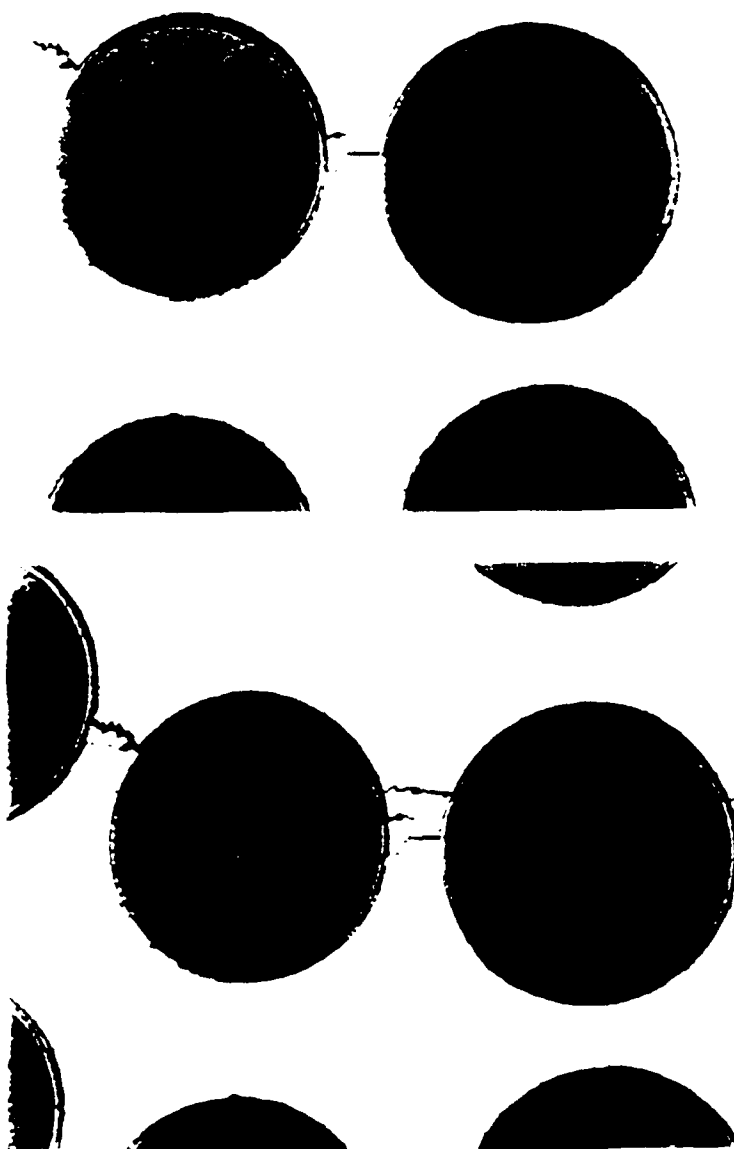
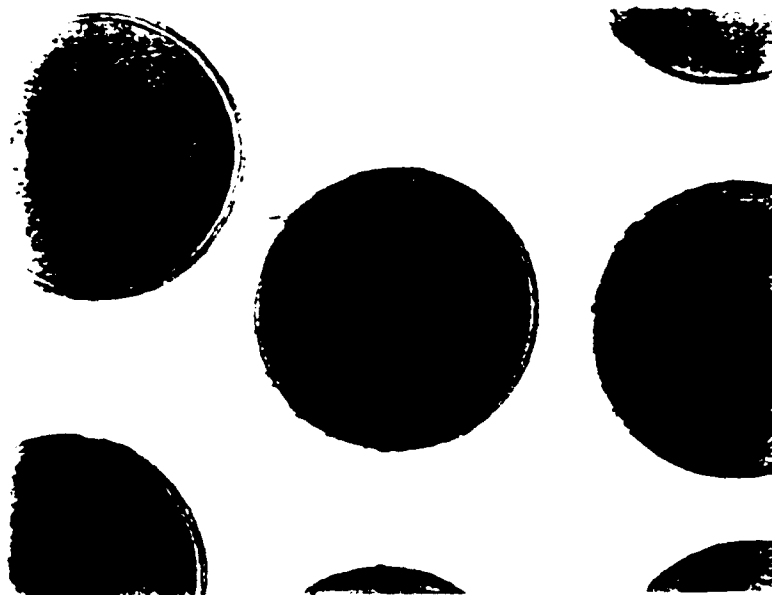








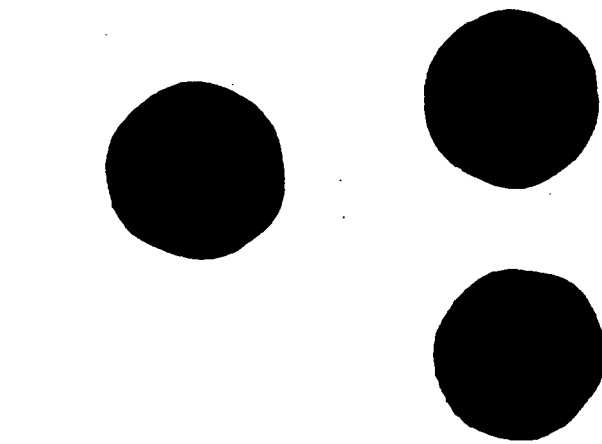
LOAD DIRECTION



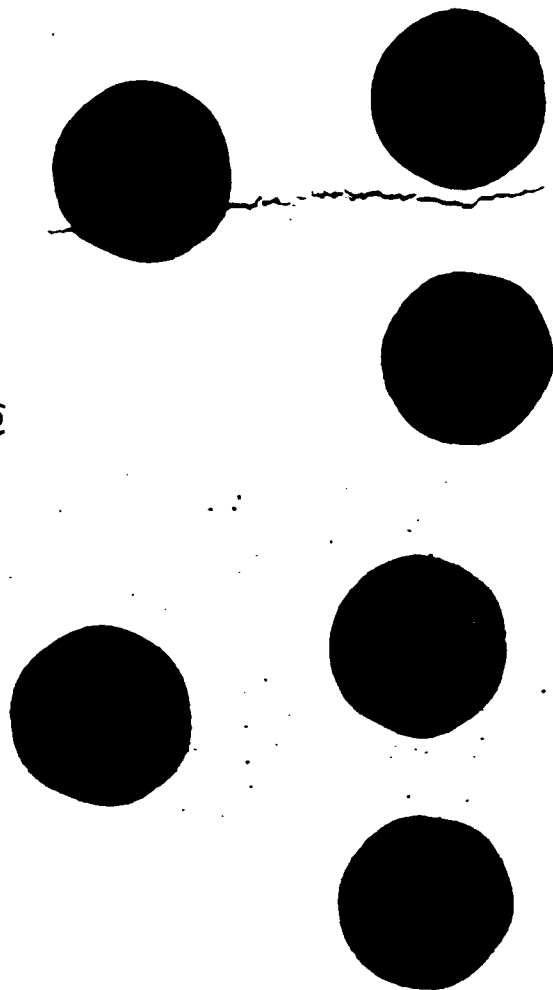
(a)



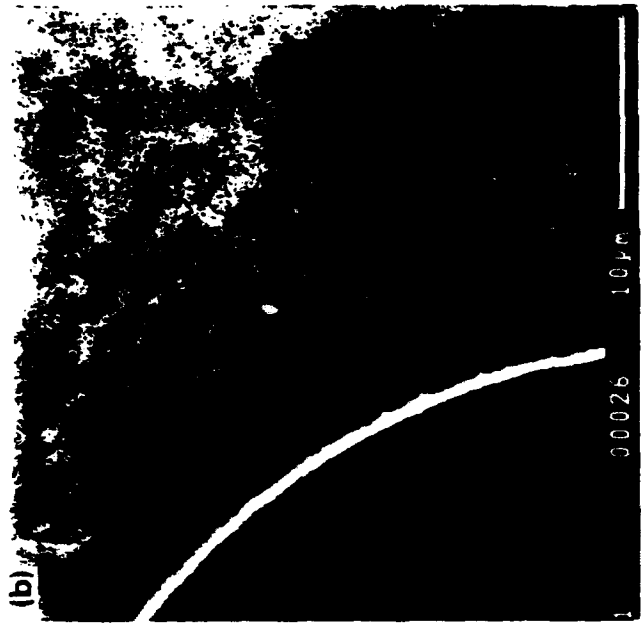
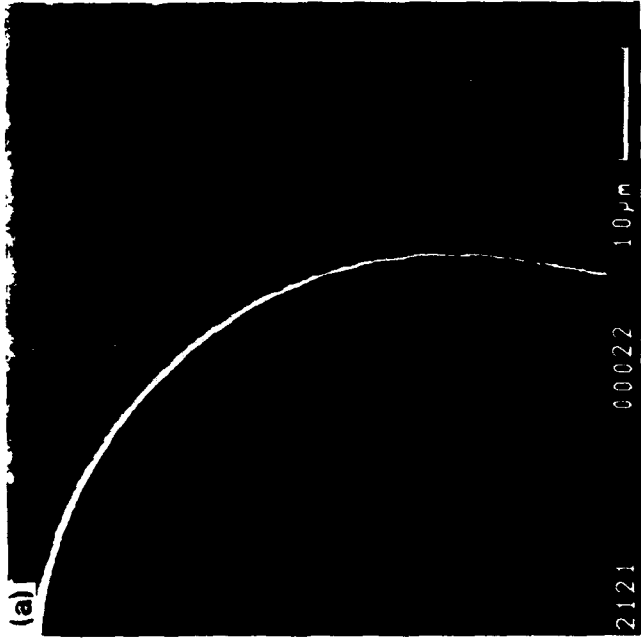
(b)



(c)



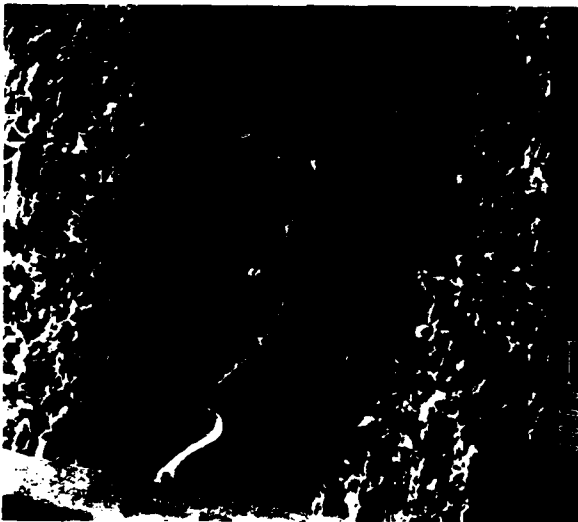
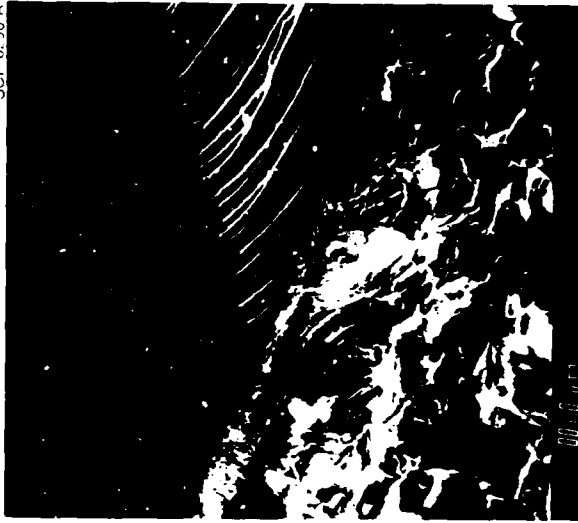
100 μm



SCP-0289-A



SCP 0250 A



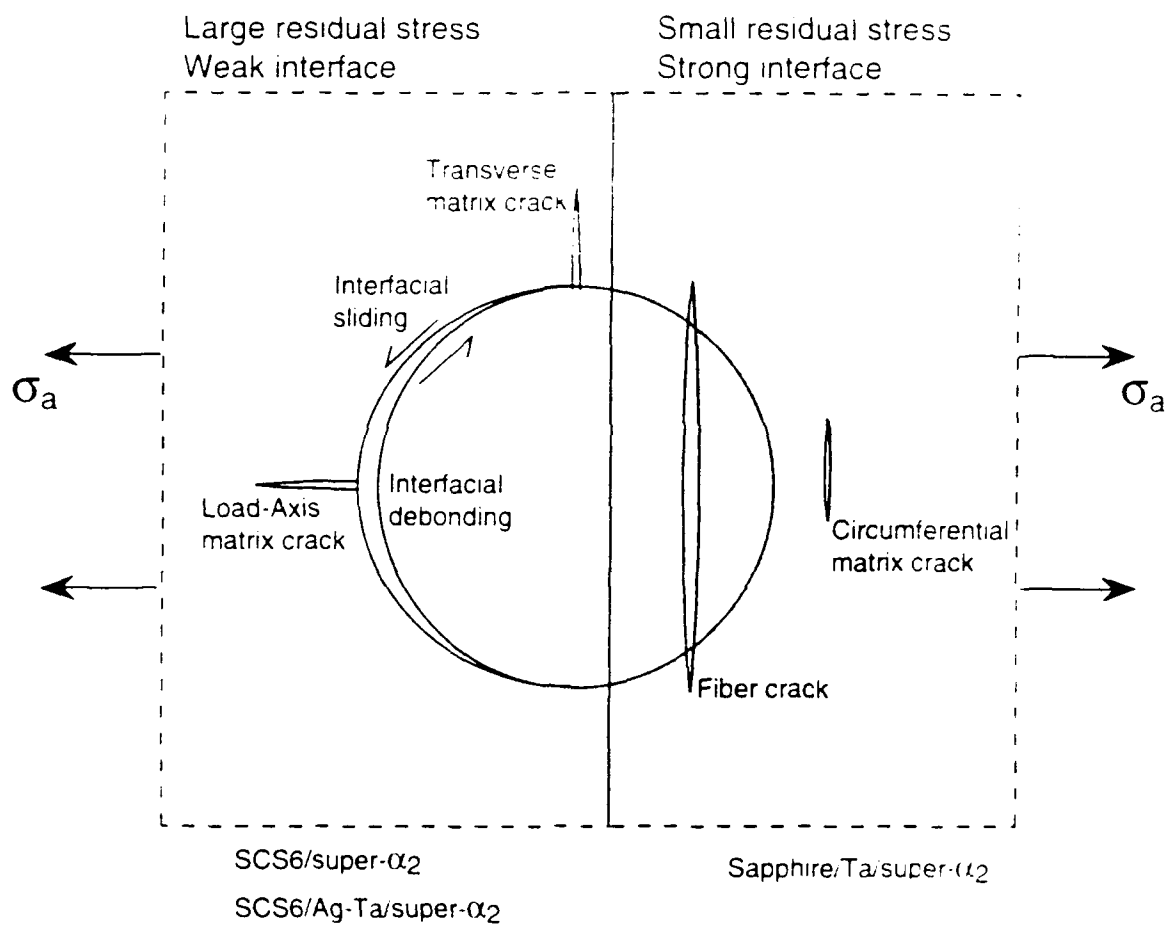


Fig. 14

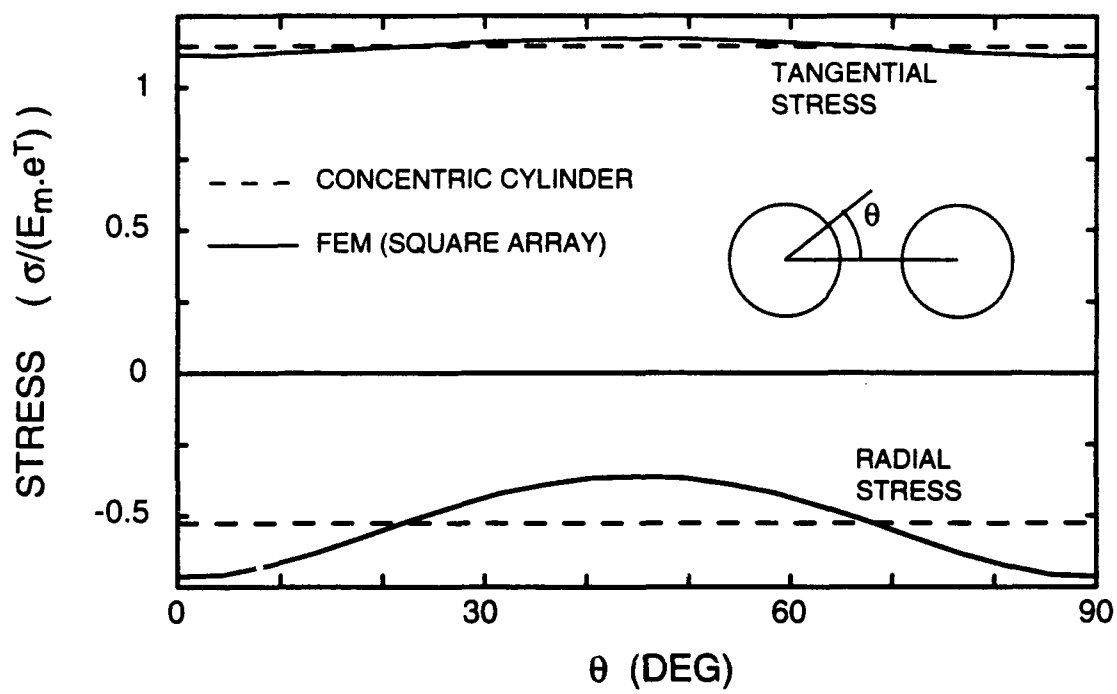


FIG. 15

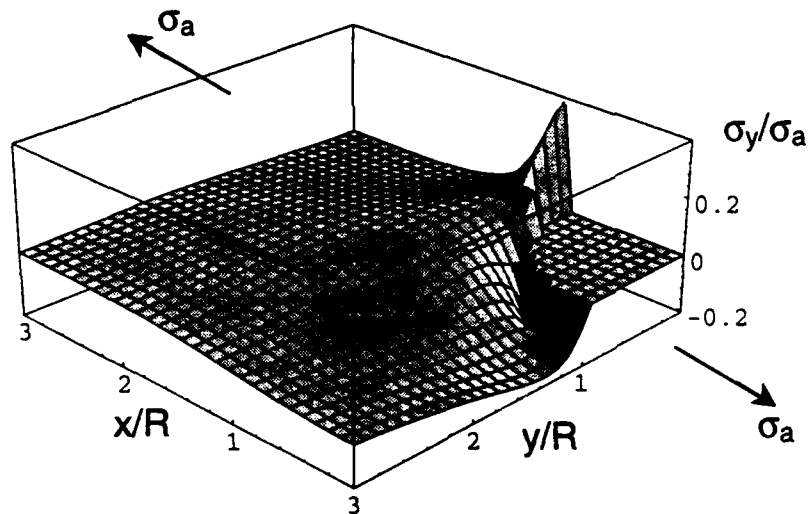
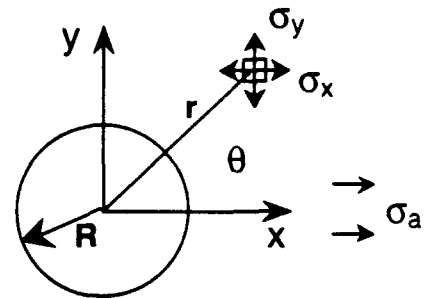
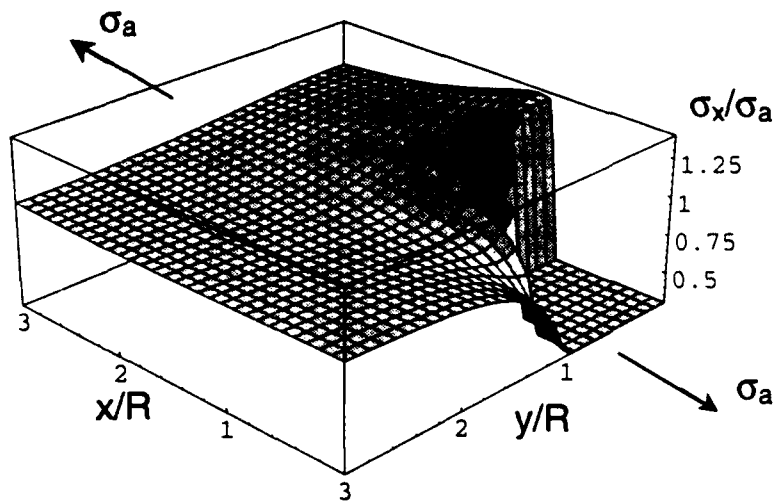


Fig. 16 (a)

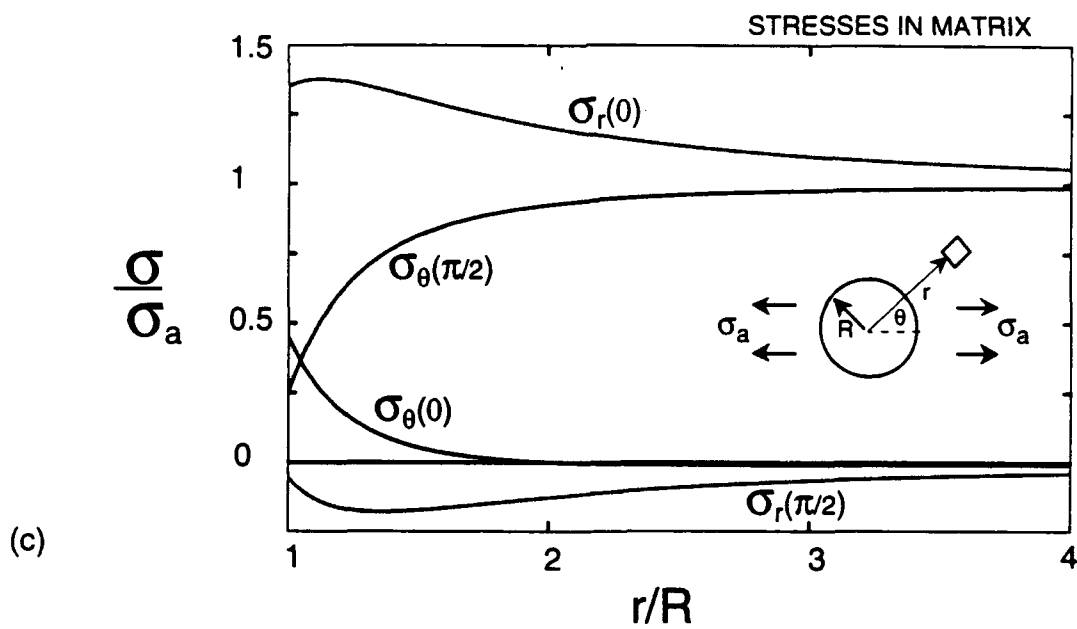
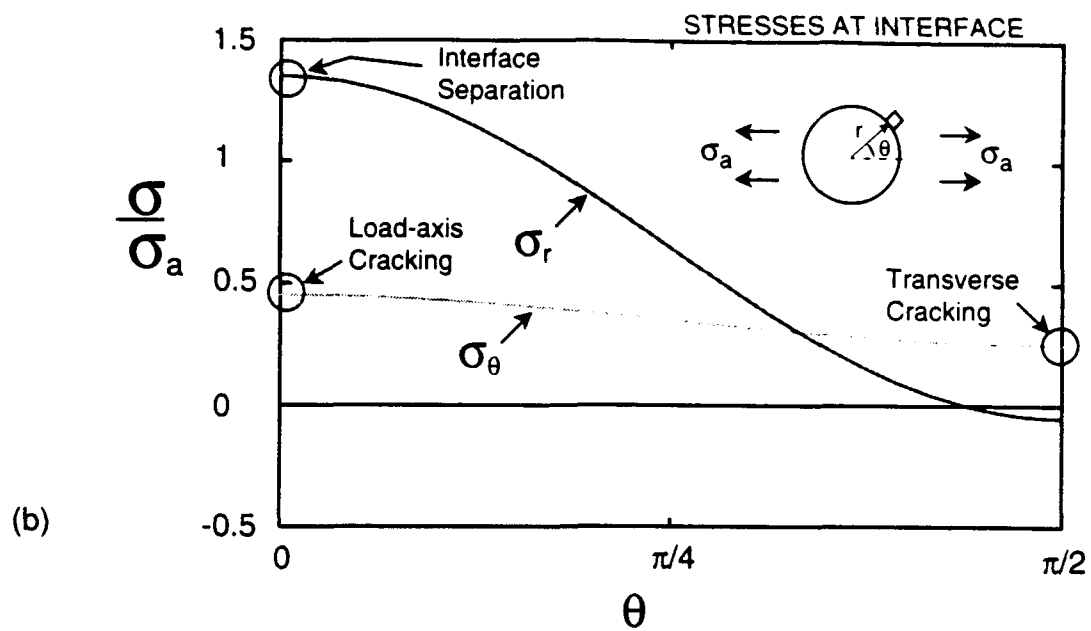


Fig. 16

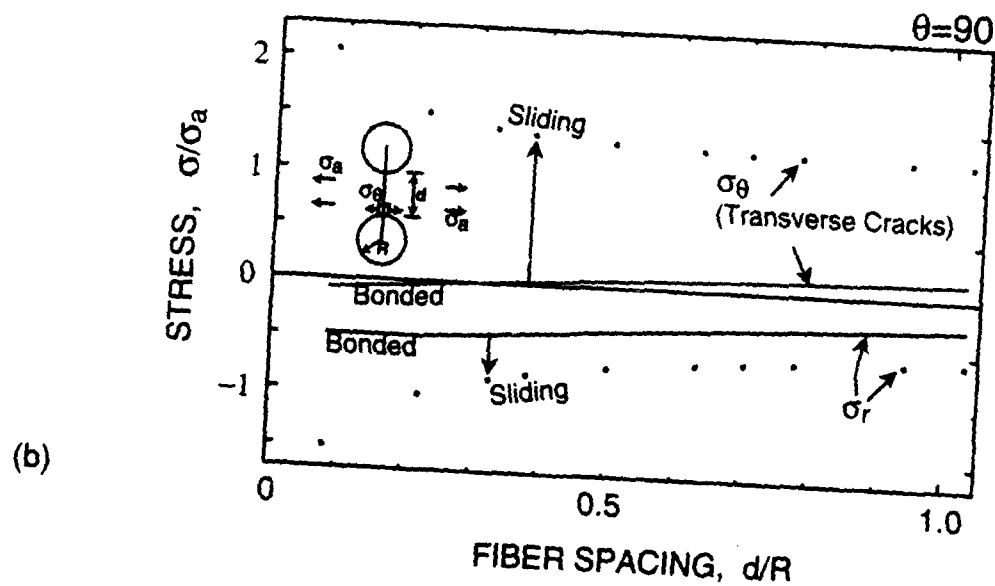
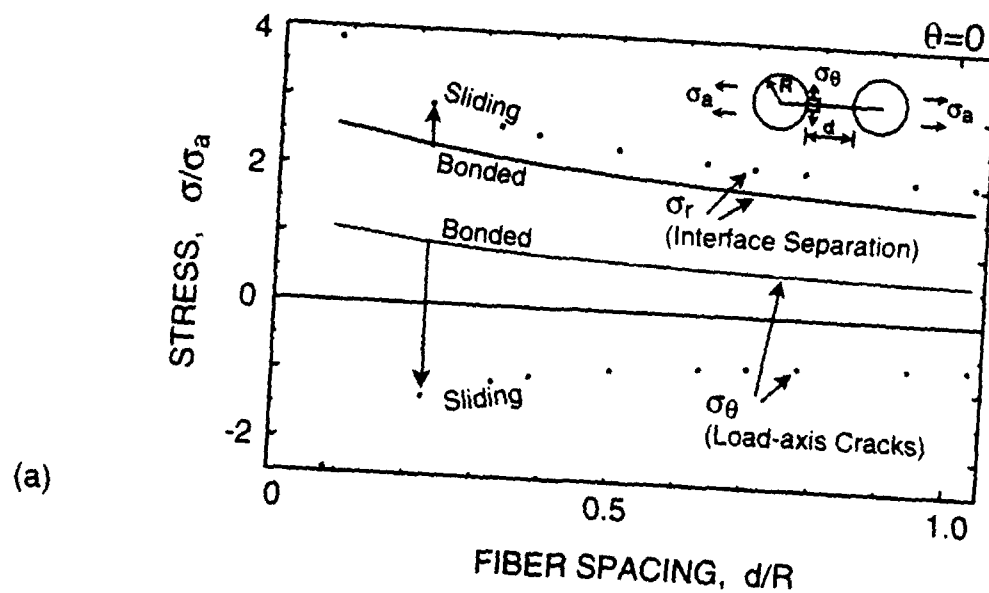
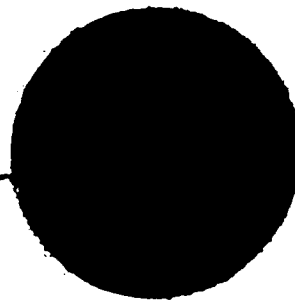


Fig. 17

SCP0390A 091493



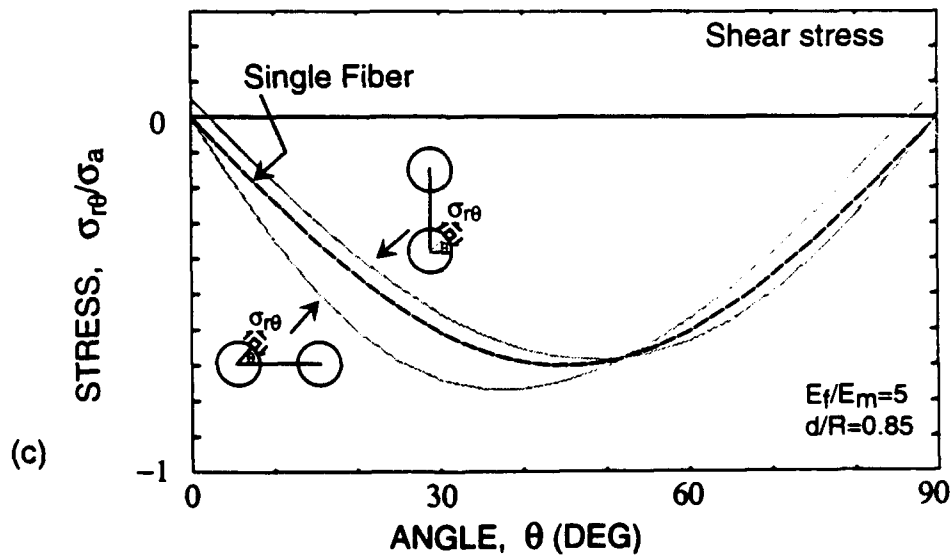
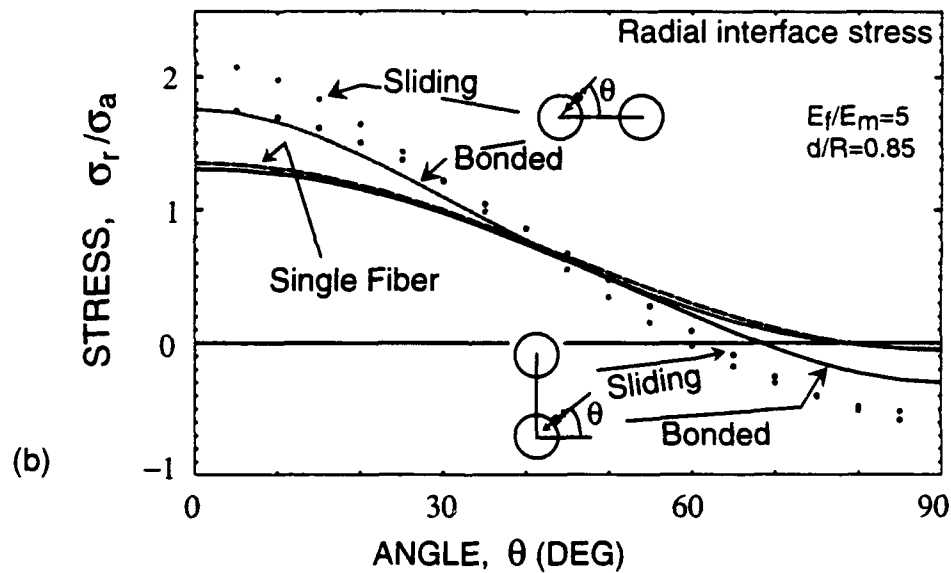
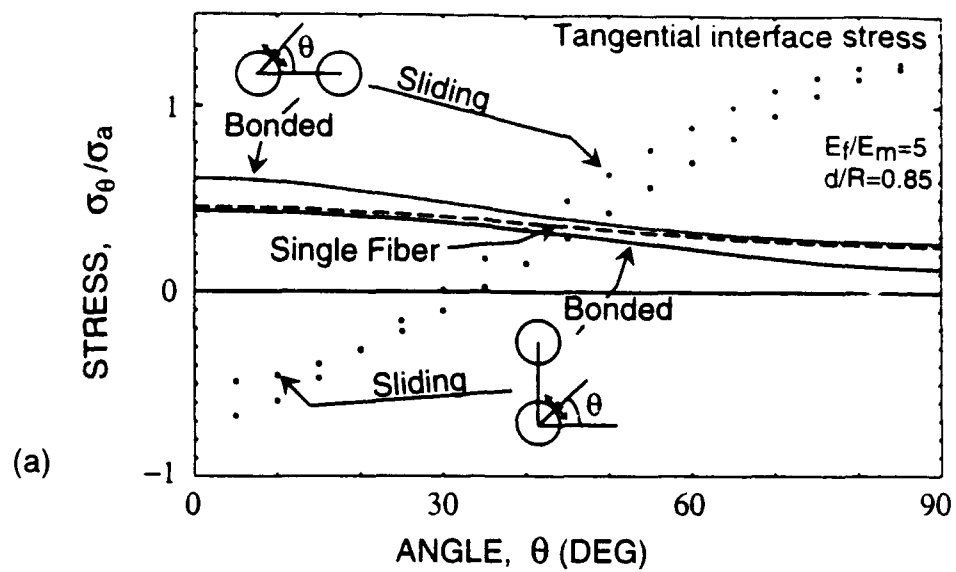


Fig A1

5.3 The Role of Frictional Sliding in Transverse Failure of Composites

in preparation

THE ROLE OF FRICTIONAL SLIDING IN TRANSVERSE FAILURE OF COMPOSITES

**D. B. Marshall, W. L. Morris and B. N. Cox
Rockwell International Science Center
1049 Camino Dos Rios
Thousand Oaks, CA 91360**

**D. Kouris
Department of Mechanical and Aerospace Engineering
Arizona State University
Tempe, AZ 85287-6106**

1. INTRODUCTION

Recent theoretical and experimental studies have suggested that circumferential sliding at debonded fiber-matrix interfaces is detrimental to the transverse strength of the composite.¹⁻³ In contrast, debonding and sliding is a prerequisite for enhanced longitudinal properties such as toughness in ceramic matrix composites^{4,5} and resistance to fatigue crack growth in intermetallic matrix composites.^{6,7} Therefore it has been suggested that optimal composite properties could be obtained with interfaces that debond readily and have low frictional sliding resistance longitudinally but large sliding resistance in the circumferential direction.

Circumferential sliding during transverse loading causes increased tensile hoop stress in the matrix adjacent to the fiber, at the location where cracking is induced normal to the applied load (Fig. 1). In composites containing fibers that are stiffer than the matrix, the stress at this location, $\sigma_\theta(\pi/2)$, is smaller than the applied stress if the interface does not slide: i.e., the stress perturbation due to the fiber is compressive thus tending to inhibit the formation of strength-degrading transverse cracks. On the other hand, the hoop stress at $\theta = 0$ is tensile, thus tending to induce cracking parallel to the applied load. Such cracks have been observed in $\text{Ti}_3\text{Al/SiC}$ composites. However, because of their orientation they do not lead to failure in unidirectional loading. If the interface is allowed to debond with unrestricted sliding, these stresses change: the stress $\sigma_\theta(\pi/2)$ becomes larger than the applied stress thus favoring the formation of transverse cracks, which lead to failure, while the stress $\sigma_\theta(0)$ becomes compressive. The magnitudes of these changes in stress increase as the spacing of nearest neighbor fibers decreases (Fig. 2).

Analytical solutions have been obtained recently for the stress fields surrounding pairs of fibers, with the possibility of limited interfacial sliding being permitted by incorporating springs of various stiffness at the interface. The results indicate a continuous transition between the stress states mentioned above for bonded and freely sliding interfaces and could be used for guidance in designing interfaces that debond, yet have sufficient frictional sliding resistance to avoid transverse cracking. In this communication we present experimental measurements of circumferential sliding (obtained by high resolution strain mapping) and preliminary comparison with analysis.

2. EXPERIMENTS

Transverse loads were applied to a titanium aluminide matrix composite as described in more detail elsewhere. The composite, which was fabricated by Textron Specialty Materials, contained three rows of SiC fibers (SCS-6) in a two phase (α_2 - β) matrix of Ti-25Al-10Nb-3V-1Mo (Super α_2). Beams with dimensions approximately 50 x 2 x 1 mm were cut from a sheet of the composite with the longest dimension normal to the fibers. The beams were polished on the sides containing the fiber ends and loaded in tension using a fixture attached to the stage of an optical microscope. High magnification micrographs were obtained from the polished sides of the beams during loading. The applied loads were measured with a load cell and the corresponding strains were measured using strain gages attached to the sides of the specimens.

The in situ optical micrographs were analyzed using a high resolution strain mapping technique.^{7,8} This involved comparing images taken before and during loading and measuring relative displacements of corresponding image features. Measurements were obtained both stereoscopically and using a computerized image analysis system (HASMAG-High Accuracy Strain Mapping), both of which provide sensitivity of ~ 10 nm in differential displacement measurements from optical micrographs. The image analysis was improved by depositing MgO crystals on the surface of the specimen to provide additional sharp image detail.

3. RESULTS AND ANALYSIS

3.1 Damage

The details of damage leading to failure are discussed in detail elsewhere. The pertinent features are: (1) at applied stress, σ_a , within the range 120-170 MPa separation of the fiber-matrix interface initiated at the position $\theta = 0$, corresponding with the onset of non linearity in the stress-strain curve, (2) formation of "load-axis" radial cracks between some fibers (Fig. 1) at $\sigma_a \approx 150$ MPa, (3) formation of transverse radial cracks adjacent to some fibers at $\sigma_a \approx 160$ MPa, and (4) stable growth and linking of transverse cracks and debonded interfaces to failure at $\sigma_a = 200$ MPa. Comparison of these results with stress field solutions for fully bonded and freely sliding interfaces suggested that significant circumferential sliding occurred between the onset of load-axis and transverse cracking at $\sigma_a \sim 150$ -160 MPa.

3.2 In-Plane Surface Displacements

A map of in-plane surface distortions at an applied load of 160 MPa is shown in Fig. 3. The arrows superimposed on the optical image are relative displacement vectors for corresponding image features located at the beginnings of the arrows within a reference micrograph at zero load and a second micrograph of the same area with the load applied. (The magnitudes of the displacement vectors are magnified by a factor of 40 compared with the dimensions on the micrograph.) The following deformations are readily discerned: tensile strains parallel to the applied load; Poisson's contraction from top to bottom of the micrograph; debonding and rotation of the right-hand fiber; and tensile strains in the matrix between the fibers in the direction normal to the applied stress.

At sufficiently high applied loads the opening and sliding displacement discontinuities at the fiber-matrix interfaces can be readily measured using stereoscopic analysis. Results for the fiber shown in Fig. 4(a) at various stages of loading are shown in Figs. 4(b) and (c).

Sliding displacements were first detected at a lower applied load (~ 100 MPa) than were normal opening displacements (120 MPa). Sliding began at the location $\theta = 30^\circ$ and spread continuously in both directions with increasing load. This result is consistent with the calculated location of the maximum shear stress from the analysis of Ref. 2 (Fig. 5). The opening displacements occurred first at $\theta = 0$ as expected and spread to higher angles with increasing load.

The calculated interfacial shear stresses and radial stresses for a pair of fibers with the separation shown in Fig. 4(a) and with strongly bonded interfaces are shown in Fig. 5. Results for the normal stress at an interface that is free to slide but constrained to have zero normal displacement are also shown in Fig. 5(b) for comparison. The radial stress at $\theta = 0$ from Fig. 5(b) is $\sim 2\sigma_a$, giving a value of ~ 240 MPa when interfacial separation began. This is very close in magnitude to the residual compressive stress normal to the interface (which has been estimated from relaxation experiments to be ~ 260 MPa), thus indicating that bonding at the interface is negligible and that the resistance to sliding is due entirely to friction. The largest shear stress occurs at $\theta \approx 35^\circ$ and is equal to $\sim 0.7\sigma_a$. At the onset of sliding ($\sigma_a = 100$ MPa) this shear stress is approximately 70 MPa. This

value is the same as the frictional stress that has been evaluated independently from fiber pulling experiments in this composite.

Transverse cracking before failure of the composite did not occur at the fibers that were analyzed here (such cracks were only observed at ~ 20% of the fibers within the test region. Nevertheless, the results in Fig. 4(a) indicate that circumferential sliding occurs over almost all of the interface at the stage where transverse radial cracking begins ($\sigma_a = 160$ MPa).

ACKNOWLEDGMENTS

Funding for this work was supplied by the U. S. Air Force Office of Scientific Research under Contract AFOSR 90-0235.

REFERENCES

1. D.B. Marshall, W.L. Morris, B.N. Cox, J. Graves, J. Porter, D. Kouris and R.K. Everett "Transverse Strengths and Failure Mechanisms in Ti_3Al Matrix Composites," submitted to Acta. Metall.
2. D. Kouris, "Stress Concentration due to the Interaction Between Two Imperfectly Bonded Fibers in a Continuous Fiber Composite," J. Appl. Mech. 60 [1] 203-206 (1993).
3. D. Kouris and E. Tsuchida, "On the Elastic Interaction Between Two Fibers in a Continuous Fiber Composite under Thermal Loading," Mech. Mat. 12 131-46 (1991).
4. J. Avestron, G.A. Cooper, and A. Kelly, "Single and Multiple Fracture" pp15-26 in the Properties of Fiber Composites, Conference Proc. of the National Physical Lab. IPL Science and Technology Press Ltd., Surrey, England, 1971.
5. D.B. Marshall and A.G. Evans, "Failure Mechanisms in Ceramic Fiber/Ceramic Matrix Composites," J. Am. Ceram. Soc. 68 [5] 225-31 (1985).

6. J.R. Jira and J.M. Larsen "Fatigue of Unidirectional SCS-6 /Ti-24Al-11Nb Composite Containing a Circular Hole (Parts I and II)," Met. Trans. in press.
7. D.P. Walls, G. Bao, and F.W. Zok, "Mode I Fatigue Cracking in a Fiber Reinforced Metal Matrix Composite," Acta. Metal. Mater. 41 [7] 2061-71 (1993).

FIGURE CAPTIONS

1. Stresses and cracking around a fiber subject to transverse loading.
2. Hoop stresses in matrix adjacent to fiber: dependence on fiber spacing and interfacial sliding.
3. In-plane surface displacements (obtained by high resolution differential image analysis) caused by applied transverse stress of 160 MPa. Reference arrow at bottom left represents displacement of 0.23 μm .
4. (a) Optical micrograph showing fiber used for measurements of (b).
(b) Normal and shear displacements at interface indicated in (a) measured by stereoscopic analysis of pairs micrographs obtained before and during loading.
5. Interfacial stresses due to applied load for pair of fibers with spacing of Fig. 4(a):
(a) normal stresses for fully bonded and freely sliding interface, (b) shear stresses.

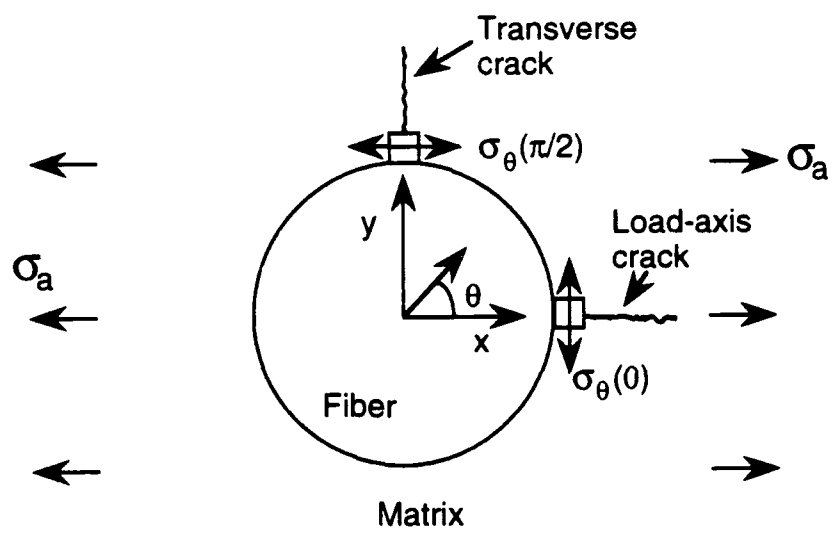


Fig 1

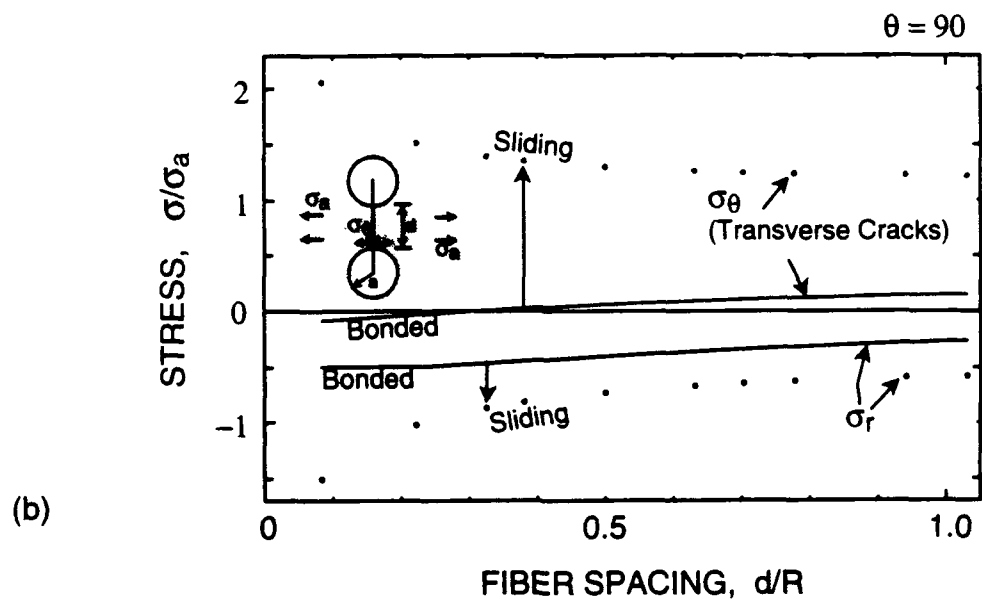
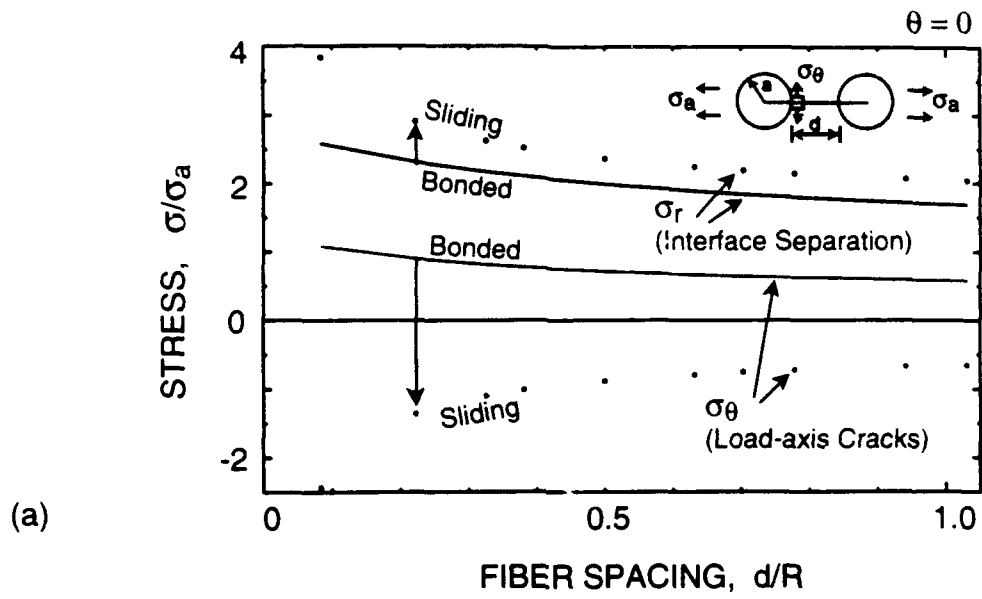
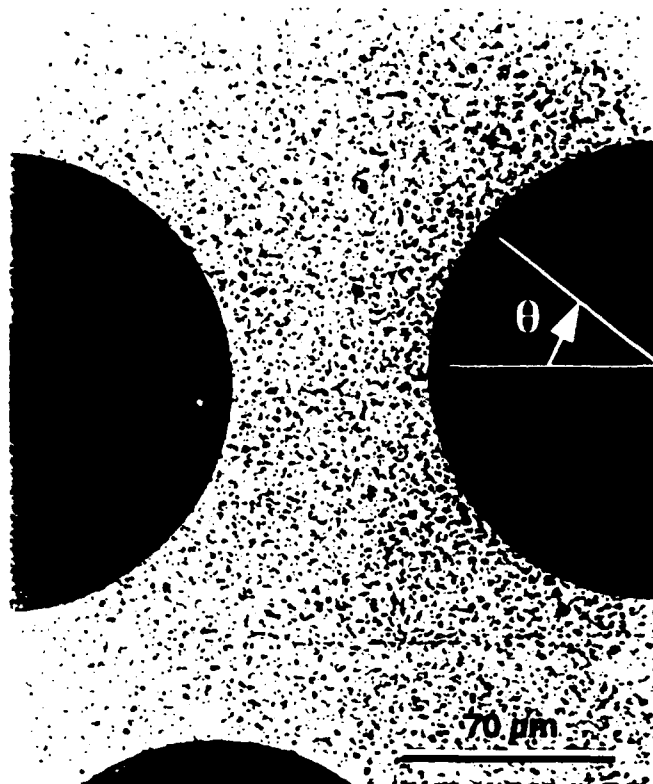
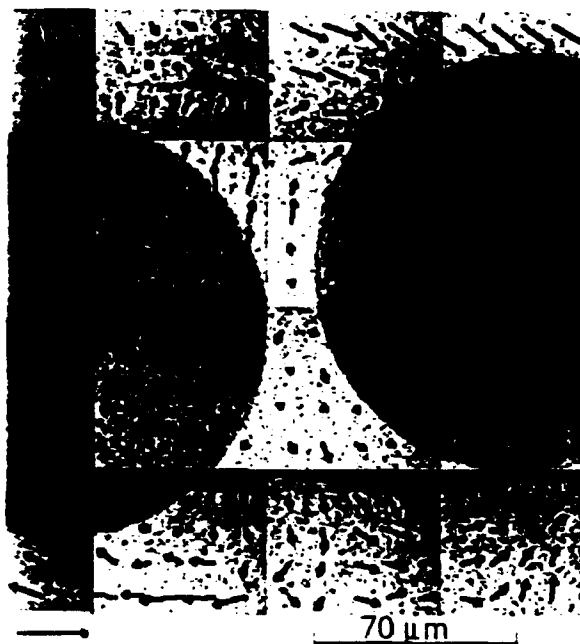
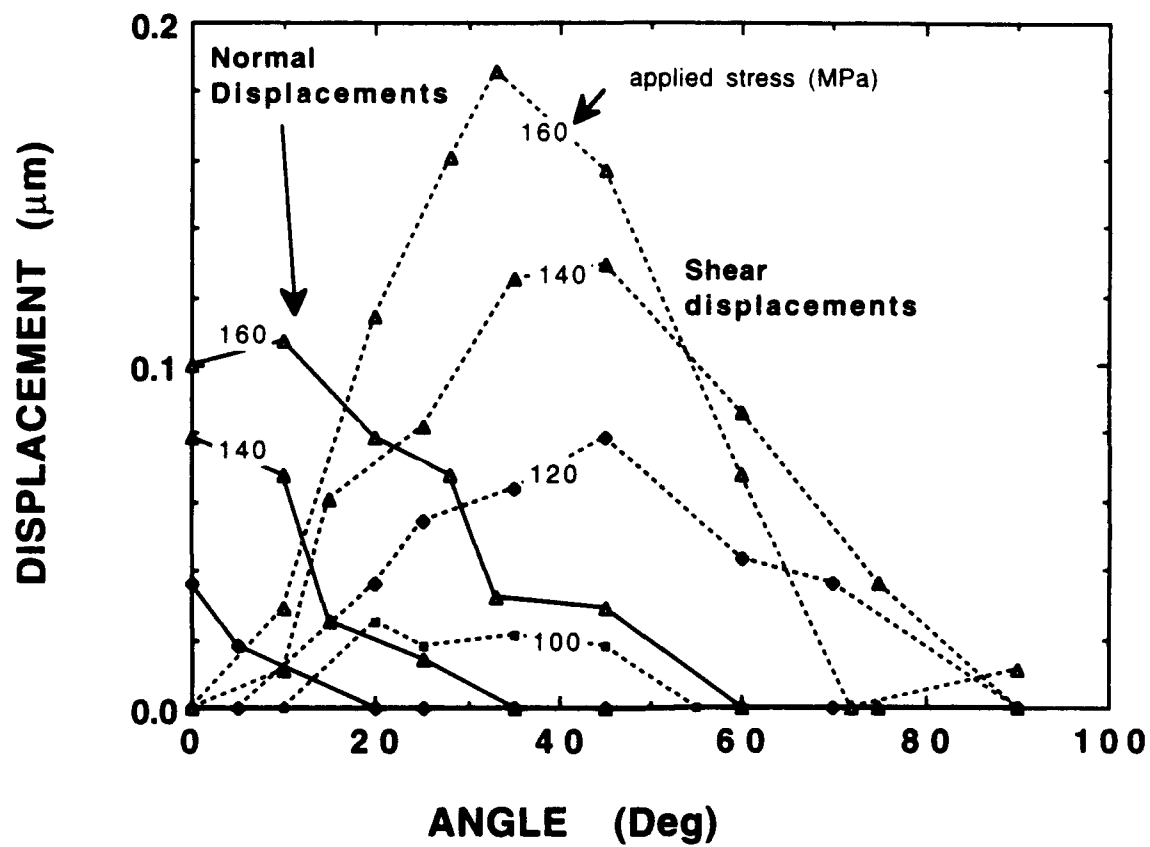


Fig. 2







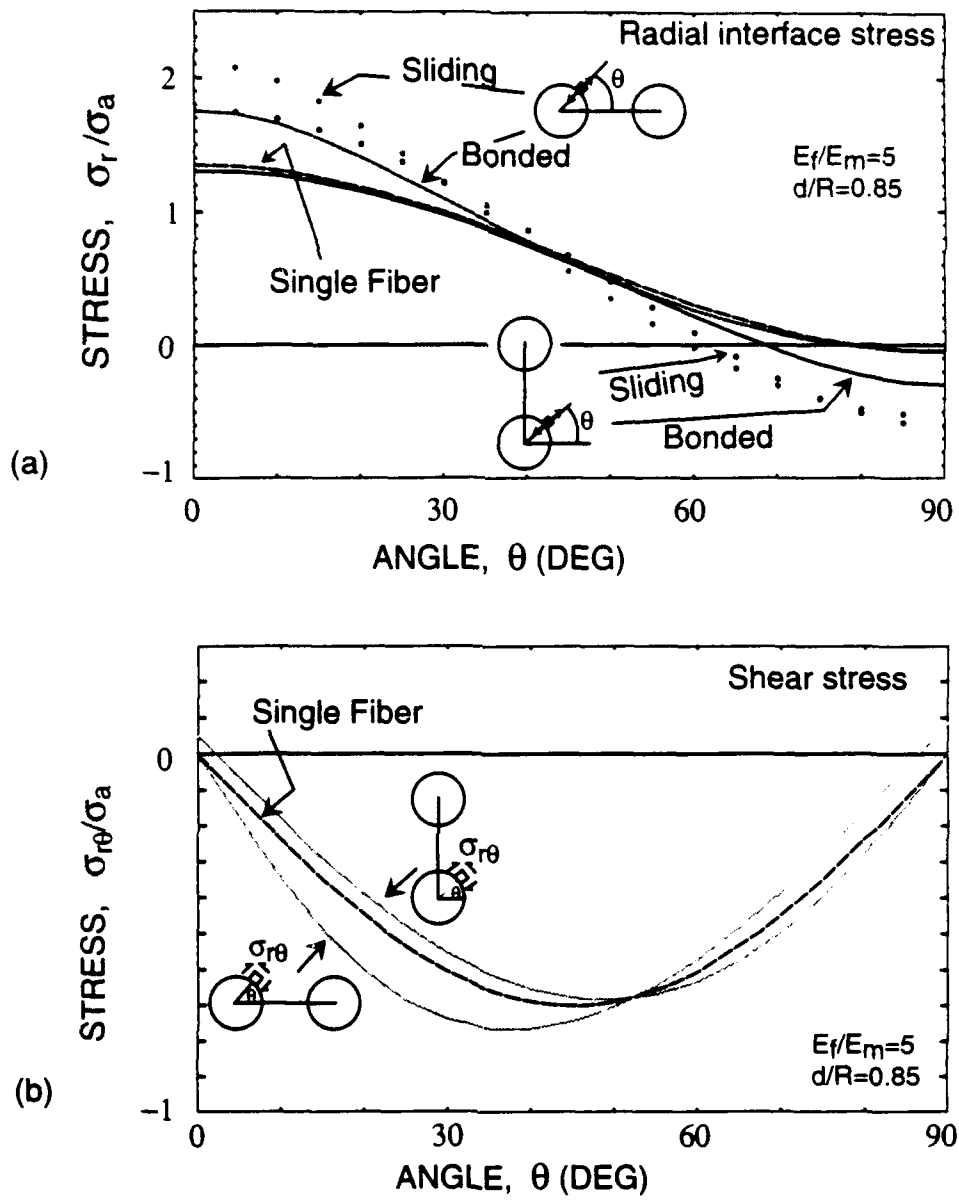


Fig 5

6.0 THE ROLE OF THE INTERFACE

6.1 Experimental Measurements of Interfacial Properties in Brittle Fibrous Composites

published in Ultramicroscopy

Experimental measurements of interfacial properties in brittle fibrous composites

B.N. Cox and D.B. Marshall

Rockwell International Science Center, 1049 Camino Dos Rios, Thousand Oaks, CA 91360, U.S.A

Received 20 February 1991; at Editorial Office 7 August 1991

The interfacial properties that control fracture in continuous-fiber-reinforced brittle matrix composites are discussed. Various methods of determining these properties are reviewed, including both experiments on individual fibers in specially prepared specimens and experiments based on observations of crack propagation. Because the information that can be acquired in any experiment is limited, deducing interfacial properties requires modeling based on prior assumptions about the underlying micromechanics. The validity of some of the more popular and convenient of these assumptions is appraised.

1. Introduction

Considerable progress has been made in the last twenty years in enhancing the damage tolerance or toughness of brittle materials by reinforcing them with strong, continuous fibers. In particular, when *aligned* fibers are coupled to a brittle matrix by weak interfaces, damage tolerance under *axial* loading can be quite remarkable: strength can become asymptotically independent of matrix flaw size as the flaw size increases [1–4]; and the overall strength of the composite is not far from the bundle strength of the reinforcing fibers [5,6].

Most of this paper will deal with the micromechanics of composite strength in just this configuration: axial loading for aligned fibers. This is in keeping with the vast majority of experimental and theoretical work in the field to date. Great emphasis has been laid on optimizing axial properties, to the exclusion and indeed detriment of properties under nonaxial loading. Some comments on how this historical omission will dictate

future developments appear at the end of the paper.

2. Failure of aligned-fiber composites under axial loading

For axial loading of aligned-fiber composites, the best damage tolerance is usually achieved if the matrix fails before the fibers, the fibers remain intact in the wake of any matrix crack, and such intact fibers supply significant shielding of the matrix crack tip by crack bridging. Under monotonic loading, the requirement that the matrix should fail first generally requires fibers of high strength, typical composites being SiC fibers in ceramics and glasses. For the fibers to remain intact in the crack wake, the interfaces must be weak, so that fiber strain can be relieved by interfacial sliding. In the recently popular Textron SCS6 SiC fiber, this condition is provided by the presence of a layer of turbostratic carbon in the carbon-rich fiber coating [7]. This layer is

essentially debonded at the outset of testing, supplying only frictional resistance to interfacial sliding. The degree to which the fibers then shield the matrix crack tip from the applied load is determined by the critical interfacial shear stress, τ , above which frictional sliding occurs [2]: the larger τ , the greater the shielding, with the proviso that if τ is too large, insufficient interfacial sliding will occur to protect the bridging fibers from failure, and most of the bridging effect will be lost altogether [8].

When ductile materials are reinforced by strong fibers (e.g., intermetallic alloys reinforced by the same SCS6 SiC fibers), matrix failure can still be the first failure, but under cyclic rather than monotonic loading [9–15]. The mechanics of the ensuing fatigue crack growth of the matrix crack are then very closely related to those of crack growth in brittle matrix composites under monotonic loading [11,12]. Greatly enhanced fatigue resistance is achieved if the interfaces are weak and the frictional sliding stress τ has a value that favors crack tip shielding by fiber bridging. Under monotonic loading, on the other hand, the first failure in such fibrous intermetallic composites is fiber failure. But once again the highest strengths are achieved if the interfaces are weak and slide easily, for then the matrix abutting each fiber break is protected from severe stress intensification and composite failure does not occur until the load is well above the fiber strength [9].

For aligned-fiber composites under axial loading, the requirements of interfacial properties are thus quite simply stated: interfacial *toughness* (the work of fracture for propagating an interfacial debond) should be low; while the resistance to interfacial sliding following debonding should be high enough to support shielding but not so high as to cause premature failure of the bridging fibers. Since the interfacial toughness should be low (ideally zero), there is little incentive for measuring it in these materials. It is enough to know from fracture experiments that it is not too high to cause trouble. In contrast, there is much to be gained from being able to measure the critical sliding stress, τ , since its magnitude is the prime controllable material parameter that deter-

mines the efficacy of bridging. The next sections describe methods of measuring τ .

3. Measuring the critical stress for frictional sliding

Methods for determining the frictional stress τ fall into two categories: experiments in which the response of an individual fiber in a composite is measured during some carefully controlled loading, and measurements of the properties of bridged cracks. All of these experiments have one very important characteristic: τ (or any other interface property) is never measured directly. The experiments yield only some kind of displacement as a function of some kind of load; and the data are never so rich as to define the underlying mechanisms of deformation *uniquely*. Values for τ (or some other property) can only be inferred when the data are interpreted according to some a priori model. The quality of the measurement ends up depending largely on the quality of the model.

3.1. Experiments on individual fibers

The most common experiments on individual fibers consist of either pushing or pulling a single fiber that has been exposed by sectioning or etching the composite and measuring its axial displacement [16–19]. When the fiber/matrix interface is strong, analyzing such an experiment is very complicated. The stress fields in the fiber and the matrix are difficult to calculate, involving some degree of interfacial debonding, singularities associated with the debond crack tip and any other flaws, plasticity, friction between debonded surfaces, statistical variance in interfacial properties, and all the complications associated with having an elastically inhomogeneous body (comprising fiber, matrix, and complex fiber coatings and reaction layers) subjected to nonuniform loads with axial symmetry disrupted by the presence of one or more free surfaces. Because of this complexity, there has not yet been a convincing demonstration of the measurement of debond energies by pushing or pulling experiments.

Fortunately, when the interface is weak, there is considerable accumulated evidence that the situation is much simpler [16,19]. With weak interfaces and moderate or low values of τ , interfacial sliding occurs over lengths much greater than the fiber radius, and the resistance to further sliding is dominated by friction along the sliding region and only weakly influenced by the energy required to propagate the debond crack. In fact, for many cases, including the SCS6 SiC fiber, the debond energy is negligible: the interface can be modeled as entirely debonded before the experiment begins. Furthermore, since sliding lengths are large, it has been shown by various experiments and theoretical calculations that the shear lag approximation [16,17,20] is very reasonable for this system. In other words, in the cylindrical coordinates of the fiber, the only nonzero shear stresses are those acting across the sliding interface itself. Fairly consistent values for τ are now available for experiments modeled using these assumptions. Nevertheless, there remain some intriguing and important problems.

One very important question is that of the interplay of Poisson's ratio and interface roughness. The usual depiction of frictional sliding is that Coulomb's law prevails: the friction stress τ is the product of the coefficient of friction and the normal stress σ_R at the interface. The normal stress is primarily a residual stress arising from thermal mismatch between fibers and matrix. The matrix usually has the higher coefficient of thermal expansion and shrinks down around the fiber during cool-down following processing. When a fiber is pushed or pulled, Poisson's effect tends to alter its radius and σ_R changes. This can have a substantial influence on the force/displacement relation for the loaded fiber and therefore on the inferred value of τ [20,21,23].

The role of interfacial roughness was recently illuminated by Jero and Kerans [24]. In their experiment, an SCS6 SiC fiber was pushed first one way through a glass matrix and then the other. The motion was resisted by friction. When the fiber returned to its initial position, there was a large drop in the load, which could be correlated with irregular features on the two sliding surfaces reseating in their original, matched posi-

tions. One infers that the friction stress rises significantly when the interface is unseated because rough features, when moved out of registry, force the sliding surfaces apart, raising σ_R . For the SCS6 SiC fiber, the spatial scale of the observed irregularities is $\sim 10 \mu\text{m}$. Since this is the same order as crack-opening displacements for matrix cracks in typical composite specimens, it must be concluded that the correct value of τ to be used in analyzing such cracks must reflect *both* the effects of Poisson's contraction and of interfacial roughness.

This question has been further illuminated by unusually precise fiber pull-out experiments conducted by Marshall, Shaw and Morris [25] using Ti-25Al-10Nb-3Mo-1V/SCS6 specimens. In their experiments, a single fiber is exposed and isolated by etching away a section of matrix in the middle of the specimen and cutting away all other fibers in the etched section. The two intact ends of the specimen, now joined by the single fiber, are gripped and loaded. The relative displacement of the fiber and the matrix is measured to within 100 Å at the point where the fiber enters the matrix using a computer-based image-matching technique [26]. The fiber is loaded in tension and unloaded at various stages during pull-out. When models are fitted to the load-displacement histories, it is found that the best model assumes that the friction stress τ is *uniform* along the sliding length of the interface. Thus, in this composite, Poisson's effect and surface roughness effects coincide in magnitude, canceling one another out in tensile loading to a good approximation. For other composites, one should not expect the same result.

The situation under cycling loading, as with fatigue crack growth in fibrous intermetallic matrix composites such as Ti₆Al/SCS6, is likely to be even more complicated. While shear lag models continue to predict force/displacement relations of simple form [11,16], repeated cycling in the fiber pull-out experiments [25] showed that the friction stress τ is affected by attrition. Unfortunately, the results of such tests on individual fibers do not necessarily reflect conditions in a composite near a matrix crack. There are large and potentially significant differences in the local

stress state, the degree of fiber bending, the range of the sliding displacement, etc. Therefore, it is desirable to develop ways of determining τ for cracks by measuring and modeling certain fracture characteristics. This is taken up in the next section.

3.2. Experiments on cracks

Analyzing a bridged crack requires a further level of modeling: not only must the sliding of individual fibers be modeled, but also the fracture mechanics of a crack with possibly large and dominant bridging tractions acting on or adjacent to the fracture surfaces. If the contribution of each bridging fiber is to be treated separately in detail and the details of the stress distributions around all fibers and near the crack tip are to be calculated in full, the fracture mechanics problem is a daunting one. Fortunately, when there are many bridging fibers, comparison with experiment shows that the problem can be greatly simplified by averaging the effect of the discrete fibers [2] to obtain a continuous bridging traction acting on an anisotropic but homogeneous medium without losing any essential aspect of the fracture or fatigue process. There then remain many interesting and unusual effects of specimen geometry and load configuration, especially when the bridging zone is large compared to specimen or crack dimensions, but these can all be dealt with conveniently and accurately [27–29]. Under the spatial averaging, the relationship between the load on an individual fiber and its displacement is replaced by a relationship $p(u)$ between the continuous bridging traction p and the crack-opening displacement u [2]. Knowledge of one is tantamount to knowledge of the other.

The relation $p(u)$ can be determined experimentally in several ways. For cyclic loading problems, they reduce to two general methods: analyzing fatigue-crack-growth data and analyzing measured crack-opening profiles. Crack-growth data are analyzed by specifying a parametric law for $p(u)$ (e.g., the predictions of shear lag theory with τ as the sole parameter), calculating the range of the crack tip stress intensity factor, ΔK_{tip} , and invoking some law (e.g., the Paris law)

to relate ΔK_{tip} to the crack-growth rate. Values of τ encouragingly consistent with those from experiments on individual fibers have been obtained in this way [15].

Information about $p(u)$ is obtained more directly from crack-opening profiles because the step of relating growth rates to ΔK_{tip} is obviated: $p(u)$ can be obtained from the profile at a single value of crack length [30]. The method is based on the relation (an integral equation) between the applied load, the specimen geometry, the bridging tractions, and the crack-opening displacement profile. This integral equation is most commonly solved for the crack-opening profile when everything else is known, with $p(u)$ taking specified form and values. Once the profile is known, ΔK_{tip} (or K_{tip}) can be calculated and all fracture properties predicted. To determine $p(u)$, the problem is simply turned around: the profile and load are measured and $p(u)$ is determined by the same integral equation.

Of course, if τ is degraded by attrition during fatigue, then there will not exist a unique relation $p(u)$ correct for the entire crack. In this case, p must be regarded simply as a function $p(x)$ of distance x from the crack front. But this function, too, is deducible from crack-opening profiles by the same method [30]. The full hysteresis loop for p and u at each position x can then be deduced from functions $p(x)$ inferred from profiles measured at successive points on a complete loading cycle for the cracked specimen. Examples of this procedure will be available at the completion of work now in progress.

4. Outlook

The fracture mechanics of mode-I cracks growing normal to unidirectional fibers are now well understood. For fatigue cracks in metal and intermetallic alloys reinforced by SCS6 fibers, the connection of engineering crack-growth data to interfacial properties measured by high-resolution microscopy is singularly complete. Interfacial sliding is known to occur in turbostratic carbon layers; experiments on single fibers have tested the validity of mechanical models of the sliding

and yielded values for the friction stress, τ : models of bridged cracks have dealt with the unusual effects of specimen shape and loading configuration when the bridging zone is large; and, after all this, a simple law between ΔK_{tip} and crack-growth rate is sufficient to reproduce with gratifying accuracy the dramatic effects of bridging. This is certainly one of the best understood, most accurately modeled shielding mechanisms ever studied in either monotonic fracture or fatigue.

However, the future remains full of challenge. Engineering applications of brittle matrix fibrous composites remain restricted by their failure under nonaxial loading. The most urgent current need is for composites with through-thickness strength and resistance to delamination or splitting under shear loading, compression, or impact. In answer to this need and in analogy to the case of polymer composites, brittle matrix composites with three-dimensional reinforcement (woven, knitted, braided, and stitched composites) are being developed. With their development entirely new research fields are being born, including studies of both composite mechanical properties (fracture, fatigue, etc.) and interfacial properties. The ideal interface for 3D brittle matrix composites may well be different from that for unidirectional composites, although it is intuitively appealing that damage tolerance will still be favored by relatively weak interfaces. However, interfacial sliding and other localized interfacial damage occurring during loading will be *strongly* influenced by the inevitably high curvature associated with 3D reinforcement. What the relevant interfacial properties are and how they are to be measured remain challenging problems for the future.

References

- [1] J. Aveston, G.A. Cooper and A. Kelly, in: *the Properties of Fiber Composites*, Conf. Proc. Nat. Phys. Lab. (IPC Science and Technology Press, Surrey, 1971) p. 15.
- [2] D.B. Marshall, B.N. Cox and A.G. Evans, *Acta Metall.* 33 (1985) 2013.
- [3] B. Budiansky, J.W. Hutchinson and A.G. Evans, *Acta Metall.* 34 (1986) 167.
- [4] L.N. McCartney, *Proc. Roy. Soc. A* 409 (1987) 329.
- [5] *The Processing and Mechanical Properties of High Temperature/High Performance Composites*, Eds. A.G. Evans and R. Mehrabian, Annu. Rep. DARPA URI Contract no. N00014-86-K-0755 (University of California at Santa Barbara, 1990).
- [6] A.G. Evans, in: *Mechanical Fatigue of Advanced Materials*, Proc. Engineering Foundation Conf., Eds. R.O. Ritchie, R.H. Dauskardt and B.N. Cox (MCE Publ., Birmingham, 1991).
- [7] X.J. Ning and P. Pirouz, *J. Mater. Res.* 6 (1991) 2234.
- [8] D.B. Marshall and B.N. Cox, *Acta Metall.* 35 (1987) 2607.
- [9] B.N. Cox, M.R. James, D.B. Marshall, W.L. Morris, C.G. Rhodes and M. Shaw, in: *Proc. 10th Int. SAMPE Conf.*, Birmingham, UK, July 1989, Eds. S. Benson, T. Cook, E. Trewin and R.M. Turner (Elsevier, Amsterdam, 1989).
- [10] W.S. Johnson, in: *Mechanical Fatigue of Advanced Materials*, Proc. Engineering Foundation Conf., Eds. R.O. Ritchie, R.H. Dauskardt and B.N. Cox (MCE Publ., Birmingham, 1991).
- [11] B.N. Cox and D.B. Marshall, *Fatigue and Fracture of Eng. Mater. and Struct.*, in press.
- [12] R.M. McMeeking and A.G. Evans, *Mech. Mater.* 9 (1990) 217.
- [13] M.D. Sensmeier and P.K. Wright, in: *Proc. TMS Fall Meeting, Symp. on Metal Matrix Composites*, Indianapolis, Indiana, November, 1989.
- [14] P. Kantzos, J. Telesman and L. Ghosn, in: *Proc. 3rd Symp. on Comp. Materials: Fatigue and Fracture*, Orlando, Florida, November, 1989, Ed. P.K. O'Brien (ASTM, Pennsylvania, 1990).
- [15] D. Walls, G. Bao and F. Zok, in: *Mechanical Fatigue of Advanced Materials*, Proc. Engineering Foundation Conf., Eds. R.O. Ritchie, R.H. Dauskardt and B.N. Cox (MCE Publ., Birmingham, 1991).
- [16] D.B. Marshall and W.C. Oliver, *J. Am. Ceram. Soc.* 70 (1987) 542.
- [17] A. Kelly and W.R. Tyson, *J. Mech. Phys. Solids* 13 (1965) 329.
- [18] A. Takuku and R.G.C. Arridge, *J. Phys. D* 6 (1973) 2038.
- [19] B.N. Cox, M.S. Dadkhah, M.R. James, D.B. Marshall, W.L. Morris and M. Shaw, *Acta Metall. Mater.* 38 (1990) 2425.
- [20] Y.-C. Gao, Y.-W. Mai and B. Cotterell, *J. Appl. Math. Phys.* 39 (1988) 550.
- [21] J.W. Hutchinson and H.M. Jensen, *Mech. Mater.* 9 (1990) 139.
- [22] B.N. Cox, *Acta Metall. Mater.* 38 (1990) 2411.
- [23] L.N. McCartney, *Proc. Roy. Soc. A* 425 (1989) 215.
- [24] P.D. Jero and R.J. Kerans, *Scripta Metall. Mater.* 24 (1990) 2315.
- [25] D.B. Marshall, M. Shaw and W.L. Morris, *Acta Metall. Mater.*, in press.
- [26] M.R. James, W.L. Morris and B.N. Cox, *Exp. Mech.* 30 (1990) 60.
- [27] B.N. Cox and D.B. Marshall, *Acta Metall. Mater.* 39 (1991) 579.
- [28] B.N. Cox, *Acta Metall. Mater.* 39 (1991) 1189.
- [29] B.N. Cox and C.S. Lo, *Acta Metall. Mater.*, in press.
- [30] B.N. Cox and D.B. Marshall, *Int. J. Fract.* 49 (1991) 159.

**6.2 Analysis of the Effect of Interfacial Roughness on Fiber Debonding and
Sliding in Brittle Matrix Composites**

to be submitted for publication in the Journal of Mechanics and Physics of Solids

ANALYSIS OF THE EFFECT OF INTERFACIAL ROUGHNESS ON FIBER DEBONDING AND SLIDING IN BRITTLE MATRIX COMPOSITES

T.A. Parthasarathy,¹ R.J. Kerans,² and D.B. Marshall³

¹ UES, Inc., Dayton, OH 45432

² Materials Directorate, WPAFB, OH 45433

³ Rockwell Science Center
1049 Camino Dos Rios
Thousand Oaks, CA 91360

ABSTRACT

Previous analyses of the relation between the force and displacement during fiber sliding (pushing or pulling) are extended to include effects of interfacial roughness. Analytical solutions are obtained for a linear roughness profile over the range of displacements that are smaller than the dominant half-wavelength of the roughness. With the equations expressed in normalized form, a convenient friction parameter, which defines the roles of the friction coefficient and the roughness angle, has been defined. For certain values of the friction parameter, the effect of the roughness negates the Poisson's contraction during fiber pulling, giving solutions that are very close to the response of a system with a constant frictional stress at the interface.

1.0 INTRODUCTION

In ceramic and intermetallic matrix composites, much of the benefit of fiber reinforcement derives from the effects of debonding and sliding at or near the interface between the fibers and the matrix.¹⁻³ Several recent studies have shown that the morphology of this debonded surface strongly influences the constrained sliding of the fibers and hence the properties of the composite. In composites with residual compression in the fibers, interfacial roughness is expected to increase the sliding resistance, while in composites with residual tension in the fibers, the coupling of the fibers and matrix may be due entirely to roughness.

Direct evidence for the influence of interfacial roughness comes from measurements of a reseating phenomenon in fiber pushout experiments, first observed by Jero and Kerans⁴ in glass matrix composites and confirmed by several other groups,⁵⁻⁷ in both pushout and pullout experiments in ceramic and titanium aluminide matrix composites. Other evidence includes: observations of stress birefringence caused by roughness mismatch after fiber sliding in glass/SiC composites;⁸ direct measurement of surface roughness in various fibers by laser interferometry and atomic force microscopy;^{9,10} the analysis of high resolution force-displacement measurements during single fiber pulling experiments in several titanium aluminide composites,¹¹ which suggested that interfacial roughness canceled the effect of Poisson's contraction of the fibers; and the observation of load oscillations during fiber pushc from composites containing sapphire fibers with periodic surface corrugations.¹²

Several analyses of fiber sliding have sought to include the effect of surface roughness. Kerans and Parthasarathy¹³ modeled the effect as a constant additional radial misfit strain between the fiber and matrix, which increased the normal stress and thus the sliding resistance (with the Coulomb friction law). This model is expected to be appropriate for a composite with nonperiodic roughness when the sliding displacements are larger than the dominant half-wavelength of the roughness, so that the asperities have slid over their nearest neighbors.

However, in many crack bridging problems, the sliding displacements are small, falling within the domain where the roughness does not become completely unseated. In that case, the misfit is related to the local sliding displacement and thus varies along the debonded region of interface. Bhihe and Evans¹⁴ obtained numerical self-consistent solutions for this problem for several glass matrix composites. Carter et al.^{5,15} analyzed the sliding of hemispherical asperities over each other and pointed out that for small displacements, the increased sliding resistance has two components; one due to the increased friction associated with the extra misfit and the other, an elastic component, due to the axial component of the normal contact force. However, the analysis focused on the large slip region where the elastic component averages to zero, although reference was made to unpublished numerical solutions for the small slip region. The purpose of this paper is to present analytical solutions for the small slip region, which allow the role of roughness to be easily identified as well as provide a means for analyzing fiber sliding experiments to extract the interfacial properties.

2.0 DESCRIPTION OF MODEL

As in previous analyses of fiber sliding with smooth interfaces, the composite with volume fraction $f = R_f/R$ of aligned continuous fibers is represented by a concentric cylinder model (Fig. 1). The analysis is restricted to composites with residual compressive stress acting across the fiber/matrix interface, as is usually the case with intermetallic matrix composites and sometimes the case with ceramic matrix composites. Pulling or pushing on the fiber at the end of the cylinder (which corresponds to a sectioned surface or a crack surface of the composite) causes a crack to grow along the fiber/matrix interface. The length of the debonded region is dictated by a fracture energy, G_c , at the crack tip and frictional sliding over the debonded surfaces.

2.1 Interfacial Morphology and Friction

The microscopic roughness over the debonded region is taken to have a linear sawtooth shape as depicted in Fig. 1, with amplitude, h , much smaller than the radius of the fiber. This roughness could arise from the debond crack following either pre-existing roughness on the surface of the fiber or an irregular path adjacent to the fiber (within the matrix or within a third phase at the fiber-matrix interface). The analysis will be restricted to cases where the local relative displacements of the fiber and matrix (i.e., sliding displacements) are everywhere smaller than the characteristic half-wavelength, d , of the roughness. In many crack bridging situations in ceramic and intermetallic matrix composites, the displacements are small enough to satisfy this condition. In this case, the actual values of h and d do not enter the analysis; the roughness is characterized by the angle θ (Fig. 1) and there is no assumption of periodicity in the roughness or uniformity in its amplitude, in either the axial or the circumferential directions.

The debond energy G_c will be affected by the roughness, because of local deflections of the crack front away from the Mode II orientation of the average fracture path. By analogy with analyses of the effect of crack-tip deflection on the Mode I fracture energy,¹⁵ G_c is also expected to be affected only by the angle θ and not by the amplitude and period of the roughness.

This model of roughness is an idealization, not only in the linear shape chosen, but also because surface roughness of real solids exists over size scales that span many orders of magnitude, from the atomic scale up to microscopic or macroscopic dimensions. Indeed, recent studies have demonstrated the fractal nature of surface roughness at size scales below some characteristic dimension, which may be determined by the method of surface preparation or by some microstructural feature such as grain size.^{10,17,18} Microscopic theories of friction invoke the presence of submicroscopic roughness to derive the friction law (e.g., Coulomb friction).¹⁷⁻²⁰

It is the dominant roughness at the upper size scale limit that is modeled here by the sawtooth shape. The influence of finer scale roughness is subsumed in the frictional stress, τ , that resists sliding, given by the Coulomb friction law applied *on a local scale* as indicated in Fig. 1:

$$\tau = \mu \sigma_n \quad (1)$$

where σ_n is the compressive stress normal to the interface (σ_n is negative) and the direction of τ is tangential to the interface.

The rough surfaces are assumed to slide over each other without locally distorting the surfaces. This has the important implication that as soon as sliding begins in say the positive direction, the facets oriented at the angle $-\theta$ (Fig. 1) lose contact, even when residual compressive residual stresses are present. At the same time, the radial misfit strain (and therefore the contact stress) increases at the facet oriented at the angle $+\theta$, by an amount ϵ_θ that is proportional to the magnitude of the local sliding displacement $u(z)$:

$$\epsilon_\theta = \frac{|u(z)| \tan \theta}{R_f} \quad (2)$$

The neglect of local elastic distortions due to the increased contact stress will be a reasonable approximation provided the asperity height and period are small compared with the fiber radius.

2.2 Sliding Displacements

The frictional sliding causes relative displacements of the fiber and matrix at the end of the cylinder ($z = \ell$). These displacements are measured in push/pull experiments and are related to the opening displacements of a bridged crack in the composite. The relative sliding displacement at position z is given by an integral of the axial strains in the fiber and matrix, which can be written (Appendix A)

$$u(z) = \left(\frac{1}{E_b} \right) \int_0^z \Delta \sigma_f dz \quad (3)$$

where E_b is an elastic modulus defined in Eq. (A11), and $\Delta\sigma_f$ is the difference between the axial stresses in the fiber at position z and at a location far ahead of the debond tip. The opening displacements of a bridged crack are given by Eq. (3) with $z = \ell$ and E_b replaced by E_b' of Eq. (A13).

The analysis of stresses and strains is summarized in Appendix A. The analysis is taken from the work of Hutchinson and Jensen²¹ who used the Lamé solution to evaluate stresses and strains in sections normal to the z -axis. This approximation is valid if the axial stresses vary slowly over distances comparable to the fiber radius, a condition that is satisfied if τ is small compared with the axial fiber stress, σ_f . The matrix is elastic and isotropic, while the fibers are transversely isotropic.

As far as possible, the notation here will follow that of Hutchinson and Jensen²¹ and a subsequent analysis of fiber sliding by Marshall,²² although some new normalizing parameters will be defined. Relations will also be given between these parameters and those used by Kerans and Parthasarathy¹³ in a related analysis.

There is a jump in the axial fiber stress, σ_f , from just behind to well ahead of the debond crack tip, which is dependent upon the fracture energy, G_c . This relation is given approximately by²¹

$$\gamma \equiv \sigma_f^- - \sigma_f^+ = 2 \left(\frac{E_b G_c}{R_f} \right)^{1/2}, \quad (4)$$

where the superscripts (+) and (-) denote quantities far ahead of, and just behind the crack tip. Comparison with full numerical solutions in Ref. 21 shows that Eq. (4) is a good approximation if the sliding distance exceeds 2 to 3 times the fiber radius. The error is shown to be $\sim \tau/\sigma_f$, and thus becomes less significant as the applied load increases.

Several other parameters defined in Ref. 22, which will be convenient to use later, are as follows:

$$\Gamma = \gamma + \sigma_{fo}^+ \quad (5a)$$

$$\sigma_{Ro} = \sigma_{fo}^+ / (A-1) \quad (5b)$$

$$\alpha = \sigma_{Ro} + \Gamma \quad (5c)$$

where σ_{fo}^+ is the residual axial stress in the fiber and A is a dimensionless elastic constant defined in Appendix A. Note that σ_{fo}^+ and σ_f^+ differ when the applied load and volume fraction are non-zero (Eq. (A1a)). For single fiber testing with $f \rightarrow 0$, the parameter Γ is equal to the applied stress needed to initiate debonding. For non-zero values of f , Γ is related to this initiation stress by $\sigma_a = \Gamma/(1-fa_1)$, where a_1 is an elastic constant defined in Eq. (A1). The residual stress parameter σ_{Ro} is equal to the applied stress at which the Poisson's contraction of the fiber cancels the residual radial stress at the fiber-matrix interface.

3.0 DISPLACEMENTS DURING FIBER PULLING

In this section, the relative displacements of the fiber and matrix at $z = \ell$ are evaluated as the stress σ_a applied to the end of the fiber is increased continuously from zero to a peak value σ_p (initial loading), decreased to a minimum value σ_{min} , and then increased again to σ_p . During initial loading, debonding and sliding progress stably along the fiber/matrix interface, whereas during unloading reverse sliding occurs. The unload/reload cycle exhibits hysteresis due to the frictional response of the interface. The fiber strength is assumed to be larger than σ_p , so that failure of the fiber does not occur.

3.1 Initial Loading

The equation governing the changes in axial fiber stresses can be derived from analysis of the equilibrium of forces acting on an element dz of fiber as shown in Fig. 2. Force resolution gives

$$\frac{d\sigma_f}{dz} = - \left(\frac{\tau}{R_f} + \frac{\sigma_n}{R_f} \tan \theta \right) \quad (6)$$

in the direction parallel to z , and

$$\sigma_r = (\sigma_n - \tau \tan \theta) / 2 \quad (7)$$

normal to z (σ_r is the average radial stress at the interface). Elimination of τ and σ_n from Eq. (6) using Eqs. (2) and (7) gives

$$\frac{d\sigma_f}{dz} = - \frac{2\mu'\sigma_r}{R_f} \quad (8)$$

where

$$\mu' = \frac{\mu + \tan \theta}{1 - \mu \tan \theta} \quad (9)$$

Two distinct effects of the interfacial roughness enter these equations: the increased friction due to the additional misfit strain of Eq. (1), which enters the analysis via the first term of Eq. (6) as well as the radial stress, σ_r ; and the direct effect of the axial component of the normal contact force at the inclined interface (second term of Eq. (6)). The second contribution can be evaluated alternatively from an energy balance argument, in which it is the rate of change in strain energy associated with the radial compression needed to accommodate the misfit strain. It is the axial force that would exist for a frictionless interface, thus giving a non-zero value for the right-hand side of Eq. (8) for $\mu = 0$, and $\theta \neq 0$. If, on the other hand, θ is zero, then Eq. (8) reduces to the familiar result for a smooth interface

$$\frac{d\sigma_f}{dz} = - \frac{2\mu\sigma_r}{R_f} \quad (10)$$

The radial stress, σ_r , differs from the stress for the smooth interface because of the additional misfit strain due to the roughness. From the analysis in Appendix B, the radial stress is given by

$$\sigma_r = \sigma_{r0}^* + \phi |u(z)| + b_1 \Delta \sigma_f(z) , \quad (11)$$

where σ_{r0}^+ is the radial residual stress ahead of the debond, $\phi |u(z)|$ is the contribution due to the roughness misfit, b_1 is a dimensionless elastic constant defined in Eqs. (A2) and (C1), and $b_1 \Delta\sigma_f(z)$ is the change in radial stress due to the change in axial stress (Poisson effect). The parameter ϕ that characterizes the roughness misfit is given by

$$\phi = \left(\frac{B E_m}{R_f} \right) \tan\theta \quad (12)$$

where E_m is the Young's modulus of the matrix and B is a dimensionless elastic constant (negative) defined in Eq. (B4).

The changes in axial fiber stresses can also be written in terms of the displacements by differentiating Eq. (3)

$$\Delta\sigma_f \equiv \sigma_f - \sigma_f^+ = E_b \frac{du(z)}{dz} . \quad (13)$$

After further differentiating Eq. (13) and combining the result with Eqs. (8), (11) and (13), the following differential equation is obtained

$$\frac{d^2 u}{dz^2} + \eta \frac{du}{dz} + \phi' |u| + \beta = 0 \quad (14)$$

where

$$\eta = 2\mu' b_1 / R_f , \quad (15a)$$

$$\phi' = \left(\frac{2\mu'}{E_b R_f} \right) \phi , \quad (15b)$$

and

$$\beta = \left(\frac{2\mu'}{E_b R_f} \right) \sigma_{r0}^+ = \frac{\eta}{E_b} (\alpha - \gamma) \quad (15c)$$

(The relation $\sigma_{r0}^+ = b_1 (\alpha - \gamma)$ from Eq. (A5) was used in Eq. (15c).) The boundary conditions are specified by conditions at the tip of the debonded region ($z = 0$):

$$u(0) = 0 \quad (16a)$$

and

$$\frac{du(0)}{dz} = (\sigma_f - \sigma_f^+)/E_b = \gamma/E_b \quad (16b)$$

the second of these being given by Eqs. (4) and (13). With these boundary conditions, Eq. (14) provides the solution for $u(z)$, i.e., the sliding displacements as a function of distance from the debond front. Once $u(z)$ is known, Eq. (13) provides the axial fiber stresses as a function of position. Then, with z equal to the debond length, ℓ , so that $\sigma_f = \sigma_a$, we have a pair of parametric equations from which the displacement $u(\ell)$ may be plotted as a function of the applied stress, with ℓ as the parametric variable.

The solution to Eq. (14) can be simplified by defining the following dimensionless parameters

$$u' = \left(\frac{\eta E_b}{\alpha} \right) u \quad (17a)$$

$$z' = \eta z \quad (17b)$$

$$x = (1 - 4\phi'/\eta^2) \quad (17c)$$

$$g = \gamma/\alpha \quad (17d)$$

Then Eq. (14) becomes

$$\frac{d^2 u'}{dz'^2} + \frac{du'}{dz'} + \left(\frac{1-x^2}{4} \right) |u'| + (1-g) = 0 \quad (18)$$

and the boundary conditions at $z' = 0$ become $u'(0) = 0$ and $\frac{du'(0)}{dz'} = g$. The solution of Eq. (18)

for $u' \geq 0$ (i.e., fiber pulling) is

$$\begin{aligned} u'(z') &= \frac{4(g-1)}{1-x^2} + \frac{g-gx-2}{x(1+x)} \exp\left(\frac{-(1+x)z'}{2}\right) - \left(\frac{g+gx-2}{x(1-x)}\right) \exp\left(\frac{-(1-x)z'}{2}\right) \\ &\equiv f_1(g, x, z') \end{aligned} \quad (19)$$

In terms of the same dimensionless parameters, Eq. (13) becomes

$$\begin{aligned}\frac{\sigma_f - \sigma_f^*}{\alpha} &\equiv \frac{du'}{dz'} = \left(\frac{g - gx - 2}{2x} \right) \exp\left(\frac{-(1+x)z'}{2} \right) + \left(\frac{g + gx - 2}{2x} \right) \exp\left(\frac{-(1-x)z'}{2} \right) \\ &\equiv f_2(g, x, z')\end{aligned}\quad (20)$$

Solution of Eqs. (19) and (20) at $z' = \ell$ provides the relation between the normalized sliding distance $(\eta E_b / \alpha)u$ and stress difference $\left(\frac{\sigma_a - \sigma_f^*}{\alpha} \right)$, which involves only two other material parameters, x and g . With Eqs. (5) and (17d), the parameter g can be written as

$$g = \frac{\Gamma - (A - 1)\sigma_{Ro}}{\Gamma + \sigma_{Ro}} = \frac{\Gamma' + (A - 1)}{\Gamma' - 1} \quad (21)$$

where $\Gamma' = -\Gamma/\sigma_{Ro}$. Therefore, g is a function only of the elastic constant A and the ratio of the debond energy to the residual stress. The range of g is from $(1-A)$ for zero debond energy to unity for zero residual stress. The dependence of A on the properties of the fibers and matrix has been evaluated in Ref. 22; values typical of ceramic and intermetallic matrix composites fall between 1.0 and ~ 1.5 for single fiber sliding and between ~ 0.5 and ~ 1.5 for multiple fiber sliding. The parameter x contains the influence of the interfacial roughness, and is dependent on the elastic properties, the angle θ , and the coefficient of friction μ (Eqs. (11), (15a), (15b) and (17c)):

$$x = (1 - 4\phi'/\eta^2)^{1/2} \quad (22a)$$

where

$$\begin{aligned}\phi'/\eta^2 &= \frac{BE_m \tan \theta}{2b_1^2 E_b \mu'} \\ &= B' \frac{(1 - \mu \tan \theta) \tan \theta}{\mu (1 + \tan \theta)}\end{aligned} \quad (22b)$$

$$B' = \frac{BE_m}{2b_1^2 E_b} \quad (22c)$$

The dimensionless elastic constant B' in Eq. (22c) is sensitive to the ratios of the elastic properties of the fibers and matrix (see Appendix C); for ceramic and intermetallic matrix composites its

value could range from approximately -5 to -25. Representative values for are: -13 for glass/SiC composites ($E_f = 200$ GPa, $E_m = 80$ GPa, $\nu_f = \nu_m = 0.3$, $f = 0.4$) and -25 for titanium-aluminide/SiC composites ($E_f = 415$ GPa, $E_m = 80$ GPa, $\nu_f = \nu_m = 0.3$, $f = 0.4$). The variation of x with θ for $B' = -25$ is shown in Fig. 3 for several values of friction coefficient μ . For most reasonable roughness angles and friction coefficients, x lies between ~ 1 and 8; $x = 1$ for a smooth interface, while x increases with increasing roughness angle or decreasing friction coefficient.

Before plotting the solutions to Eqs. (19) and (20), it is convenient to rewrite them as

$$u^* \equiv \left(\frac{\eta E_b}{-\sigma_{R0}} \right) u = (\Gamma' - 1) f_1(g, x, \ell') \quad (23)$$

and

$$S_a \equiv \frac{\sigma_a(1 - a_1 F)}{-\sigma_{R0}} = (1 - A) + (\Gamma' - 1) f_2(g, x, \ell') \quad (24)$$

The normalized displacements u^* during initial loading are shown in Fig. 4 for a composite with elastic properties typical of the titanium aluminide/SiC composites mentioned earlier ($A = 1.141$). In Fig. 4(a), curves $S_a(u^*)$ are plotted for various values of x with $\Gamma' = 0$, corresponding to $\gamma = \sigma_{fo}^+$ (i.e. the stress required to initiate debonding being zero). In Fig. 4(b), curves are plotted for three values of Γ' : (1) $\Gamma' = -(A-1)$ corresponding to $\gamma = 0$ (i.e., an unbonded interface), (2) $\Gamma' = 0$, and (3) $\Gamma' = (A-1)$, corresponding to $\gamma = 2\sigma_{fo}^+$. For each value of Γ' , curves are plotted for both smooth ($x = 1$) and rough ($x = 5$) interfaces.

While trends in the normalized displacement u^* can be evaluated in terms of the single roughness parameter x , which combines the effects of the friction coefficient μ and roughness angle θ , calculation of the absolute displacements requires that μ and θ be defined separately.* Since u^* is proportional to μ' (through the dependence of η on μ' in Eq. (15(a))), which increases

* More specifically, the parameter μ' is required. However, defining both x and μ' is equivalent to defining μ and θ .

with increasing θ , the relative decrease in absolute displacement with increasing θ (at given μ) is larger than the corresponding decrease in the normalized displacements in Fig. 4.

Spontaneous debonding and sliding can occur during formation of the free surface at $z = \ell$, if $\Gamma' \leq 0$. The spontaneous sliding displacement, u_0 , is given by the intercept on the u -axis in Fig. 4(b). In the modeling of bridged cracks, this displacement is part of the crack opening displacement. However, in fiber pulling experiments, the displacement measurements usually begin after formation of the free surface, so the curves should be shifted along the u -axis by $-u_0$.

3.2 Alternative Notation In Terms of Single Fiber Loads

In an earlier analysis of single fiber pushing experiments by Kerans and Parthasarathy,¹³ which is equivalent to the analyses of Refs. 21 and 22 in the limit $f = 0$, the applied loads were expressed in terms of the force, P , applied to the end of the fiber. An equivalent set of parameters were defined: P^* , the load at which the Poisson's contraction of the fiber cancels the residual normal stress; P_R , the residual axial stress in the fiber; and P_d , the load to initiate debonding. These parameters are related to those in this paper by

$$P^* = \pi R_f^2 \sigma_{R0} \quad (25a)$$

$$P_R = \pi R_f^2 \sigma_{f0}^+ \equiv (A - 1)P^* \quad (25b)$$

and
$$P_d = \pi R_f^2 \gamma \quad (25c)$$

Conversely, the parameters in Eqs. (19) and (20) are related to these forces by

$$\alpha = (P^* + P_d + P_R) / \pi R_f^2 \quad (26a)$$

$$\sigma_a - \sigma_f^+ = (P - P_R) / \pi R_f^2 \quad (\text{for } f = 0) \quad (26b)$$

$$g = \frac{P_d}{P^* + P_d + P_R} \quad (26c)$$

With these substitutions, Eqs. (19) and (20) become

$$\left(\frac{\pi R_f^2 \eta E_b}{P^*} \right) u = \left(1 + \frac{P_d + P_R}{P^*} \right) f_1 (g, x, z') \quad (27)$$

and

$$\frac{P}{P^*} = \frac{P_R}{P^*} + \left(1 + \frac{P_d + P_R}{P^*} \right) f_2 (g, x, z') \quad (28)$$

3.3 Unload/Reload Cycle

The axial fiber stresses during unloading, after loading initially to a peak load σ_p , are shown schematically in Fig. 5(a). Reverse sliding occurs within a distance $(\ell_p - s)$ of the end of the cylinder. The sliding distance, ℓ_p , during the initial loading to σ_p is defined by Eq. (20) with $\sigma_f = \sigma_p$ at $z' = \eta \ell_p$.

Within the region of reverse sliding, the direction of the frictional stress τ in Fig. 2 is reversed. With the appropriate sign changes in Eqs. (6) and (7), the counterpart of Eq. (8) becomes

$$\frac{d\sigma_f}{dz} = \frac{+2\mu^\dagger \sigma_r}{R_f} \quad (29)$$

where

$$\mu^\dagger = \frac{\mu - \tan \theta}{1 + \mu \tan \theta} \quad (30)$$

Then, following the same steps as those leading to Eq. (18), the normalized differential equation defining the displacements becomes

$$-\frac{d^2 u^\dagger}{d(z^\dagger)^2} + \frac{du^\dagger}{dz^\dagger} + \left(\frac{1 - (x^\dagger)^2}{4} \right) |u^\dagger| + (1 - g) = 0 \quad , \quad (31)$$

which differs from Eq. (18) only in the sign of the leading term and in the replacement of μ' by μ^\dagger in the definitions of all quantities with the superscript (\dagger), i.e.,

$$u^\dagger = u' (\mu^\dagger / \mu') \quad (32)$$

$$u^\dagger = u' (\mu^\dagger/\mu') \quad (32)$$

$$z^\dagger = z' (\mu^\dagger/\mu') \quad (32b)$$

and

$$1 - (x^\dagger)^2 = (1 - x^2) (\mu'/\mu^\dagger)^2 \quad (32c)$$

The boundary conditions are defined by matching u and du/dz at $z = s$ to the values at the peak load condition defined by

$$u'(s') = f_1(g, x, s') \quad (33a)$$

$$\frac{du'(s')}{dz'} = f_2(g, x, s') \quad (33b)$$

where $s' = \eta s$. The solution of Eq. (31) has the form

$$u^\dagger(z^\dagger) = f_3(g, x, s^\dagger, z^\dagger) \quad (34a)$$

$$\frac{\sigma_f - \sigma_f^\dagger}{\alpha} = \frac{du'}{dz'} = f_4(g, x, s^\dagger, z^\dagger) \quad (34b)$$

with $\sigma_f = \sigma_a$ at $z = \ell_p$. The solutions f_3 and f_4 are very lengthy and are not reproduced here. However, they are readily obtained using the symbolic mathematical program Mathematica.²³ To plot $u(\sigma_f)$ during unloading from $\sigma_a = \sigma_p$ to $\sigma_a = \sigma_{\min}$, s in the parametric Eqs. (34) is varied between $s = \ell_p$ and $s = s_{\min}$, with s_{\min} defined by Eq. (34b) with $\sigma_f = \sigma_{\min}$ at $s = s_{\min}$ and $z = \ell_p$. To plot the displacements with the same normalization as for the initial loading, it is necessary to multiply the solutions to Eq. (34) by (μ'/μ^\dagger)

During reloading (Fig. 5(b)), the differential equation for the displacements is the same as Eq. (18), and the boundary conditions, defined by matching u and du/dz at $z = t$ to the values at the minimum load, σ_{\min} , are

$$u'(t') = (\mu'/\mu^\dagger) f_3(g, x, s_{\min}^\dagger, t') \quad (35a)$$

and

$$\frac{du'(t')}{dz'} = f_4(g, x, s_{\min}^\dagger, t') \quad (35b)$$

The solution of Eq. (18) with these boundary conditions has the form

$$u(z') = f_5(g, x, s_{\min}^\dagger, t', z') \quad (36a)$$

$$\frac{\sigma_f - \sigma_f^\dagger}{\alpha} = f_6(g, x, s_{\min}^\dagger, t', z') \quad (36b)$$

with $\sigma = \sigma_a$ at $z = \ell_p$. Again, the functions f_5 and f_6 are not reproduced but are straightforward to obtain. To plot $u(\sigma_a)$ for reloading from σ_{\min} back to σ_p , the range of the parameter t in Eqs. (32a) and (32b) is the same as during unloading ($s_{\min} < t < \ell_p$).

The effect of roughness on the displacements during a load-unload-reload cycle is illustrated by the comparison in Fig. 6(a) for a smooth ($x = 1$) and a rough ($x = 5$) interface in a composite with $A = 1.14$, $\Gamma' = 0$, and $\theta = 11$ degrees. The roughness causes a reduction in the displacement during initial loading, and an increase in the relative amount of recovery and hysteresis during the unload-reload cycle. For a given value of x , the relative recovery and hysteresis increase with increasing roughness angle as shown in Fig. 6(b) (different values of θ give different unload-reload curves, but the same initial loading curve).

If the interfacial debond energy is sufficiently large ($\Gamma' > 0$), unloading from small values of σ_p can allow reverse slip over the entire debonded region (i.e., $s = 0$ in Fig. 5(a)). Then, for further unloading different boundary conditions are required. The equations are the same as discussed in the following section when spontaneous debonding occurs.

4.0 DISPLACEMENTS DURING FIBER PUSHING

The displacements caused by fiber pushing follow from an analysis that is similar to that for fiber pulling. With the applied stresses and the displacements being negative for pushing, the

differential equations defining the displacements are given by the corresponding equations for fiber pulling (Eqs. (18) and (31) with the signs of the first terms changed:

$$-\frac{d^2u'}{d(z')^2} + \frac{du'}{dz'} + \left(\frac{1-x^2}{4}\right)|u'| + (1-g) = 0 \quad (37)$$

for initial loading and

$$+\frac{d^2u^\dagger}{d(z^\dagger)^2} + \frac{du^\dagger}{dz^\dagger} + \left(\frac{1-(x^\dagger)^2}{4}\right)|u^\dagger| + (1-g) = 0 \quad (38)$$

for unloading.

The boundary conditions are dependent upon whether or not spontaneous debonding occurs. In the absence of spontaneous debonding, or for sufficiently high pushing forces, the sign of the stress jump at the debond is reversed (Fig. 7(a)), i.e., γ in all of the equations is replaced by

$$\gamma_c = -\gamma \quad (39)$$

With this sign change in γ_c , the parameters g and Γ take different values, g_c and Γ_c , given by substituting γ_c for γ in Eqs. (5), (17d) and (21). Thus, the stress-displacement relation during initial loading is given by Eq. (37) with the boundary conditions $u'(0) = 0$ and $\frac{du'(0)}{dz'} = g_c$.

If spontaneous debonding occurs ($\Gamma < 0$), the axial fiber stresses are altered, as shown schematically in Fig. 7(b) and analysis is somewhat more convoluted. The initial displacements are positive and are given by the equations for fiber pulling (Eqs. (19) and (20)) with peak load $\sigma_p = 0$. The displacements at low pushing forces ($|\sigma_a| < |\sigma_1|$) in Fig. 7(b)) are equivalent to those occurring during unloading in pulling (Eqs. (31) and (33)) from a peak load of $\sigma_p = 0$. However, with continued pushing, at stresses between σ_1 and σ_2 , the boundary conditions change. Within this stress interval, the stress jump at the debond tip varies from γ to γ_c as the applied load changes from σ_1 to σ_2 . The boundary conditions become $u'(0) = 0$ and $\frac{du(0)}{dz} = \gamma'$, where γ' is the stress jump at the debond tip. If we define g' from Eq. (21) by substituting γ' for γ , the second

boundary condition is $\frac{du'(0)}{dz'} = g'$. Then with the debond length fixed at $\ell = \ell_0$ (the solution of Eq. (20) at $\sigma_f = 0$), the solution to Eq. (31) provides a pair of parametric equations for stress and displacement with g' as the parametric variable ($g_c < g' < g$). This solution holds as long as the displacements are positive. At some stress between σ_1 and σ_2 , the displacement at $z = \ell_0$ becomes zero and, with further load increase up to σ_2 , a zone over which the displacements are negative spreads along the debonded region from $z = \ell_0$ to $z = 0$. Within this stress range, it is necessary to solve for the position $z = z_0$ at which $u(z_0)$ is zero, calculate the displacements over the interval $0 \leq z \leq z_0$ using the solution for positive displacements (Eq. (31)), and then calculate the displacements over the interval $z_0 \leq z \leq \ell_0$ using Eq. (37) with the boundary conditions defined by matching the solutions for u and $\frac{du}{dz}$ at $z = z_0$. At stresses between σ_2 and σ_3 , the displacements are negative over the entire debonded region and the displacements are given by Eq. (37) with the abovementioned boundary conditions with γ' varying from 0 to γ_c . At stresses larger in magnitude than σ_3 , the solutions are the same as for no spontaneous debonding, as described in the previous paragraph.

Stress-displacement curves for fiber pushing are plotted in Figs. 4 and 6 for the same range of parameters as used for the fiber pulling curves. Similar trends are evident, although the displacements, both with and without roughness, are smaller in fiber pushing; and the effect of a given roughness (i.e., given x) is larger in pulling than in pushing. In addition, the relative recovery of displacement during unloading is larger in fiber pushing than in pulling.

5.0 DISCUSSION

During fiber pullout the additional misfit strain ϵ_0 due to interfacial roughness tends to cancel the transverse Poisson's contraction of the fiber. The degree to which these effects can cancel may be seen by comparing the curves of Fig. 4(a) with the stress-displacement relation for a smooth interface with a constant frictional stress, τ_0 , over the debonded region.²² In terms of the normalized parameters defined here, this relation is

$$u^* = \left(\frac{\mu' \sigma_{ro}}{\tau_o} \right) \left[S_a^2/2 + (A-1)S_a - \Gamma'^2/2 - (A-1)\Gamma' \right] \quad (34)$$

The result for $\tau_o = \mu' \sigma_{ro}$ is plotted in Fig. 8. Since σ_{ro} is the normal interfacial stress when the axial stress in the fiber is zero, this value of τ_o is the corresponding frictional stress given by the Coulomb friction law with friction coefficient μ' . For applied stresses in the range $0 < \sigma_a < \sigma_{ro}$ the constant friction results are very close to those of the rough interface with $x = 3$. At higher applied stresses some deviation towards lower values of x is evident. For a friction coefficient of 0.4 the value $x = 3$ corresponds to $\theta = 2^\circ$, a reasonable value for typical interfaces in composites containing SiC fibers produced by CVD.⁹

Measurements of stress-displacement relations in titanium-aluminide/SiC composites have been reported with very close fit to the constant friction model up to applied stresses as high as $\sim 2\sigma_{ro}$.¹¹ Such response, which deviates from the linear roughness results in Fig. 8, could be produced by a non-linear roughness profile that would more closely model the asperities typically observed on SiC fibers. The analysis of a nonlinear roughness profile would begin with the same formulation developed here, but would require some local elastic distortion of the asperities (to avoid point contacts that would result from sliding of nondistorting surfaces with nonlinear profiles), and would lead to a different functional dependence on $u(z)$ in Eq. (2) and hence in the third term of the differential equations (e.g., Eq. (14)).

ACKNOWLEDGEMENT

Funding for the work at Rockwell Science Center was supplied by the U.S. Air Force Office of Scientific Research under Contract No. AFOSR 90-235 and by Rockwell Independent Research and Development funds.

REFERENCES

1. J.G. Aveston, Cooper and A. Kelley (1971), Single and multiple fracture, in Properties of Fiber Composites, *Proceedings of the National Physical Laboratories*, IPC Science and Technology Press Ltd., U.K., 1971, 15-26.
2. K.M. Prewo and J.J. Brennan, "High Strength Silicon Carbon Fiber Reinforced Glass Matrix Composites," *J. Mater. Sci.* 15[2], 463-68 (1980).
3. D.B. Marshall and A.G. Evans, "Failure mechanisms in ceramic fiber/ceramic matrix composites", *J. Am. Ceram. Soc.* 68, 225-231 (1985).
4. J.D. Jero and R.J. Kerans, "The Contribution of Interfacial Roughness to Sliding Friction of Ceramic Fibers in a Glass Matrix", *Scripta Metall. Mater.* 24, 2315-18 (1990).
5. W.C. Carter, E.P. Butler and E.R. Fuller, "Micro-Mechanical Aspects of Asperity-Controlled Friction in Fiber-Toughened Ceramic Composites", *Scripta Metall. Mater.* 25, 579-584 (1991).
6. P.D. Warren, P.D., T.J. Makin and A.G. Evans, "Design, Analysis and Application of an Improved Push-Through Test for the Measurement of Interface Properties in Ceramics", *Acta Metall. Mater.* 40[6], 1243-49 (1992).
7. T.J. Makin, P.D. Warren and A.G. Evans, "Effects of Fiber Roughness on Interface Sliding in Composites", *Acta Metall. Mater.* 40[6], 1251-57 (1992).
8. P.D. Jero, R.J. Kerans and T.A. Parthasarthy, "Effects of Interfacial Roughness on the Frictional Stress Measured Using Push-Out Tests", *J. Am. Ceram. Soc.* 74[11], 2793-2801 (1991).
9. P.D. Jero,

10. T.L. Warren, A. Majumdar and D. Krajcinovic, "Atomic-Force Microscope Imaging of the Surface Roughness of SCS and TiB₂ Coated SiC Fibers and Uncoated Sapphire Fibers", *Composites*, in press.
11. D.B. Marshall, M.C. Shaw and W.L. Morris, "Measurement of Interfacial Debonding and Sliding Resistance in Fiber Reinforced Intermetallics", *Acta Metall. Mater.* 40[3], 443-454 (1992).
12. T.J. Makin, J.Y. Yang, C.G. Levi and A.G. Evans, "Environmentally Compatible Double Coating Concepts for Sapphire Fiber Reinforced γ -TiAl", *Mater. Sci. Eng.* A161, 285-93 (1993).
13. R.J. Kerans and T.A. Parthasarathy, "Theoretical Analysis of the Fiber Pull-out and Push-out Tests", *J. Amer. Ceram. Soc.* 74[7], 1585-1596 (1991).
14. C.K. Bhihe and A.G. Evans, "Rough Fiber Pullout in Brittle Matrix Composites: Experiments and Simulations", *Ceramic Engineering and Science Proceedings*, 17th Annual Conference on Composites and Advanced Ceramics, January 1993.
15. E.R. Fuller, E.P. Butler and W.C. Carter, "Determination of Fiber-Matrix Interfacial Properties of Importance to Ceramic Composite Toughening", *Proc. of NATO Conf. on Toughening Mechanisms in Quasi Brittle Materials*, Kluwer Academics Press, S.P. Shah, ed., 385-403 (1991).
16. K.T. Faber and A.G. Evans, "Crack Deflection Processes—I. Theory", *Acta Metall.* 31[4], 565-76 (1983).
17. A. Majumdar and B. Bhushan, "Fractal Model of Elastic-Plastic Contact Between Rough Surfaces", *Trans ASME Journal of Tribology* 113[1], 1-11 (1991).

18. B. Bhushan and A. Majumdar, "Elastic Plastic Contact Model for Bifractal Surfaces", *Wear* **153**, 53-64 (1992).
19. F.P. Bowden and D. Tabor, Friction and Lubrication of Solids, Parts I and II, Clarendon Press, Oxford, UK (1964).
20. J.A. Greenwood and J.B.P. Williamson, "Contact of Nominally Flat Surfaces", *Proc. Roy. Soc. Lond.* **A295**, 300-319 (1992).
21. J.W. Hutchinson and H.M. Jensen, "Models of fiber debonding and pullout in brittle composites with friction", *Mech. of Matls.*, **2**, 139-163 (1990).
22. D.B. Marshall, "Analysis of fiber debonding and sliding experiments in brittle matrix composites, *Acta Metall. Mater.* **40**, 427-441 (1992).
23. Wolfram Research, Inc., Mathematica, A System for Doing Mathematics, Pub. Addison-Wesley, Redwood City, CA.
24. B.N. Cox, "Interfacial Sliding Near a Free Surface in a Fibrous or Layered Composite During Thermal Cycling", *Acta Metall. Mater.*, **38**[12], 2411-24 (1990).

APPENDIX A: STRESS-STRAIN RELATIONS

The analysis of stresses and strains is based on the work of Hutchinson and Jensen.²¹ The matrix is taken as elastic and isotropic with Young's modulus E_m . The fiber is taken to be transversely isotropic with Young's moduli E_f and E_r in the axial and transverse directions; and Poisson's ratios ν_f and ν_r governing transverse Poisson's strains due to axial and transverse loading, respectively.* The properties ν_r and E_r enter the analysis via the parameter $\xi_f \equiv \left(\frac{1 - \nu_r}{1 - \nu_f} \right) \frac{E_f}{E_r}$; for isotropic fibers $\xi_f = 1$.

There are two contributions to the elastic misfit strain between the fibers and matrix. One arises from the difference in thermal contraction of the fibers and matrix during cooling from the fabrication temperature, with components ϵ_r^T and ϵ_z^T in the radial and axial directions (defined alternatively by the parameters $\epsilon^T \equiv \epsilon_r^T$ and $\lambda = \epsilon_r^T / \epsilon_z^T$). If the residual stresses cause yielding of the matrix during cooling from the fabrication temperature, *both* ϵ^T and λ may differ from values calculated for a purely elastic response during cooling. The other contribution is a radial misfit strain associated with the sliding displacements of the rough interface. This contribution is proportional to the magnitude of the local sliding displacement, $u(z)$, and is therefore dependent on the applied load and position along the fiber, as defined in Eq. (1).

Stresses and strains in any section transverse to the z axis were evaluated on the basis of the Lamé solution, an approximation that is valid if the axial stresses vary slowly over distances comparable to the fiber radius. This condition is satisfied if τ is small compared with the axial stress in the fiber, σ_f . Two types of boundary conditions on the outer cylindrical surface were considered: Type I has zero normal and shear tractions, whereas Type II also has zero shear tractions, but has radial displacement, u_r , constrained to be the same as its value far ahead of the

* For a transversely isotropic material loaded in the axial or transverse directions there are three Poisson's ratios ν_{zz} , ν_{zz} and ν_{rr} , where ν_{ij} refers to strain in direction i due to stress in direction j . However, since ν_{zz} and ν_{rr} are related by $\nu_{zz} = \nu_{zz} E_r / E_f$, only two of the Poisson's ratios, $\nu_{rz} \equiv \nu_f$ and $\nu_{rr} \equiv \nu_r$, in addition to the Young's moduli E_f and E_r , are needed to specify the elastic response.

debond crack. Type I conditions are appropriate for single fiber pulling or pushing experiments and in general at positions well ahead of the debond crack. Type II conditions are appropriate over the debonded region of a composite in which all fibers are pulled equally (such as bridging fibers within a crack), provided the slip length is small compared with the specimen width. Type II conditions were also used by Cox²⁴ in analyzing sliding of fibers near a free surface during thermal cycling, whereas earlier analyses used only Type I boundary conditions. Large differences in load-displacement relations can result from these different boundary conditions.²²

The axial stresses, σ_f , in the fiber during initial loading are shown schematically in Fig. 1(b). Well ahead of the debonded region the stresses and strains are constant and given by the Lamé problem with Type 1 boundary conditions, as well as the conditions that the axial strains ϵ_f and ϵ_m in the fiber and matrix be equal and the normal stresses and displacements at the fiber/matrix interface be continuous. With the superscript (+) denoting positions well ahead of the debond crack, the subscript (r) denoting radial stresses, strains and displacements at the interface, and the subscripts (f) and (m) denoting axial quantities in the fiber and matrix, the stresses and strains* in the absence of roughness effects are given by:

$$\sigma_f^+ = a_1 f \sigma_a - a_2 E_m \epsilon^T \quad (A1a)$$

$$\sigma_r^+ = a_3 f \sigma_a - a_4 E_m \epsilon^T \quad (A1b)$$

$$\epsilon_f^+ = \epsilon_m^+ = a_5 f \sigma_a / E_m + a_6 \epsilon^T \quad (A1c)$$

where the a's are nondimensional functions of f , E_f/E_m , ν_f , ν_f/ν_m , ξ_f , and λ , given in Ref. 21, and σ_a is the axial stress in the loaded end of the fiber. The residual stresses in the fibers, in the absence of debonding and sliding, given by Eq. (A1) with $\sigma_a = 0$, will be denoted σ_{fo}^+ and σ_{ro}^+ . To maintain analytical tractability, the analysis will be restricted to cases where the radial stresses

* Strains in both the fibers, ϵ_f^+ , and matrix ϵ_m^+ are measured relative to the unstressed state of the matrix.

ahead of the debond crack are independent of the applied load, i.e., $\sigma_r^+ = \sigma_{r0}^+$. This is satisfied for either $f = 0$ or $v_f = v_m$ (which gives $a_3 = 0$).

Behind the debond crack tip the *changes* in stresses and strains relative to their values far ahead of the crack (i.e., $\Delta\sigma_f = \sigma_f - \sigma_f^+$, $\Delta\epsilon_f = \epsilon_f - \epsilon_f^+$, etc.) are given by the Lamé problem without mismatch strain and, since there is relative sliding, with $\Delta\epsilon_f \neq \Delta\epsilon_m$. With continuity of $\Delta\sigma_r$ and Δu_r across the interface, and the equilibrium requirement $f\Delta\sigma_f + (1-f)\Delta\sigma_m = 0$, the stresses and strains may be written as

$$\Delta\sigma_m = \left(\frac{f}{1-f}\right) \Delta\sigma_f \quad (\text{A2a})$$

$$\Delta\sigma_r = b_1 \Delta\sigma_f \quad (\text{A2b})$$

$$\Delta\epsilon_f = b_2 \Delta\sigma_f / E_m \quad (\text{A2c})$$

$$\Delta\epsilon_m = -b_3 \Delta\sigma_f / E_m \quad (\text{A2d})$$

where the b 's are another set of nondimensional functions of the same parameters as the a 's (with the exception of λ) given in Ref. 21. There are two sets of b 's corresponding to Type I and Type II boundary conditions.

The radial stresses just behind the crack tip, σ_r , and well ahead of the crack tip, σ_r^+ , are related by

$$\sigma_r = \sigma_r^+ + b_1 \Delta\sigma_f \quad (\text{A3})$$

With γ defined in Eq. (4) and α defined as

$$\alpha = \sigma_r^+ / b_1 \quad (\text{A4})$$

Eq. (A3) becomes

$$\alpha = \frac{\sigma_r^+}{b_1} + \gamma \quad (\text{A5})$$

Then with the approximation $\sigma_f^+ = \sigma_{f0}^+$, as discussed above, and with the relation $\sigma_{f0}^+ = (a_4/a_2) \sigma_{f0}^+$ from Eqs. (A1a) and (A1b), Eq. (A5) can be written as

$$\alpha = \sigma_{R0} + \Gamma \quad , \quad (A6)$$

where

$$\Gamma = \gamma + \sigma_{f0}^+ \quad , \quad (A7)$$

$$\sigma_{R0} = \sigma_{f0}^+ / (A - 1) \quad , \quad (A8)$$

and

$$A = \left(1 - \frac{a_2 b_1}{a_4} \right)^{-1} \quad . \quad (A9)$$

Two displacements are of interest. The relative displacement of the fiber and matrix at $z = \ell$ (which corresponds to the measurements obtained in fiber pulling/pushing experiments) is given by

$$\delta = \int_0^\ell (\epsilon_f - \epsilon_m) dz = \frac{1}{E_b} \int_0^\ell \Delta \sigma_f dz \quad , \quad (A10)$$

where

$$E_b = E_m / (b_2 + b_3) \quad (A11)$$

and is, therefore, proportional to the shaded area in Fig. 1(b). The displacement that is used as the crack opening in continuum models of crack bridging is the additional fiber displacement due directly to debonding and sliding, given by

$$\Delta = \int_0^\ell (\epsilon_f - \epsilon_f^+) dz = \frac{1}{E_b} \int_0^\ell \Delta \sigma_f dz \quad . \quad (A12)$$

where

$$E'_b = E_m/b_2 \quad (A13)$$

The displacements δ and Δ are related simply by

$$\Delta = \left(\frac{b_2}{b_2 + b_3} \right) \delta \quad (A14)$$

Equation (A14) relates the displacements measured in a *multiple* fiber pulling experiment directly to the crack opening in bridging models for given fiber stress, σ_a . However, the relation is less direct for single fiber pulling experiments, because in that case δ is evaluated using Type I boundary conditions, whereas δ for the multiple fiber pulling (and crack opening) is evaluated with Type II boundary conditions over the debonded region.

APPENDIX B: RADIAL INTERFACIAL STRESS IN SLIP REGION

The radial stress over the debonded region of interface is given by (Eq. (A2b)):

$$\begin{aligned}\sigma_r &= \sigma_r^+ + b_1 \Delta\sigma_f \\ &= \sigma_r^+ + b_1 \sigma_f - b_1 \sigma_f^+ .\end{aligned}\quad (B1)$$

In the absence of interfacial roughness, Eq. (B1) can be written (with Eqs. (A1a) and (A1b)) as

$$\sigma_r = (a_3 - b_1 a_1) f \sigma_a + (b_1 a_2 - a_4) E_m \epsilon^T + b_1 \sigma_f . \quad (B2)$$

The second term in Eq. (B2) represents the contribution to σ_r from the radial component of the misfit strain ($\lambda \epsilon^T$). Therefore, the additional radial misfit strain ϵ_θ due to interfacial roughness results in superposition of the following radial stress

$$\sigma_r^\theta = B E_m \epsilon_\theta \quad (B3)$$

where

$$B = \frac{(b_1 a_2 - a_4)}{\lambda} = \frac{-a_4}{A\lambda} \quad (B4)$$

The dimensionless elastic parameter B is negative and independent of λ . The resultant radial stress over the debonded region of a rough interface is (Eqs. (B1), (B3) and (1))

$$\sigma_r = \sigma_r^+ + \phi |u(z)| + b_1 \Delta\sigma_f \quad (B5)$$

where

$$\phi = \left(\frac{B E_m}{R_f} \right) \tan \theta . \quad (B6)$$

APPENDIX C: ELASTIC CONSTANTS

The elastic constants a_i and b_i that appear in Appendix A can be evaluated from expressions given in Hutchinson and Jensen²¹ or are available on a computer file from the authors. For the case $f = 0$, with isotropic mismatch strain, and an isotropic fiber, the elastic constants that appear explicitly in the body of this paper are given by the following expressions:

$$b_1 = \frac{E_m v_f}{E_f(1 + v_m) + E_m(1 - v_f)} \quad (C1)$$

$$B = \frac{b_1 a_2 - a_4}{\lambda} = \frac{-E_f}{E_f(1 + v_m) + E_m(1 - v_f)} \quad (C2)$$

$$A = \left(1 - \frac{b_1 a_2}{a_4}\right)^{-1} = \frac{(1 + v_f)[E_f(1 + v_m) + E_m(1 - v_f)]}{E_f(1 + v_m) + E_m(1 - v_f - 2v_f^2)} \quad (C3)$$

$$E_b = \frac{E_m}{(b_2 + b_3)} = \frac{E_f[E_f(1 + v_m) + E_m(1 - v_f)]}{E_f(1 + v_m) + E_m(1 - v_f - 2v_f^2)} \quad (C4)$$

$$E'_b = E_b \quad (C5)$$

$$B' \equiv \frac{BE_m}{2b_1^2 E_b} = \frac{E_f(1 + v_m) + E_m(1 - v_f - 2v_f^2)}{-2E_m v_f^2} \quad (C6)$$

These results would apply for a single fiber in an infinite matrix. For the more common testing configuration involving pushing or pulling of a single fiber within a composite containing many fibers, the constants a_i should be evaluated using the value of f corresponding to the composite, whereas the constants b_i should be evaluated using $f = 0$. For the pulling or pushing of multiple fibers, all of the constants a_i and b_i are evaluated using the value of f for the composite, with b_i being evaluated using type II boundary conditions.

Figure Captions

- Fig. 1 (a) Composite cylinder model used for analysis. (b) Axial stresses in fiber during initial loading (shown for case $f = 0$).
- Fig. 2 Stresses acting on an element dz of fiber.
- Fig. 3 Variation of roughness parameter x with μ and θ for $B' = 25$.
- Fig. 4 Stress-displacement relations for single fiber sliding in pushing and pulling: (a) effect of roughness parameter x for $\Gamma = 0$; (b) results for several values of Γ and x .
- Fig. 5 Axial stresses in fiber subjected to pulling force: (a) unloading and (b) reloading after loading initially to peak local σ_p (shown for case $f = 0$).
- Fig. 6 Stress-displacement curves with an unload/reload cycle for a composite with $A = 1.14$ and $\Gamma = 0$, corresponding to $\text{Ti}_3\text{Al/SiC}$ composites. (a) Comparison of fiber pulling responses for smooth and rough interfaces ($\theta = 0.2$ rad for unload/reload curves of rough interface). (b) Influence of roughness angle on unload/reload curves for rough interface ($x = 5$). (c) Comparison of fiber pushing responses (σ_a and u both negative) for smooth and rough interfaces ($\theta = 0.2$ rad).
- Fig. 7 Axial fiber stresses during pushing: (a) system that does not spontaneously debond at free surface ($\gamma > |\sigma_{fd}^+|$); (b) system that undergoes spontaneous debonding ($\gamma < |\sigma_{fd}^+|$). Lightly shaded area represents positive contributions to the displacement; darker areas represent negative contributions.
- Fig. 8 Comparison of stress-displacement response for an interface that has constant sliding resistance over the debonded region with the responses for rough interfaces with Coulomb friction.

(a)

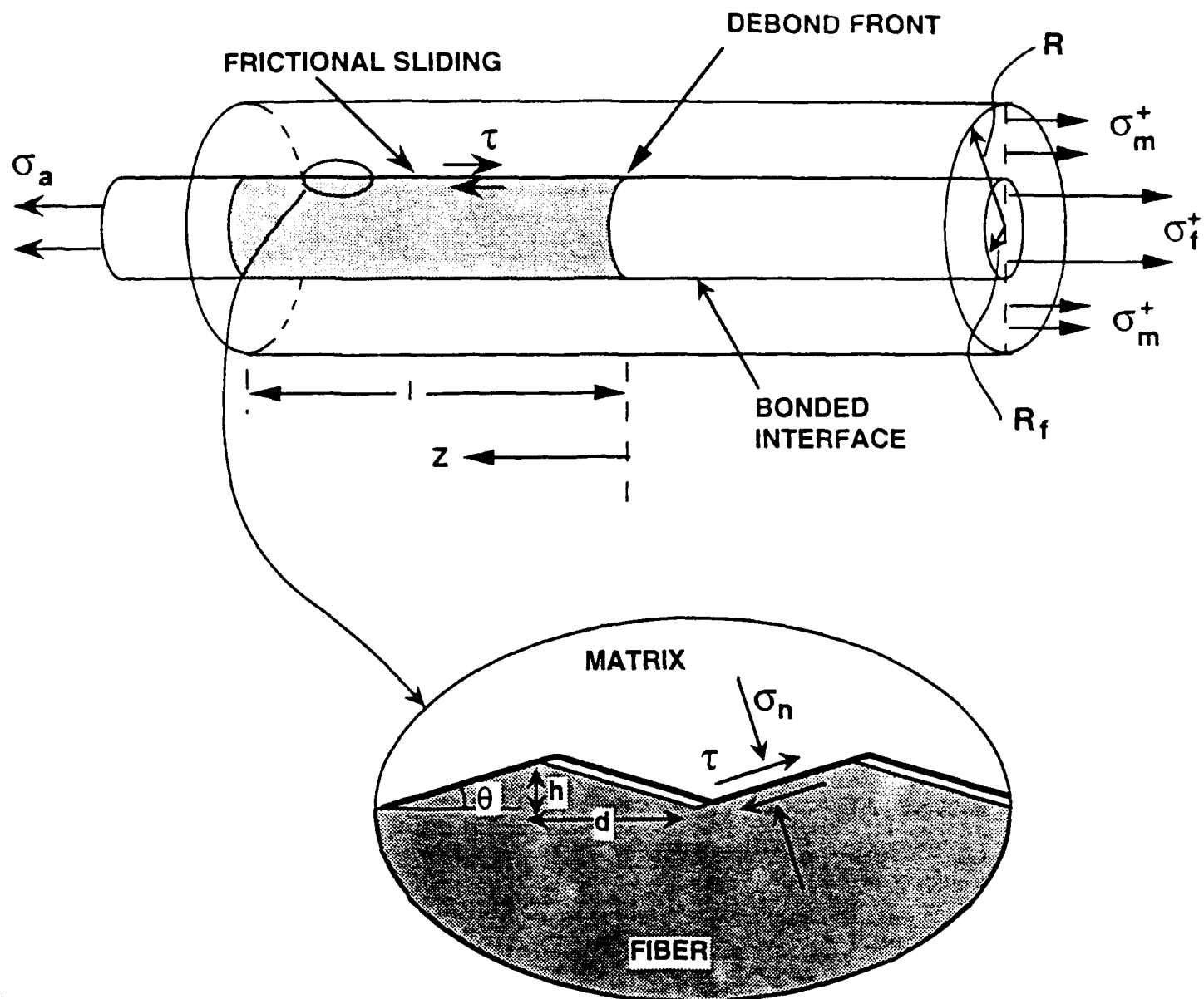


FIG. 1

(b)

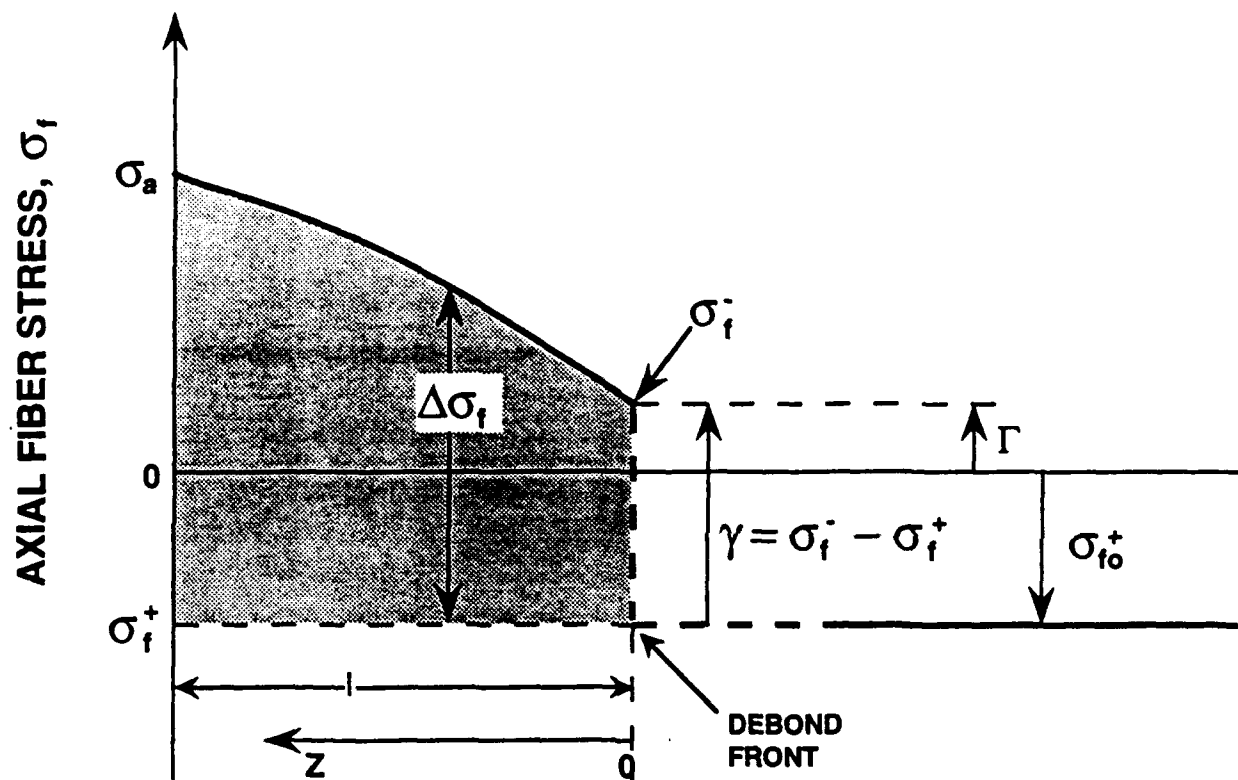


FIG. 1 (b)

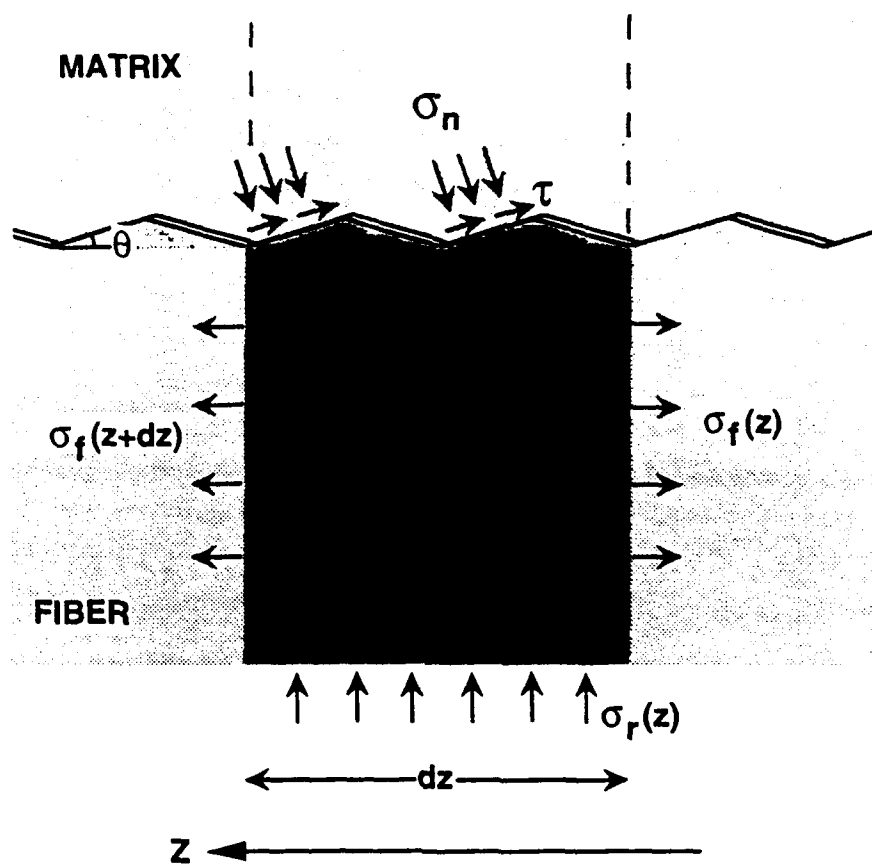


Fig. 2

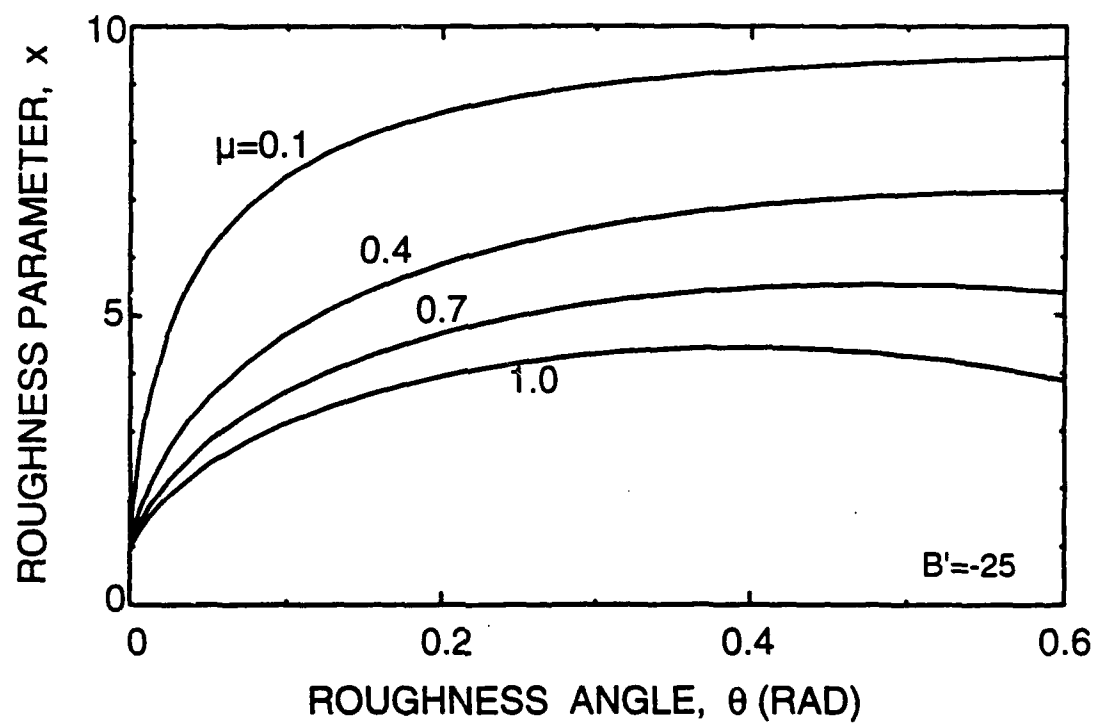


Fig.3

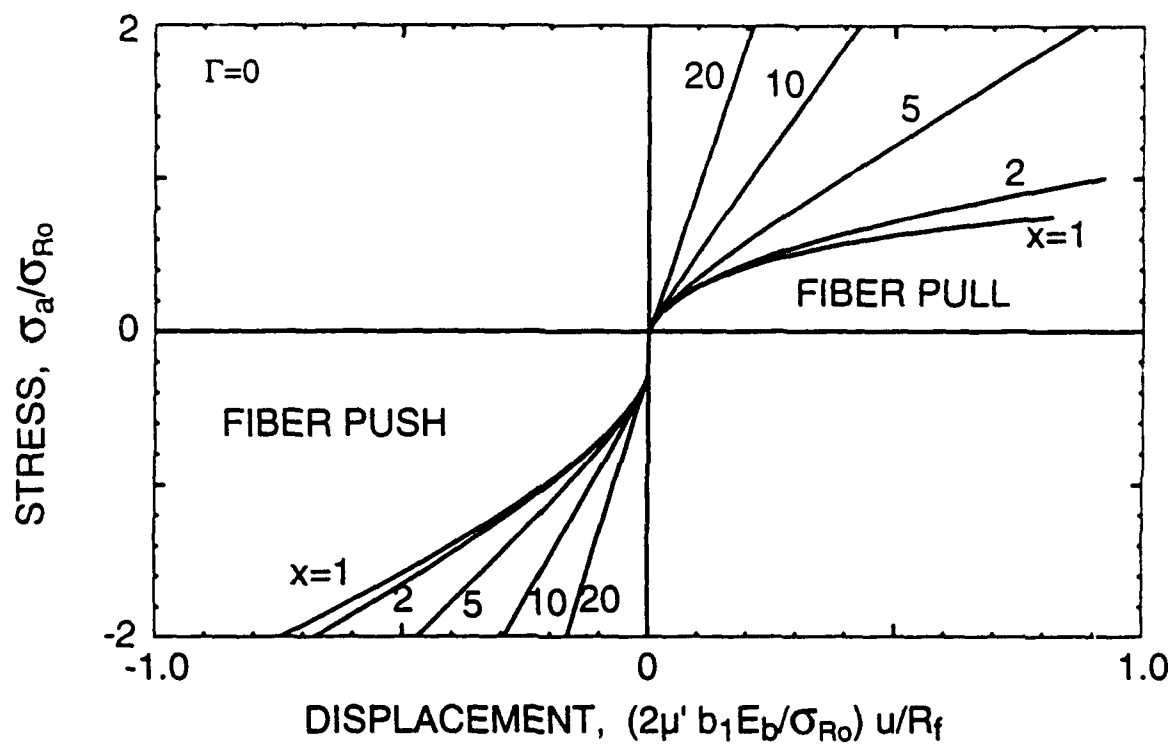


Fig. 4

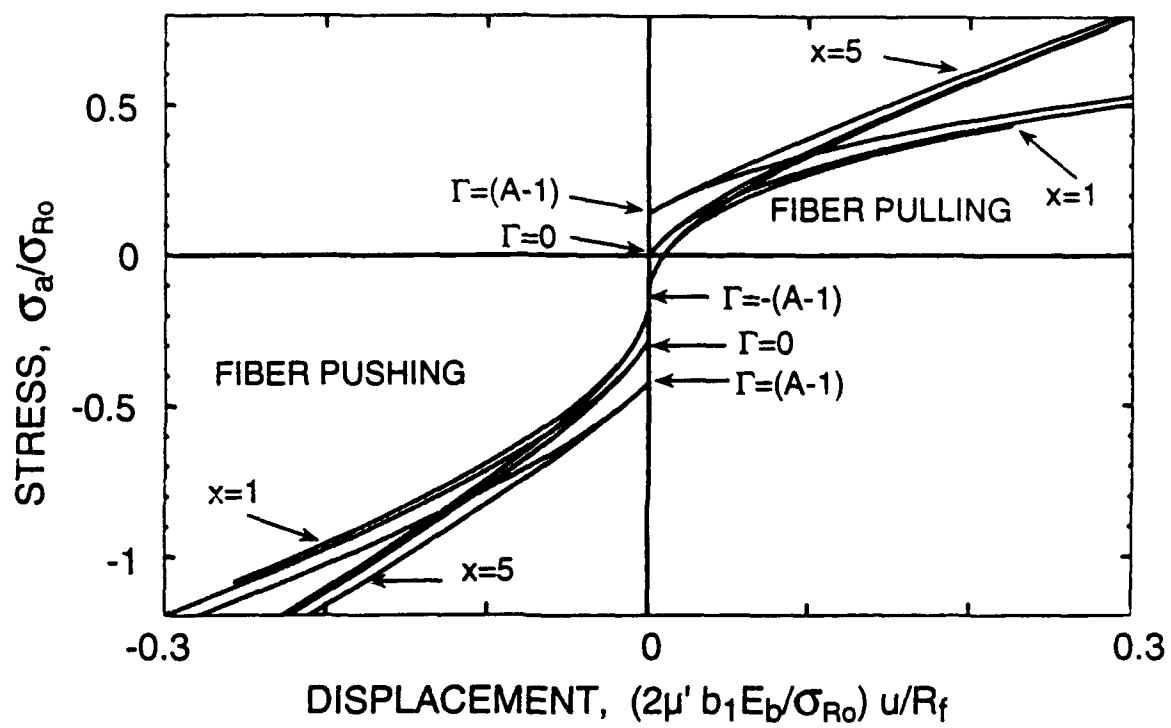
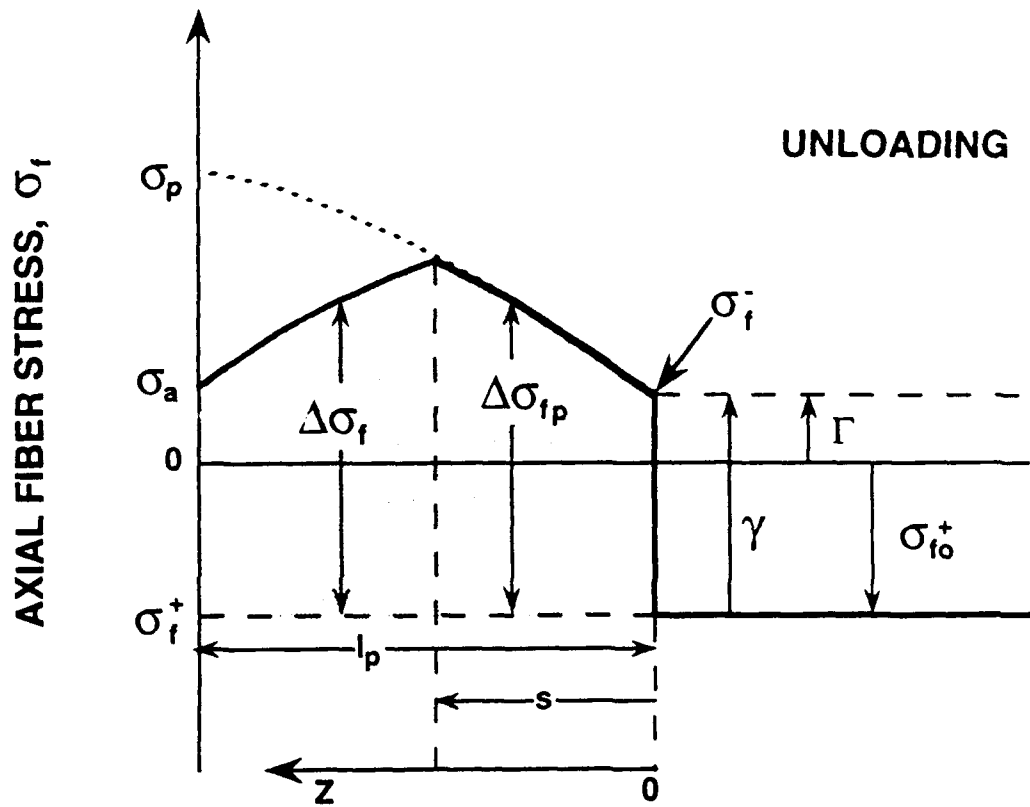


Fig 4.

(a)



(b)

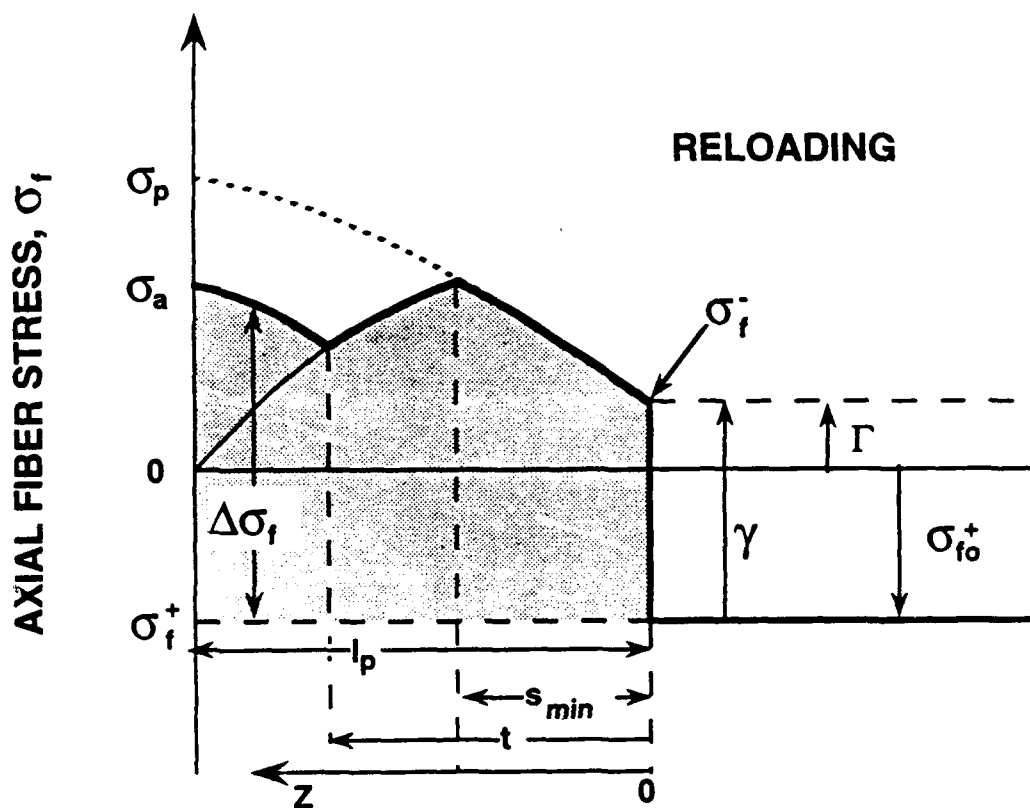


FIG. 5

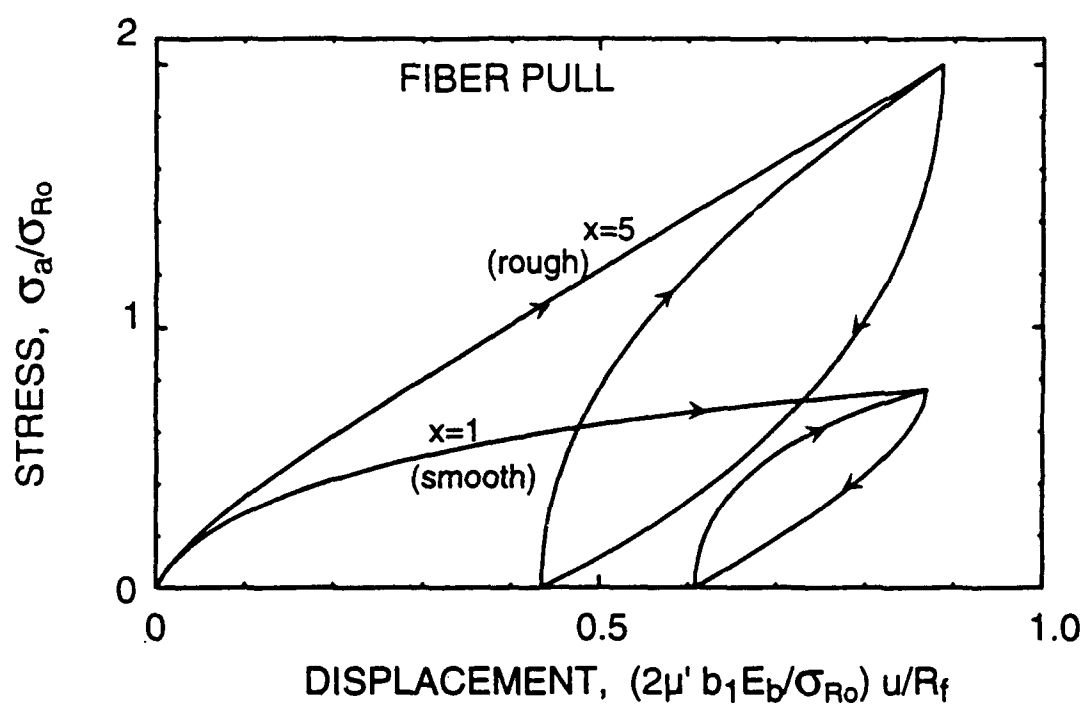


Fig. 6(a)

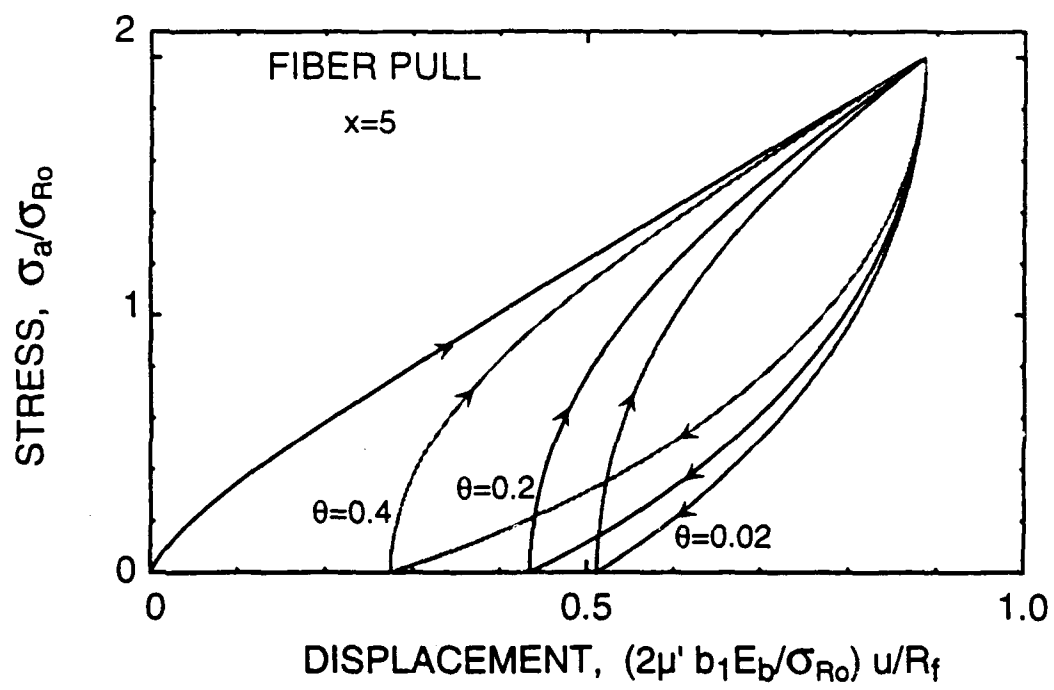


Fig. 6 (b)

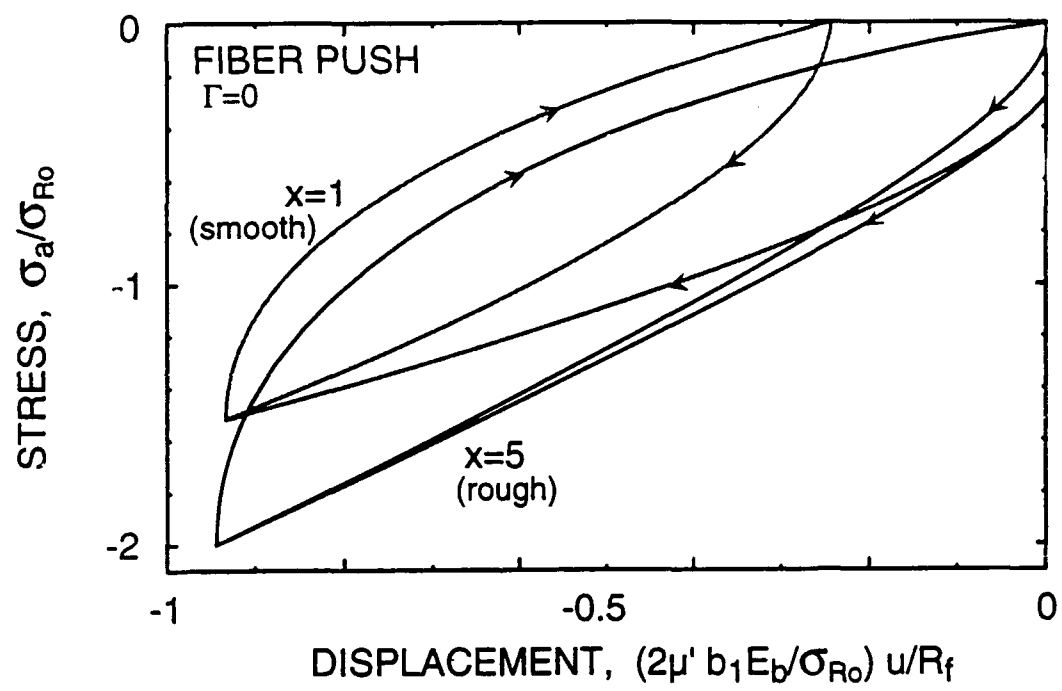
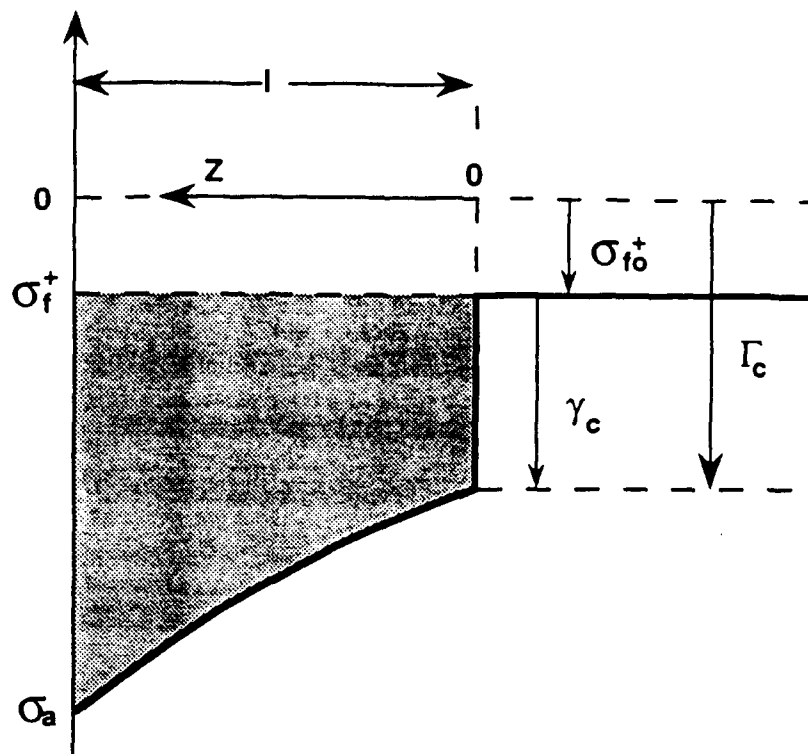


Fig. 6 (c)

(a)

AXIAL FIBER STRESS, σ_f



(b)

AXIAL FIBER STRESS, σ_f

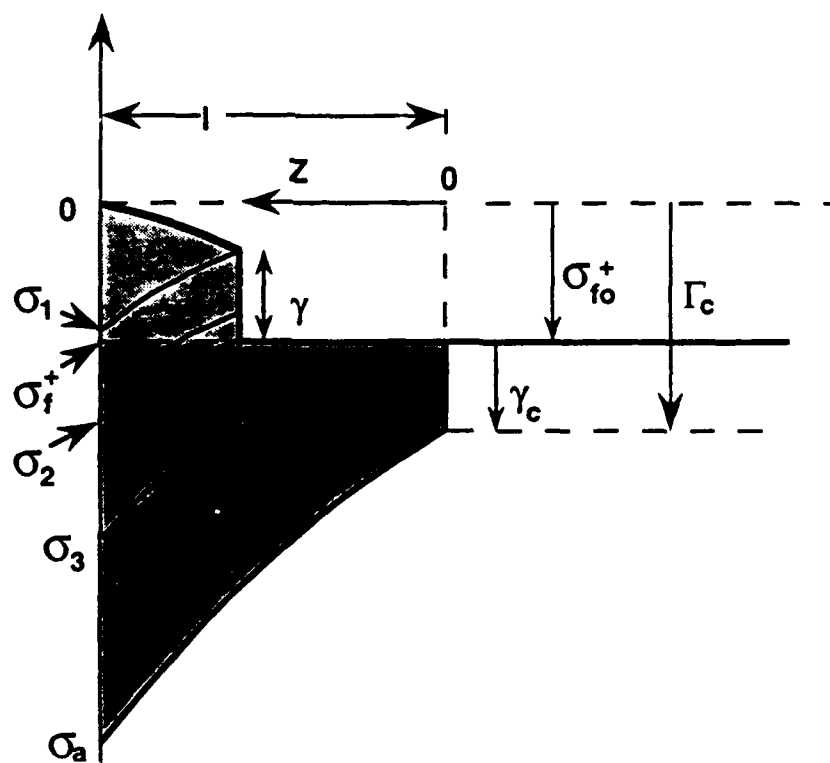


Fig.7

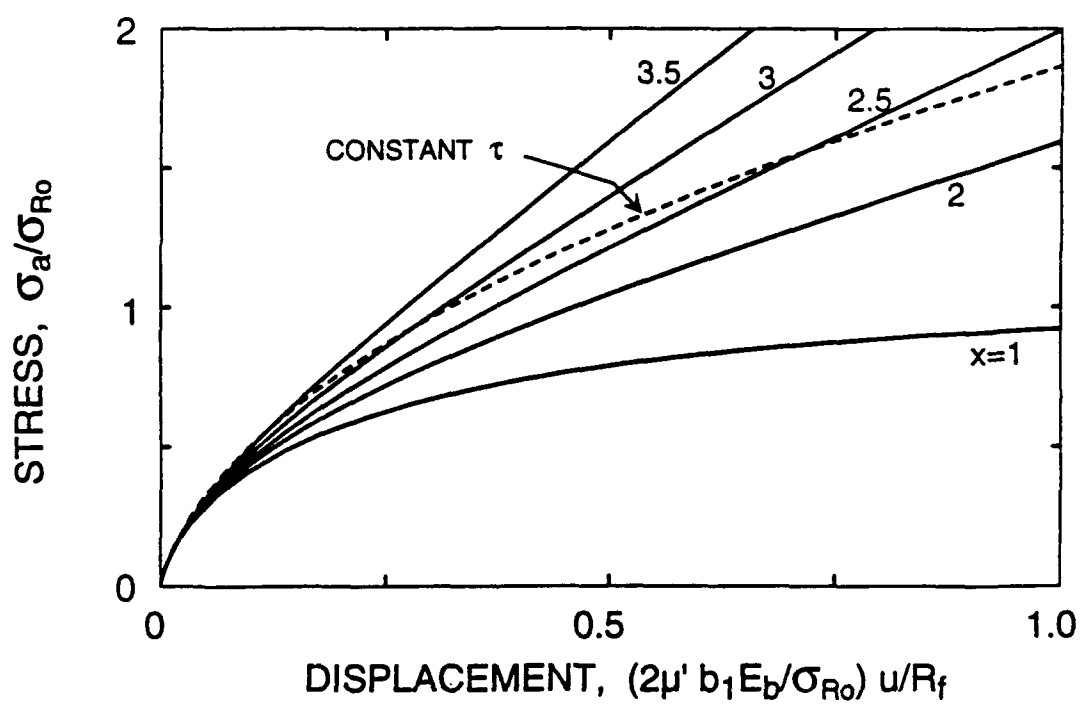


Fig. 8

6.3 The Determination of Interfacial Properties from Fiber Sliding Experiments

in preparation